The Electronic States and Electron-Lattice Interaction in the Silver Halides: Photoemission Studies

by

Robert Steven Bauer

December 1970

Technical Report No. 5218-3

CASE FILE
COPY

SOLID-STATE ELECTRONICS LABORATORY

STANFORD ELECTRONICS LABORATORIES

STANFORD UNIVERSITY · STANFORD, CALIFORNIA

THE ELECTRONIC STATES AND ELECTRON-LATTICE INTERACTION IN THE SILVER HALIDES: PHOTOEMISSION STUDIES

by

Robert Steven Bauer

December 1970

Solid-State Electronics Laboratories
Stanford Electronics Laboratories
Stanford University   Stanford, California

DEDICATED TO

ROSYLAND

FOR EVERYTHING

ABSTRACT

Photoemission from the silver halides has been studied between
room and liquid nitrogen temperatures in order to investigate the elec-
tron energy states of these solids. Certain structure in the energy
distribution curves (EDCs) of electrons photoemitted from these com-
pounds was discovered to sharpen by over an order of magnitude more
than the change in thermal energy. The techniques are described which
were developed to measure for the first time the dependence of UV photo-
emission on temperatures ranging continuously from 295 to $80°K$. From a
detailed discussion of the possible effects of temperature variation on
photoemission from solids, it is suggested that the dramatic EDC tempera-
ture dependence is due to a very strong interaction of the electrons with
lattice. A model is proposed to describe this wherein the dynamic varia-
tions of the electronic states are caused by a fluctuating valence,
halogen p-silver d mixing due to the thermal vibrations of the lattice.
Applying this dynamic wavefunction hybridization model in a very general
way, the silver states with almost pure 4d symmetry could be located
by experiment with reasonable certainty for the first time; these loca-
tions were 3.7, 3.3, and 4.4 eV below the highest filled states in AgBr,
AgCl, and AgI respectively. By using a very simple approximation of
$k = 0$ optical phonons and restricting the extent of the interaction to
about one nearest neighbor distance, the proposed model was applied to
the AgCl energy bands and pressure dependent optical absorption data.
These computations demonstrate its plausibility by predicting magni-
tudes for dynamic broadenings of peaks in the density of states and
their temperature dependences which are quite comparable to the corre-
sponding EDC values. Many other complex features of the data are examined
in detail and first order interpretations are presented. The information
about the optical excitation process and electronic states determined
from these studies is summarized and compared to existing estimates for
the band structures of these solids.

iii

TABLE OF CONTENTS

LIST OF FIGURES

LIST OF TABLES

LIST OF SYMBOLS

α Absorption Coefficient

β The Hexagonal (Wurtzite) Phase of AgI

γ The Cubic (ZnS) Phase of AgI

$\delta(\epsilon_n - \epsilon_m)$ Kronecker Delta,

         $= 1$ if $n = m$

         $= 0$ otherwise

Δ Change in a Quantity

$\Delta\alpha$ Error in the Absorption Coefficient

$\Delta\alpha_f$ Error in the Absorption Coefficient at the Highest Photon
Energy of Reflectance Measurement

ΔS Discontinuity in the Slope of the Reflectance at the Highest
Photon Energy of Measurement

ϵ_2 Imaginary Part of the Dielectric Constant

ϵ_n Energy Eigenvalue for the Free Atomic Level of Quantum Number   n

θ Angle of X-ray Diffraction

Θ Phase of the Reflectivity

Θ_D Debye Temperature

κ Extinction Coefficient

ξ Wave Vector Dependent Parameter, $|k|a$

ρ Density

τ Thickness

ϕ Angle of the Quartz Crystal Monitor to the Source Measured
from the Vertical

Φ_n Electronic Wavefunction in the Solid Corresponding to the Atomic
Orbital with Quantum Number   n

χ Integration Parameter

Ψ_n Atomic Wavefunction (or Orbital) with Quantum Number   n

a   Lattice Constant for the NaCl Lattice, the Shortest Distance
Between Like Atoms

A	Reflectance Extrapolation Power Law, Photon Energy Dependence Parameter
a	Number of Atoms in the Solid
APW	Augmented Plane Wave Method of Energy Band Calculation
C	90% EDC Peak Width Exponential, Temperature Dependence Parameter
C$'$	Density of States Peak Width Exponential Temperature Dependence Parameter
d	Differential of a Quantity
D	Vertical Distance of the Quartz Crystal Monitor from the Source
e	Natural Exponential Base
E	Electron Energy Referred to the Highest Occupied State
E_{EX}	Exciton Energy
E_F	Fermi Energy
$E_n^{(M)}$	Madelung Energy for the States Derived from the Atomic Orbital with Quantum Number n
E_v	Energy of the Valence Band Maximum
$\mathcal{E}$	Energy Difference Between the Energy in the Solid and the Free Atom Value
EDC	Energy Distribution Curve
f	Frequency of the Quartz Crystal Monitor
F	Incident Photon Flux
h	Planck's Constant
$\hbar$	$\dfrac{h}{2\pi}$
$\mathcal{H}$	Hamiltonian
hν	Photon Energy
hν_D	Debye Energy
hν_f	Highest Photon Energy of Reflectance Measurement
hν_m	Highest Photon Energy of Calculation of the Kramers-Krönig Integral
hν_0	Photon Energy of the Phase of the Reflectance Calculated by the Kramers-Krönig Integral
HV	High Vacuum
i	$\sqrt{-1}$

I   Photocurrent

j   Unit Cell Index

$k, \vec{k}$ Reduced Wave Vector, Crystal Momentum

k_B Boltzmann Constant

k_f Crystal Momentum of the Final State of a Transition

k_i Crystal Momentum of the Initial State of a Transition

k_{PHONON} Phonon Wave Vector

LN_2 Liquid Nitrogen

LV   Low Vacuum

m   Atomic Mass

$\bar{m}$ Mean Mass of Two Atoms

n   Quantum Number

N   Energy Distribution of Photoemitted Electrons Normalized to Quantum Yield (Per Incident Photon)

$\mathscr{n}$ Energy Distribution of Photoemitted Electrons Normalized to Absolute Quantum Yield (Per Absorbed Photon)

$(pd\sigma)_1, (pd\sigma)_2$ Typical Tight-Binding Matrix Element Parameter for First, 1, and Second, 2, Neighbors

P_{MAX} Maximum Pressure During Evaporation

q_e Charge of an Electron

r   Reflectivity

$\vec{r}$ Position Vector

$\vec{r}_j$ Position Vector of the jth Atom Relative to the Origin

R   Reflectance, $|r|^2$

R_f Reflectance at the Highest Photon Energy of Measurement

R_m Reflectance at the Highest Photon Energy of Calculation of the Kramers-Krönig Integral

s   Atomic Orbital for s State

$S_{k,n}$ Normalization Correction to the Energy of the States Derived from the Atomic Orbital with Quantum Number n for Crystal Momentum k

SS   Sodium Salicylate

t   Time

T   Sample Temperature

T_s Substrate Temperature during Film Deposition

$T(E)$ Threshold Function

u RMS Ionic Displacement

u_0 Zero-point RMS Ionic Displacement

$U_n^{(1)}$ "Crystal Field" Energy for the States Derived from the Atomic Orbital with Quantum Number n

$U_{k,n}^{(2)}$ Two-center Overlap Energy for the States Derived from the Atomic Orbital with Quantum Number n for Crystal Momentum k

UHV   Ultra-High Vacuum

UV   Ultraviolet

v Free Atomic Potential Energy

$v^{(M)}$ Madelung Potential

V Potential Energy of the Solid

V_R Retarding Voltage

$\dfrac{\Delta V}{V_0}$ Fractional Volume Change

w Width of Density of States Peak

w_0 Frozen Lattice, Density of States Peak Width

W Width of EDC Peak at 90% of its Maximum Height; 90% Width

W_0 Frozen Lattice, 90% EDC Peak Width

x,y,z Atomic Orbitals for p States

$xy,yz,zx,x^2-y^2,3z^2-r^2$ Atomic Orbitals for d States

Y Quantum Yield; Yield of Electrons Photoemitted per Incident Photon

$\mathcal{Y}$ Absolute Quantum Yield; Yield of Electrons Photoemitted per Absorbed Photon

ACKNOWLEDGEMENTS

I. INTRODUCTION

The proximity in energy of the Ag(4d) electronic states to the halogen p states makes the valence structure of the silver halides very complex. Because of this, it is very difficult to determine theoretically or experimentally even such basic characteristics as the atomic origin of the highest filled valence states. The present investigation was undertaken to experimentally determine features of the electronic structure of the silver halides. The location and role of the states derived from the atomic Ag(4d) orbitals in the overall valence structure was of particular interest.

Perhaps the most powerful technique available to study the electron states over a broad energy range is the measurement of the energy distribution curves (EDCs) of electrons photoexcited by ultraviolet (UV) light and emitted from the solid into vacuum. One measures not only the transition energy of a photoexcited electron, as in the usual optical experiment, but also the final state energy of the electron. In the past, the primary method for using this data to determine features of the electronic structure was first to determine the nature of the optical excitation process (i.e., whether crystal momentum, k , was conserved in the transitions). Depending on these findings, the EDCs would then either (1) be compared with distributions predicted from transitions in a calculated energy band structure, or (2) if k is not conserved, be used to predict a density of states which could then be compared with theoretical calculations. These procedures have proved very fruitful for (1) solids whose bands can be calculated with a reasonable degree of accuracy (e.g., group IV or III - V semiconductors) or, if such detailed information is lacking, for (2) materials whose electronic structure is sufficiently simple that one can estimate its nature with reasonable accuracy (e.g., the alkali halides) or even if nothing is known theoretically, for (3) solids in which non-conservation of k is a good approximation. Unfortunately the silver halides do not fit into

any of these categories. Their EDC structure behaves with hν varia-
tion as if k were conserved in at least some of the transitions. In
addition, its electronic structure is so complicated and poorly under-
stood that it has been the subject of speculation for nearly two decades.
Thus, standard photoemission investigation techniques could not be un-
ambiguously used to determine details of the silver halide electronic
states.

In an attempt to sharpen the EDC structure, which at high hν was
quite broad, and thereby perhaps gain more detailed information, the
samples were cooled to liquid nitrogen (LN_2) temperatures using exist-
ing equipment of Krolikowski[1] and DiStefano[2] with modified cooling tech-
niques. Some structure in the EDCs showed enormous changes upon cooling
(i.e., many tenths of an eV) compared to changes observed for other
solids, while other structure showed only small changes, if any (i.e.,
changes on the order of the change in $k_B T$). This effect was not only
interesting for its own sake but also could be utilized as a valuable
new experimental tool in the study of the electronic states. The dif-
ferences in temperature dependence of the various EDC peaks were used
to identify the nature of the states from which the corresponding elec-
trons were photoexcited. This appears to be the first example of tempera-
ture dependent photoemission data yielding significant additional in-
formation about the electronic states of the solid being studied. This
is because the silver halides possess a number of unique properties; of
primary importance is that only the hybridized electronic states strongly
interact with the lattice. By varying the vibrational energy of the
lattice through temperature variation, we thereby have a method of sepa-
rating out these states from the "purer" electronic states. The existing
equipment was not suited for the detailed temperature dependent photo-
emission study needed to take advantage of this new electronic state
analysis technique. Major modifications of existing equipment had to be
made, new apparatus was designed and built, and new techniques were
developed to measure, for the first time, the dependence of EDCs on
temperatures ranging continuously from room to liquid nitrogen values.
Using these techniques, the Ag states with almost pure 4d symmetry

could be experimentally located, for the first time. More information was determined about the electronic states than was ever known before. The methods of using UV photoemission to study the electronic states of solids were thereby extended to yield information about the states of the silver halides which at best would have otherwise been mere speculation.

This very strong electron-lattice interaction in the silver halides also can be used in the study of the optical excitation process. In addition to its significance in the photographic process, the photoexcitation process is of particular interest because these compounds are intermediate between classic narrow band gap semiconductors and wide band gap insulators. This suggests that crystal momentum might be conserved in some transitions while not in others. Since cooling the solid will reduce the lattice vibrational effects on the electronic states, a temperature dependence of the selection rules for the photoexcitation processes may be observed. In particular, k-conservation may become an important selection rule at low temperatures for transitions in which k is not conserved at high temperatures.

This investigation of the electronic states and optical excitation process of the silver halides using temperature dependent photoemission techniques is described in detail in this report. The amount of knowledge accumulated over the years for AgCl and AgBr far exceeds that for AgI. One reason for this is that the former compounds are more similar to each other than to AgI. This is true for such characteristics as crystal structure and ionicity. Not only does the greater knowledge accumulated on AgCl and AgBr make their photoemissive properties simpler to analyze, but also some of their characteristics make them easier to interpret (e.g., greater ionicity and simpler crystal structure). In addition, the EDCs of AgI differ significantly in character from the other silver halides. Thus, AgCl and AgBr are treated together first and then the photoemission from AgI is discussed and compared with the other halides. This thesis is written differently from previous ones. Rather than presenting the experimental data all at one time or dividing it by individual materials or experiments (e.g., high and low temperatures), the

3

data is presented according to the conclusions which are determined from it. Only the new aspects of this work will be discussed. References to previous papers or theses will suffice for such things as standard photoemission experimental techniques and theoretical models.

Following a discussion of the effects of temperature variation on photoemission from solids in the next chapter, relevant AgCl and AgBr properties are presented in Chapter III. A discussion of experimental techniques will be presented in Chapter IV which includes not only the sample preparation and cooling techniques but also sample reproducibility and stability and parameters affecting silver halide EDCs. In Chapter V, the temperature dependent broadening of AgCl and AgBr EDCs is discussed. The data in the low hν region (< 11 eV) is presented. The dynamic hybridization model is discussed in detail and calculations are presented using a tight-binding band model,[3] pressure dependent optical data,[4] and atomic wavefunctions and potentials.[5] In Chapter VI, the Ag(4d) electron states in these two halides are located from the temperature dependent EDC data above 11 eV. Windowless experiments (hν > 11.8 eV) performed to confirm these locations by probing the entire valence band width are also discussed. The other major temperature dependent AgBr and AgCl EDC features are related to the characteristics of the conduction states in Chapter VII. In Chapter VIII, the new information about the AgCl and AgBr electronic states determined by this study is summarized. These results are compared to published energy bands[3,6] and the photoemissive properties of the cuprous halides.[1] The optical excitation process in these silver halides is also discussed in this chapter. The photoemission EDCs of AgI are discussed in Chapter IX and by comparison to the other silver halides, estimates are made for the electronic states of this solid. Some of the conclusions of this work and suggestions for future studies are presented in Chapter X.

II. EFFECT OF TEMPERATURE ON PHOTOEMISSION FROM SOLIDS

In this chapter the temperature dependence of the photoemission
EDCs observed for many classes of solids will be reviewed. As will be
seen, the dependence of silver halide photoemission on temperature is
fundamentally different from that measured from most other solids
studied to date. Theories which have been used in the past to explain
temperature dependent optical phenomena will be discussed. A dynamic
hybridization of the electronic wavefunctions is proposed as the most
plausible explanation for the difference in silver halide photoemission
from that of other solids. Only the main features of the data and of
the arguments that explain the effects are presented. Detailed discus-
sion is deferred to the main text; in particular, calculations based on
the dynamic hybridization model, which support the applicability of this
model to the silver halides, are given in Chapter V.

A. Temperature Dependent Mechanisms Affecting the Photoemission Process

To understand the changes which occur in photoemission upon cooling
a solid, one must consider the physics of both the temperature varia-
tion and photoelectron emission processes. The temperature of a solid
is lowered by reducing the vibrational energy of the crystal lattice.
Thus, any changes which occur in the photoemission must be related to
the altered ionic vibrations. Probably the most convenient temperature
parameter describing the dynamical motion of the lattice is the Debye
temperature, Θ_D. For our purposes, this temperature can be thought
of as the thermal energy corresponding to the high energy cutoff of the
phonon dispersion in the Debye approximation. That is, if the phonons
are considered as having a constant distribution from zero to the Debye

energy $h\nu_D$, then the Debye temperature is defined as

$$\Theta_D = \frac{h\nu_D}{k_B} \qquad (2.1)$$

The Debye approximation is most applicable to the acoustic phonon modes.
Thus, for a real solid one can think of the Debye temperature as the
temperature at which the most energetic acoustic phonons are just
excited. In most cases, this is very nearly the energy at which the
optical modes are first excited. A couple of good references to this
viewpoint of the Debye temperature are Smith[7] and Ziman.[8] The
references[9-12] were used as sources for the Debye temperatures quoted
in this thesis.

Photoemission can be thought of as a three-step process: optical
excitation of an electron followed by transport to the surface of the
solid with eventual escape into vacuum. In considering the effects of
temperature variation on photoemission, it is most helpful to consider
the effects in each of these steps separately.

1. Escape

In order for the photoelectron to escape from the solid into vacuum,
it must overcome the potential energy barrier at the surface. The energy
associated with the velocity component normal to the surface must be
greater than the electron affinity. This defines a "cone" of velocities
with which an electron can escape the solid. A "threshold function",
$T(E)$, defined as the probability for an electron with energy, E ,
at the surface to escape from the solid is used to account for this.[1]

In practice, $T(E)$ is usually taken as a step function, a free-
electron escape function with an $E^{\frac{1}{2}}$ dependence, or used as a phenome-
nological variable. This function will be affected by any changes in
the surface potential (e.g., change in population of the surface states)
and of course, by a change in the electron affinity. The important
point to realize is that a change in $T(E)$ upon cooling will be seen
primarily near threshold and will be uniform for all the EDCs. Since,
as will be seen, there are large EDC changes upon temperature variation
many eV above the threshold, it appears that an enhanced photoelectron

escape is not the process which is of primary importance. The possibility of an increased escape probability due to enhanced scattering into the escape cone will be considered in the next section on transport.

2. Transport

The photoelectron can change its energy on the way to the surface by scattering. The scattering processes of importance when considering temperature variations are those which involve the interaction of the electron with the lattice. The most common mechanism of this type is the change in electron energy caused by the creation (emission) or annihilation (absorption) of a phonon. The resulting changes in the electron energy will appear in the measured EDC as a replica of the actual final state energy just after the optical excitation which is broadened and slightly shifted to lower energies. Since the escape depths of the photoelectrons at these energies are normally less than 100 $\overset{\circ}{A}$, the total scattering history of any electron usually involves only a small number of phonons. In the silver halides, the LA phonon energy is on the order of 8 meV and the LO phonon energy around 20 meV.[13,14] Thus, the energies involved in such scattering events are normally much less than 0.1 eV. As the temperature is lowered, the probability of absorbing a phonon is greatly diminished and hence the electron-phonon scattering will be reduced. This will cause a sharpening in EDC structure and a shift due to the asymmetry of this narrowing. However, since the energies in the high temperature broadening are so small to begin with, the sharpening and shifting of EDC structure will be very small, normally being comparable to the change in $k_B T$. As will be seen in section C, the changes in the photoemission upon cooling a wide variety of solids are quite small. For the most part, these changes can be explained simply by this process of absorption or emission of a few phonons by the photoexcited electron.

One other transport mechanism involving the electron-lattice interaction which we must consider is that of the electron energy being perturbed by the energy of the polaron. A polaron is formed by an electron moving in an ionic crystal and the polarization of the lattice around it which will move with the electron.[8] This moving electron thus

7

has the possibility to excite or absorb "virtual phonons" no matter what its velocity. The effective energy of the electron will be decreased continually as it moves through the solid with the loss being a function of the electron's velocity.[15] This polaron "scattering", consisting of the photoelectron surrounded by a cloud of "virtual phonons",[8] is only applicable to ionic crystal like the silver or alkali halides. This process will be temperature dependent since one can imagine the amount of lattice polarizability being affected by the amplitude of the vibrations of the ions about their equilibrium lattice sites. The major limitation of this mechanism is that the interaction can only result in a loss in electron energy and hence an asymmetric EDC broadening with a peak shift to lower energy. As will be seen by the data presented in this thesis, the measured peak shift is at least an order of magnitude less than the broadening and is negligible in most cases. Thus, this mechanism is probably not applicable.

The final state energy of the photoelectron following excitation may be greater than the electron affinity of the solid but because of the direction of its velocity, it does not fall within the escape cone; thus, if its velocity remains unperturbed, it will not be emitted into vacuum. The electron may however interact with the lattice thereby changing its real momentum but not appreciably changing its energy. There is then the possibility of scattering into the escape cone and obtaining an enhanced number of electrons emitted.[16] Such a scattering process would be temperature dependent by virtue of the temperature dependence of the lattice vibration. The major effect this would have on the EDCs is a modulation of the peak strengths. However, this would probably only broaden the structure on the order of the optical phonon energy, about 20 meV.[13,14] This is clearly too small to explain the measured silver halide temperature dependent broadening.

3. Optical Transition

The optical excitation process is a light-induced transition of an electron between two states of the solid. In considering the affect of temperature variation on the excitation, we must examine the transition and the states involved in the transition separately. The former will

8

be discussed here while the latter is presented in section B. Transitions which conserve crystal momentum, k, may do so not only by being "vertical" ($k_f - k_i = 0$) but also by phonon emission or absorption ($k_f - k_i = \pm k_{PHONON}$). Such "indirect" transitions (not to be confused with "nondirect" which need not conserve k) would be temperature dependent since at very low temperatures only phonon emission would be possible. This type of transition would be very difficult to observe in photoemission except near threshold since it is a second-order process. Since the large temperature dependence which is observed in the silver halides occurs many eV above threshold for quite strong EDC structure (≈ 0.05 electrons per incident photon per eV), it is unlikely that this is an important process.

The matrix elements involved in the optical transitions may be dependent on temperature. This would occur if one of the states has a hybridized basis function which was temperature dependent because of a vibrationally dependent mixing (this dynamic hybridization will be discussed fully below). The temperature dependence of the dipole transition matrix element will be much smaller than that of the energy of the hybridized state itself. Thus, this will probably be a second-order process and not of primary importance in analyzing the observed photoemission temperature dependence.

The mechanisms discussed above deal directly with the photoemission process itself. As was indicated and will be abundantly clear in section C, none of these involve large enough energies to explain the giant changes in silver halide EDCs upon cooling. It is reasonable to expect that what is occurring in the EDCs is characteristic of the electronic states of the solid rather than the photoemission used to study them. Temperature dependent processes which affect the electronic states directly are discussed below.

B. Temperature Dependent Mechanisms Affecting the Electronic States
    of Solids

There are many temperature dependent processes which have been proposed to explain various optical phenomena. Most of these deal with

changes in the optical absorption edge resulting from the temperature dependence of the energy band gap. This is done because optical absorption is an integrated effect from the onset of transitions up to the photon energy of measurement. Thus, only the edge will be characteristic of the effect on a particular set of electron energy levels. In photoemission, however, at each photon energy the distribution in energy of the photoemitted electrons is measured. Therefore, even though most theories have been applied to the band gap and are discussed in these terms below, the physical processes are equally applicable to all the states and hence the measured EDCs. Only those theories which are most prominent will be discussed. As will be clear, none of these involve energies large enough to explain the observed silver halide EDC changes. As an extension of two of these treatments a dynamic hybridization model is proposed to explain the effects. Though a fairly extensive search of the literature was made, we have not found such a process discussed.

1. Deformation Potential

The effect on the electronic states of the thermal contraction of the lattice has been considered in the covalent bonding case.[17] This is the classical treatment of the temperature dependence of the band gap in terms of deformation potential theory. The decrease of the lattice constant is expressed in terms of an average dilatation of the lattice. The theory predicts an increasing band gap with decreasing temperature. Such an effect certainly occurs in solids as is evidenced by the normal shift of absorption coefficient, α , to higher photon energy upon cooling (e.g., the silver and alkali halides shown in Figures 3.8 and 3.9 in Chapter III). However, a purely thermal lattice contraction effect can only account for a small part of the observed shifts.[17] In fact, there appear to be no known cases where such a treatment of the temperature dependence is adequate.[18] This is significant not only because it shows that this is not the only mechanism, but also because many other processes are comparable in magnitude to the thermal expansion effect.

One of the most extensively investigated temperature dependent optical phenomena is Urbach's empirical relationship between the optical absorption edge of nonmetallic solids and temperature which was first discovered for the silver halides.[19] At present there is no single satisfactory theory which can explain its existence in such a wide variety of solids over such a large range of temperature and absorption coefficient. A good general review is given by Knox.[20] We will briefly discuss a couple of mechanisms proposed by Dexter which appear to be the most physically sound. Dexter[18] extended the deformation potential approach, which had been used to explain the uniform contraction of the periodic lattice, to account for the non-periodicity of the vibrating lattice. Because of the expansions and contractions associated with the lattice, there exist local deformation potentials which result in local variations in the band gap. The band gap will be statistically distributed in accordance with the probability that a constant uniform dilatation is realized. After taking the proper probabilities and averages, the resulting function behaves like Urbach's rule, but only over a much smaller range of temperature and absorption coefficient than is observed. The failure of this theory to lead to quantitatively correct results is probably due to the use of a simple dilatation for the lattice distortion.[20] In the thermal contraction case it can be used effectively since the lattice is undergoing a uniform deformation. However, using it for the lattice vibrations completely smooths the details of the electron-phonon interactions. In the former case, one could conclude that the thermal contraction was clearly not the dominant process in producing a shift in α with temperature variation. In this case, all that can be concluded is that a local distortion of the lattice cannot be treated by deformation potential theory.

2. Dynamic Stark Shift

Another method of treating the local distortion is to consider its effect in terms of the local electric fields which are produced by the optic modes of the lattice vibrations.[21] This approach is based on the usual quadratic Stark shift of the electron energy which is produced by the application of a uniform electric field to a solid. For the optical

phonon modes of a polar crystal, a vibrating atom in a crystal experiences electric fields due to the local deformations of the lattice. The magnitude of the field is determined by the degree of ionicity and/or the amount of overlapping of the charge distributions. Thus, the line shape for an optical transition will be shifted in proportion to the square of the local field and then averaged over the field with a weighting factor which is proportional to the probability of finding a given field strength at an atomic site. This approach is very promising for explaining Urbach's rule because it does not require a periodic potential and can thus be applied to the many diverse solids in which the rule is applicable (e.g., amorphous solids and impurities in alkali halides). For the temperature dependent changes in photoemission EDCs, this is precisely one of its shortcomings. This theory (and Urbach's rule for that matter) is applicable to amorphous solids and the alkali halides; in fact, KBr obeys Urbach's empirical relation over the largest temperature and absorption coefficient range of any solid studied.[20] As will be seen in section C, the effect on the EDCs of cooling the silver halides is different from the effect on most of the alkali halides. Thus, it would be difficult to understand how a theory which explains optical phenomena common to both could also explain a property so vastly different. In addition, Dexter's vibrational Stark shift assumes small phonon field strengths and uses second-order perturbation theory.[21] The effects on the silver halides are too large to be explained by such a second-order effect; the broadenings predicted by this vibrational effect (Figure 1 of reference 21) appear to be too small.

3. Polarization Field

This field effect of the optic phonon modes can be taken one step further for polar crystals in which the cooperation of many atoms produces a polarization field. This has a much greater perturbing effect on the electronic states than the effect of the local distortion of the lattice field.[22] The electron collides with the thermally vibrating lattice and thereby scatters into another state. Since the interaction is so strong in these solids, the scattering time, and thus the lifetime

of the states, is short. By the Heisenberg Uncertainty Principle, this shortened lifetime is equivalent to a minimum uncertainty in the energy of the unscattered electronic state. One of the significant things about this mechanism is that it deals with electronic states of the solids which change with time (i.e., nonstationary states). When averaged over an appropriately long period of time or large number of optical excitations, a broadened level would be detected. For polar solids, which the treatment applies to, this effect is about four times larger than the almost insignificant thermal contraction effect.[22] The theory has at least two shortcomings for our applications. First, the polarization field would be greater for the alkali than the silver halides since the former are more ionic. Thus, one would predict a larger broadening for the alkali halide energy levels and hence their EDCs. As will be seen in section C, this is the opposite of what has been measured to date. In addition, all electronic states would be affected the same by this process; this also is counter to the silver halide data.

4. Electron-Lattice Interaction Energy

Of course, the electrons are not only scattered by the vibrating lattice, they also interact with it. The electron-lattice interaction energy will change due to the lattice distortion. This interaction will thus depend on the state of the electron because of differing charge distributions among the states. Fan has found that in calculating this effect on an optical transition, it is only comparable to the thermal lattice contraction effect.[17] It is, however, three orders of magnitude larger than the scattering broadening of Radkowsky[22] for nonpolar solids. The small magnitude of Fan's treatment is perhaps the result of calculating a second-order perturbing effect on the stationary, frozen-lattice states of the solid. It should be noted that this method can only explain an increasing band gap upon cooling while the opposite effect has been observed.[23]

13

5. Temperature Dependent Pseudopotential

One can explain both directions of band gap change upon cooling if the "stationary" (i.e., time-independent), vibrating-lattice states of the solid are used. This is a method of taking into account the temperature dependence of the electronic states explicitly rather than calculating how the states, computed in a periodic, non-vibrating lattice, are shifted or broadened due to a departure from periodicity or a change in the lattice constant. This is done in the pseudopotential formalism by replacing each atomic form factor with a temperature-dependent form factor;[23] it is obtained by multiplying the normal form factor by the x-ray broadening, Debye-Waller factor. This is the same factor which is used to determine the rms ionic displacement discussed in Chapter V. The success of this method indicates that the electronic states are affected directly by the lattice rather than merely through a phonon perturbation of the electron's energy. (The author is grateful to Professor A. Bienenstock for pointing out the temperature dependent band gap work and helpful discussion of this last point.) This theory cannot be used directly for our considerations because it only applies specifically to solids which can be treated by pseudopotentials (i.e., where the "weak-binding" approximation is valid). For this reason, the calculated shifts are small; for PbTe, about 0.10 eV change is calculated.[23] Different considerations are needed for tight-binding solids, like the silver halides, but the general principle of temperature dependent electronic states is still important. To gain a full appreciation of this, the tight-binding approximation will be discussed fully below. The discussion will also be most valuable in understanding the factors which contribute to the energy bands of the silver halides discussed in Chapter III and the calculations presented in Chapter V.

6. Dynamic Hybridization

(a) The Tight-Binding Approximation.

In the tight-binding approximation for the electron energy states in solids, the electronic wave functions are formed from Bloch sums of atomic orbitals.[24] That is, a linear combination of atomic orbitals

(LCAO) is made in which the expansion coefficients are chosen to satisfy the Bloch periodicity condition. The electronic wavefunction in the solid is then given by

$$\Phi_{k,n}(\vec{r}) = \frac{1}{\sqrt{a}} \sum_{j}' e^{i\vec{k}\cdot\vec{r}_j} \Psi_n(\vec{r} - \vec{r}_j) \qquad (2.2)$$

formed by a superposition of the normalized atomic orbital for the quantum number n , $\Psi_n(\vec{r}-\vec{r}_j)$, centered on each atomic site, j (i.e., the atom j is displaced $\vec{r}_j$ from the origin). Note that even though each orbital is normalized, the sum will not be normalized due to the overlap between wavefunctions on neighboring sites. As a first approximation, we can use these unnormalized states to find the expectation value of the energy in the solid. From the eigenvalue equation

$$(\mathcal{H} - E_{k,n}) \Phi_{k,n} = 0 \quad , \qquad (2.3)$$

the electronic energy $E_{k,n}$ corresponding to the state derived from the atomic orbital n , for a given crystal momentum k , will be given by the solution of the secular equation for the hamiltonian, $\mathcal{H}$, which involves all the significant atomic states. The potential energy, V , of the hamiltonian is simply given by the superposition of atomic potentials, v , centered on the individual atoms:

$$V(\vec{r}) = \sum_{j} v(\vec{r} - \vec{r}_j) \qquad (2.4)$$

This potential is consistent with the assumed wavefunctions given in Eq. (2.2). In fact, the atomic energy eigenvalue ϵ_n , corresponds to the free atomic state Ψ_n found from this atomic potential v . (It is equal to the term for i = j = ℓ, m = n in Eq. (2.6) below.) Thus, the expectation value of the energy $E_{k,n}$ in the solid will be given as corrections to these free atom values:

$$E_{k,n} = \epsilon_n + \mathcal{E}_{k,n} \qquad (2.5)$$

15

The corrections, $\mathcal{E}_{k,n}$, will be, in general, solutions to matrices which involve all the significant atomic orbitals. The matrix elements for these energy corrections will be of the general form,[25]

$$\mathcal{E}_{k,nm} \rightarrow \frac{\frac{1}{\bar{a}} \sum_{j} \sum_{\ell} e^{i\vec{k}\cdot(\vec{r}_j - \vec{r}_\ell)} \int \Psi_m^*(\vec{r}-\vec{r}_\ell) \sum_{i \neq j} v(\vec{r}-\vec{r}_i) \, \Psi_n(\vec{r}-\vec{r}_j) \, d\vec{r}}{\left[\delta(\epsilon_n - \epsilon_m) + (\epsilon_n + E_n^{(M)}) - (\epsilon_m + E_m^{(M)}) \right] \int \Phi_{k,m}^*(\vec{r}-\vec{r}_\ell) \, \Phi_{k,n}(\vec{r}-\vec{r}_j) \, d\vec{r}}$$

$$(2.6)$$

where the delta function is a Kronecker delta (i.e., equal to 1 if $n = m$ or 0 otherwise). $E_n^{(M)}$ is the Madelung energy for the nth atomic orbital. (It is calculated from Eq. (2.6) for $i = j = \ell$, $n = m$ with the Madelung instead of the atomic potential.) The energy term of the denominator is not actually part of the matrix element but is included to indicate the form of the resulting contribution takes if two different states are involved. When the hamiltonian matrix is diagonalized using perturbation theory to find the energy, these "off-diagonal" matrix elements enter the energy with a denominator proportional to the difference in energy of the two states they "connected". The actual term in the secular determinant of course does not have such a denominator. However, it is important to consider its effect when studying the contributions to the electronic energy states in the solid. The multi-center corrections (i.e., all terms except those for $i = j = \ell$) to the free atomic energies will be important if the overlap between neighboring wavefunctions and potentials is not negligible. If there were no overlap, then the integrand would be zero for all $\vec{r}$ since one of the three terms (i.e., the potential and two wavefunctions) would be zero for any $\vec{r}$. For the general case of $i \neq j \neq \ell$, each of these terms will have its origin on a different atomic site. In most cases such three-center integrals will be much smaller than the two-center terms and are thus neglected in the usual tight-binding approximation. There are two types of two-center terms, U , to be considered. Those for $\ell = j \neq i$ involve the two atomic wavefunctions on the same center and potential from the neighboring atoms. Since the energies of any two

16

orbitals of a given atom usually are not in close proximity in the
solid, the term between the same orbitals (i.e., m = n) will dominate
this case because of the energy denominator. Note also in Eq. (2.6),
for l = j , the exponential term is unity for all values of k . This
k-independent term is simply the expectation value at each ion of the
potential from all the neighbors. It is thus a "crystal field" cor-
rection to the atomic energy eigenvalues defined as

$$U_n^{(1)} = \int \Psi_n^*(\vec{r}-\vec{r}_j)\, \Psi_n(\vec{r}-\vec{r}_j) \sum_{i \neq j} v(\vec{r}-\vec{r}_i)\, d\vec{r} \quad . \quad (2.7)$$

This term is of little interest here since it has little bearing on the
electronic structure itself.[25]

The other two-center term for l = i $\neq$ j is of primary interest
since it involves atomic functions on different sites with the potential
at one of the centers. In diatomic solids, like the silver halides,
the nearest neighbor atom is of the other constituent. Thus, the smallest
energy denominator in Eq. (2.6) and hence the largest contribution, will
be for two different orbitals (i.e., m $\neq$ n) with nearly equal energies
on neighboring sites. In the usual tight-binding approximation, only
such contributions of nearest neighbors are considered. These k-dependent
terms are usually referred to as the two-center overlap integrals and are
defined as

$$U_{k,nm}^{(2)} = \sum_{i \neq j} e^{i\vec{k}\cdot(\vec{r}_j - \vec{r}_i)} \int \Psi_m^*(\vec{r}-\vec{r}_i)\, v(\vec{r}-\vec{r}_i)\, \Psi_n(\vec{r}-\vec{r}_j)\, d\vec{r}$$

$$(2.8)$$

where the sum is only over the nearest neighbors i of the atom j
(i.e., $\vec{r}_j - \vec{r}_i$ is the nearest-neighbor distance). When this matrix is
diagonalized, the resulting energy for the hybridized orbital n ,
$U_{k,n}^{(2)}$, will be temperature dependent, as will be explained in part (b).
In part, this causes the energy states of the solid to depend on tempera-
ture in the tight-binding approximation.

There is a term identical to Eq. (2.8) but with the Madelung potential replacing the atomic potential at the neighboring site (i.e., $v^{(M)}(\vec{r}-\vec{r}_j)$). This is normally lumped in with the term of Eq. (2.8) and both are referred to as $U_{k,n}^{(2)}$.[3] We shall adopt this convention here; in future discussions this multi-center Madelung term will be understood to be part of the two-center overlap term $U_{k,n}^{(2)}$.

Terms coupling states on two neighboring atoms also occur in the normalization integral in the denominator of Eq. (2.6). This two-center wavefunction overlap term is usually defined as a correction to unity. (The result would be unity if there were no overlap or mixing.) Thus, we can write

$$S_{k,nm} = \int \Phi_{k,m}^{*}(\vec{r}-\vec{r}_\ell)\ \Phi_{k,n}(\vec{r}-\vec{r}_j)\ d\vec{r} - \delta(\epsilon_n - \epsilon_m) \qquad (2.9)$$

where the delta function is the Kronecker delta. From the discussion above of the significant terms, it is clear that for $\ell = j \neq i$, $n = m$ while if $\ell = i \neq j$, one only considers $n \neq m$ contributions of nearly equal energies. The normalization correction for the n-derived state, $S_{k,n}$, which results from diagonalizing this matrix, will also be temperature dependent as will be clear from the discussion in part (b).

The energy correction $\mathcal{E}_{k,n}$ in Eq. (2.5) is a combination of all these factors. Taking into account the Madelung energy, $E_n^{(M)}$, we have for the energy of the state derived from the atomic orbital n ,[26]

$$E_{k,n} = \epsilon_n + \left[\frac{E_n^{(M)} + U_n^{(1)} + U_{k,n}^{(2)}}{1 + S_{k,n}} \right] \qquad (2.10)$$

The magnitudes of each of these contributions to the energy bands of the silver halides will be discussed in Chapter III.

(b) Dynamic Wavefunction Hybridization

One must now consider what effect the temperature of the solid has on each of the energy terms in Eq. (2.10). In other words, how will these contributions to the energy be affected when the interatomic distance is changed due to the thermal vibration or contraction of the lattice? The terms which involve wavefunctions and potentials all on

18

the same center will not be temperature dependent. This is simply because these integrals are insensitive to the location of the atoms in the adiabatic approximation. That is, if one assumes that the wavefunctions can instantaneously adjust to a change in position of the atomic core (i.e., potential), then the product of the wavefunctions and potential centered on a given atom will be independent of the position of the atom. Of course, if there were a uniform contraction of the lattice, the Madelung energy would be significantly changed.[27] However, for thermal vibrations of the ions, the long range nature of the Madelung sum will cause the changes in this contribution to the energy to average to zero. Thus, both ϵ_n and $E_n^{(M)}$ will be temperature independent since the lattice contraction is negligible over the temperature range of interest.[28]

The multi-center terms will be dependent on the interatomic separation. It should be recalled that the atomic potential falls off quite rapidly with distance away from the core.[5] In addition, to get a reasonable result for a band calculation, this potential has to be screened[26] thereby further reducing its range. One would thus expect the $U_n^{(1)}$ term of Eq. (2.7) which involves the wavefunctions on a given site and the potential on a neighboring site to be much less dependent on ionic separation than the terms involving neighboring wavefunction overlap. Its dependence on temperature can therefore be neglected.

The contributions of the wavefunctions on neighboring sites both with and without a potential at one of the sites (i.e., $U_{k,n}^{(2)}$ and $S_{k,n}$, respectively) are of primary interest. If these contributions cause significant changes in the frozen lattice band calculations, then their changes with temperature will be large. That is to say, if the contribution is large, then both the overlap of the wavefunctions is quite significant and the energy of the neighboring states m and n are nearly equal. If these circumstances occur in a solid, the resulting mixing of the overlapping atomic states will be considerable, thereby producing highly hybridized states with energies significantly shifted from the free atom values. (It should be recalled that these hybridized states are just the basis functions of the diagonalized hamiltonian

matrix, formed from a "mixture" of the unperturbed atomic orbitals in the process.) Further, since the amount of this wavefunction overlap is obviously dependent on the separation of the ions, the energies of the hybridized states will be affected by changes in this spacing. Thus, as the atoms vibrate about their equilibrium lattice position, the dynamic changes in atomic separation caused by the optic modes will produce considerable modulation of the energies of the hybridized states via the $U_{k,n}^{(2)}$ and $S_{k,n}$ terms. Such energy broadening will, of course, be temperature dependent, for as the temperature is lowered below the Debye temperature, Θ_D, the dynamical motion of the lattice is significantly reduced. This will result in smaller fluctuations of the hybridization with a corresponding reduction in broadening of the energy. Since the wavefunction hybridization is affected by the dynamic motion of the lattice, we refer to this effect as "dynamic hybridization". The energy shifts caused by the contraction of the lattice upon cooling are negligible compared to this effect (see Chapter V).

This is the dominant mechanism producing the temperature dependent changes in the photoemission EDCs of the silver halides. As will be discussed in the next chapter, the Ag $4d$ and halogen p states are in close proximity in energy in these compounds. The mixing of these wavefunctions is therefore quite large; these two states would correspond to the two orbitals $(n \neq m)$ in the two-center overlap case $(\ell = i \neq j)$. As will be seen from calculations presented in Chapter V which use the silver and halogen atomic potentials and wavefunctions,[5] the rms displacement of the atoms produces quite significant changes in the $U_{k,n}^{(2)}$ overlap integrals [Eq. (2.8)] and $S_{k,n}$ normalization integrals [Eq. (2.9)]. At room temperature, where the amplitude of the lattice vibration is large, we calculate that the energy levels are broadened by as much as 1 eV by the fluctuating p-d overlap.[29] At liquid nitrogen (LN_2) temperature, where the amplitude of atomic vibrations is small, the hybridized levels become sharper and more well defined.

It is interesting to note that since the lattice vibrations greatly affect the electronic states directly, the Born-Oppenheimer approximation, which allows wavefunctions of the states of the solid to be separated into

an electronic and a nuclear part,[30] is not applicable to the hybridized states of the silver halides. This implies that one cannot consider separate electron and phonon states of the solid whose interaction can be treated by perturbation theory. This is, of course, consistent with the finding that the changes in the silver halide photoemission EDCs with temperature variation cannot be treated simply by phonon absorption or emission of the photoexcited electron (section A, part 2 above).

Of all the processes discussed above, the observed silver halide EDC changes can only be explained by a temperature dependent dynamic hybridization of the electronic states. For this reason, the changes upon cooling observed in the EDCs of many types of solids, which are to be discussed in section C, will be examined primarily in terms of this model.

C. Survey of Temperature Dependent Measurements of Photoemission EDCs

There have been very few reports of temperature dependent EDC changes in the literature. This is because the salient features of the EDCs for most solids change only slightly (the order of k_BT) upon cooling to LN_2 temperature. The changes observed for Ge by Donovan are typical.[31] As seen in Fig. 2.1, the largest change is the slight sharpening of the peak at $E \approx 7.7$ eV (all energies, E , are referred to the highest occupied electronic state). Caution should be taken in comparing the heights of curves, which are normalized relative to the incident rather than the absorbed photon flux, since changes in the optical properties may be significant and have not been accounted for. Ge is characteristic of solids which have Debye temperatures, Θ_D , near room temperature and have their wavefunctions extended in space. Other examples of materials with highly covalent bonding which fit into this class include GaAs and GaSb. These two compounds also do not exhibit large changes upon cooling to $77^\circ K$.[32] Though Cu has a different bonding scheme, it also falls into the class of solids with reasonably low Θ_D ($342^\circ K$) and extended wavefunctions. Preliminary Cu photoemission measurements at LN_2 temperature by Smith indicate that the low temperature EDCs
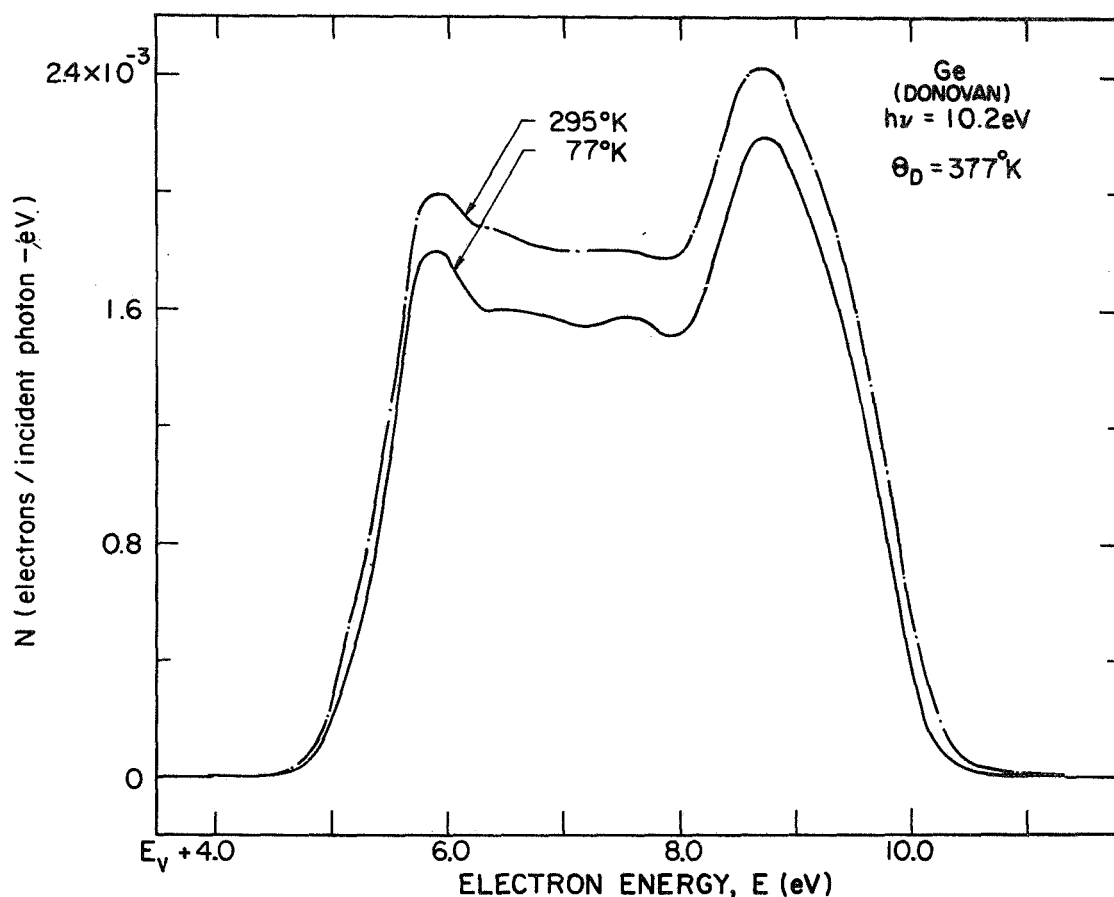
FIGURE 2.1. Comparison of energy distributions normalized to quantum yield (per incident photon) for electrons photoemitted from Ge at 77 and 295°K for a photon energy of 10.2 eV from the work of T.H. Donovan (reference 31).

are not significantly different from those at room temperature.[33] It is interesting to note that Cu has considerable hybridization (s-p bands with d states). Because the wavefunctions are so extended, this hybridization will not change much with temperature. In fact, this hybridization causes only small changes in the energy bands (i.e., opens small gaps) and does not involve many states.[34]

It is very interesting to consider now a case where Θ_D is still low but the wavefunctions are localized. The alkali halides are a good example of such a case. The changes observed for LiI, measured by DiStefano,[2] are shown in Fig. 2.2.
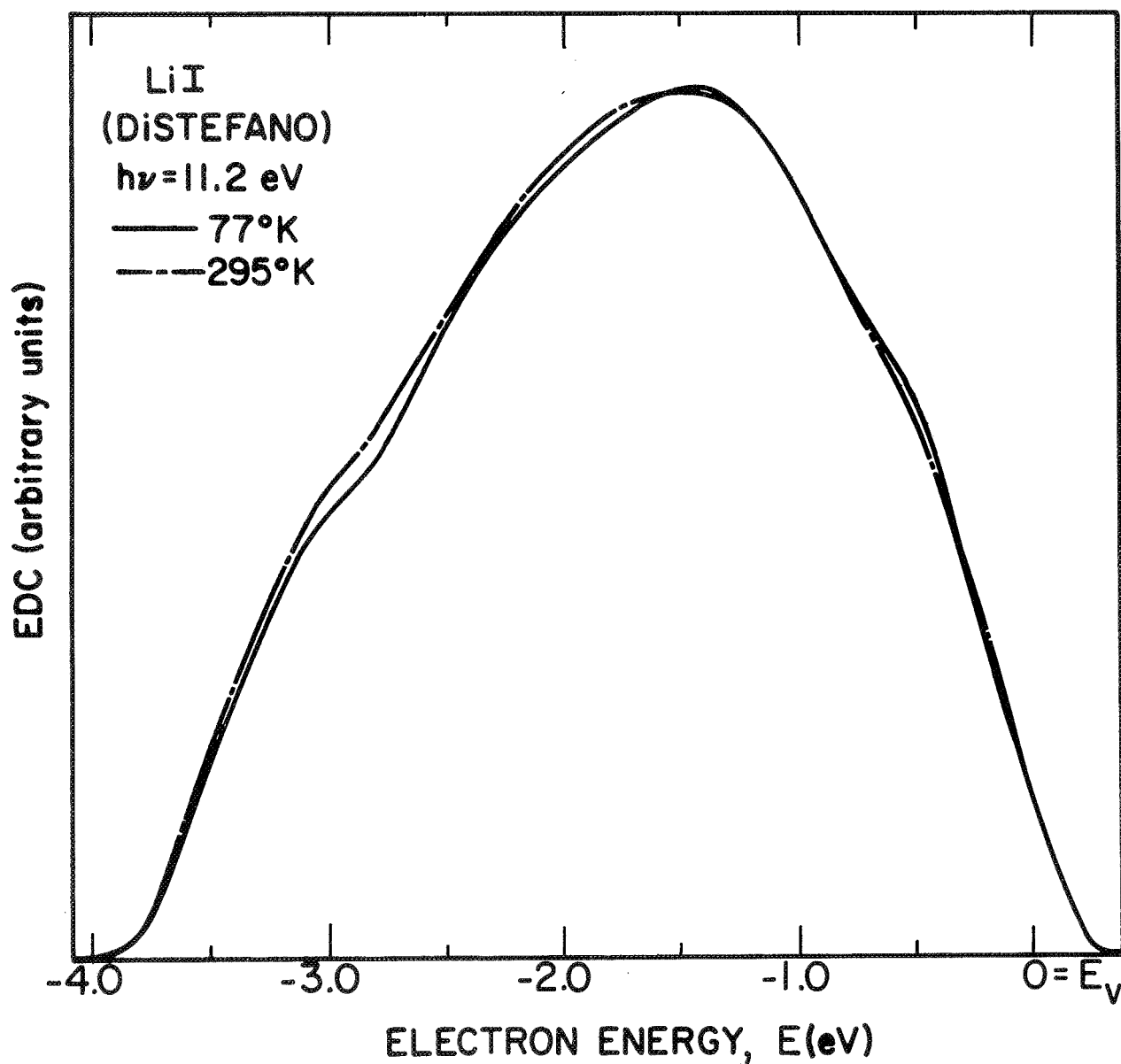
FIGURE 2.2. Comparison of un-normalized energy distributions for electrons photoemitted from LiI at 77 and 295°K for a photon energy of 11.2 eV from the work of T.H. DiStefano (reference 2).

The heights of these curves are not significant since the scale factors were chosen arbitrarily to facilitate comparison. Note that the changes again are extremely small as indicated by the changes in the structure at -1.4 and -0.6 eV. The wavefunctions in this case are very highly localized and there is very little, if any, wavefunction hybridization. This point will be discussed in detail in Chapter III. It is particularly interesting that even though the electron-phonon coupling is large in the alkali halides, the EDC changes are of the order of $k_B T / 2$. CsI has also been studied at room and LN_2 temperatures by DiStefano.[2] The observed changes for this compound are comparable to the small effects described for LiI above for all but one particular piece of structure. The temperature dependence of the leading CsI EDC peak above $h\nu \approx 10.5$ eV is roughly comparable to some of the silver halide structure. This may be an indication of a significant hybridization for the corresponding initial electronic states. From these examples of different types of solids (semiconductors, metals, and insulators), all with low Debye temperatures, it is clear that a Debye temperature in or near the region of temperature variation is not a sufficient condition for observing large temperature effects on external photoemission.

This condition may be necessary, however. Let us consider another class of solids with localized valence electronic wavefunctions as before, and in addition with a significant amount of hybridization. V_4O_8 is a good example of materials in this class which have Debye temperatures much higher than previously considered. As Derbenwick determined,[35] the uppermost O_2 (2p) states appear to have mixed significantly with the filled V (3d) states. The EDCs for cesiated V_4O_8 taken by Derbenwick[35] are shown in Fig. 2.3. As in the examples discussed above, there are only slight changes upon cooling. The greatest effect is seen as a sharpening of a shoulder into a peak at $V_R \approx 3.7$ volts. $SrTiO_3$ has also been studied by Derbenwick and similarly shows only slight changes with temperature variation.[35] Molecular solids also probably fit into the same class as the transition metal oxides. In Fig. 2.4, the temperature dependent EDCs for metal-free phthalocyanine, H_2Pc, as measured by Schechtman are illustrated.[36] In this case, the EDC changes slightly again
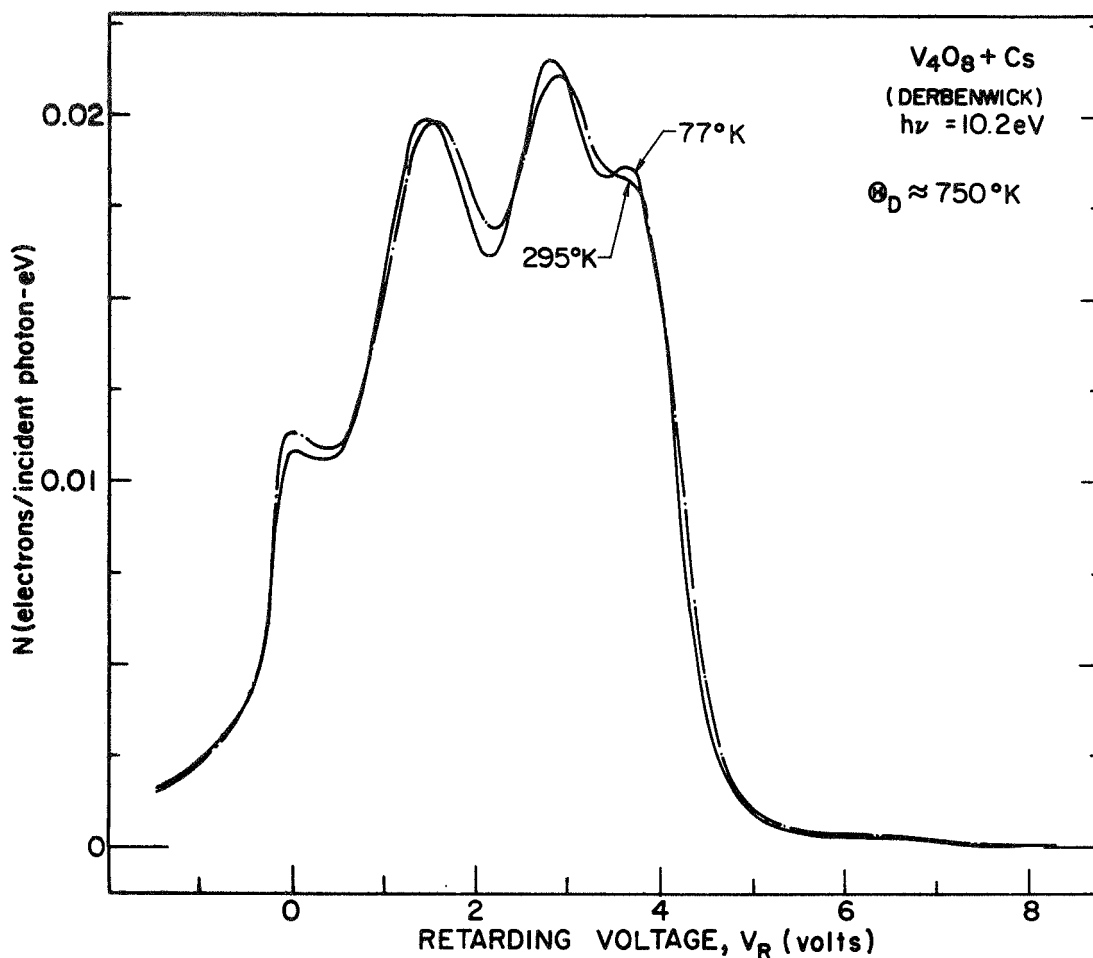
FIGURE 2.3. Comparison of energy distributions normalized to quantum yield (per incident photon) for electrons photoemitted from cesiated V_4O_8 at 77 and 295°K for a photon energy of 10.2 eV from the work of G.F. Derbenwick (reference 35).

and even seems to broaden a bit upon cooling. This may be indicative of a straining of the thin film upon cooling (see Chapter IV for a discussion of strain effects on photoemission). Schechtman also measured copper phthalocyanine, CuPc, photoemission at room and LN_2 temperatures and found its EDCs were relatively insensitive to cooling.[37] Thus, the occurrence of localized wavefunctions which are significantly hybridized
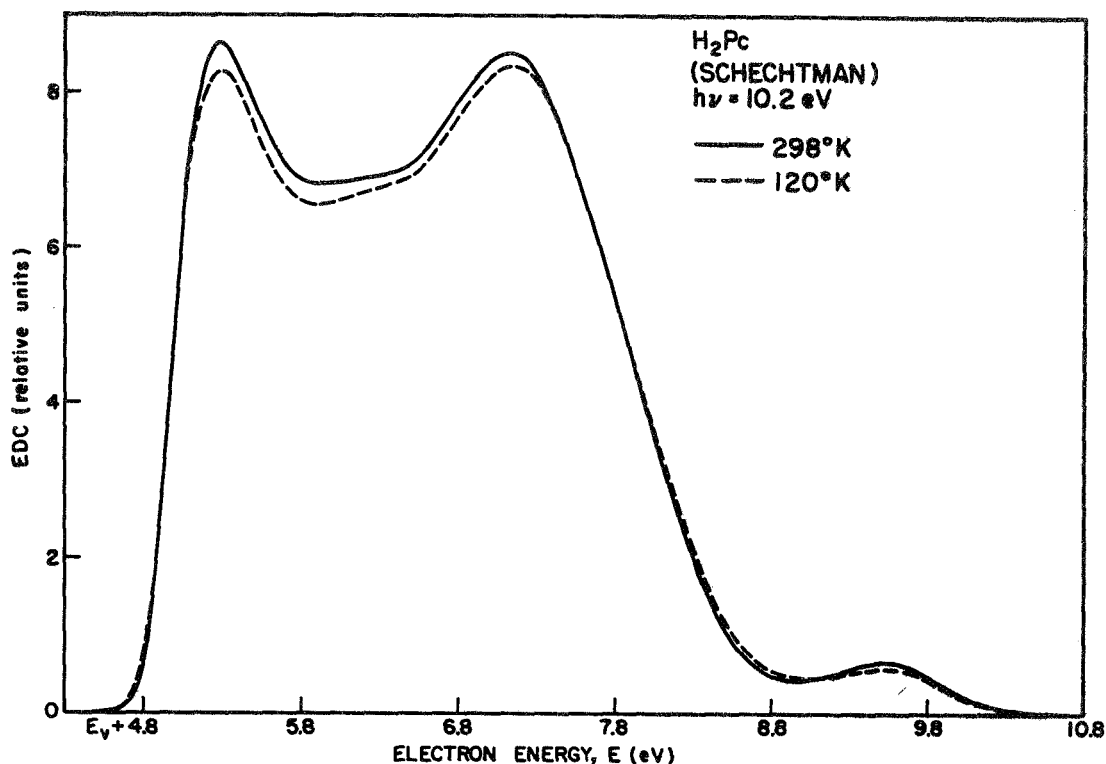
FIGURE 2.4. Comparison of un-normalized energy distributions for
electrons photoemitted from H_2Pc at 120 and 298°K
for a photon energy of 10.2 eV from the work of
B.H. Schechtman (reference 36).

is not sufficient to cause a large temperature dependent photoemission
but a Debye temperature in the region of temperature variation may also
be necessary.

If we consider lowering the Debye temperature while maintaining
the localized, hybridized wavefunction criterion of the previous case,
then we have the characteristics of the Ag halides. In Fig. 2.5, the
temperature dependence of the AgBr EDC at 10.2 eV is illustrated as
an example. Note that the Debye temperature (144°K) is about midway
between the limits of temperature variation. In sharp contrast to the
data, presented above, photoemission from the silver halides changes
quite dramatically upon cooling. The greater than 0.3 eV change upon

26
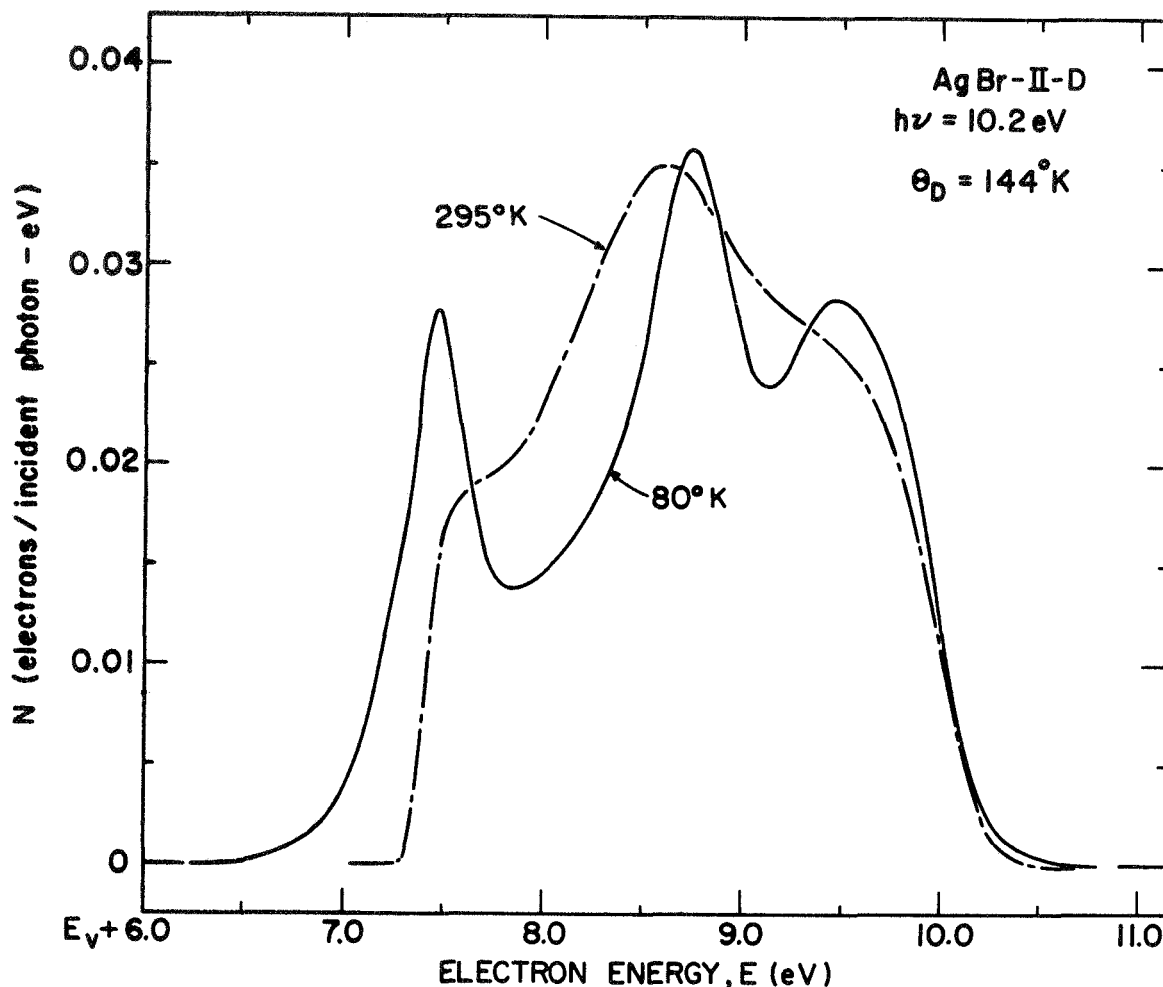
FIGURE 2.5. Comparison of energy distributions normalized to
quantum yield (per incident photon) for electrons
photoemitted from AgBr at 80 and 295°K for a
photon energy of 10.2 eV.

cooling in the full width of the central peak at 90% of its maximum

height in Fig. 2.5 is an order of magnitude larger than the changes in

photoemission from other solids studied to date. Note how room

temperature shoulders are resolved into well-defined peaks at 80°K.

Such sharpening also occurs for AgCl as is seen in the 10.4 eV EDCs

in the lower half of Fig. 2.6. As can be seen in this figure, these
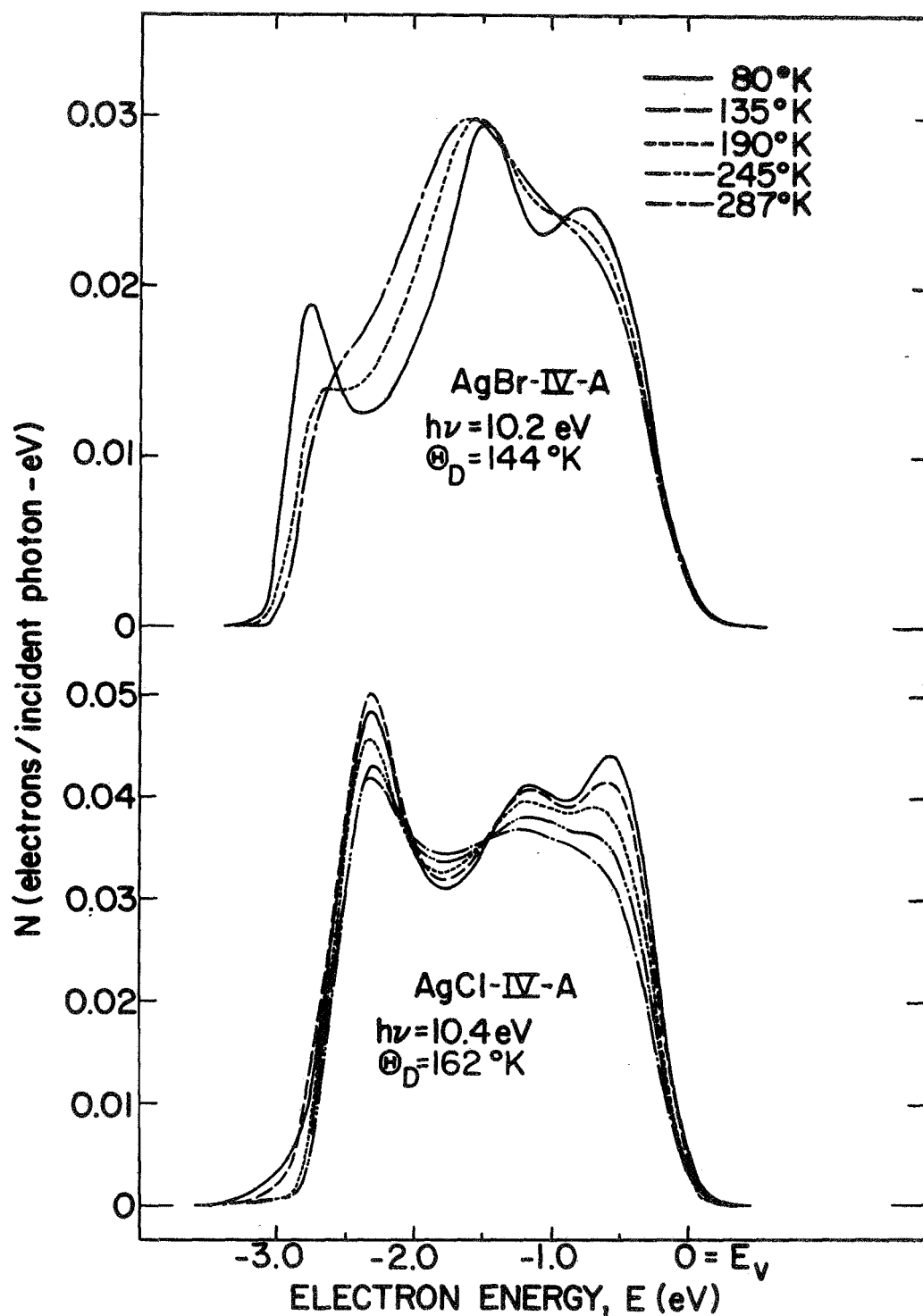
FIGURE 2.6. Comparison of energy distributions normalized to quantum
yield (per incident photon) for electrons photoemitted from AgBr
and AgCl at 80 through $287°$K for photon energies of 10.2 and 10.4 eV
respectively.

changes occur gradually as the temperature is varied. As will be shown in Chapters VI and VII, these strong temperature effects are seen only for certain transitions depending on the nature of the electronic states between which the transition is being made. The fact that these effects do not occur for the vast majority of alkali halide EDC structure measured to date, even though both of these halide families exhibit strong electron-phonon coupling effects in their optical properties, argues that these strong temperature dependent photoemission changes are caused by a mechanism fundamentally different from a normal strong electron-phonon effect.

The only physical process which rationalizes all the data presented above is a temperature dependent dynamic hybridization of the electronic wavefunctions. Only in this way can the very small temperature effects observed in such a large variety of solids be reconciled with the occurrence and magnitude of the striking changes in some of the silver halide EDC data. Thus, it appears that the characteristics of the silver halides which are necessary, and possibly sufficient, to have such large temperature dependent photoemission are (1) a Debye temperature in the region of temperature variation, (2) electronic wavefunctions which are: (a) fairly localized on the atomic sites, and (b) of two compatible species in close enough proximity in energy for the resulting hybridization to be a significant portion of the mixed state's energy, and (3) a large enough amplitude of ionic vibration above the Debye temperature to cause a significant modulation of the wavefunction hybridization.

In this section we have not considered the temperature dependent change in the photoemission yield. This was done because these changes are not particularly revealing as to the physical process causing them. The information in the energy distribution of the photoelectrons emitted at a given $h\nu$ is many times greater than that obtained from knowing the total number of electrons photoemitted (i.e., the quantum yield). Changes in yield are sometimes insignificant compared to changes in the EDCs. In fact, the changes in yield can even be deceiving. For example, the yield may decrease noticeably while the EDC structure sharpens considerably as is the case for the AgBr EDCs presented in Fig. 2.5. On

29

the other hand, the quantum yield of Ge measured by Donovan decreases
substantially upon cooling, but as seen in Fig. 2.1 the corresponding
EDCs show only slight structure changes. Thus, even though the tempera-
ture dependence of photoyield has been studied much more extensively
than that of EDCs, it is not of primary interest in this discussion.

III. THE ELECTRONIC STATES AND OPTICAL TRANSITIONS
IN THE SILVER HALIDES

Properties of the silver halides which are relevant to this dis-
cussion are reviewed in this chapter. This includes a discussion of
the state of the knowledge of the electronic states of the silver
halides previous to this investigation, and a review of past photo-
emission studies. In addition, the optical properties are examined in
terms of their temperature dependence and the information which they
yield concerning the electronic states. Comparison to the alkali halides
is made throughout the chapter to emphasize the key role the Ag d-halogen
p mixing plays.

A. Electronic States

The electronic states of this interesting class of noble halide
insulators differ in a fundamental way from those of the classic wide
band gap insulators, the alkali halides. It is the differences between
the metallic constituents which causes this. The noble and alkali metal
in the same row of the periodic table have the same inert gas core and
valence electron level. The difference is that the lowest d states,
outside the core, are occupied in the noble metal while they are empty
in the alkali case. This means that the valence states of the noble
halides will be a "mixture" of the filled d states of the metal ion
and the occupied p states of the halogen ion. In comparison, the
alkali halide valence band will be formed simply from one atomic consti-
tuent. This is illustrated in Fig. 3.1 by the approximate atomic origin
of regions of the electronic structure of a typical alkali halide, RbI,
from the work of DiStefano,[2] and a typical silver halide, AgBr , from
this work. The photoemission thresholds are also shown in this figure
by the lines on the right side of each of the energy diagrams. The
valence band structure of RbI is relatively simple since to a very
good approximation, one can consider only one set of atomic states

31
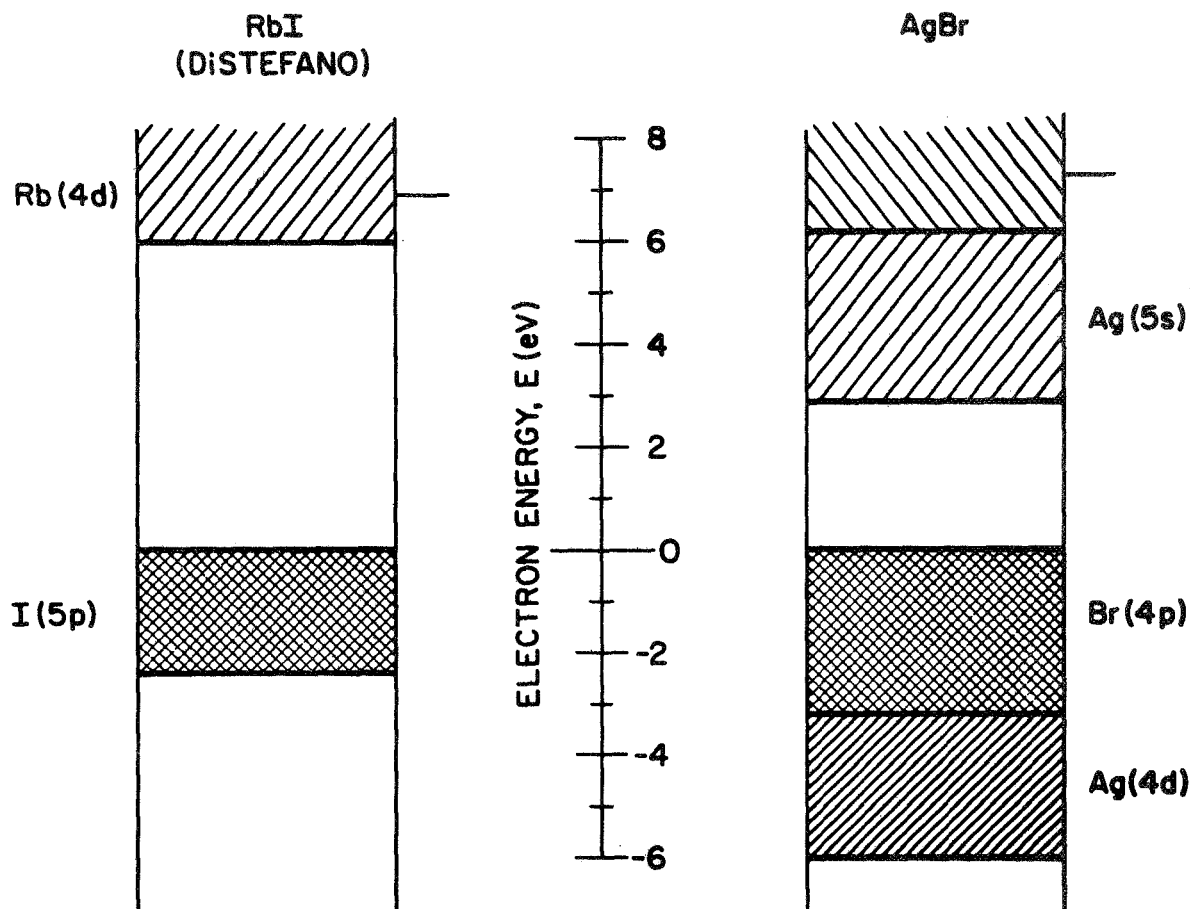
FIGURE 3.1. Comparison of the electronic states of a typical
          alkali halide, RbI , and silver halide, AgBr .
          The RbI states are from the work of T. H. DiStefano
          (reference 2).

[i.e., I(5p)]. On the other hand, the Br(4p) and Ag(4d) states lie
almost at the same energy. This leads to very strong mixing and a large
hybridization of the valence wavefunctions in the solid, as discussed in
Chapter II. Thus, the valence band will be quite complex in the silver
halides.

To understand the complexities of this electronic structure and the relative importance of the halogen p-silver d mixing, the valence states of AgCl were calculated using the tight-binding approximation discussed in the last chapter. The tight-binding matrix elements were obtained using the Slater-Koster method.[38] Though the matrix elements are given only for the simple cubic lattice in Table III of this paper, the terms for the cubic (NaCl) structure, O_h^5, can be derived from them. Since our interest here is in determining the importance of the various contributions to the energy in Eq. (2.10) and in particular the effect of the wavefunction hybridization on the states, calculations of the energies at Γ and L alone are sufficient. The Hamiltonian matrix elements along the line $\Gamma \rightarrow \Lambda \rightarrow L$ for first and second nearest neighbors, in the two-center approximation, are given in Table III.1. In our calculations, the secular equation is a 9×9 determinant whose basis functions are the one Cl 3s orbital (s), three Cl 3p states (x,y,z), and the five Ag 4d states (xy,yz,zx, x^2-y^2, $3z^2-r^2$). (Note that by neglecting the spin, the matrix size is reduced by a factor of 2.) The numerical values used for the parameters in the matrix elements (e.g., pdσ) were those determined by Bassani, Knox, and Fowler for the assumption that only the nearest neighbor interactions were important.[3] The k-dependence of these matrix elements is contained in ξ as indicated at the bottom of the table. The k-dependent terms in Eq. (2.10) were determined by solving for the eigenvalues of this matrix. The diagonalization was accomplished using a computer program written by J. Rinzel and R. E. Funderlic of Union Carbide Co., Oak Ridge, Tennessee and supplied to the author by G. F. Derbenwick. The results are summarized in Fig. 3.2 where the magnitudes of each of the contributions to the energy of Eq. (2.10) are shown. The designations of the states are found by determining the irreducible representation of the group O_h^5 by which the eigenfunction, corresponding to a given eigenvalue, transforms. This is done using standard group theoretical techniques.[39,40]

TABLE III.1. The Hamiltonian, tight-binding matrix elements for the cubic (NaCl) lattice, O_h^5, along the line $\Gamma \to \Lambda \to L$ for first, 1, and second, 2, neighbors in the two-center approximation.

Orbital pair	Matrix element
(s/s)	$12(ss\sigma)_1 \cos^2\xi + 6(ss\sigma)_2 \cos 2\xi$
(s/x)	$[2\sqrt{2}\, i(sp\sigma)_1 + 2i(sp\sigma)_2]\sin 2\xi$
(s/xy)	$-2\sqrt{3}(sp\sigma)_1 \sin^2\xi$
$(x/x),\,(y/y),\,(z/z)$	$[4(pp\sigma)_1 + 8(pp\pi)_1]\cos^2\xi + [2(pp\sigma)_2 + 4(pp\pi)_2]\cos 2\xi$
(x/y)	$[2(pp\pi)_1 - 2(pp\sigma)_1]\sin^2\xi$
(x/xy)	0
(x/yz)	$\left[\dfrac{\sqrt{6}}{2} i(pd\sigma)_1 + \sqrt{2}\, i(pd\pi)_1 + 2i(pd\pi)_2\right]\sin 2\xi$
(x/x^2-y^2)	$\left[\dfrac{3}{\sqrt{2}} i(pd\pi)_1 - \dfrac{1}{2}\sqrt{3/2}\, i(pd\sigma)_1 + \sqrt{3}(pd\sigma)_2\right]\sin 2\xi$
$(x/3z^2-r^2)$	$\left[\dfrac{\sqrt{2}}{4} i(pd\sigma)_1 - \dfrac{\sqrt{6}}{2} i(pd\pi)_1 - i(pd\sigma)_2\right]\sin 2\xi$
$(z/3z^2-r^2)$	$\left[\dfrac{1}{\sqrt{2}} i(pd\sigma)_1 + \sqrt{6}\, i(pd\pi)_1 + 2i(pd\sigma)_2\right]\sin 2\xi$
(xy/xy)	$[3(dd\sigma)_1 + 4(dd\pi)_1 + 5(dd\delta)_1]\cos^2\xi + [4(dd\pi)_2 + 2(dd\delta)_2]\cos 2\xi$
(xy/xz)	$[2(dd\delta)_1 - 2(dd\pi)_1]\sin^2\xi$
(xy/x^2-y^2)	0
$(xy/3z^2-r^2)$	$[\sqrt{3}(dd\sigma)_1 - \sqrt{3}(dd\delta)_1]\sin^2\xi$
(xz/x^2-y^2)	$\left[\dfrac{3}{2}(dd\delta)_1 - \dfrac{3}{2}(dd\pi)_1\right]\sin^2\xi$
$(xz/3z^2-r^2)$	$\left[\dfrac{\sqrt{3}}{2}(dd\delta)_1 - \dfrac{\sqrt{3}}{2}(dd\sigma)_1\right]\sin^2\xi$
$(x^2-y^2/x^2-y^2),\,(3z^2-r^2/3z^2-r^2)$	0
$(x^2-y^2/3z^2-r^2)$	$\left[6(dd\pi)_1 + \dfrac{3}{2}(dd\sigma)_1 + \dfrac{9}{2}(dd\delta)_1\right]\cos^2\xi + [3(dd\sigma)_2 + 3(dd\delta)_2]\cos 2\xi$

$$\xi = k_x a = k_y a = k_z a \quad \begin{cases} = 0 & @\ \Gamma \\ = \dfrac{\pi}{2} & @\ L \end{cases}$$
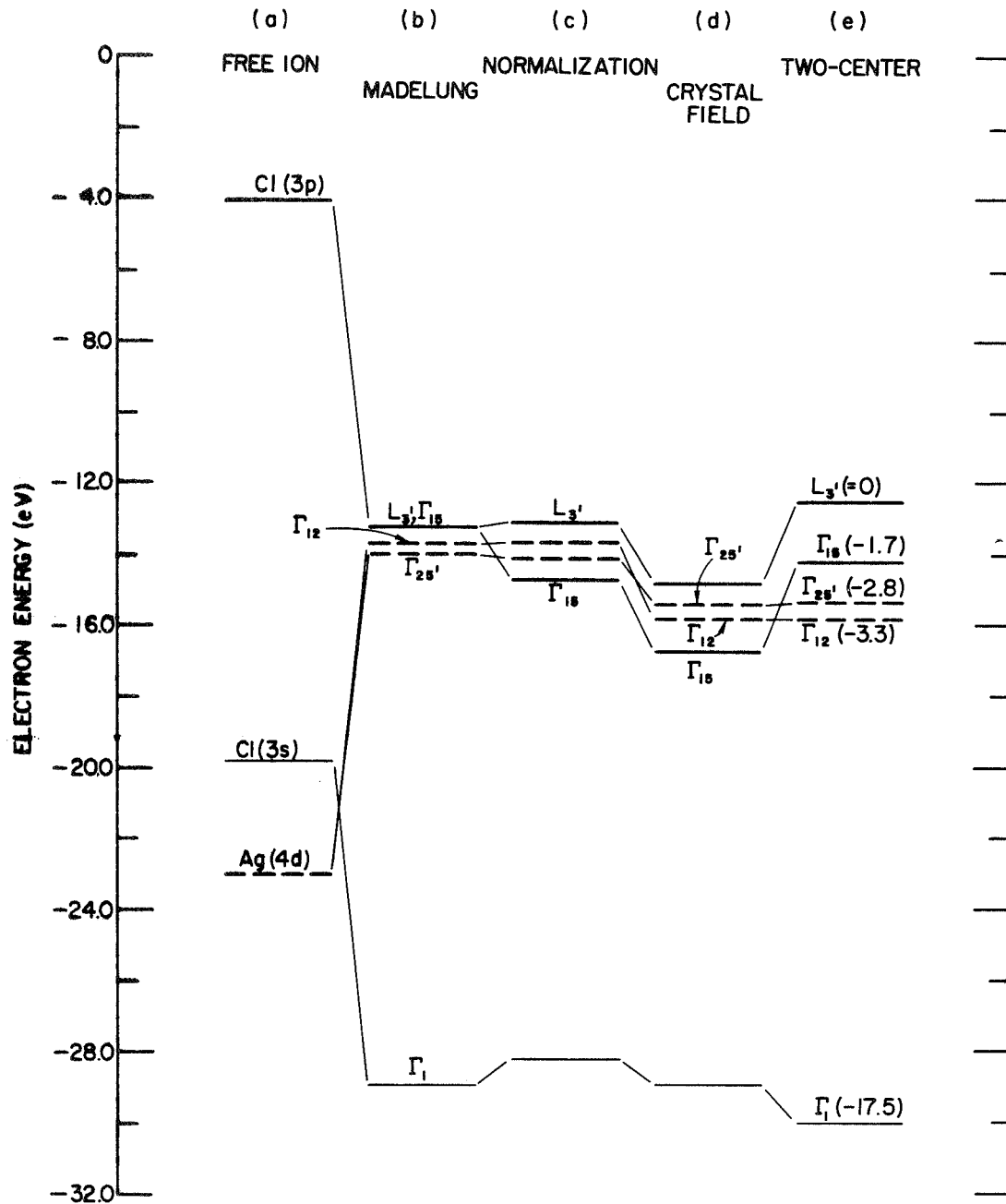
FIGURE 3.2. The contributions to the valence band structure of AgCl at
Γ and the highest valence state at L calculated by the tight-binding
approximation: (a) the free ion energy, ϵ_n ; to which we add (b) the
Madelung energy, $E_n^{(M)}$; then (c) the wavefunction normalization cor-
rection, $S_{k,n}$, is accounted for; followed by the turning on of
(d) the crystal field, $U_n^{(1)}$, of the neighbors; and finally (e) the
two-center wavefunction overlap, $U_{k,n}^{(2)}$, is included. The energies
of the states, referred to the valence band maximum, are shown in
parentheses in part (e).

In part (a) of the figure, the free ion energies, ϵ_n , are plotted. Upon adding the Madelung energy, $E_n^{(M)}$, in (b), the Cl 3p-derived states lie very close in energy to the Ag 4d-derived levels. As can be seen, this is by far the largest contribution to the energy states of AgCl ; while the other terms significantly affect the relative position of the various levels that are in close proximity, on a large scale the positions of the states are pretty well determined by the free-ion and Madelung terms. The Cl 3s-derived states are around 14 eV lower in energy than the p and d derived states and can be neglected in considering wavefunction mixing and interpreting the EDCs of these solids. To study the other contributions to these highest valence states in more detail, this region of the figure is expanded in Fig. 3.3. The Cl 3p-derived states are shwon by the solid line while the Ag 4d-derived states are drawn dashed. When the normalization, $S_{k,n}$, is taken into account in (c), it appears that the d-derived states at Γ are higher in energy than the p-derived Γ orbitals. It is interesting to note that this contribution which involves overlap between the wavefunctions of the two atomic species causes the order of the levels to reverse at Γ and produces the large separation between the energies of the p-derived state at $\Gamma(\Gamma_{15})$ and the highest L point $(L_3\prime)$. The crystal field contribution, $U_n^{(1)}$, in (d), simply shifts all the states by roughly the same amount without producing any sizable changes in their relative positions. The two-center overlap term, $U_{k,n}^{(2)}$, which is turned on in (e) shifts the p-derived states relative to the d-derived ones thereby producing the ordering of the bands which we deduce from these photoemission results, as will be explained in this thesis. It is quite significant that the overlap terms $S_{k,n}$ and $U_{k,n}^{(2)}$ which depend on the p-d mixing have such profound influences on the energy states of the silver halides. It should be recalled that it is these same terms which are the most dependent on temperature (see Chapter II). Thus, the importance of the various contributions to the energy is such that the hybridized states will be greatly dependent on temperature due to the dynamic motion of the lattice.
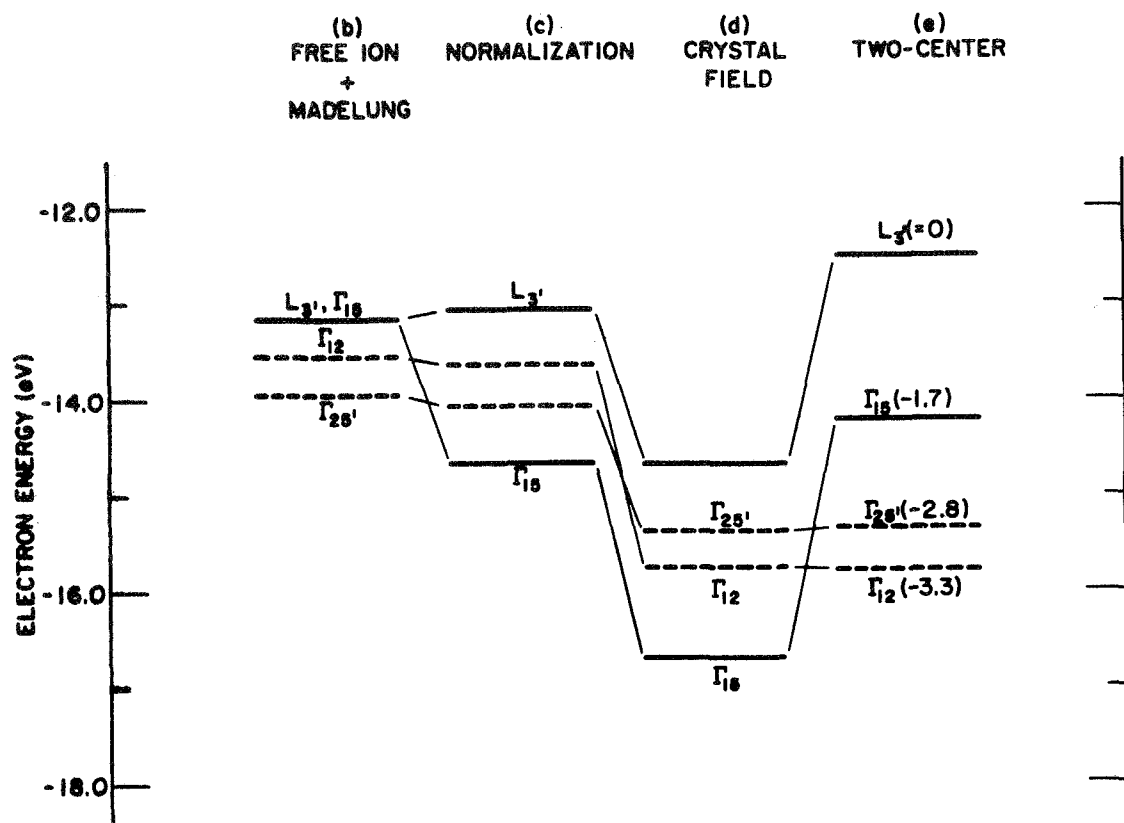
FIGURE 3.3. Expansion of the valence band structure of AgCl
presented in Fig. 3.2 showing the valence states at
Γ and the highest one at L which are derived
from the Cl 3p (———) and Ag 4d (– – – –) atomic
orbitals. The energies of the states, referred
to the valence band maximum, are shown in paren-
theses in part (e).

Because of the close proximity of the Ag 4d states and the
halogen p-derived states, the resulting mixing is quite strong and
produces a complex valence band structure. The energies would have
to be calculated accurately to even predict the proper ordering of
the levels. Thus, there has been disagreement over which states form
the valence band maximum. Seitz, as early as 1951, suggested that the
halogen p-derived states would be the highest filled levels, having a
maximum away from the Brillouin zone center.[41] Krumhansl noted that

such behavior of the bands could be due to the close proximity of Ag $4d$ states.[42] Brown formalized these predictions by proposing a set of valence bands which could explain the available silver halide data.[43] On the other hand, Martienssen suggested that the highest valence states could be Ag $4d$-derived and still explain the long-wavelength tail on the fundamental absorption.[44] It was not until 1965 that attempts were made to calculate the energy bands of AgCl and AgBr . Using the Augmented Plane Wave (APW) method of Slater, Scop calculated the valence bands and some conduction states.[6] Though the lowest conduction band appears to be too wide and the d-band to highest filled state energy is too small, two very important features were determined by Scop's work. The highest silver halide valence states are p-derived and they have their maximum at a point other than the center of the zone (Γ). Bassani, Know, and Fowler used the tight-binding approximation to calculate the valence states of AgCl and then estimate the over-all band structures of AgCl and AgBr based on available optical data.[3] The important point to realize is that even their calculations of the AgCl valence states were not accurate enough to explain the optical experiments. Rather, these bands were adjusted in the "speculative band structures" presented in their paper. Since these bands were proposed on the basis of both experiment and theory, they are actually quite good and have been successfully applied to more recent data. For this reason, we compare these bands with the results determined for the electronic states from the present work in Chapter VIII. Since the tight-binding energies presented in Figs. 3.2 and 3.3 were computed using their inaccurate calculation parameters, the $L_3 \to \Gamma_{25'}$ energy presented above is understandably smaller than experimentally measured, but these calculations serve as a good estimate of general energy band features. Their calculations did further establish the highest filled states as being p-derived and not occurring at Γ . Thus, the over-all features of the energy bands have been calculated but there is much further work which needs to be done to obtain any kind of agreement with experiment. Fowler is presently working on a calculation of the AgCl band structure using a mixed-basis method similar to that developed by Kunz.[27]

All these calculations have established the great similarity between the AgBr and AgCl electronic structures. It is thus a good approximation to apply the general conclusions determined for one compound to the other halide. This is often necessary because of the limited knowledge of these materials. For example, since we are only able to calculate the tight-binding valence bands for AgCl , it is thus important to know that the general features will also be common to AgBr .

B. Optical Properties

As noted in section A, the optical properties of the silver halides have been extensively used in determining the electronic structure of the silver halides. The major effort to date has been in the extreme UV (30 < hν < 240 eV),[45] and visible and near UV (hν < 6.7 eV) regions of the spectrum. In these regions the optical constants have been determined quite well from 300° to $4.2^{\circ}K$. Unfortunately, the vacuum ultraviolet region which is of interest to us, has only been explored satisfactorily at room temperature by White and Straley. This AgCl reflectivity data through 12.0 eV is shown in Fig. 3.4 by the solid line except in the region from 3.2 through 4.3 eV where the points and not the curve are the data.[46] When these optical measurements by White and Straley are compared[47] with other reflectivity[48] or absorption[49] data in this region, they are clearly seen to be the best to date. The optical constants obtained by a Kramers-Krönig analysis of this reflectivity exhibited unphysical negative dips at 3.2 eV in α, ϵ_2, and κ . The first two of these quantities are shown by the dashed curves in Figs. 3.5 and 3.6, respectively.

A close inspection of the starting data, which was generously supplied by White,[50] reveals a discontinuity in slope at 3.2 eV and through 4.3 eV values greater than the underlying smooth "envelope" by up to 11% (see Fig. 3.4). When the White and Straley reflectivity data from 3.3 eV through 4.3 eV is smoothed to the solid line shown in Fig. 3.4, in accordance with earlier measurements,[51-54] the Kramers-Krönig analysis yielded the same structure as reported by White and
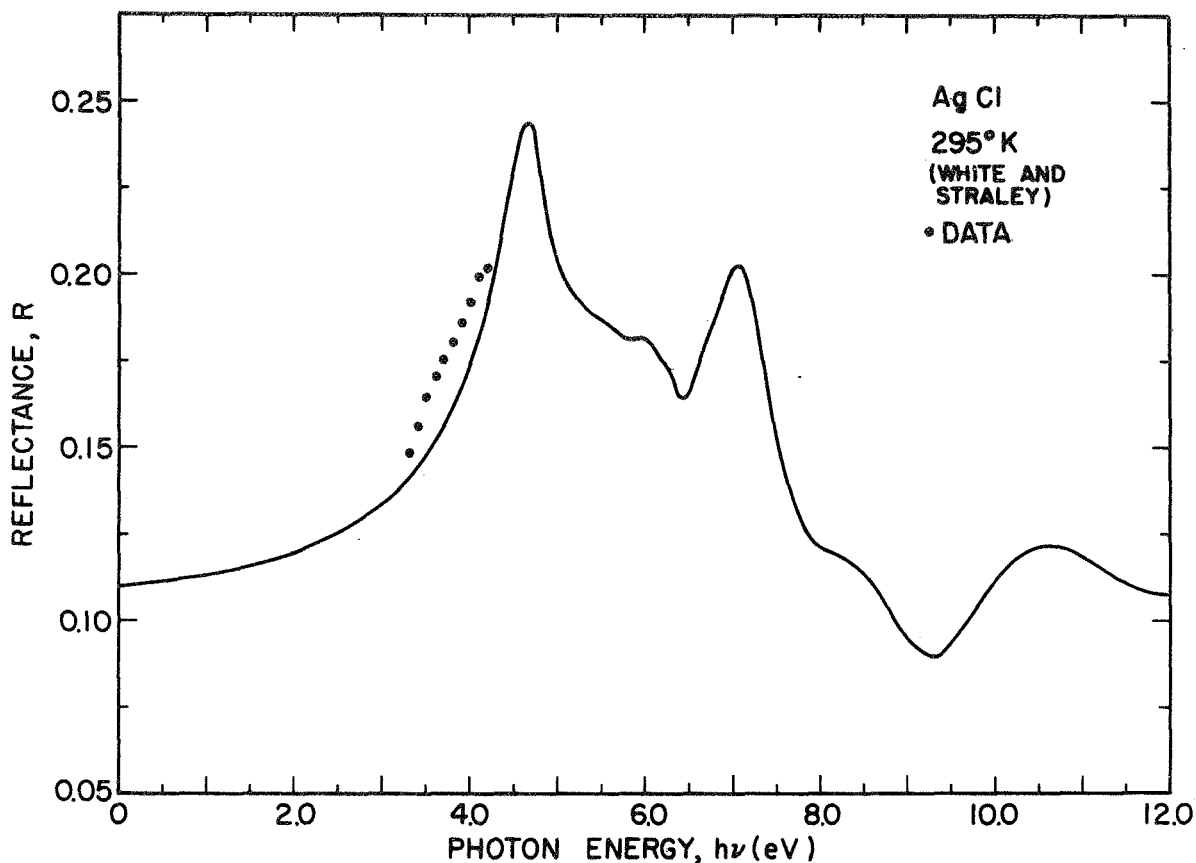
FIGURE 3.4. The spectral distribution of the reflectance of AgCl at 295°K from the work of White and Straley (reference 46). In the region from 3.2 through 4.3 eV the points and not the curve are their data.

Straley except for the complete absence of the unphysical dips at 3.2 eV. As seen in Figs. 3.5 and 3.6, the magnitude of these two sets of optical constants differ by less than 10%. Details of this calculation are given in Appendix A. The same error appears to be present in White's unpublished AgBr data as is evident from the calculated absorption coefficient presented in Fig. 3.7.[55] The negative dip in α around 4 eV may be caused by poor reflectivity data in this region. This was not studied in detail since based on our AgCl findings the optical constants determined with corrected input data would probably differ only slightly
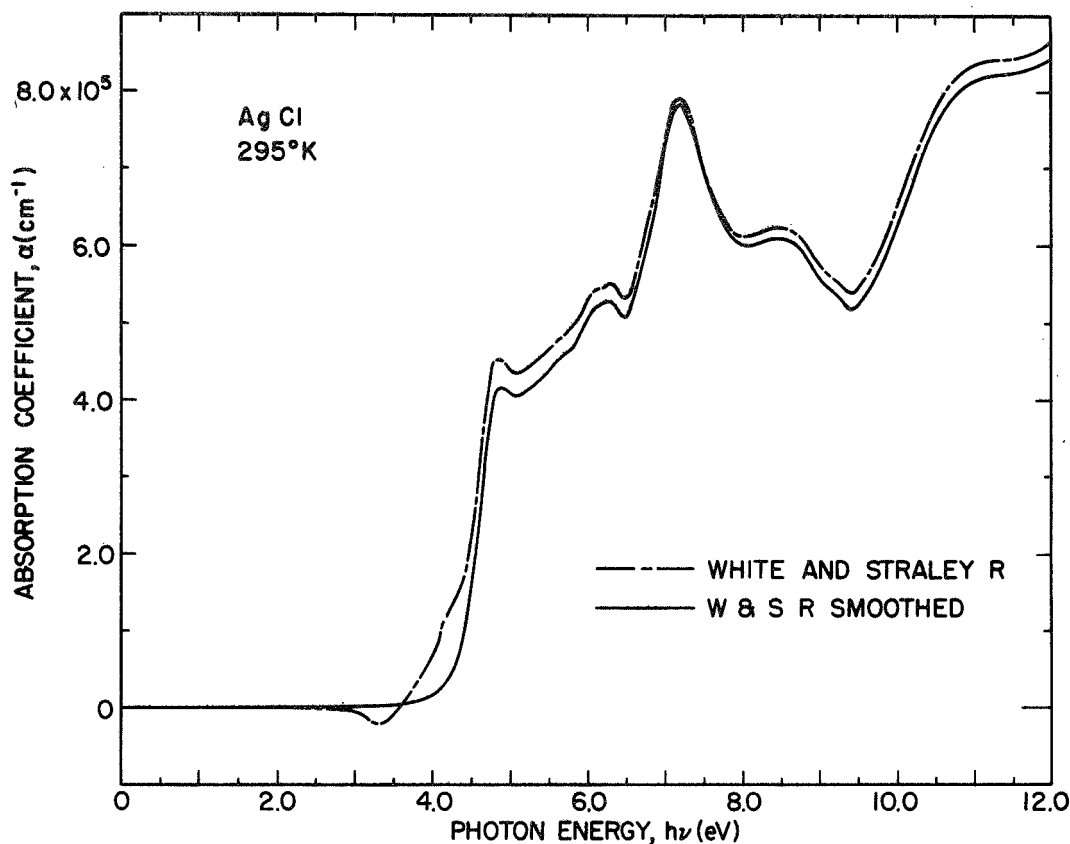
FIGURE 3.5. Comparison of the spectral distributions of the absorption
coefficient of AgCl at 295°K calculated from the reflec-
tance of White and Straley (reference 46) (———·———) and
the same values but smoothed from 3.2 through 4.3 eV (————).

in magnitude at all energies other than the region of the unphysical dip.

The absorption edge has been studied in more detail than any other
part of the spectrum. This is at least in part because its behavior is
indicative of indirect transitions and thus yielded direct evidence as
to the nature of the electronic structure around the band gap. There
have been only minor discrepancies in the values reported for the in-
direct threshold of both AgCl and AgBr . These are summarized in
Table III.2. The values of Joesten and Brown[57] are probably the most
reliable. Because the lowest conduction states derived from the Ag 5s
levels are quite simple in form (free-electron like with a minimum at. Γ),
the overwhelming evidence for an indirect gap was clearly indicative of

41
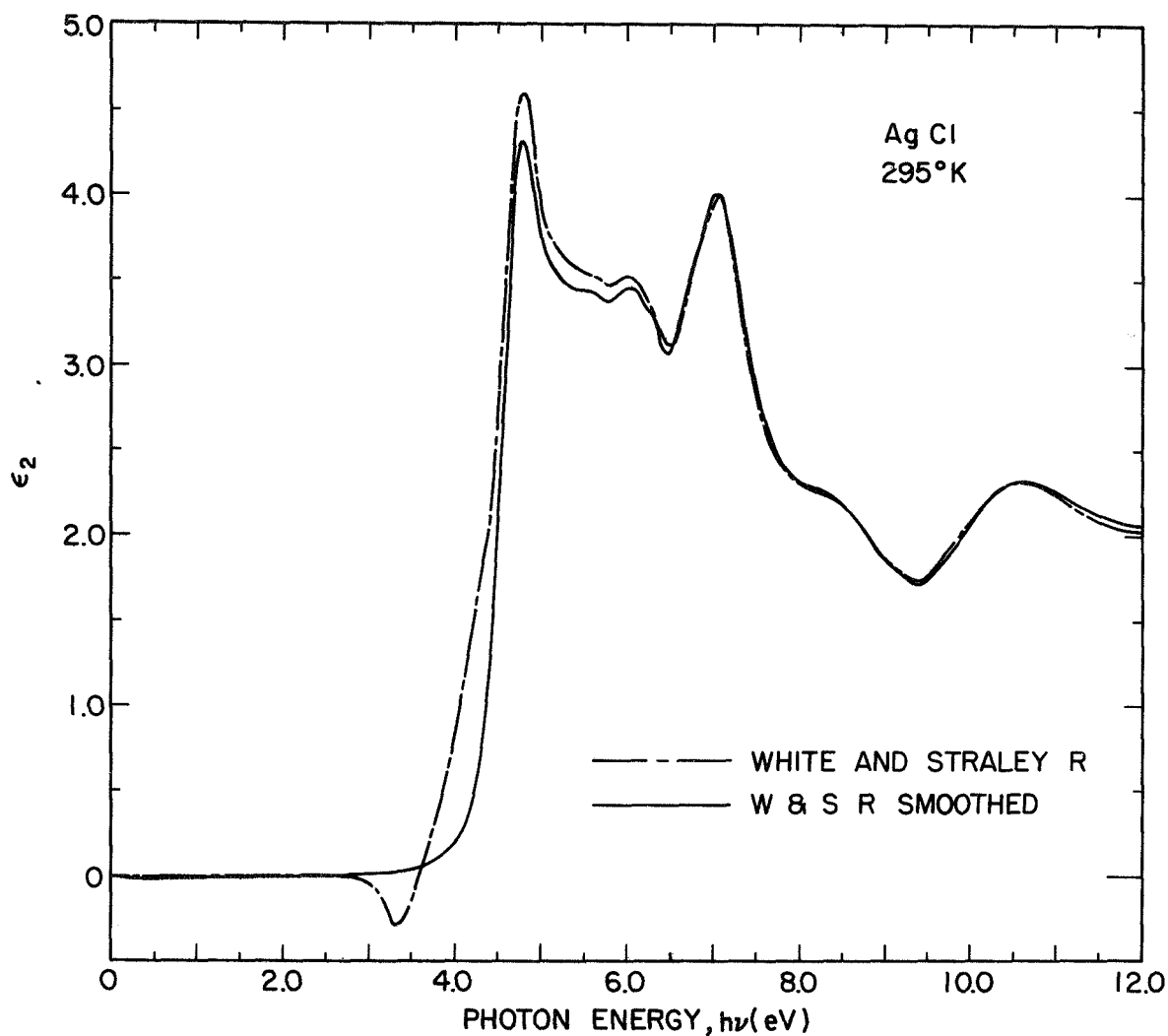
FIGURE 3.6. Comparison of the spectral distributions of the
imaginary part of the dielectric constant of
AgCl at 295°K calculated from the reflectance
of White and Straley (reference 46) (— - —)
and the same values but smoothed from 3.2
through 4.3 eV (———).

a valence band with a maximum at a point other than Γ . This was
conclusively shown to be the case for AgBr by the piezotransmission
studies of Ascarelli.[13] He found that the valence band maximum was in
the (111) (L) direction. Since the maximum would be at Γ if there
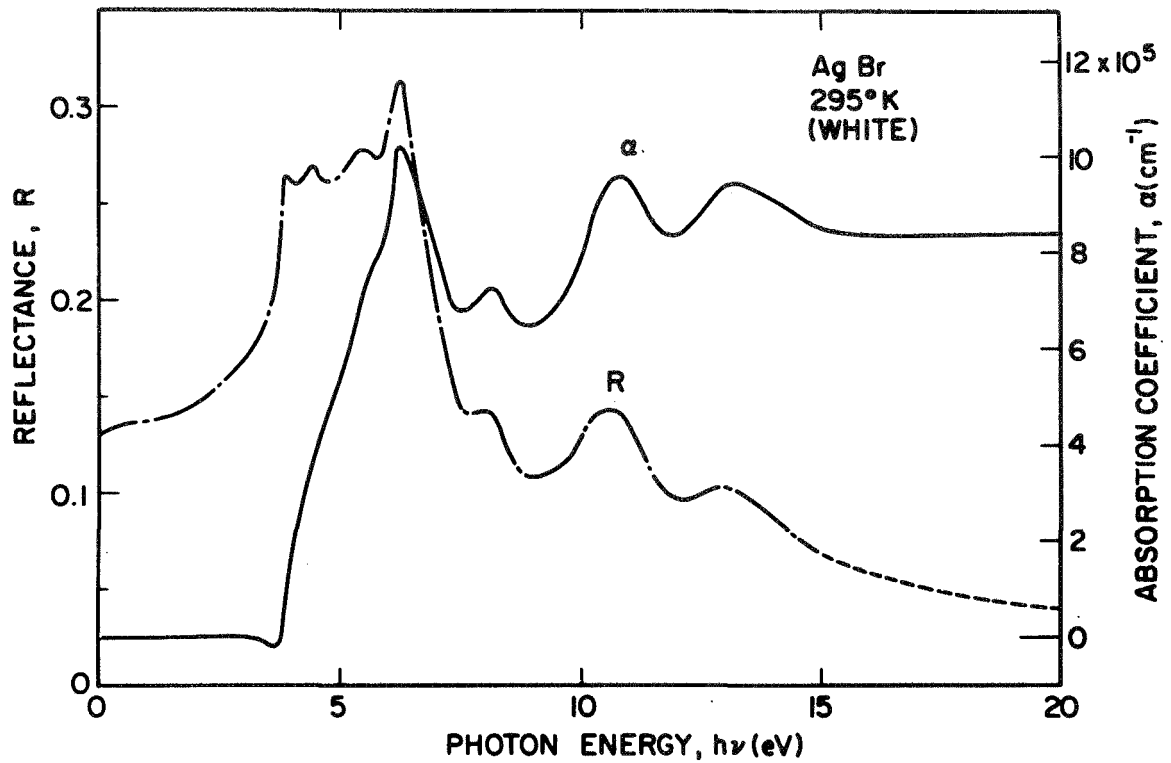
FIGURE 3.7. The spectral distributions of the reflectance and absorption coefficient of AgBr at 295°K from the work of White (reference 55).

TABLE III.2. Values reported for the indirect threshold of AgCl and AgBr at 4.2°K

Indirect Threshold (@ 4.2°K)		Reference
AgCl	AgBr	
	2.691	56
3.252	2.691	57
3.253	2.691	58
3.254	2.690	59

were not p-d coupling,[26] these optical studies of the (indirect)
absorption edge established the profound importance of this mixing.

This threshold absorption region has been measured from 2 to $300^\circ K$.
It is quite interesting that the well-defined fine structure in the
absorption edge is "washed out" above approximately $15^\circ K$ (i.e., for
$T >$ approximately $0.1\ \Theta_D$).[56,57,60,61] This is a very strong dependence
on temperature; when the temperature gets high enough to cause any
vibration of the lattice (at $T \approx 0.1\ \Theta_D$), the optical transition
energy is broadened. This importance of the thermal motion of the lat-
tice in determining the optical properties of the silver halides is
consistent with the dynamic wavefunction hybridization model discussed
in Chapter II. It is also interesting that the cyclotron resonance of
AgBr is "washed out" in the same temperature range.[62]

This strong temperature dependence of the optical properties is even
more strikingly evident in the studies of the direct transition edge.
In Fig. 3.8, the absorption measurements of AgBr by Okamoto[51] are
presented. These have recently been remeasured by Carrera[45] and found
to be virtually the same. It is quite dramatic how the very sharp
structure in α at $90^\circ K$ is almost completely "smoothed" when AgBr is
warmed to room temperature. Note especially the first exciton peak which
is broadened into a slight shoulder. It is quite significant that even
through structure in the optical properties of the alkali halides is
slightly diminished in strength and a bit broadened at room temperature,
peaks and even some fine structure which is present at liquid N_2
temperature is preserved at $300^\circ K$. This can be seen in the insert in
Fig. 3.8 where the reflectivity of RbBr by Baldini and Bosacchi[63] is
shown. (Though the reflectance is not comparable to the absorption,
trends can be elucidated.) Note that even the fine structure present
at $55^\circ K$ at about 7.8 eV is retained in the $300^\circ K$ spectrum. This dif-
ference in behavior with T between these two bromides, which have
about the same Debye temperatures, is especially significant since the
only difference in electronic structure is that the 4d states are
unoccupied in the alkali halide. This importance of the filled d

44
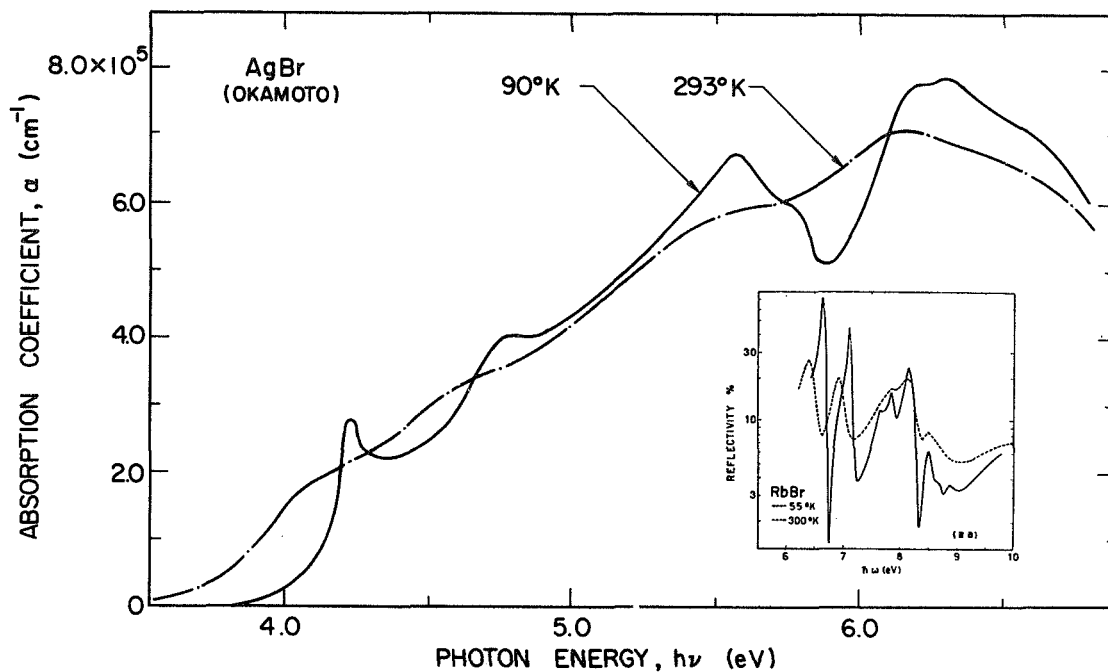
FIGURE 3.8. Comparison of the spectral distributions of the absorption coefficient of AgBr at 90 and 293°K from the work of Okamoto (reference 51) and of RbBr at 55 and 300°K from the work of Baldini and Bosacchi (reference 63).

states in the silver halides is also seen by comparing the AgCl [51] and RbCl [63] spectra in Fig. 3.9. The apparent fundamental importance of the p-d coupling in the silver halides is consistent with the dynamic wavefunction hybridization model proposed in Chapter II. One would expect this first direct exciton peak to not only be dependent on temperature but also on pressure in such a model. This is because the pressure reduces the inter-ionic spacing which results in a "static" change in the p-d mixing. Such a pressure dependence of the absorption has been measured by Aust[4] and will be used in Chapter V to predict the amount of broadening which can be expected for a hybridized state due to the vibrations of the lattice. When the exciton binding energy is taken into account, this peak in the absorption is a direct
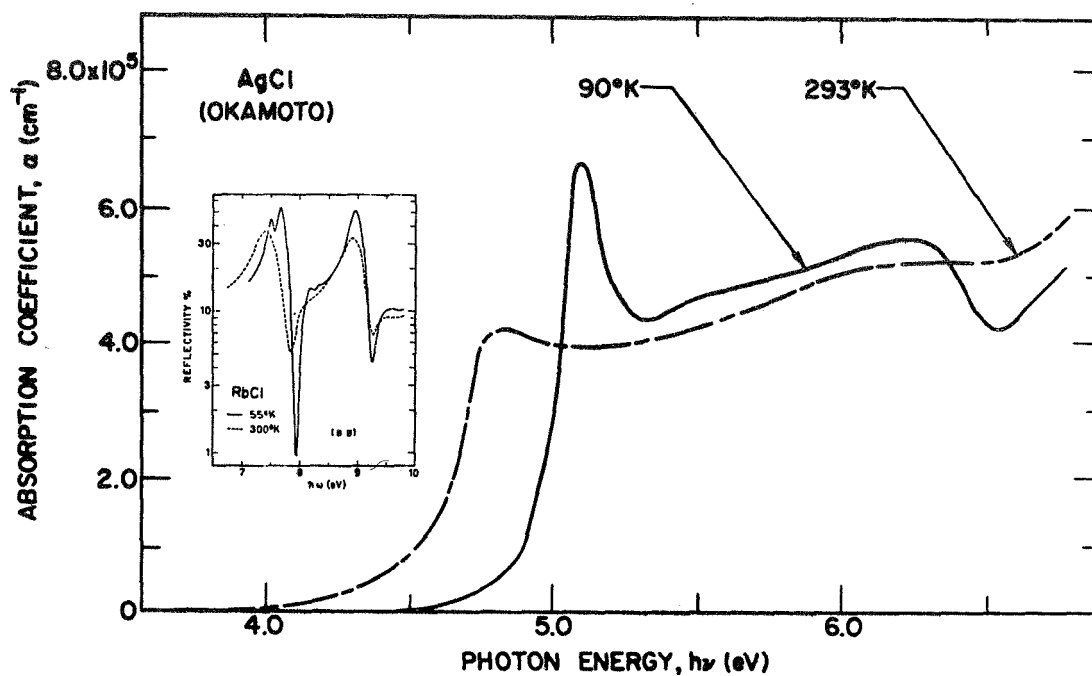
FIGURE 3.9. Comparison of the spectral distributions of the
absorption coefficient of AgCl at 90 and 293°K
from the work of Okamoto (reference 51) and of
RbCl at 55 and 300°K from the work of Baldini and
Bosacchi (reference 63).

measure of the fundamental band gap. A list of the most reliable values
estimated to date are summarized in Table III.3.

TABLE III.3. Values reported for the direct threshold of
AgCl and AgBr at the indicated temperatures.

Direct Threshold		Temperature (°K)	Reference
AgCl	AgBr		
5.15 ± 0.05	4.292 ± 0.002	4.2	45
5.13		20	64
5.10	4.20	89	65
5.13	4.29	20	51

The recent values of Carrera[45] are the most reliable. The difference between the direct (Table III.3) and indirect (Table III.2) thresholds is a quantitative measure of the amount of upward bending of the highest valence band from Γ to the maximum at L since both gaps are measured relative to the same conduction band state, Γ_1 . Since this upward bending from Γ is due entirely to the halogen p-silver d coupling,[26] the optical data shows that the hybridization influences the energy of the mixed states by several eV. (1.90 ± 0.05 eV in AgCl and 1.601 ± 0.002 eV in AgBr are measured upward from a "flat-band" condition. One expects at least an equivalent downward bending for a pure p-band.) This is consistent with the conclusions of the tight-binding calculation discussed in section A (see Fig. 3.3).

C. Photoemission

There has been a fairly large amount of work on the photoemission quantum yield from the silver halides (references 66, 67, 48, 68, 69, 70, 71, 41, 72, 73, 74). In addition, studies of photoemission from silver into the silver halides has also been the subject of investigation[75,76] because of its importance in the photographic process. There has only been one previous attempt at measuring photoemission energy distributions from the silver halides[48] and as will be shown, these are not representative of properties of this class of solids. We will not attempt a comprehensive discussion of each of these investigations but will rather choose representative examples of the earlier work to illustrate their shortcomings and the reasons for them. The references given above will serve as a bibliography on the subject.

A comparison of AgBr yield measured in this study and selected previous work of Peterson,[77] Taft, Philipp, and Apker,[70] and Fleischmann[74] is made in Fig. 3.10. Each of these measurements saturates at a yield of around 8% electrons per incident photon. The interesting differences occur in the threshold region. The previously reported yields exhibit thresholds which are more than 1 eV lower than the value measured in these studies and the rate of decrease of the yield to lower $h\nu$ (i.e., slope) in this range is less for the other works. The most
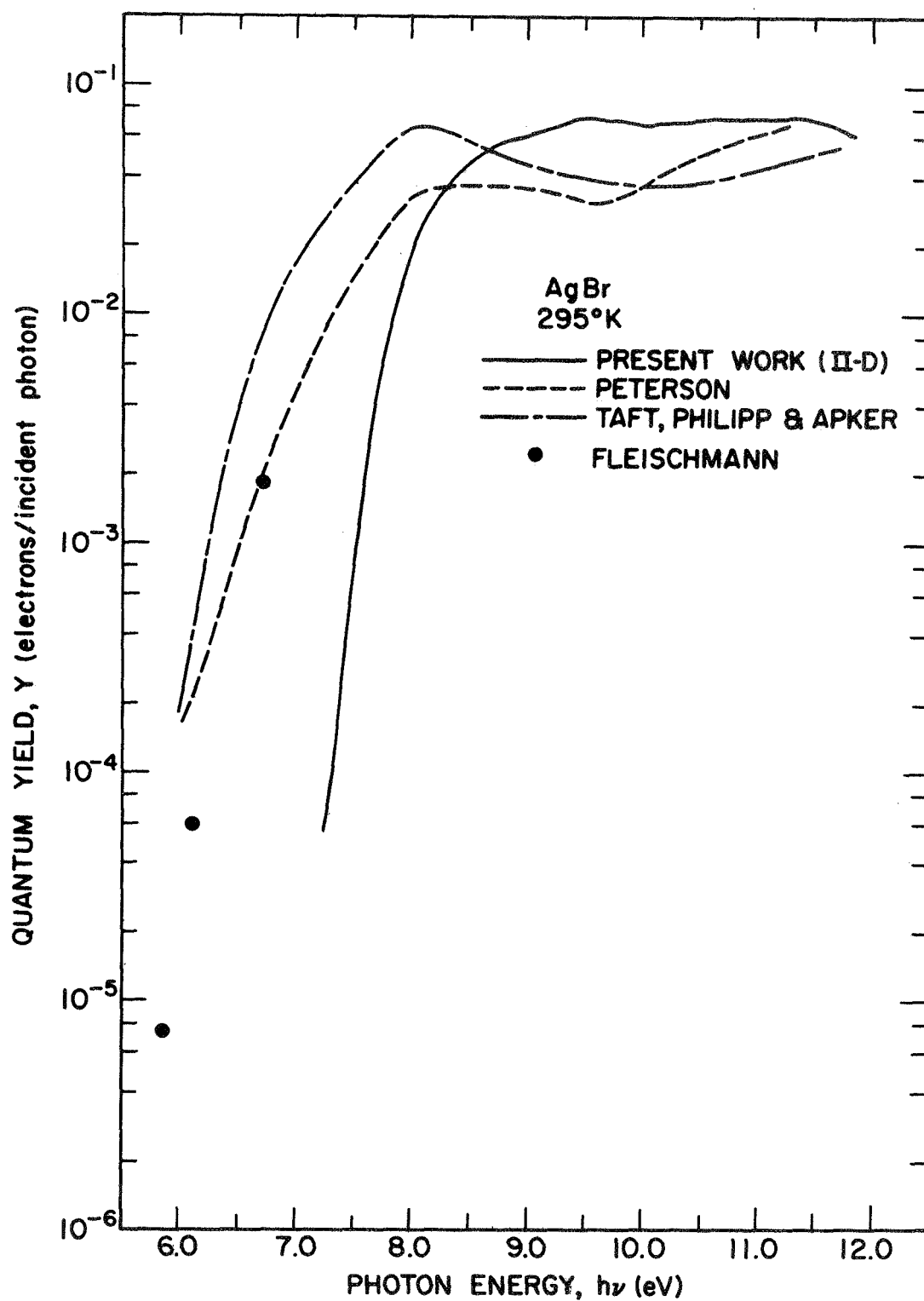
FIGURE 3.10. Comparison of the spectral distributions of the yield of electrons photoemitted per incident photon from AgBr at 295°K from this work and the works of Peterson (reference 77), Taft, Philipp, and Apker (reference 70), and Fleischmann (reference 74).

significant difference of our study from the others is that our samples
were prepared in vacuum in the same apparatus which was used for the
photoemission measurements. They were thus measured in situ and had
clean surfaces. The surface condition of the samples in the previous
works was clearly poorer because they were prepared external to the
measurement apparatus with no further cleaning after being mounted in
this vacuum chamber. In this entire procedure, "no special precautions
with the surface were taken".[48] The experience from the work done in
our laboratory shows that the condition of the surface can have profound
effects on the external photoemission from a sample. The effect of
surface contamination is in general to cause a lower threshold and an
energy distribution which has a Gaussian-like shape for all photon
energies (i.e., "universal curve").[78] The measurements of the yield by
Taft, et al.,[70] give indications that the lower yield threshold of AgBr
is not representative of the bulk properties of the solid but rather due
to surface conditions. These workers found that thin film samples pre-
pared in evacuated phototubes and measured in situ exhibited thresholds
more than 1 eV higher than thresholds obtained for bulk samples mounted
in their tubes following preparation. These film results were not repro-
ducible, possibly because of inadequate vacuum (pumping) during evapora-
tion. Peterson also measured the EDCs of AgBr and AgCl ;[48] a typical
AgBr curve is compared to the present work in Fig. 3.11. (These curves
are drawn on an absolute energy scale and cannot be shifted to bring
structure into agreement.) As can be seen in this figure, there is only
a slight correlation between the high energy shoulders and the peaks in
the curve from this study; even this agreement may be fortuitous. In
Peterson's AgBr curves "most of the external photoelectrons emerge
with energies between 0 and 2.5 eV (above the threshold, with) only a
small tail moving out to higher energies with increasing incident (photon)
energy".[48] This is characteristic of curves which are dominated by sur-
face contamination effects ("universal" curves[78]). The same comparison
can be made for AgCl . In Fig. 3.12, the yield near threshold has a
smaller slope, and it has a lower onset by over 1 eV in earlier work by
Peterson[48] and Fleischmann.[74,79] (Note, the break in the yield at 7.7 eV
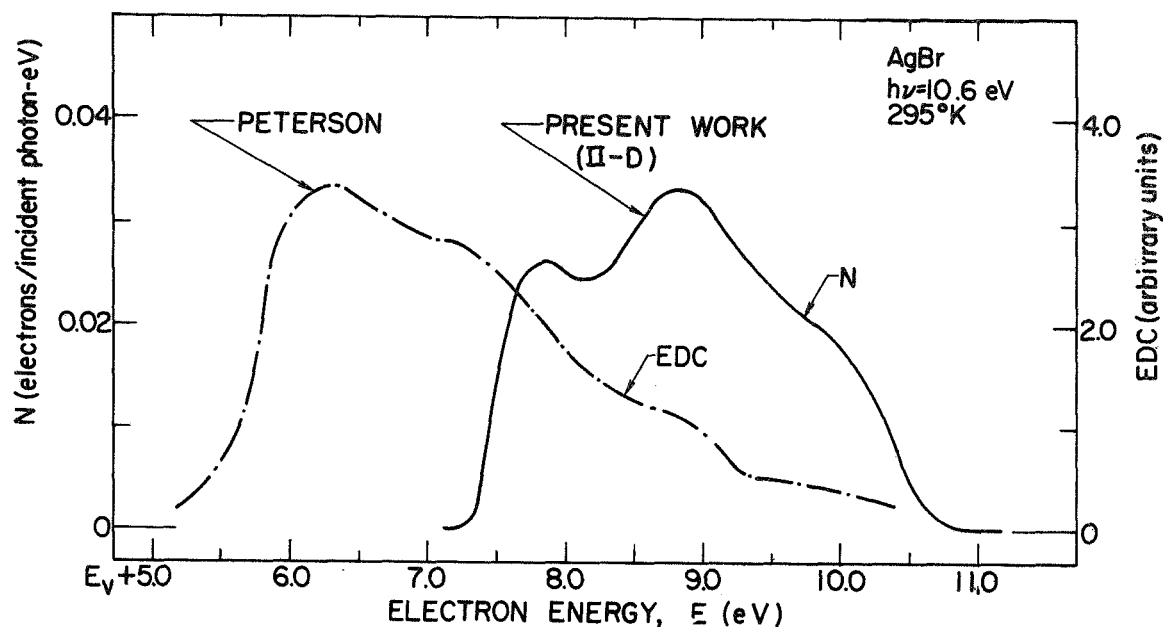
FIGURE 3.11. Comparison of energy distributions for electrons photo-
             emitted from AgBr at 295°K for a photon energy of 10.6 eV
             from the present work (normalized to the quantum yield per
             incident photon) and the work of Peterson (reference 48)
             (un-normalized).

and the lower energy region is due to electrons photoemitted from the
silver substrate through the AgCl sample film as will be discussed in
the next chapter.) A comparison of the AgCl EDCs of Peterson to this
work, as shown in Fig. 3.13, again shows virtually no agreement and a
fundamentally different behavior with changing $h\nu$. These character-
istics of the data and the sample preparation and handling techniques
suggest that the lower thresholds previously reported for AgCl and
-AgBr and significantly different EDCs are due to sample surface con-
tamination. The results of this investigation are the first photoemission
measurements which are representative of silver haldide properties.
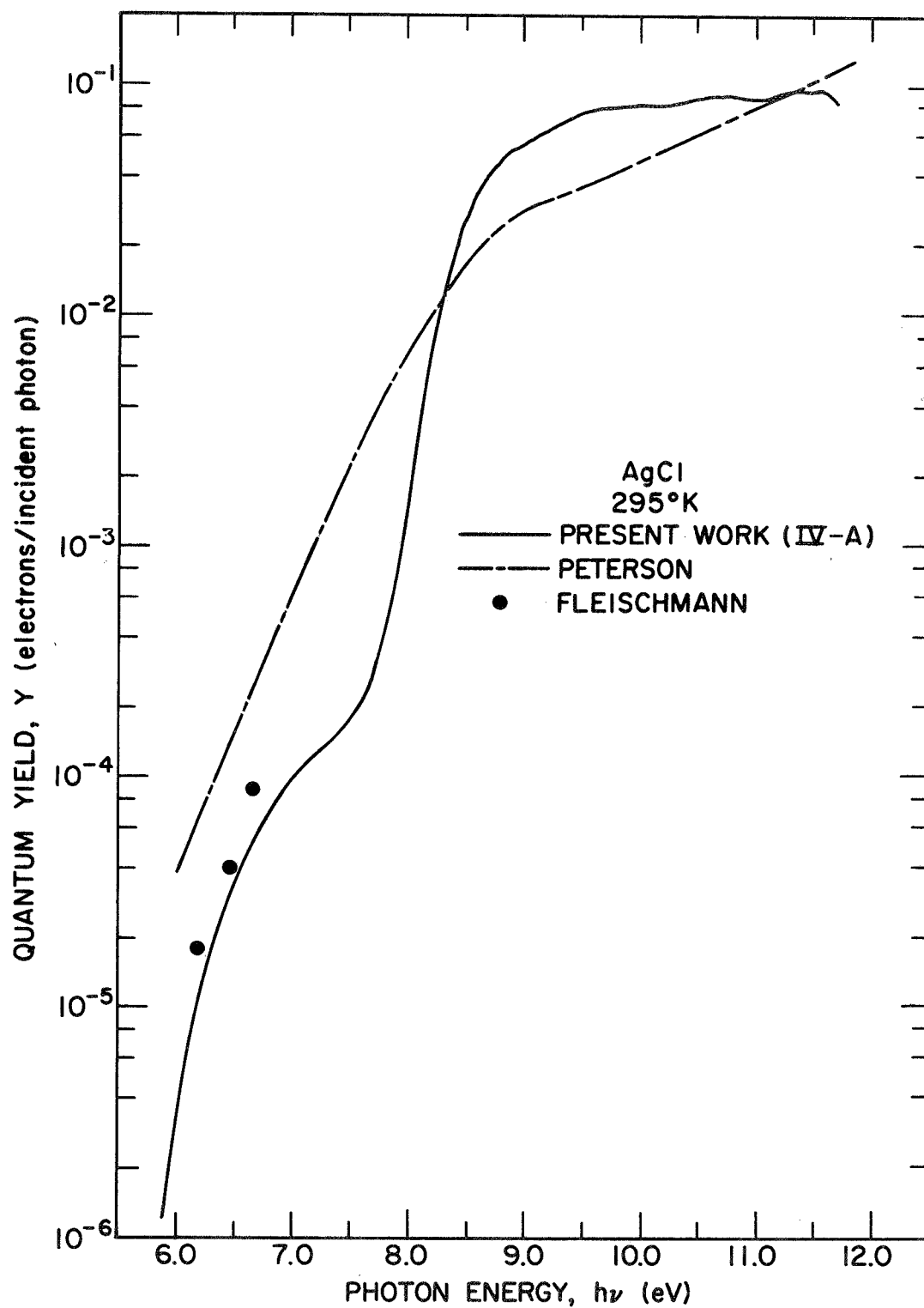
FIGURE 3.12. Comparison of the spectral distributions of the yield of electrons photoemitted per incident photon from AgCl at 295°K from this work and the works of Peterson (reference 48) and Fleischmann (reference 74).
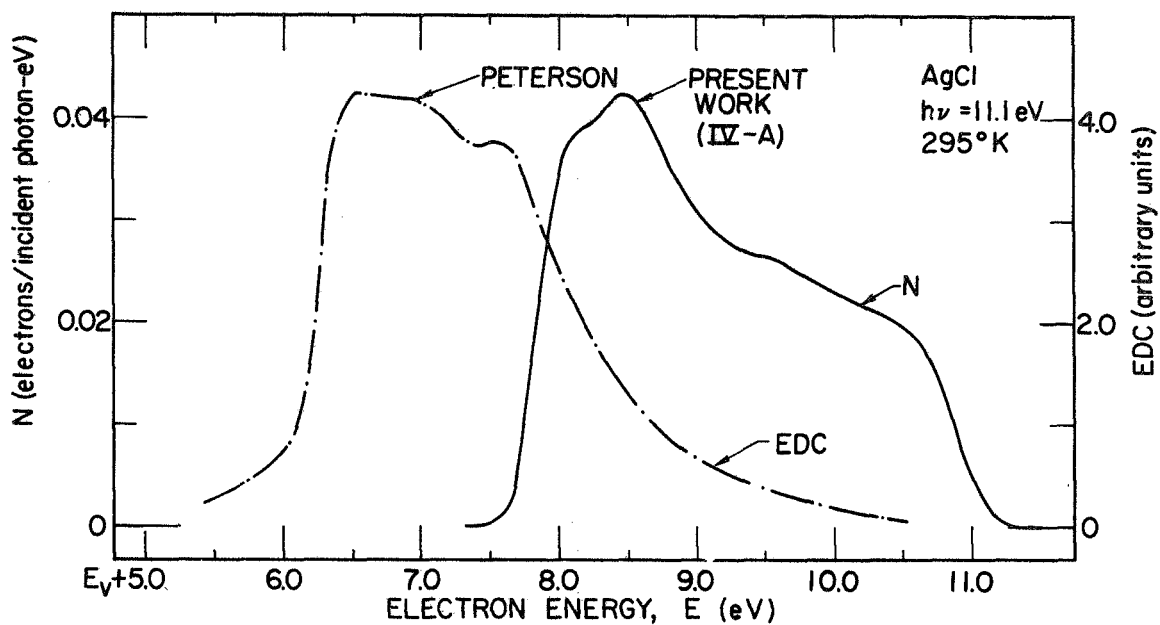
FIGURE 3.13. Comparison of energy distributions for electron
photoemitted from AgCl at 295°K for a photon
energy of 11.1 eV from the present work
(normalized to the quantum yield per incident
photon) and the work of Peterson (reference 48)
(un-normalized).

IV. EXPERIMENTAL TECHNIQUES

In this chapter the experimental techniques are discussed which
were used to make what was perhaps the first definitive low temperature
study of photoemission from solids. The sample preparation and handling
procedures are presented which led to the first measurement of external
photoemission which was representative of bulk silver halide properties.
The affect of various sample parameters on silver halide photoemission
are considered in detail at the end of the chapter. Since there has
been such considerable emphasis on quantum yield and photoemission
thresholds in the literature (e.g., in the pressure dependent absorption
work of Aust[4] and the energy bands of Bassani, et al.,[3]) not only will
the EDC data be presented, but also the yield data will be examined. To
gain a full appreciation for both the techniques employed and the appa-
ratus used to accomplish then, simplified schematic diagrams of the
equipment are accompanied by detailed photographs of the actual hardware.
Emphasis will be placed on the new experimental aspects developed for this
study.

A. Vacuum

To obtain meaningful data in a photoemission experiment, it is
necessary to study samples with atomically clean surfaces. As discussed
in the last chapter, the measurements made on silver halide samples which
have been prepared without regard to surface condition result in EDCs
which have indistinct thresholds and much anomolous structure. Therefore,
a clean surface must be properly prepared and the samples measured _in
situ_ in an adequate vacuum environment to maintain the clean surface
condition. The vacuum equipment used to accomplish this is shown sche-
matically in Fig. 4.1. The all 304 stainless steel system can be divided
into three sections: ultra-high vacuum (UHV), high vacuum (HV), and low
vacuum (LV). All of the pumps, chamber, oven, etc., existed at the time
this study was begun; however, it was not assembled in this configuration
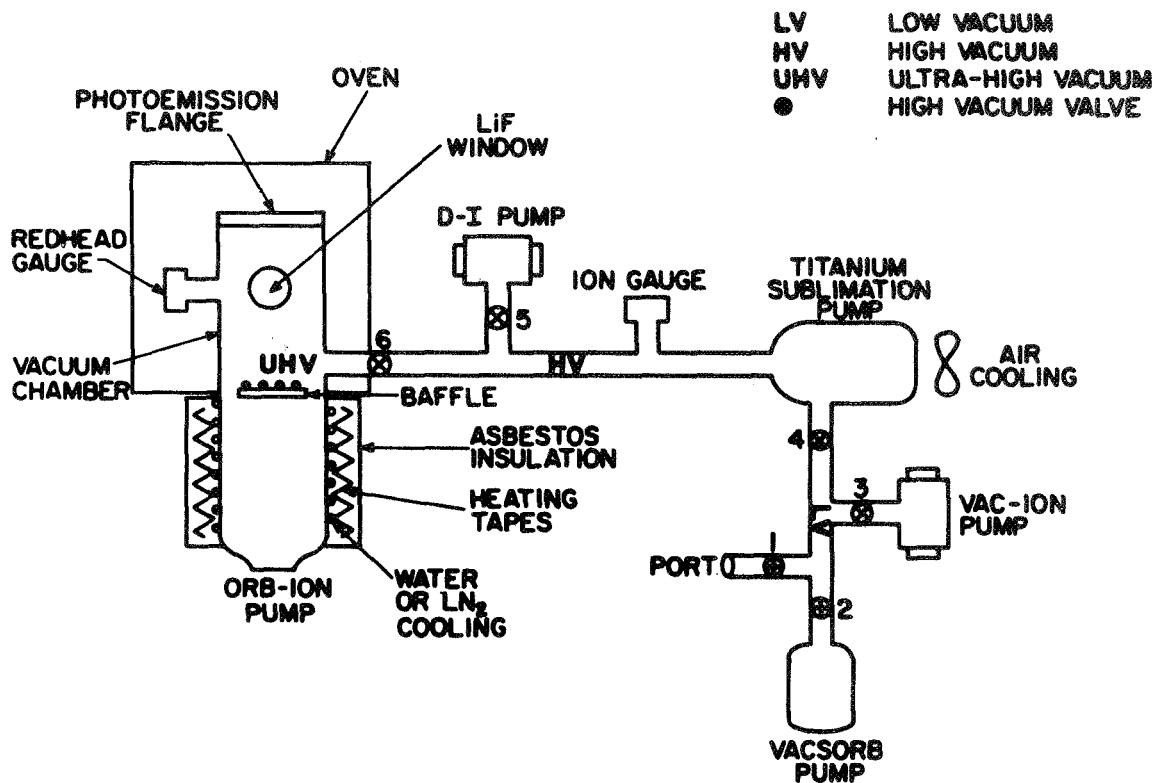
FIGURE 4.1. Schematic diagram of the vacuum system.

and new pumpdown-bakeout techniques were developed to lower the system base pressure by an order of magnitude. These procedures will be briefly described. Initially, valves 4 and 6 are open and the rest closed. The system is roughed to less than 5μ in the LV section with a portable Varian Vacsorb attached to the external port (valve 1 opened) followed by a second Vacsorb attached to the system (valve 2 opened). The Varian titanium sublimation pump filaments and orb-ion pump body are outgassed into this second Vacsorb. The vacuum chamber (designed by W.F. Krolikowsli[1] and Orb-ion pumps are baked at $175^\circ C$ (limited by AgCl seal of the LiF window) and $500^\circ C$ respectively into the titanium sublimation and Varian 8 l/s Vac-ion pumps (valve 3 opened). At a pressure of 1.5×10^{-7} Torr on the Varian nude ion gauge, the low vacuum section is isolated with

valve 4 and the Ultek 20 l/s D-I pump is used with the titanium pump as a second stage of bakeout. This HV section is left pumping in this mode so it can be used as an auxiliary pumping section during sample preparation if the pressure gets too high in the UHV section. At 4×10^{-8} Torr in the HV section and 7×10^{-8} Torr in the chamber, the HV section is isolated by closing valve 6. The heat tapes are turned off on the NRC 206-1 Orb-ion and the pump is activated for the first time with water used to cool the body and Ti baffle. The chamber continues to be baked into this pump to a pressure of 6×10^{-9} Torr. With the oven finally turned off, the Orb-ion pump efficiently pumps the chamber since the conductance is so high. This procedure, which takes about 5 days, leads to a base pressure of about 4×10^{-11} Torr in the experimental chamber; this is about an order of magnitude lower than was previously possible. To gain further pumping speed during sample evaporation, the entire Orb-ion body is made a large cryopump by running liquid nitrogen in the water lines (this procedure was first developed by J. G. Endriz). This reduces the base pressure in the chamber to about 2×10^{-12} Torr as measured by the NRC 554 Redhead gauge. Photographs of the LV and HV sections are shown in Fig. 4.2 and the UHV section with the photoemission flange removed in Fig. 4.3. The major innovation of this system which allowed such low pressures to be achieved was the mounting of the roughing sections so close to the UHV experimental part. The increased conductance to the rough pumps and addition of the extra roughing section (LV) allowed a lower bakeout pressure prior to using the Orb-ion pump.

B. Sample Preparation

In preparing samples for these experiments, consideration must be given to both the properties of the silver halides and the requirements imposed by the measurement. As noted above, perhaps the most important material characteristic for photoemission studies is the condition of the surface. Many methods have been used in the past on various materials to prepare samples with atomically clean surfaces in ultra-high vacuum. Though high purity single crystals of AgCl are available, it
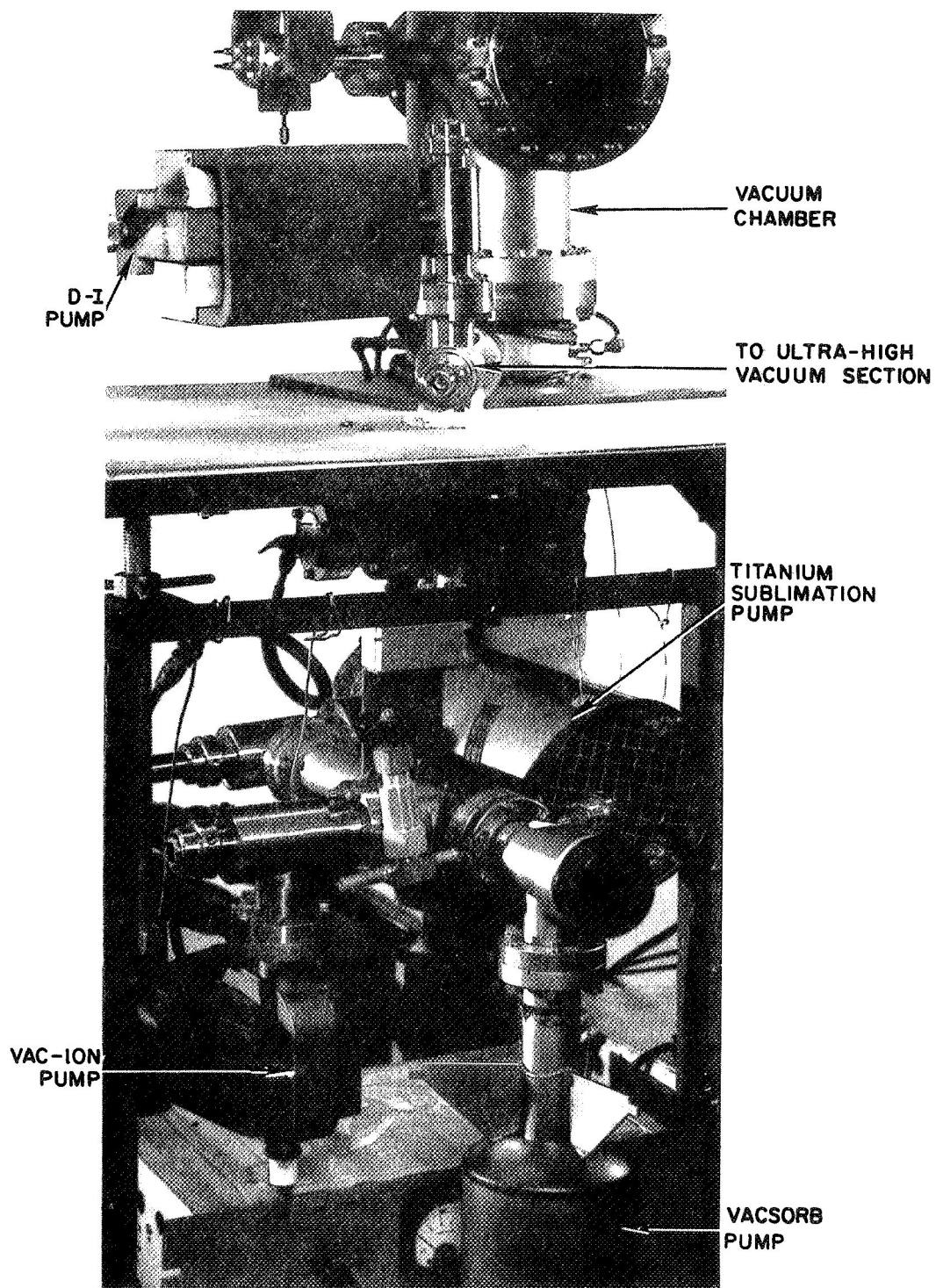
FIGURE 4.2. Photograph of the low and high vacuum sections of the vacuum system.

TO LOW
VACUUM SECTION

REDHEAD
GAUGE

PHOTOEMISSION
FLANGE

LiF
WINDOW

VACUUM
CHAMBER

COLLECTOR

ORB-ION
PUMP

WATER
PUMP
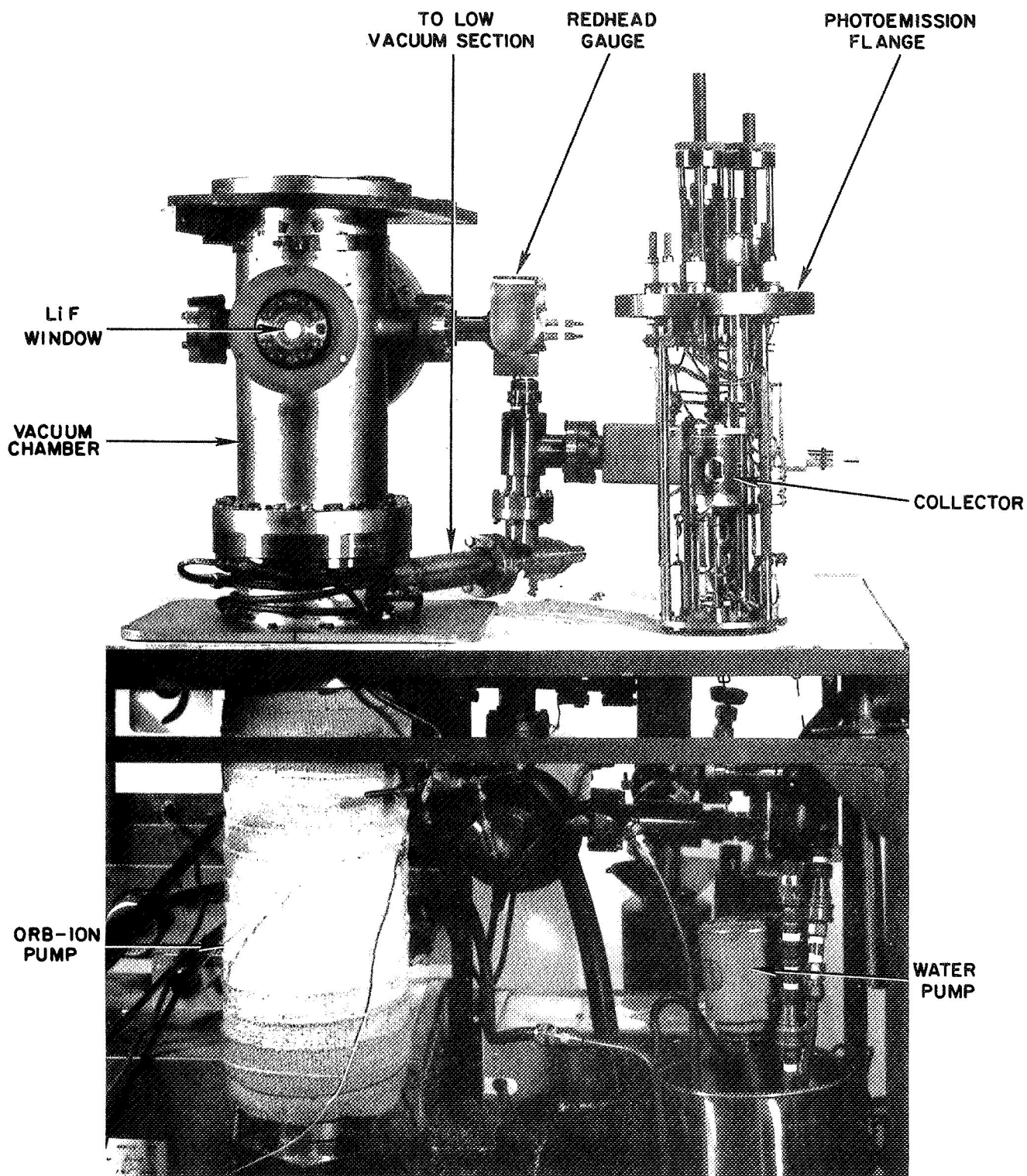
FIGURE 4.3.   Photograph of the ultra-high vacuum section of the vacuum
system and the photoemission flange.

is not possible to cleave them because of their plastic characteristics.[80]
For the same reason, heat cleaning or sputter cleaning of single crystals
is impractical for the silver halides. Thus, in this study, crystal-
line thin films of all three halides were prepared in the experimental
chamber by high vacuum vapor deposition of greater than 99.999% pure
powder. This high purity silver halide starting material was purchased
from Atomergic Chemetals Co., Carle Place, Long Island, New York.
Electron microscopy[81] and optical[65,49,82] studies have established that
evaporated thin films are good model systems for bulk silver halide
properties. Details of the thin film preparation procedures and con-
ditions are discussed in this section.

1. Evaporation

The evaporation pressures varied from 2×10^{-9} Torr to 3×10^{-8} Torr
with gas bursts as high as 5×10^{-6} Torr for AgCl . The difficulties
in achieving lower evaporation pressure appear to be two-fold. Firstly,
during evaporation some of the silver halide melt decomposes into silver
and halogen gas since the amount of photolytic decomposition is known to
greatly increase at elevated temperatures.[83] Fortunately, the evapora-
tion temperature (to be discussed next) is low enough so the silver does
not evaporate with the molecular silver halide but remains in the evapora-
tion vessel. The halogen gas that is emitted is very difficult to pump
and is part of the cause for the high pressures. Secondly, the Orb-ion
pump is very poorly suited for evaporations. This is because the amount
of titanium sublimation is controlled by the impact of electrons on the
Ti cartridges on the anode and hence the pressure. Unfortunately, it
takes time for this process to react to rapid pressure changes which
occur over a short time period such as the evaporation period. This
amounts to a loss of Ti pumping during the evaporation and hence a
higher pressure. As noted in section A, the pressure was reduced during
evaporation by using the high vacuum section (HV in Fig. 4.1) which was
normally at 1×10^{-9} Torr (i.e., opening valve 6 during evaporation).
In addition, the pumping speed was increased by cooling the pump and
baffle with LN_2 running in the cooling line. It is interesting that
after evaporation the Ti deposited on top of the adsorbed halogen gas

helped to keep the pressure when the LN_2 was turned off, well below the maximum pressure encountered during evaporation.

A compilation and extrapolation of existing vapor pressure data[84-86] predicts that AgCl evaporates at between $180^\circ C$ at 10^{-10} Torr and $390^\circ C$ at 5×10^{-6} Torr. This is very significant since it means that at these low evaporation temperatures very little heating of the chamber and subsequent outgassing will occur. The evaporator used in these studies was designed by B. H. Schechtman[36] and is shown in the background of Fig. 4.4. The quartz buckets which hold the starting

(a)   (b)   (c)
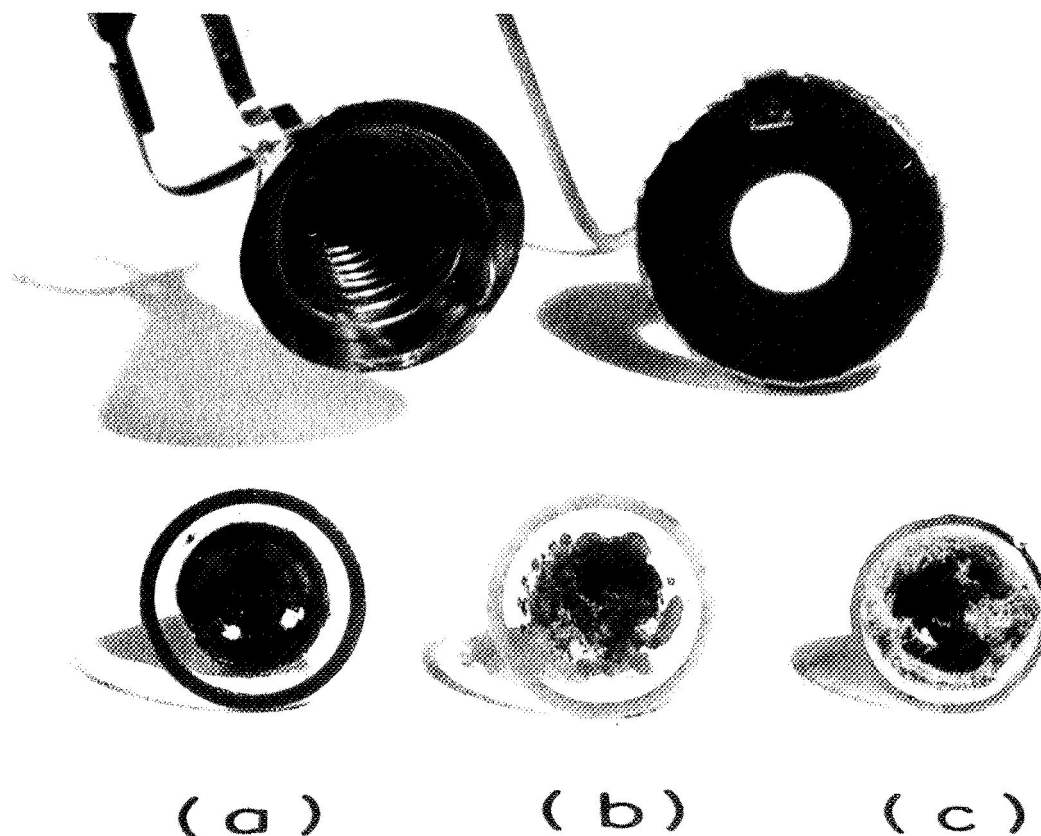
FIGURE 4.4.   Photograph of the evaporator with the residue left follow-
              ing evaporation of (a) AgBr, (b) AgCl, and (c) AgI shown
              in the foreground.

powder (foreground) fit within a conical tantalum heater filament. These are then surrounded by a molybdenum conical shield and top (to the right of filament) with only a small hole in this top to allow evaporation. This shield serves the dual role of keeping the light emitted by the Orb-ion pump from the powder and reflecting the filament heat back to the melt. This allows the evaporator to be operated at low current levels in order to reduce the heater filament light emission, and thereby reduce possible photolytic decomposition of the thin film as it is being deposited. The three buckets in the foreground show typical examples of the residue left following evaporation of the three halides: (a) AgBr, (b) AgCl, and (c) AgI. Both AgBr and AgCl evaporate from the liquid state. As can be seen by the clear AgBr but silvery AgCl , AgCl seems to decompose much more readily during evaporation. This is consistent with the higher evaporation pressure encountered for this halide. AgI sublimes from the solid state and behaves quite differently. As can be seen in (c), during evaporation a gray, hairy, ash-like residue is left in the boat. Such a AgI residue was also observed by Brady.[87]

This evaporator is mounted on the photoemission flange (Fig. 4.4) as shown in the full photograph of the flange, Fig. 4.5. In its original form, this flange was designed by W. F. Krolikowski.[1] The powders were stored in a light-tight dessicator since they are slightly hygroscopic. The evaporator was filled under red safelight, and the viewports of the chamber were covered with red cellophane to avoid exposure to room light.

2. Substrate

Consideration had to be given to the reaction of the silver halides with materials used in the experimental apparatus. This was an especially important factor in choosing an appropriate conducting substrate for photoemission measurements. It is known that many metals react readily with AgCl and cause its decomposition by a simple replacement reaction.[30] It has been found in this study that both copper and nickel are unsuitable as substrate materials because of their interaction with the AgCl

SHIELDS

LIGHT

SHIELDS

EVAPORATOR

SHUTTER
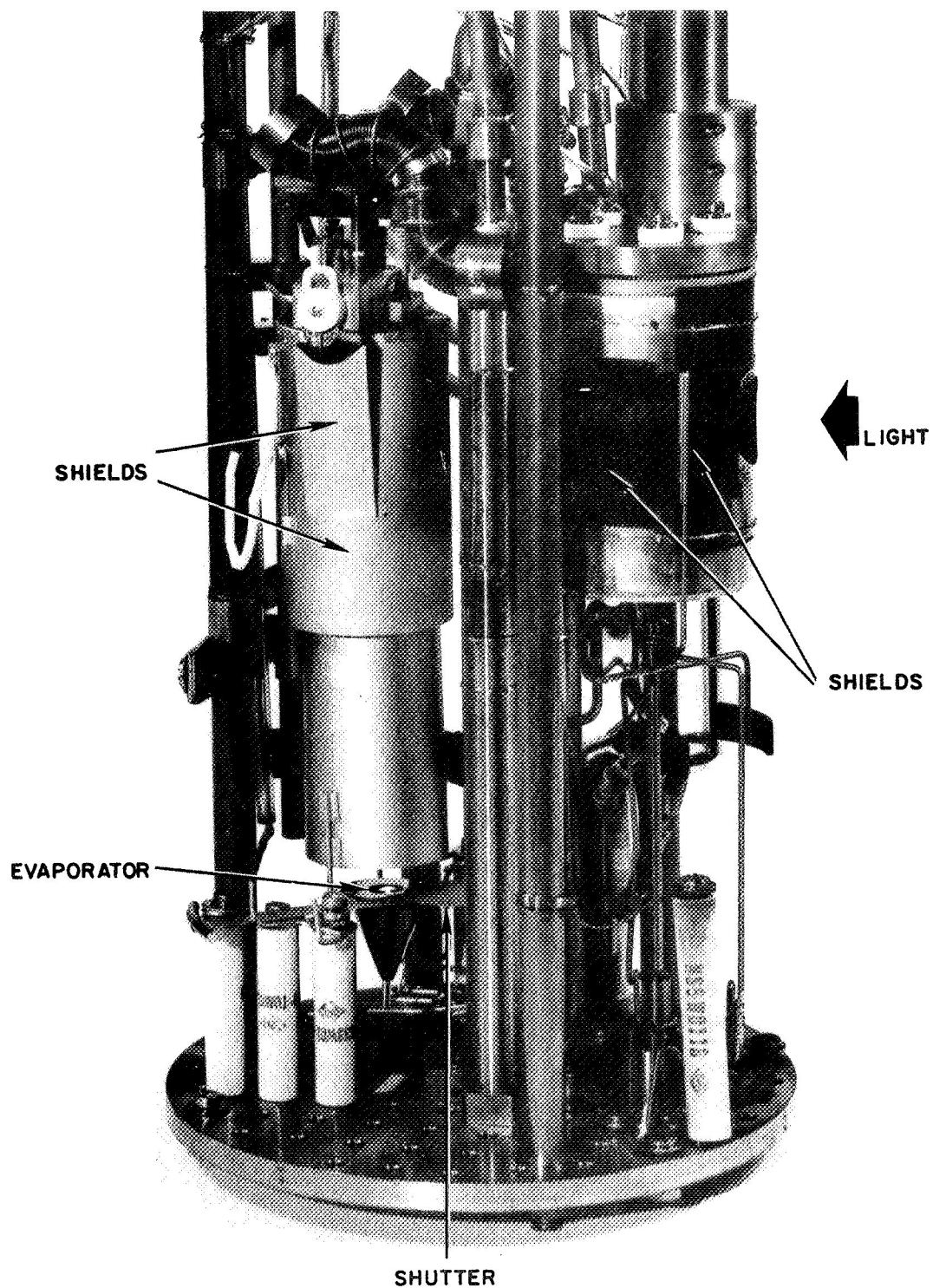
FIGURE 4.5. Photograph of the photoemission flange.

being deposited onto their surface. Silver was used as a substrate material for AgCl and AgBr since it was non-reactive with these halides, but platinum had to be used for AgI since this halide is reactive with silver.[88] An experiment was conducted with AgCl on a Pt substrate and no effect other than a higher trheshold was found due to the substrate material. (This will be discussed in detail in section E.) The substrates were 0.87" X 0.67" to fit the holder on the flange (a photograph is seen in Fig. 4.17). Rolled 99.99% pure silver sheet and a pressed 99.99% Pt piece were used as starting materials. The work hardening of these soft metals allowed them to be polished to a mirror finish. They were heat-cleaned at 450°C and 1×10^{-10} Torr in the measurement chamber prior to evaporation. (This temperature is limited by the physical limitations of the flange.) EDCs were measured for the cleaned substrates to insure a contamination free surface. Some of the best measurements for these metals to date were obtained. These curves are presented in Appendix B. This problem of the reaction of the silver halides with other solids is particularly important for stainless steel from which most of the flange parts are built. Since AgCl does react with stainless steel,[89] shields were constructed of Mo to restrict the silver halide vapor from depositing on any surfaces except the substrate and thickness monitor as indicated on the left side of Fig. 4.5. For the evaporation, the temperature of the substrate could be controlled from 80 to 725°K as shown schematically in Fig. 4.6. The substrate is heated above room temperature with a resistance heater mounted in the substrate holder.[1] The substrate can be cooled to any temperature down to 80°K by the same gas cooling techniques described in the next section. For studies of the silver halides, it has been found that thin films form epitaxially on a crystalline substrate for temperatures just above room temperature to around 150°C.[81] As will be discussed in section E, it was found that the photoemission EDCs from AgBr were independent of the substrate temperature during growth, T_s, over this range. Most films were formed at $T_s = 75^{\circ}$C to insure epitaxial formation.
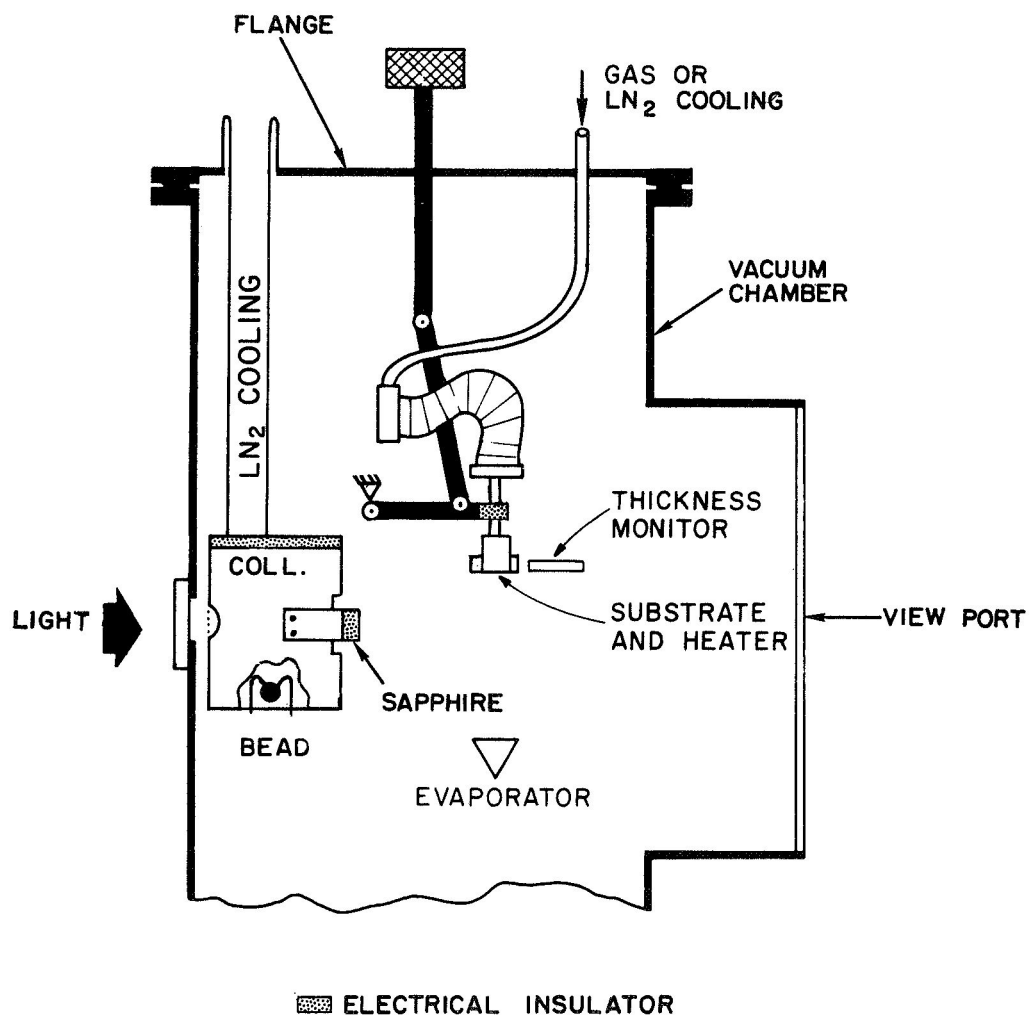
FIGURE 4.6. Schematic diagram of the photoemission flange apparatus in the evaporation position.

3. Thin Film Properties

In choosing a desired thickness for the silver halide films, consideration must be given to the effects of the high resistivity of these compounds. Typically, AgCl has a room temperature resistivity of 10^8 Ω-cm,[80] and a much higher value at 80°K. It has been found in previous work on low conductivity insulating thin films that structure in the measured EDCs can be distorted in both position and relative magnitude.[36] This is due to both a potential difference across the film,[36] and a charging of the surface by the holes left behind by the photoemitted electrons.[2] It is found that for many insulators these effects can be eliminated, even at LN_2 temperature, by making the sample films sufficiently thin.[2] In order to accurately deposit films of 200 to 400 Å thickness, a quartz crystal microbalance, designed and built by T. H. DiStefano,[2] is used to monitor the evaporation. A much improved frequency stability of the AT cut quartz crystals was achieved by annealing them at 300°C in evacuated tubes and slowly cooling to relieve the crystal strains produced during evaporation of the metallic electrode.[90] This thickness monitor is mounted beside the substrate during the evaporation, as shown in the schematic (Fig. 4.6). The deposition thickness, τ , is simply related to the frequency change of the quartz crystal Δf by the density of the film, ρ :[2]

$$\tau = \frac{\Delta f}{0.56\,\rho}\ \text{Å} \qquad (4.1)$$

The factor 0.56 was experimentally determined by the author and T. H. DiStefano by calibrating the crystals with thick films and checking the thickness both with a Varian Å scope and weighing the film with a microgram balance. The evaporator is shuttered to accurately control the evaporation time (see Fig. 4.5). It is of considerable aid in controlling the evaporation to establish a stable, known evaporation rate prior to the actual deposition. For this purpose, a second quartz crystal monitor is located between the evaporator and shutter as shown in Fig. 4.7. The apparatus shown in this photograph mounts into an ion-pumped bell jar and was used for preliminary materials testing; it was
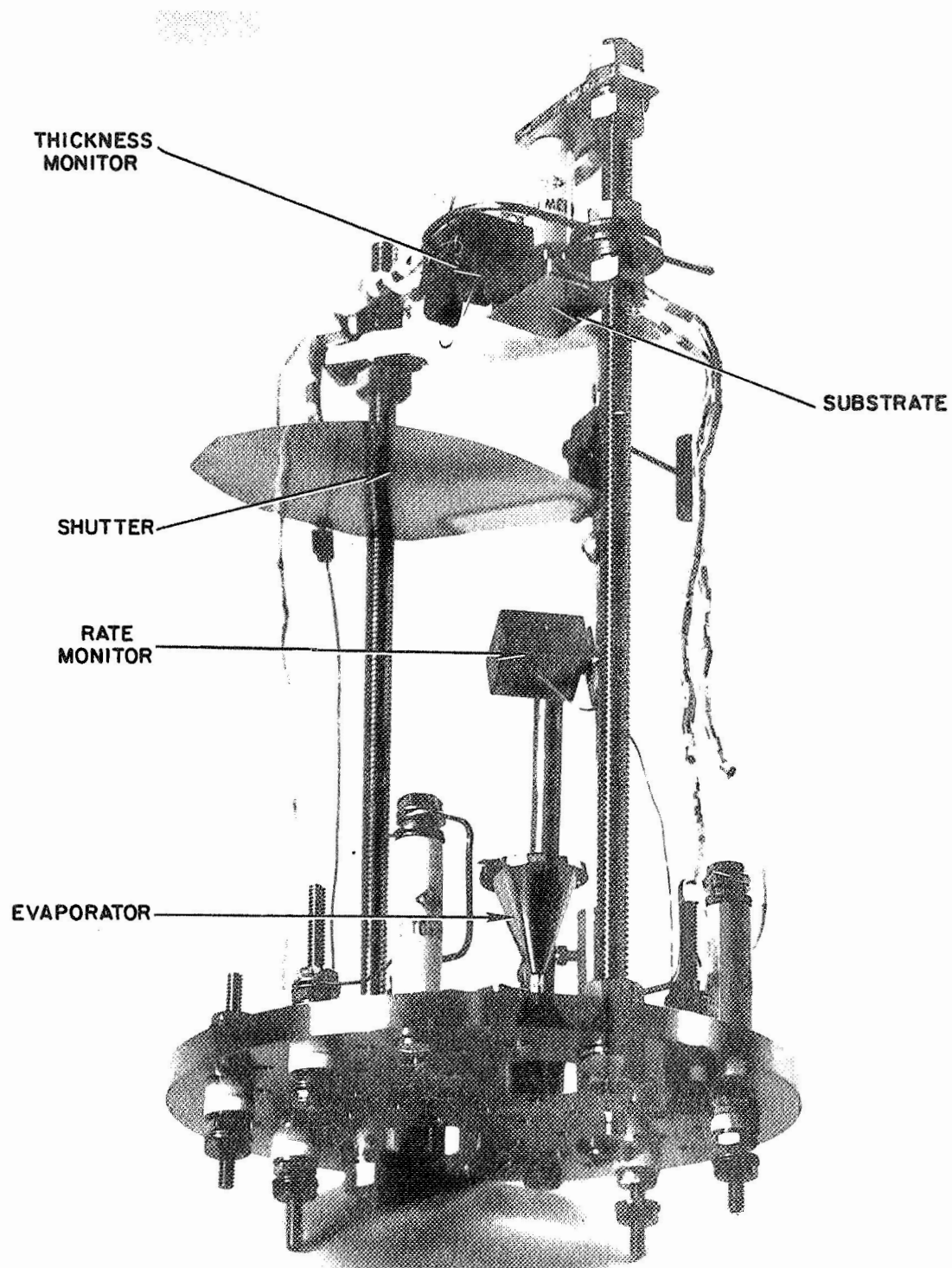
FIGURE 4.7. Photograph of the bell jar evaporation apparatus showing the arrangement used for preparation of samples.

built to the same dimensions as the evaporation section of the photo-emission flange. The actual film deposition rate, $d\tau_T/dt$, at the substrate is just geometrically related to the measured rate monitor value, $d\tau_R/dt$, by:[91]

$$\frac{d\tau_T}{dt} = \frac{d\tau_R}{dt} \frac{\cos^4\phi_T}{\cos^4\phi_R} \frac{D_R^2}{D_T^2} \qquad (4.2)$$

where ϕ is the angle of the thickness (T) or rate (R) monitor to the source (measured from the vertical), and D is the vertical distance of each monitor from the source. The films in these studies were typi-cally evaporated at 1-3 $\overset{o}{A}$/s. Such slow rates were used to enhance the epitaxial formation of the films.[92] The actual evaporation apparatus on the photoemission flange is shown in Fig. 4.8.

The actual preparation conditions for each of the samples studied are summarized in Table IV.1. The samples are identified by material (e.g., AgCl), by the pumpdown (e.g., III), and by the film (e.g., B). Because of the low evaporation temperature of the silver halides, the substrate could be heated to 450°C, and the sample film evaporated off. Thus, more than one film could be studied in each pumpdown. The maxi-mum pressure which occurs during evaporation is tabulated as P_{MAX}. Also included in this table is the metal film which was deposited on the inside of the cylindrical collector. A fresh film was evaporated from a premelted bead on a Mo wire for each pumpdown to provide a uniform collector work function (see Fig. 4.6). The front and back openings in the collector are closed with shields to keep the metal from deposit-ing on the LiF window and substrate (see right side of Fig. 4.5). The bead is mounted on a linear motion so it can be removed from the col-lector during measurement (see Fig. 4.9).

As discussed at the beginning of this section, it has been estab-lished that thin films of the silver halides are good model systems for the study of bulk properties. In order to determine if the very thin films used in these studies are "good" films from the viewpoint of their photoemissive properties, a very thick film was the last sample deposited
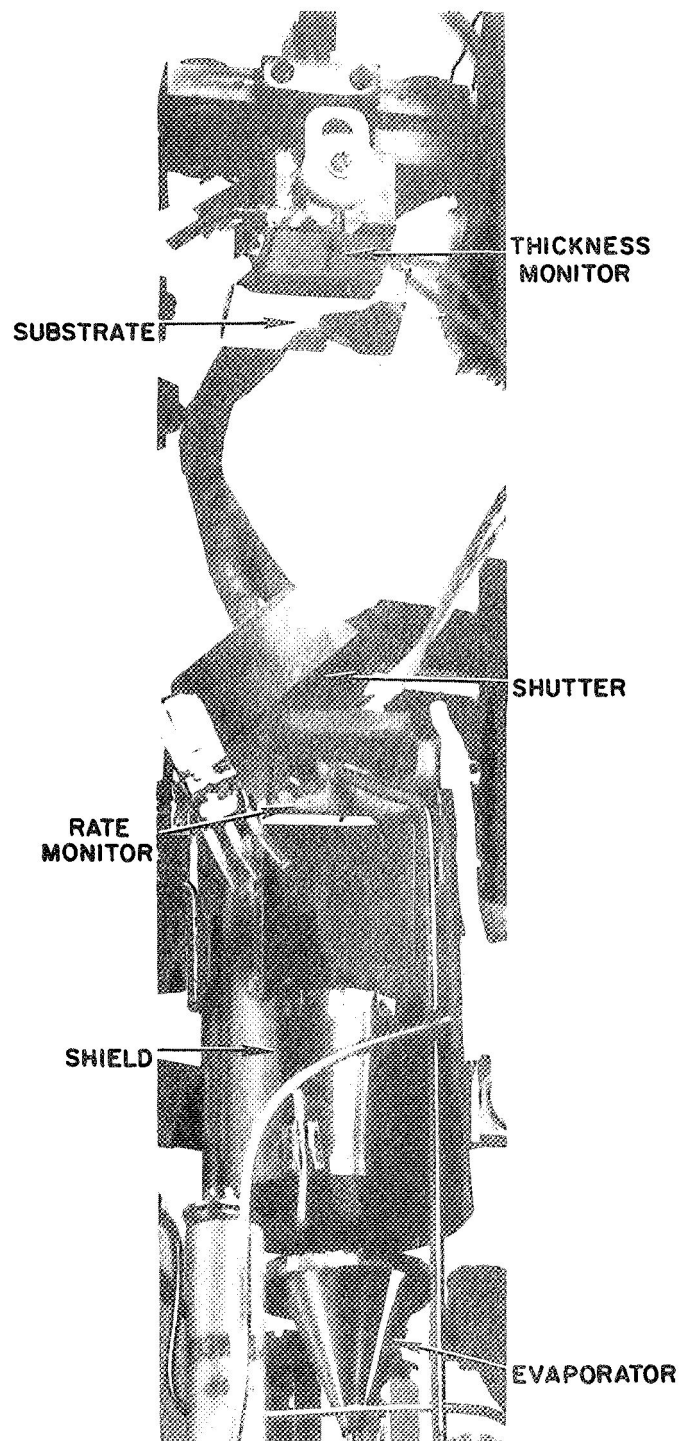
FIGURE 4.8. Photograph of the evaporation section of the photoemission flange.

67

TABLE IV.1. Material parameters for the samples used in this work including the thickness, τ, evaporation rate, $d\tau/dt$, maximum pressure during evaporation, P_{MAX}, and substrate temperature during deposition, T_s.

	SAMPLE	τ (Å)	$d\tau/dt$ (Å/sec)	P_{MAX} (TORR)	T_s (°C)	SUBSTRATE	COLLECTOR
	I-A	250	2.5	2.2×10^{-8}	22	Ag	Au
	I-B	185	1.3	3.8×10^{-9}	22	Ag	Au
	I-C	6,100	2.7	9.5×10^{-8}	22	Ag	Au
	II-A	230	2.6	3.1×10^{-8}	22	Ag	Au
AgBr	II-B	305	1.9	2.5×10^{-8}	75	Ag	Au
	II-C	< 265	2.3	1.6×10^{-8}	175	Ag	Au
	II-D	365	2.5	2.5×10^{-8}	50	Ag	Au
	II-E	6,070	1.8	5.5×10^{-8}	50	Ag	Au
	III-A	270	1.5	1.5×10^{-8}	75	Ag	Au
	IV-A	200	1.1	3.2×10^{-9}	75	Ag	Au
	I-A	150?			22	Ag	Au
	I-B	215			22	Ag	Au
	I-C	5,550	1.0		22	Ag	Au
	II-A	320	6.4	1.4×10^{-7}	29	Ag	Au
	II-B	175	0.3	1.0×10^{-9}	22	Ag	Au
	II-C	6,050	3.4	1.2×10^{-7}	22	Ag	Au
	III-A	325	2.5	1.4×10^{-7}	75	Pt	Cu
AgCl	III-B	290	2.1	5.4×10^{-7}	22	Pt	Cu
	III-C	215		3.3×10^{-7}	50	Pt	Cu
	III-D	5,630	3.6	2.0×10^{-6}	75	Pt	Cu
	IV-A	185	3.0	6.0×10^{-8}	75	Ag	Cu
	IV-B	150	1.7	4.0×10^{-9}	125	Ag	Cu
	IV-C	165	0.6	8.0×10^{-10}	75	Ag	Cu
	IV-D	6,150	1.2	3.5×10^{-9}	75	Ag	Cu
	V-A	195	1.6	4.0×10^{-7}	75	Ag	Au
	I-A	405	1.4	2.0×10^{-7}	75	Pt	Au
AgI	II-A	220	0.8	1.0×10^{-6}	75	Pt	Au
	II-B	200	0.7	1.0×10^{-6}	75	Pt	Au
	II-C	3,010	1.6	2.1×10^{-6}	75	Pt	Au

each pumpdown. These films were evaporated under the same conditions
(e.g., evaporation rate and substrate temperature) as the very thin
films. As will be discussed in section E, it was found that at room
temperature there were no significant differences in the EDCs and yield
between films that were 300 Å and 0.6 μm thick. As explained above,
the thick films could not be measured at LN_2 temperatures because of
their high resistance. These samples were removed from the chamber and
were investigated by X-ray diffraction. The results are summarized in
Table IV.2.

TABLE IV.2. Orientation and particle size from X-ray diffraction
measurements of thick films used in this work.

	SAMPLE	PARTICLE SIZE (Å)	FILM ORIENTATION	SUBSTRATE ORIENTATION	SUBSTRATE
AgBr	I-C	860	(200)	(422)	Ag
	II-E	13,810	(200)	(200)	Ag
	IV-A	1,150	(200)	(200)	Ag
	EVAP	920	(200)	(422)	Ag
AgCl	I-C	670	(111)	(111)	Ag
	II-C	4,480	(111)	(111)	Ag
	III-D	1,060	(111)	(200)	Pt
	IV-D	8,960	(111)	(200)	Ag
	EVAP	9,370	(200)	RANDOM	GLASS
AgI	II-C	1,080	β(002)	(220)	Pt
	EVAP	510	β(002)	(111)	Pt

(The "EVAP" samples were from bell jar evaporation studies.) As can be
seen, these thick films are characteristic of pure polycrystalline silver
halide films which were highly oriented in the (200) direction for AgBr,
(111) for AgCl, and hexagonal, β phase (002) for AgI. The particle
size, as calculated from the broadening of the X-ray lines (assuming
negligible straining),[93] was from 4,000-5,000 Å for AgCl and AgBr

and around 800 Å for AgI . Thus, the very thin films are representative of bulk silver halide photoemission.

These X-ray measurements were unable to detect any impurities, such as Ag , within the 3% resolution of this technique. The purity of the samples is very important since the amount of photolysis is dependent on the purity of the silver halide and the concentration of crystalline imperfections. The question of photolysis is especially important in performing photoemission experiments since it is well known that photolytic darkening is produced by light quanta having the same range of energies as those which produce photocurrents.[41] The basic process of this photolytic decomposition can be summarized as follows.[94] The thermal energy required to displace a silver ion from its normal lattice position into an interstitial sight is relatively small. At room temperature, the jump frequency of these interstitial Ag^+ ions is very large being near 10^{11} Hz. The photoelectrons produced by the incident photon flux combine with the migrating interstitial silver ions to form atoms of metallic silver. These atoms act as electron traps thereby capturing additional photoelectrons. This cycle is repeated many times until a silver speck is formed. The net effect is a decomposition of the AgCl with chlorine gas appearing at the illuminated surface and a noticeable darkening of the sample volume. The concentration of imperfections affects this process since it is found that the specks of silver metal are deposited on imperfections, such as dislocations, within an AgCl crystal.[95] In extremely pure samples, one cannot form a visible volume darkening.[96] From observation of silver halide thin films prepared for this investigation and the stability with time of the EDCs (see section E), the films are of sufficient purity (higher than that of the 99.999% pure starting material) and uniformity that even if there is any photolytic decomposition occurring, it is very slow and has no major effects on the photoemission data. This is also consistent with the observation that at low levels of photoproduct formation, the effects on the absorption spectrum are very slight and add no fine structure.[97]

C. Cooling

As noted in Chapter I, prior to this study equipment had been built by W. F. Krolikowski[1] and T. H. DiStefano[2] to measure EDCs at LN_2 temperature. These earlier experimental techniques did not allow for measurements at temperatures intermediate to 295 and $80^\circ K$ and did not overcome the cooling limitations imposed by the photoemission measurement. The latter include primarily the large electrical noise introduced by the bubbling of the LN_2 and the leakage current caused by condensation of water vapor on the electrodes. In this section, emphasis will be placed on the major modifications made on the existing equipment, the new apparatus designed and built for this study, and the new techniques developed to measure the dependence of EDCs on temperatures ranging continuously from room to LN_2 values.

1. Setting Sample Temperature

After the sample thin film is prepared as described in the previous section, the substrate is pivoted using a linear motion from the horizontal position shown in Fig. 4.6 into the collector and a vertical position normal to the incident monochromatic light beam as shown in Fig. 4.9. This flange was originally built with a hollow box in the substrate holder which could serve as a reservoir for LN_2 feed to it through hollow stainless steel tubes and bellows.[1] The major difficulties with this design were that (1) the output had to be vacuum pumped to draw the LN_2 to the reservoir since the back pressure of vaporized liquid prevented the LN_2 from reaching the reservoir, and (2) even when pumped, the bubbling of the LN_2 in the reservoir caused severe vibrations and hence electrical noise in the EDCs. To overcome these difficulties, cold gas was forced under pressure through the reservoir to accomplish the cooling as pictured in Fig. 4.10. Further, by adjusting the flow rate of the gas, the heat losses in the support members could be compensated by varying amounts. In this way, the temperature of the sample was controllable. At low gas pressures, the vibration of the substrate was negligible, and the EDCs could be measured without noise degradation while the gas was flowing.

71
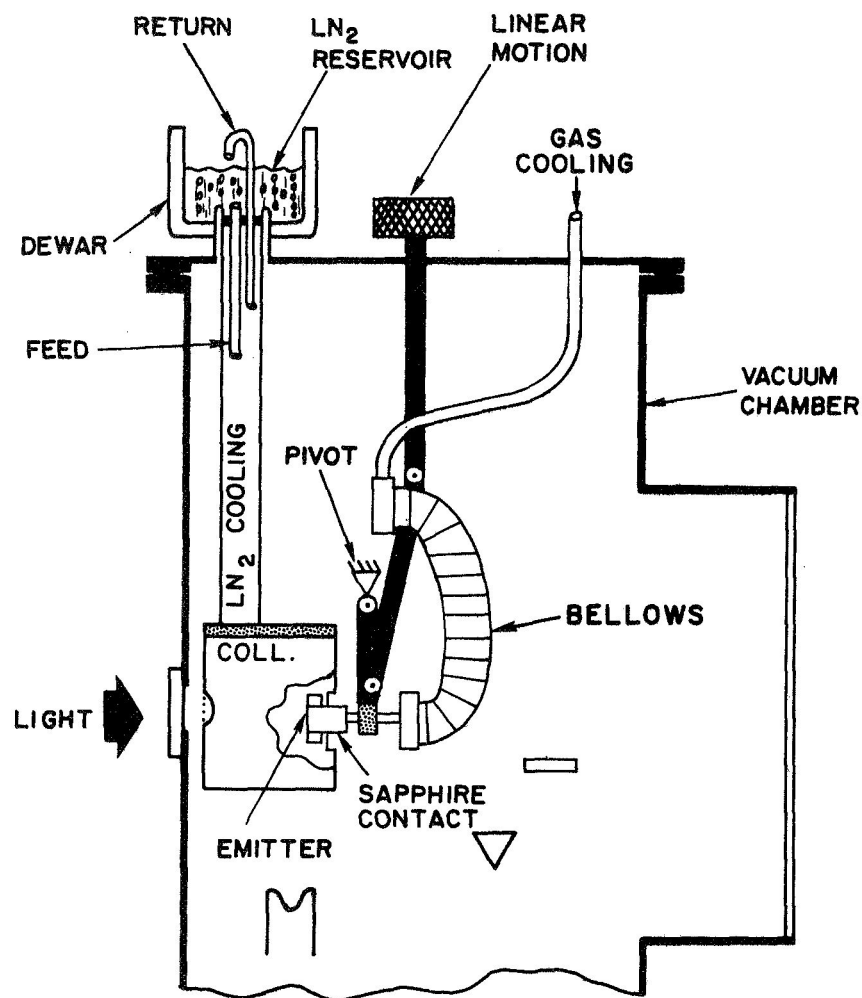
FIGURE 4.9. Schematic diagram of the flange apparatus used to measure
photoemission at temperatures ranging continuously from
room to liquid nitrogen values.

GAS IN   GAS OUT

RESERVOIR   SAMPLE   THERMOCOUPLE
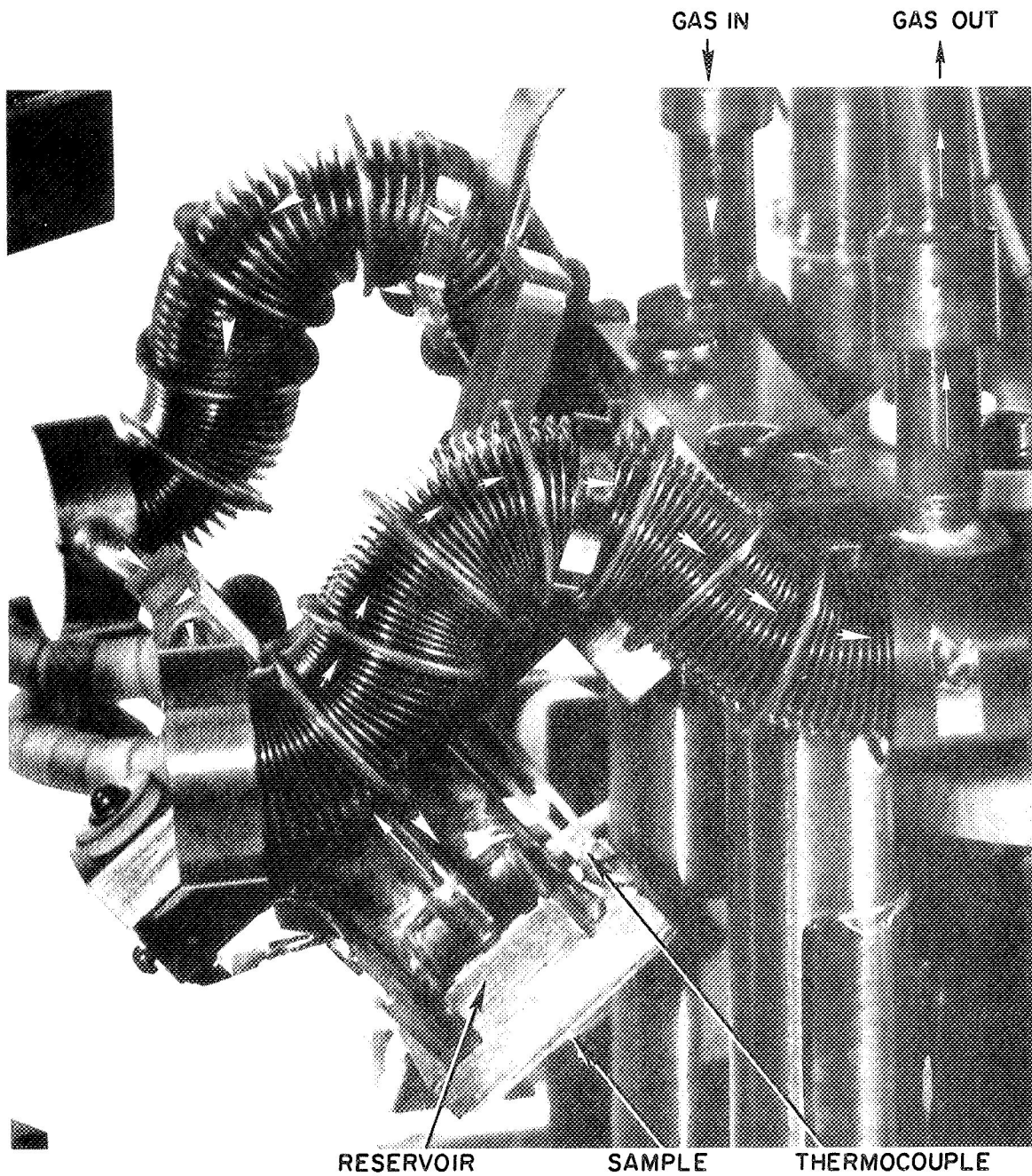
FIGURE 4.10. Photograph of the cooling gas flow path in the photo-
emission flange.

The temperature was set to any value between 80 and 295°K not only by balancing the heat losses but also by using and mixing various gases. The gas was cooled in a LN_2 heat exchanger shown schematically in Fig. 4.11. N_2 gas was liquified so efficiently by the copper heat
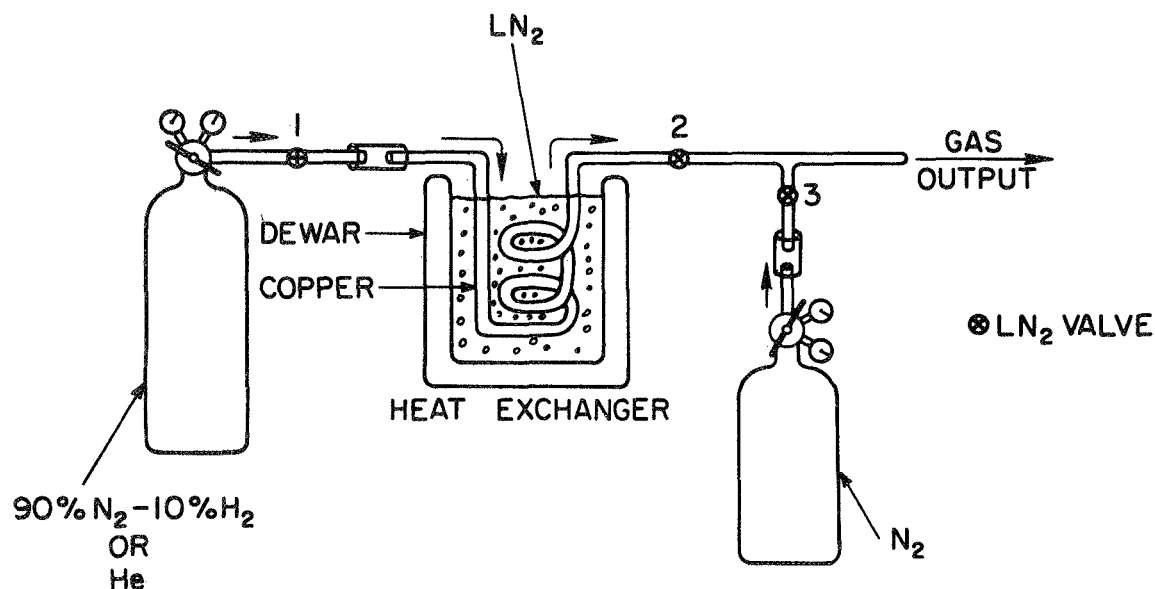
FIGURE 4.11. Schematic diagram of the apparatus used to control the cooling gas temperature.

exchanger that a uniform flow could not be maintained except at very high pressures. By using forming gas (90% N_2 - 10% H_2), this diffi- culty was overcome; since the small amount of H_2 in the gas would not liquify, it would serve as a vehicle for the semi-liquified N_2. Thus, a uniform flow rate could be achieved. Helium was found to be a very poor gas since in this exchanger it did not cool much below 200°K. This made it a useful gas for higher temperature where the cooled forming gas was at too low a temperature. The flow rate for both gases were controlled by the heat exchanger input gas pressure (valve 1 in Fig. 4.11) since at very low rates a nearly closed output valve (2) produces a large

amount of liquid in the exchanger which makes the flow erratic. A second valve (3) was placed after the heat exchanger output (valve 2) to either be used as a second output port (useful in balancing the flow of the primary output) or a warm gas input as shown in this figure. The latter was its purpose in this study as will be discussed in section 2. A photograph of the heat exchanger is shown in the top half of Fig. 4.12.
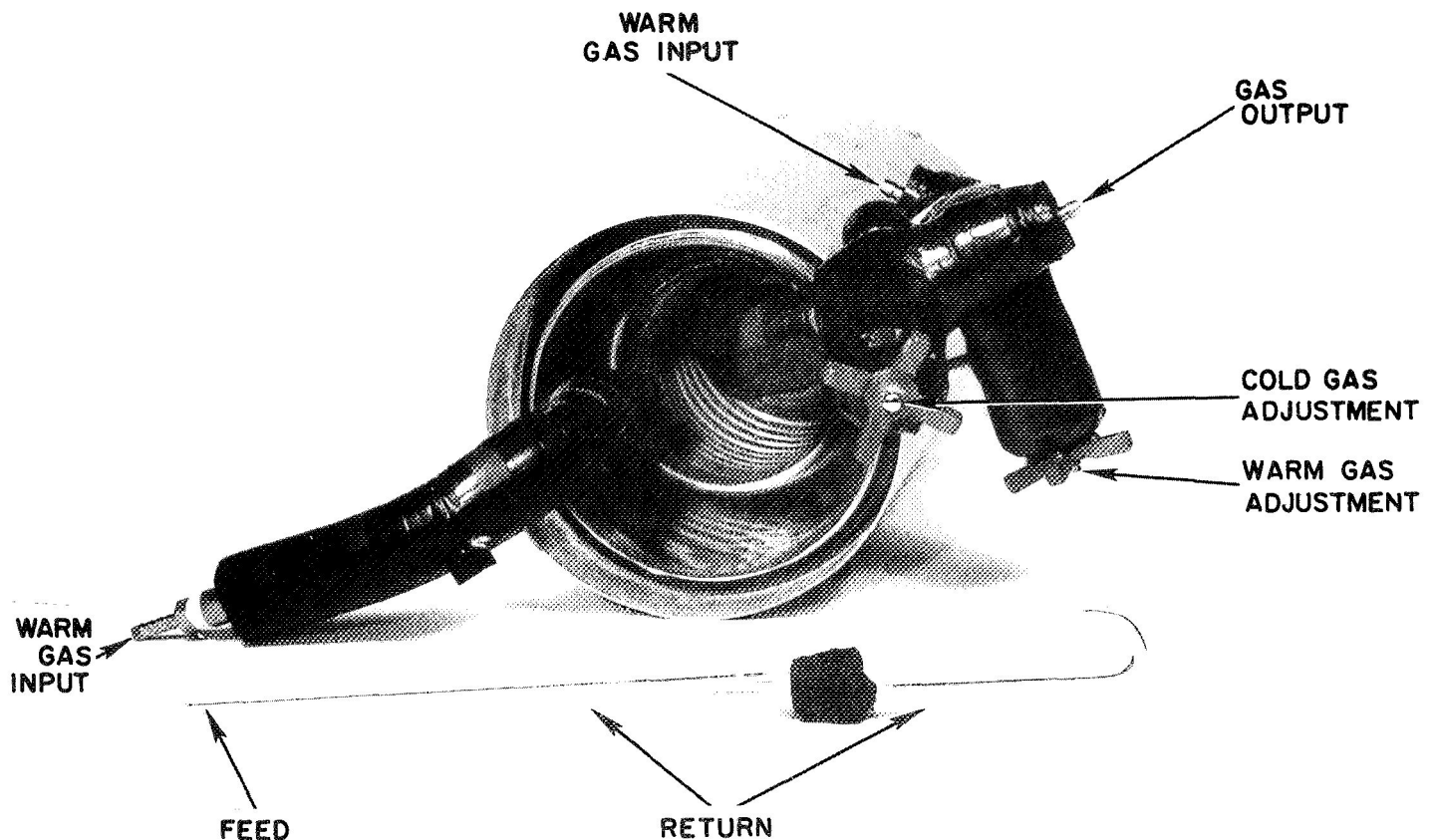
FIGURE 4.12. Photograph of the LN_2 heat exchanger and, in the foreground, the LN_2 cold finger control tubes.

The important thing to note in the photograph is that the use of multiple windings of small i.d. copper tubing in the dewar was in part responsible for the high cooling efficiency of the heat exchanger. A photograph of this heat exchanger in actual operation is shown in Fig. 4.13. As can be seen in the lower right corner of this figure, the thermocouple reads precisely 77°K (-5.70 mV referred to 0 mV at 0°C).

2. Maintaining Sample Temperature

The photoemission flange was very poorly designed originally from the standpoint of thermal insulation of the substrate holder from the support structure. The large heat losses necessitate the use of very high flow rates of chilled forming gas to achieve LN_2 temperature. At such high rates the substrate holder begins to vibrate sufficiently to cause considerable noise in the EDCs. It was thus necessary to turn off the gas while taking data. The large heat losses of the flange caused the temperature to rise by some 25°K during the four minutes required to trace an EDC. As will be shown in Chapter VII (Fig. 7.1) there is some EDC structure which changes considerably over this temperature range. Thus, the flange had to be modified to maintain the temperature set by the cold gas reasonably constant after the gas was turned off. The flange already had a provision whereby the collector could be cooled to LN_2 temperature; the collector is actually mounted on a LN_2 cold finger as shown in Fig. 4.14. To electrically isolate the collector from the cold finger, it was mounted with sapphire washers (shown in the figure) so that any possible water condensation on the glass insulation of the cold finger on the top of the flange could no longer cause EDC noise. Sapphire acts as a better thermal conductor than copper at LN_2 temperature but is still a good electrical insulator. We took advantage of this collector heat sink by contacting the sample emitter to the collector through sapphire as shown in Fig. 4.15.

The sapphire is mounted on the end of a copper-backed stainless steel spring which is connected to the collector. A special copper plate was brazed onto the substrate holder to contact the spring when the sample was inside the collector. The spring provides sufficient

76
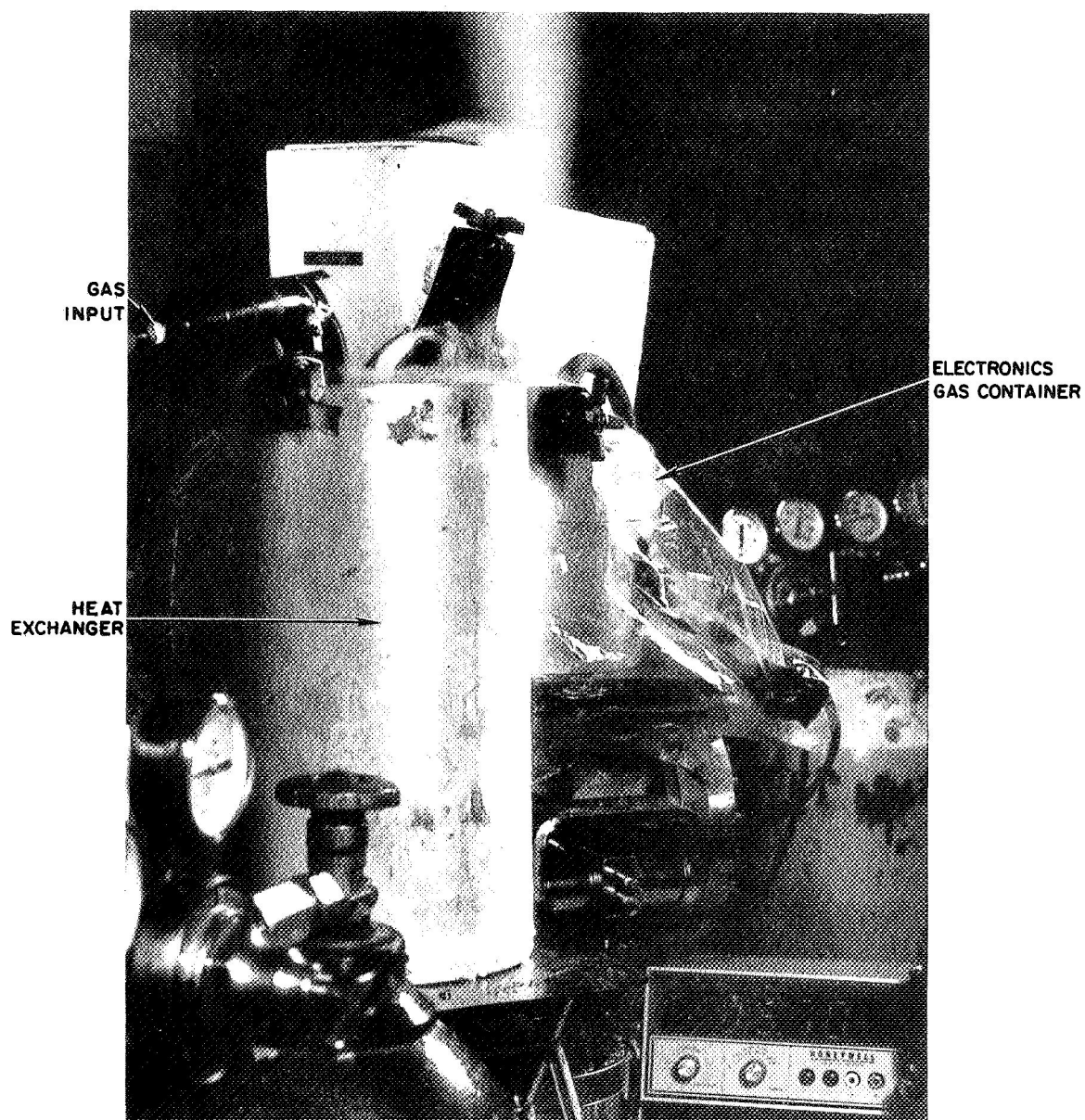
FIGURE 4.13(a). Photograph of the apparatus used to control the
temperature of the sample continuously from room to
liquid nitrogen values.
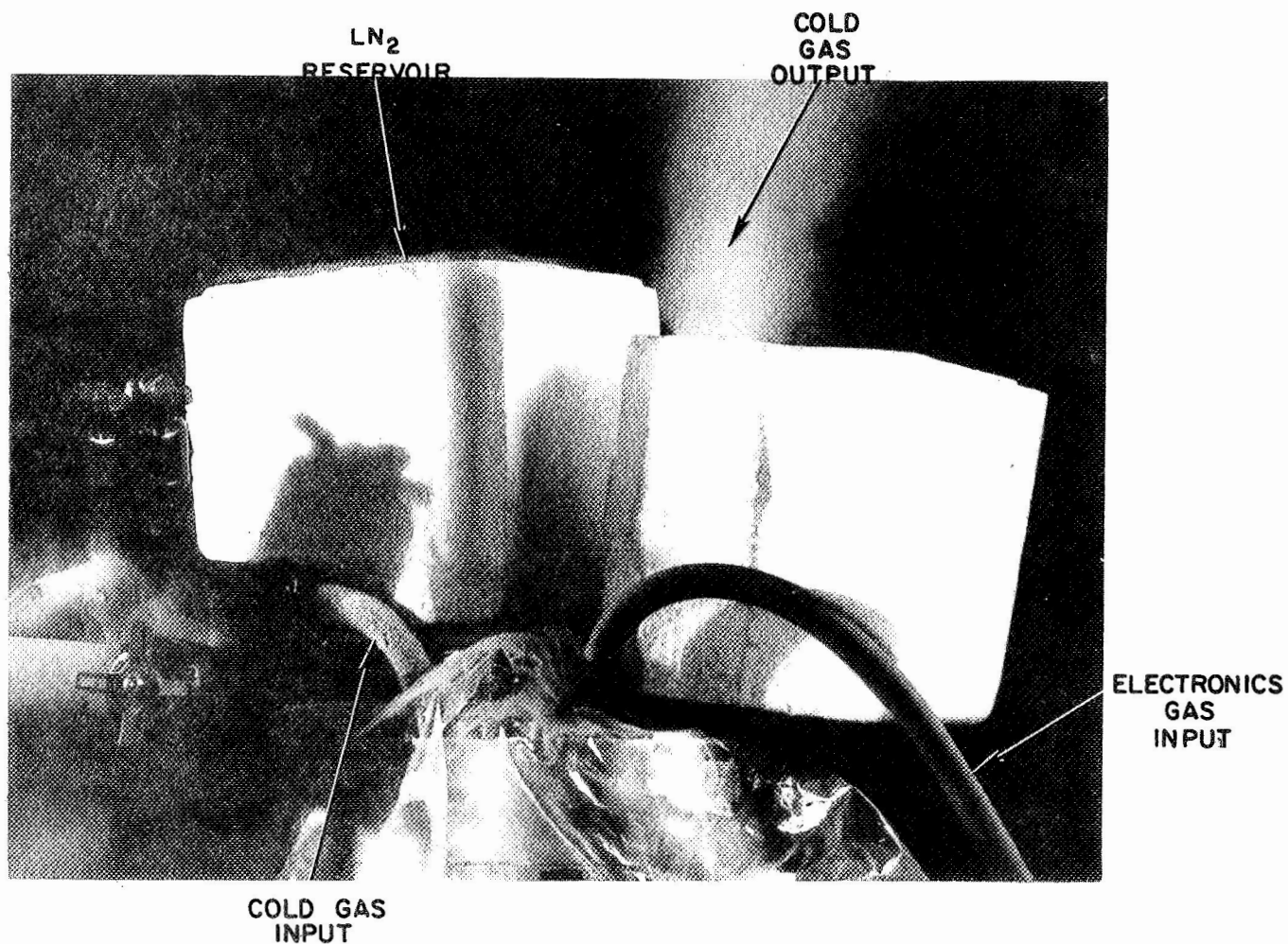
FIGURE 4.13(b). Photograph of the apparatus used to control the temperature of the sample continuously from room to liquid nitrogen values.
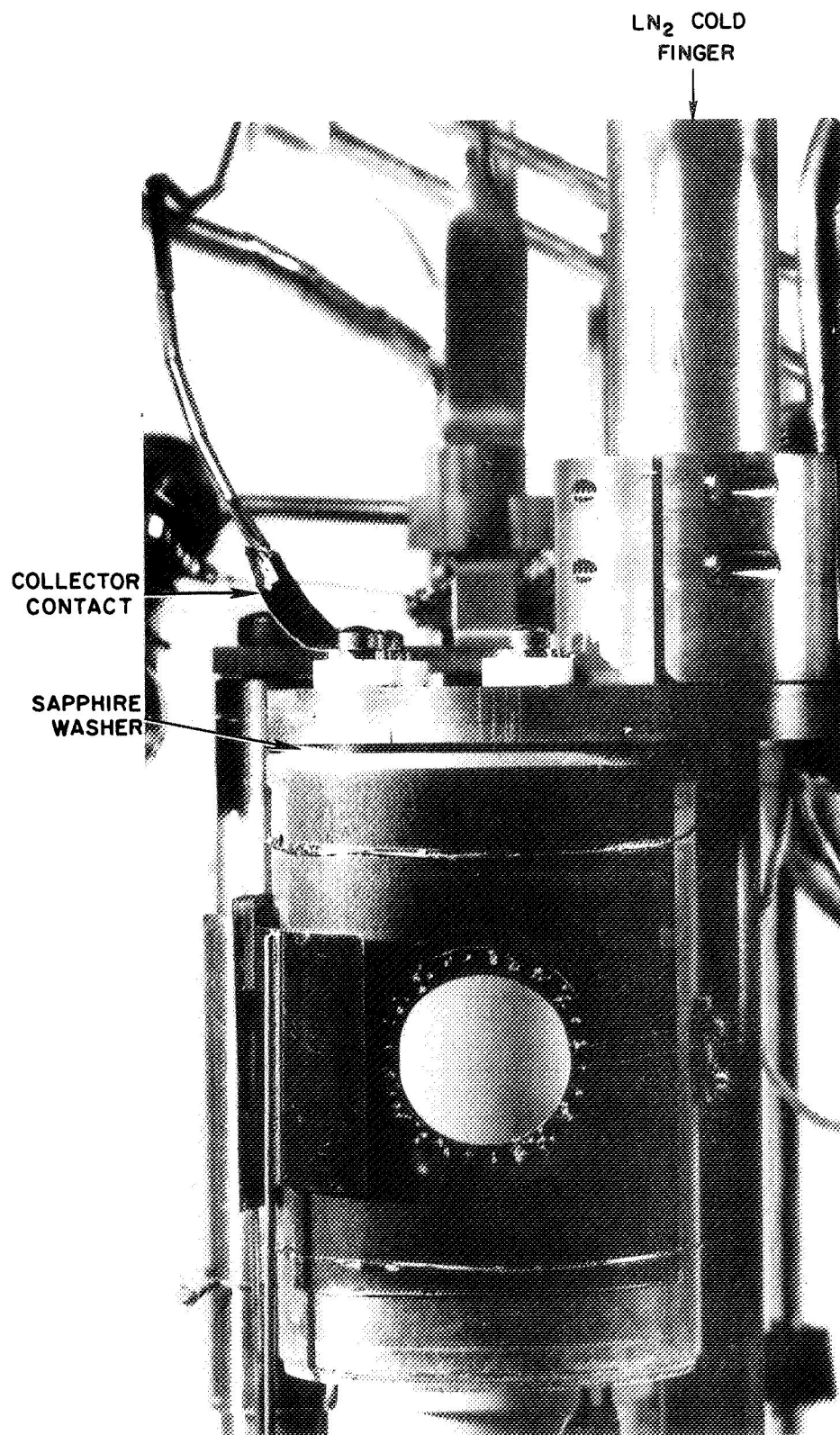
FIGURE 4.14. Photograph of the LN$_2$ cooled collector.

79
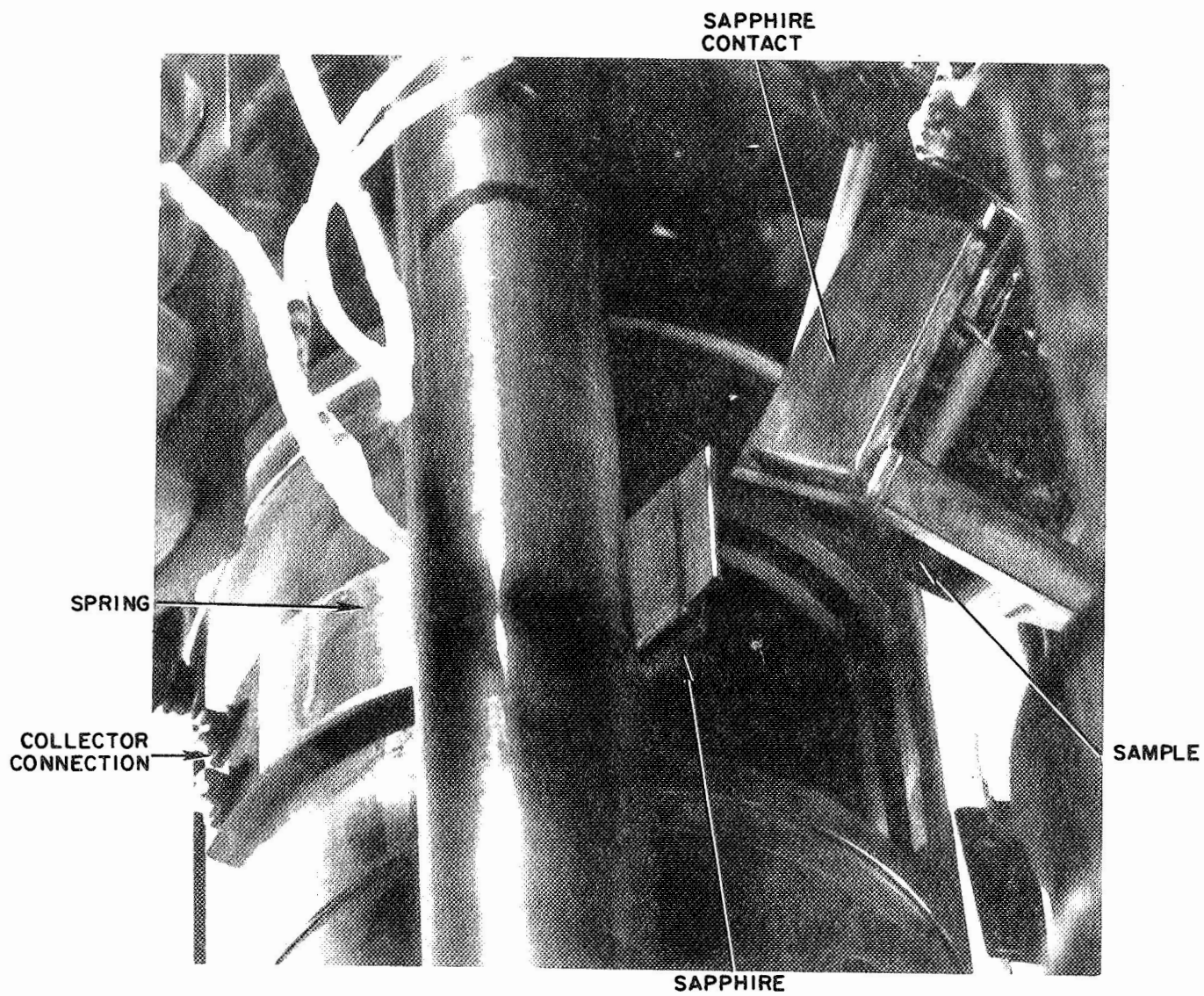
FIGURE 4.15. Photograph of the apparatus used to thermally contact the emitter to the collector.

tension between the sapphire and contact to reduce the warming of the sample to only 8°K during the period of EDC measurement. As will be discussed in section E, no change in EDC structure occur over such a small temperature range. The contact with the LN_2 cooled collector lowers the temperature of the sample to about 195°K without any other cooling. This creates the circumstance where one is warming above as well as cooling below this temperature with the gas; this is the reason for using warm N_2 gas (Fig. 4.11). Because of this "precooling", very slow flow rates can be used in setting the temperature, except at the extreme temperatures of the range. In fact, the rates are so low that a micrometer regulating valve had to be used to accurately set the gas pressure (valve 1 in Fig. 4.11). At these low flow rates, there is negligible gas-produced vibration. This vibration is also somewhat damped due to contact with the collector spring. This contact, however, transmits vibrations to the emitter due to the bubbling of the LN_2 in the cold finger. This vibration produced considerable noise in the EDC when LN_2 was poured directly into the cold finger. To overcome this, the cold finger was plugged with a stopper with two tubes mounted in it (see Fig. 4.9). One tube feeds LN_2 to the cold finger and the second was used for returning N_2 gas and also circulate the LN_2 when the finger gets cold enough. This produces a back pressure on the LN_2 thereby suppressing the bubbling to a level where it did not cause additional EDC noise. It is important that the tubes be constructed as shown in the foreground of Fig. 4.12; namely, the feed tube needs to be longer than and have half the i.d. of the return tube.

Cooling the collector to LN_2 temperature also provides a cryo-pumping action on the environment surrounding the sample. Since the sample is always as warm or warmer than the collector, the probability of adsorbing a large enough amount of impurities on the sample surface to distort the EDCs is very low.

3. Measurement and Calibration of Temperature

Since changes in EDCs occur over such a small temperature range (i.e., about 25°K), it is very important to accurately measure the sample temperature. It was found at the beginning of this study that the thermocouples used for measuring sample temperature were improperly installed in the flange. Since this situation may also occur in other flanges, the steps taken to accurately measure temperature are reviewed in detail here.

The crucial fact about thermocouples is that the voltage measured is characteristic of the difference between the measuring junction temperature at the point of measurement and the reference junction temperature at the point where the thermocouple wires terminate. Since thermocouple millivolt calibration tables are usually referred to either 0° or 25°C reference junctions, it is important for the thermocouple termination to be at a known, constant ambient. The thermocouple in our flange had been wired as in part (a) of Fig. 4.16. The terminal block whose temperature served as the reference value was part of the photo-emission flange. Due to the heat losses of the substrate holder, when the samples were either cooled or heated, the terminal block would also change temperature in the same sense. Thus, if the meter readings were converted relative to room temperatures, the predicted temperature of a cooled sample would always be warmer than the actual value. It was found that such errors were typically 30°K at LN_2 temperature reflecting an equivalent cooling of the terminal block. Such absolute errors are clearly unacceptable. The errors were corrected by extending the chromel-alunel wire to the flange feed-throughs and by using the same materials for cables from the feed-throughs to the measuring device as -shown in part (b) of the figure. Even though feed-throughs and connectors are not made of the thermocouple material, since they are not terminations of these materials, no error is introduced by them if both feed-throughs (or connectors) are at the same temperature. We actually used an Omega model CJ-K thermocouple compensator before the meter. This device electronically sets the reference junction voltage to that corresponding to 0°C to within $\pm$ $1/2^{\circ}$C for ambient temperatures from

82
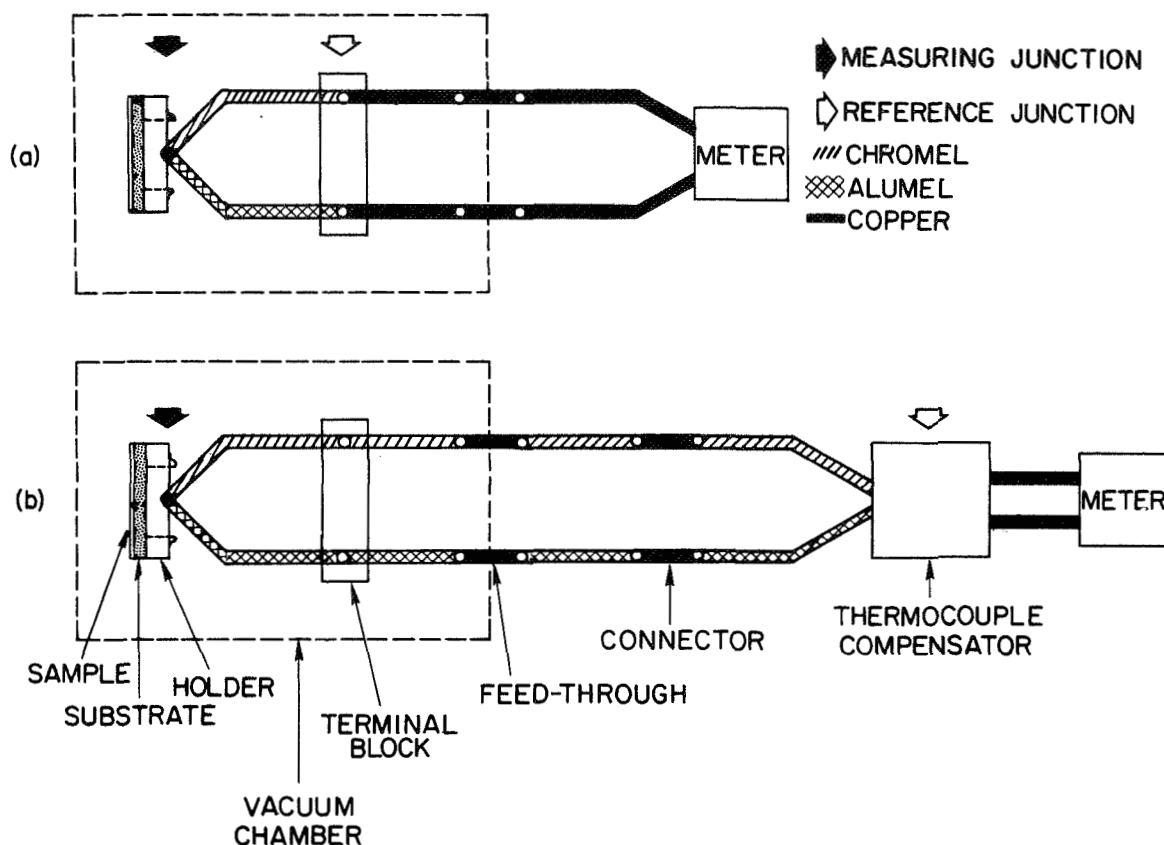
FIGURE 4.16.   Schematic diagram of the thermocouple circuit used in
(a) previous work, and (b) the present work.

15 to 35°C. This was a useful addition since the ambient temperature
near the meter could drop substantially due to the proximity of the
cold gas output of the flange. With this improved thermocouple circuit
(part (b), Fig. 4.16) no effects due to the cooling of the terminal
block were seen, and a temperature of precisely 77°K was measured
(see the meter in Fig. 4.13(a)).

Because the thermocouple was actually mounted in the substrate
holder, there was some concern that the temperature of the substrate,
which was only held to the holder by four wires, might be at a dif-
ferent temperature. To calibrate the sample temperature, a thermocouple
was mounted in the center of a substrate as shown in Fig. 4.17. By

83
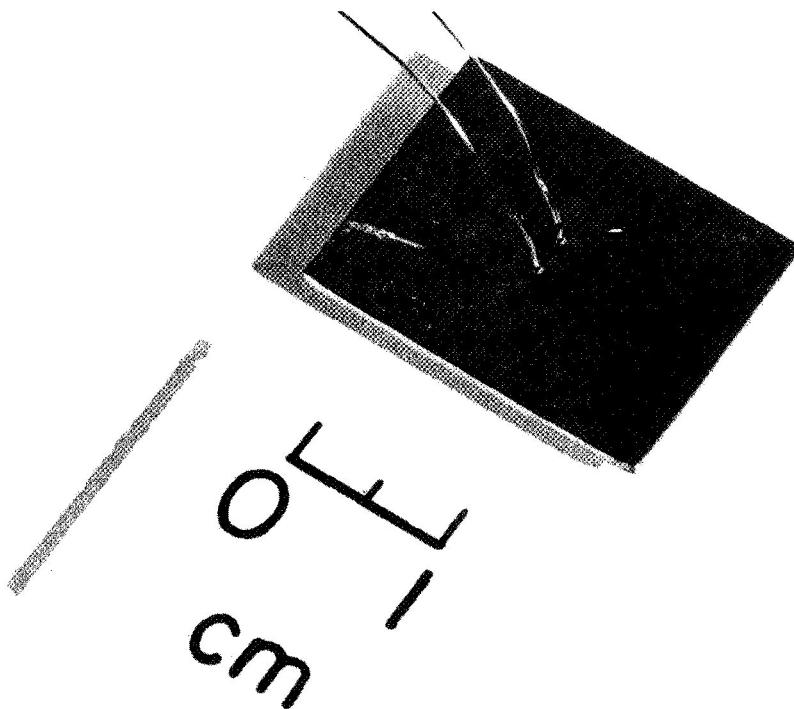
FIGURE 4.17.   Photograph of a substrate with a thermocouple mounted
in its center to calibrate the substrate holder thermo-
couple.

comparing this thermocouple reading to the holder thermocouple (shown in
Fig. 4.10) value, it was found that there is some heat transfer problem
between the two measurement points.   While the substrate was usually
3°K warmer than the holder when the gas was turned off, it would continue
to cool initially as the holder warmed up.   At the end of the EDC measure-
ment period, the holder (now 8°K warmer) would be warmer than the substrate.

In general, the average substrate and holder temperatures were the same over the EDC measurement time with the actual range of temperatures of the substrate being about half that of the holder. Thus, the uncertainty quoted for the sample temperature of $\pm 4^{\circ}K$ is a very conservative, worst case estimate.

The cooling of the flange caused by sample cooling not only caused erroneous thermocouple readings in early measurements, it also causes water vapor condensation on the flange electrodes. This was remedied quite efficiently by surrounding the top of the flange and the electronics with a sealed plastic bag (see Fig. 4.13(a)) and blowing dry N_2 gas at less than 1 psi pressure into it (see Fig. 4.13(b)). This process used a negligible amount of gas, produced no vibrational noise in the electronics leads, kept the electrodes dry indefinitely, and required no major modifications of the electronics container.

Using all the newly developed apparatus and procedures described in this section, photoemission could be measured at temperatures ranging continuously from room to LN_2 values without an increase of even a factor of two in the EDC noise.

D. Photoemission Measurement

As has been emphasized throughout this chapter, the measurement of photoemission EDCs has presented many requirements on all the experimental phases of this work from the vacuum to cooling the samples. In this section, the restrictions on EDC resolution imposed by the apparatus and the measurement parameters are discussed following a review of the basic principles of the measurement of EDCs and yield. The electrical circuitry used for measuring photoemission by the standard a-c technique[98] is shown schematically in Fig. 4.18. The actual circuitry used in these studies and the detailed methodology on the photoemission measurements was mostly developed by R. C. Eden.[99,100] The solid to be investigated serves as the emitter. It is surrounded by a metal cylinder that is used to collect the electrons photoemitted by incident monochromatic light which enters the chamber through a LiF window. By
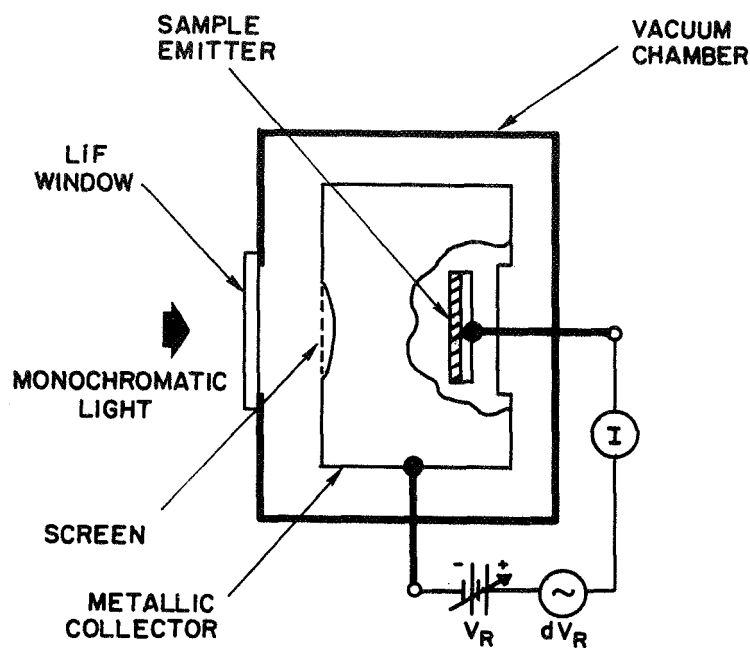
FIGURE 4.18. Schematic diagram of the photoemission measurement circuit.

biasing the collector sufficiently positive, V_R , all of the photo-emitted electrons are collected and the measured external current, I , is proportional to the yield. Comparing this current with the photo-current measured from a calibrated Cs_3Sb tube gives the quantum yield, Y , of photoemitted electrons per incident photon. Correcting for sample reflectivity, we have the absolute quantum yield, $\mathcal{Y}$, of photo-emitted electrons per absorbed photon. The Cs_3Sb tube used in these studies (F-7) was calibrated to ±4% using new techniques described in Appendix C. If the collector is biased negative, only those electrons which have energies greater than the retarding potential difference are collected. By superimposing a small a-c signal, dV_R , on the retard-ing voltage, V_R , the a-c current, dI , flowing in the external

circuit will be proportional to the number of electrons having an energy equal to the retarding potential difference. Thus, by sweeping the retarding voltage and measuring the a-c current the distribution in energy of the photoemitted electrons is measured directly. One must consider the limitations on the resolution set by both the apparatus and the measurement.

One of the major limitations of the apparatus is that due to the geometry of the photodiode. DiStefano and Pierce have studied this in detail.[101] The narrowest peak width measured at 90% of the maximum height was 0.12 eV for a threshold piece of structure at 10.2 eV for AgBr-II-D at 80°K (see Fig. 4.20(a) below). Assuming a sharp threshold function, this is a good measure of the geometrical resolution. However, it should be recalled that this resolution becomes worse at higher final state energies.[101] As shown on the schematic, a 98.0% transmitting screen, made from 0.001" diameter wire arranged in a 0.010" spaced square matrix, was placed over the front of the collector to make the fields more spherical around the emitter and thus aid this resolution (the screen is pictured in Fig. 4.14). As noted in section B, a fresh metallic film is evaporated on the inside of the collector each pumpdown to produce a more uniform work function.

The apparatus external to the flange also effects the EDCs. For example, the fields from external magnets can distort the energy distributions. At the sample position, 0.55 gauss was measured with the Redhead gauge and ion pump magnets in place compared to 0.4 gauss without them (i.e., the earth's field). The EDCs showed no changes due to this 40% increase in ambient magnetic field. This low field is one main advantage of the NRC Orb-ion pump over the large, magnet-laden ion pumps. However, the electron emission of the Orb-ion leads to EDC noise and is turned off during the measurement period. The NRC 554 Redhead gauge is left on and serves as a 1 l/s ion pump to maintain the chamber pressure within a factor of two of the base pressure with the Orb-ion running.

There are parameters of the measurement which produce other limitations on the resolution. For example, both the uncertainty in the energy of the light and the amplitude of the a-c voltage, dV_R, artificially broaden the EDC structure. As discussed by Eden,[99] the total photon

energy uncertainty and the a-c peak-to-peak voltage both overestimate
the true uncertainty but are good for comparison to each other. The
total photon energy spread was calculated for the McPherson 225 mono-
chrometer with equal input and output slit settings as a function of
photon energy. The a-c peak-to-peak value was always set equal to this
spread. This net resolution, which resulted in negligible EDC noise,
was usually from 0.10 eV to 0.15 eV for all sets of silver halide EDCs.
Since this is an overestimate of the true uncertainty, these values
represent quite a good resolution relative to other experimental errors.
The sweep of the retarding voltage produces a net shift in the position
of the EDCs because of the time constant of the system. As will be
seen in Fig. 4.19, this shift is only about 0.06 eV. Thus, the un-
certainty in a peak position due to the sweeping voltage is ± 0.03 eV,
well within the other resolutions discussed above.

The method of analyzing the EDCs can actually introduce a shift of
the energy scale by more than any of these resolution limits. Since the
work functions of the collector could not be measured, the absolute
energy scale was set by fitting a straight line of unit slope to the
highest values of a plot of the EDC leading edge extrapolations versus
$h\nu$. This extrapolation is taken by extending the straight line por-
tion of the edge before its slope is a maximum. The remaining tail on
the EDC after this slope maximum is usually less than 0.2 eV longer than
the intercept of this extrapolation and the EDC baseline. Even if using
the extrapolated edge were a complete error, this would merely cause
less than a 0.2 eV shift of all the structure to lower energy. It should
be noted, however, that this EDC tail is believed due to experimental
broadening and not characteristic of the electronic states. Thus, the
procedure of setting the energy scale probably introduces less than
0.1 eV error in the results.

FIGURE 4.19. Comparison of energy distributions normalized to quantum
yield (per incident photon) for electrons photoemitted
from AgCl at temperatures ranging across the curves
from $77 \rightarrow 85^{\circ}K$ (——) and $85 \rightarrow 77^{\circ}K$ (—·—) for a photon
energy of 11.4 eV.

E. Effect of Parameters on Silver Halide Photoemission

In this section, EDC and yield data is presented to illustrate the
effects on the silver halides of parameters ranging from time to air
exposure. Since so much emphasis in the literature has been placed on
the yield and photoemission threshold, yield data has been included.
For the most part, the data is self-explanatory and no extensive dis-
cussion will be given. Only AgBr and AgCl results will be presented

here. The parameters affecting AgI photoemission are deferred to Chapter IX.

As noted in the last section, the sweeping of the retarding voltage shifts the entire EDC because of the time constant for the system to respond. This is illustrated in Fig. 4.19. As can be seen, the peaks are shifted by only 0.06 eV from scanning in the two directions. This means, the position of the peak is only uncertain by 0.03 eV which is much less than the other errors in the EDCs. This figure also illustrates that the curves are not significantly effected by the 8°K warming which occurs during the scan. Since the scan directions are different for the two illustrated curves, the temperature of these two EDCs differ by 8°K at each end.

The data was reproducible among the samples measured. The most sensitive test of this is a comparison of the LN_2 temperature EDCs. A number of these are presented in part (a) of Fig. 4.20 for AgBr . The two sets of curves are individually normalized to their own yield and have their absolute energy scales referred to the valence band maximum, E_V , independently. The agreement is really excellent especially in the position of the EDC structure. In part (b), the AgBr yields from three thin film samples are compared. As can be seen the saturation yield and threshold regions are quite reproducible. The tail below 7.5 eV in the yield will be discussed below. EDCs and yield from representative AgCl samples are presented in Fig. 4.21. As in the case of AgBr , the data is quite reproducible among samples.

The data is also reproducible following numerous temperature cycles between room and liquid nitrogen values. This is shown in Fig. 4.22 for AgBr . The number of times the sample was cooled to 80°K is indicated in parentheses. Since the two curves taken 18 cycles apart are independently normalized, the stability of the yield is also seen to be quite good. The increased strength of the trailing peak is indicative of a threshold function which has slightly sharpened. AgCl can also be seen to be unaffected by numerous sample coolings in part (a) of Fig. 4.23.

FIGURE 4.20(a). Comparison of energy distributions normalized to quantum yield (per incident photon) for electrons photoemitted from two AgBr samples at 80°K for photon energies of 9.6 through 11.8 eV.

FIGURE 4.20(b). Comparison of the spectral distributions of the
yield of electrons photoemitted per absorbed photon
from three AgBr samples at 295°K.

FIGURE 4.21(a). Comparison of energy distributions normalized to quantum yield (per incident photon) for electrons photoemitted from two AgCl samples at 295°K for photon energies of 10.5 and 11.8 eV.

FIGURE 4.21(b). Comparison of the spectral distributions of the yield of electrons photoemitted per absorbed photon from three AgCl samples at 295°K.

FIGURE 4.22. Comparison of energy distributions normalized
to quantum yield (per incident photon) for
electrons photoemitted five days and eighteen
cooling cycles apart from AgBr at 80°K for a
photon energy of 10.2 eV.

FIGURE 4.23(a). Comparison of energy distributions normalized to
quantum yield (per incident photon) for electrons
photoemitted thirteen days and nine cooling cycles
apart from AgCl at 80°K for a photon energy of
11.4 eV.

These last two figures also illustrate the stability of the samples
with time. Over a period of a month no significant changes in EDCs
occurred for either AgBr or AgCl . As discussed above, if photo-
lytic decomposition was significant in these thin films, one would
expect a slow degradation of the EDCs with increasing exposure to UV
radiation. Thus, the data is consistent with the conclusion that light
induced chemical reactions were not significant for the samples studied.
In part (b) of Fig. 4.23, the AgCl yield stability over a month is

FIGURE 4.23(b). Comparison of the spectral distributions of the yield of electrons photoemitted per absorbed photon from AgCl at 295°K twenty-four days apart.

examined in detail. The coincidence of the data after such a long time
period, even in the threshold region, shows both the sample stability
and the accuracy of the yield measurement. For example, the two LiF
windows on the Cs_3Sb tube and vacuum chamber could be reproducibly
cleaned.

As noted above, the photoemission from the very thin films studied
(200 - 400 $\overset{o}{A}$) was the same as that measured from very thick films. This
is illustrated for AgBr in Fig. 4.24. Though there are slight changes
in height in the EDC structure [part (a)], all the salient features of
the data are independent of thickness. Neglecting the low energy tail
for a moment, the yield is also seen to be relatively thickness inde-
pendent in part (b). AgBr-II-C was actually very much thinner than the
265 $\overset{o}{A}$ measured on the thickness monitor. This is because the substrate
temperature for this film was nearly at the evaporation temperature of
AgBr . Thus, only a very small amount was actually deposited. The
lower saturation yield value for this sample is indicative of the elec-
tron escape depth being greater than the film thickness. The thickness
dependence of the low energy yield tails ($h\nu$ < 7.5 eV) suggests strongly
that this photoemission is produced by electrons photoexcited in the
silver substrate and then emitted through the silver halide film into
vacuum. Since these hot electrons scatter in the film, their measured
yield will decrease with increasing film thickness. This is certainly
the case for the strength of the tails in Fig. 4.24(b) and can also be
seen in the AgBr yield data in Fig. 4.20(b). Since this yield is at
least two order of magnitude less than the fundamental yield, its effect
on the EDCs is negligible except in the threshold region. This is
illustrated in Fig. 4.25. In addition to the fundamental AgBr photo-
emission, there is a tail to higher energies for very thin films at
these low photon energies near threshold where the fundamental EDC
magnitude is reduced by more than an order of magnitude [compare the
vertical scale of this figure to that of Fig. 4.24(a)]. The thickness
dependence of this data can be seen by comparing the two 7.4 eV EDCs.
This substrate photoemission through sample II-C is essentially $h\nu$
independent as compared to the fundamental AgBr emission which is

FIGURE 4.24(a). Comparison of energy distributions normalized to
quantum yield (per incident photon) for electrons
photoemitted from thick and thin AgBr samples
at 295°K for photon energies of 9.6 and 11.4 eV.
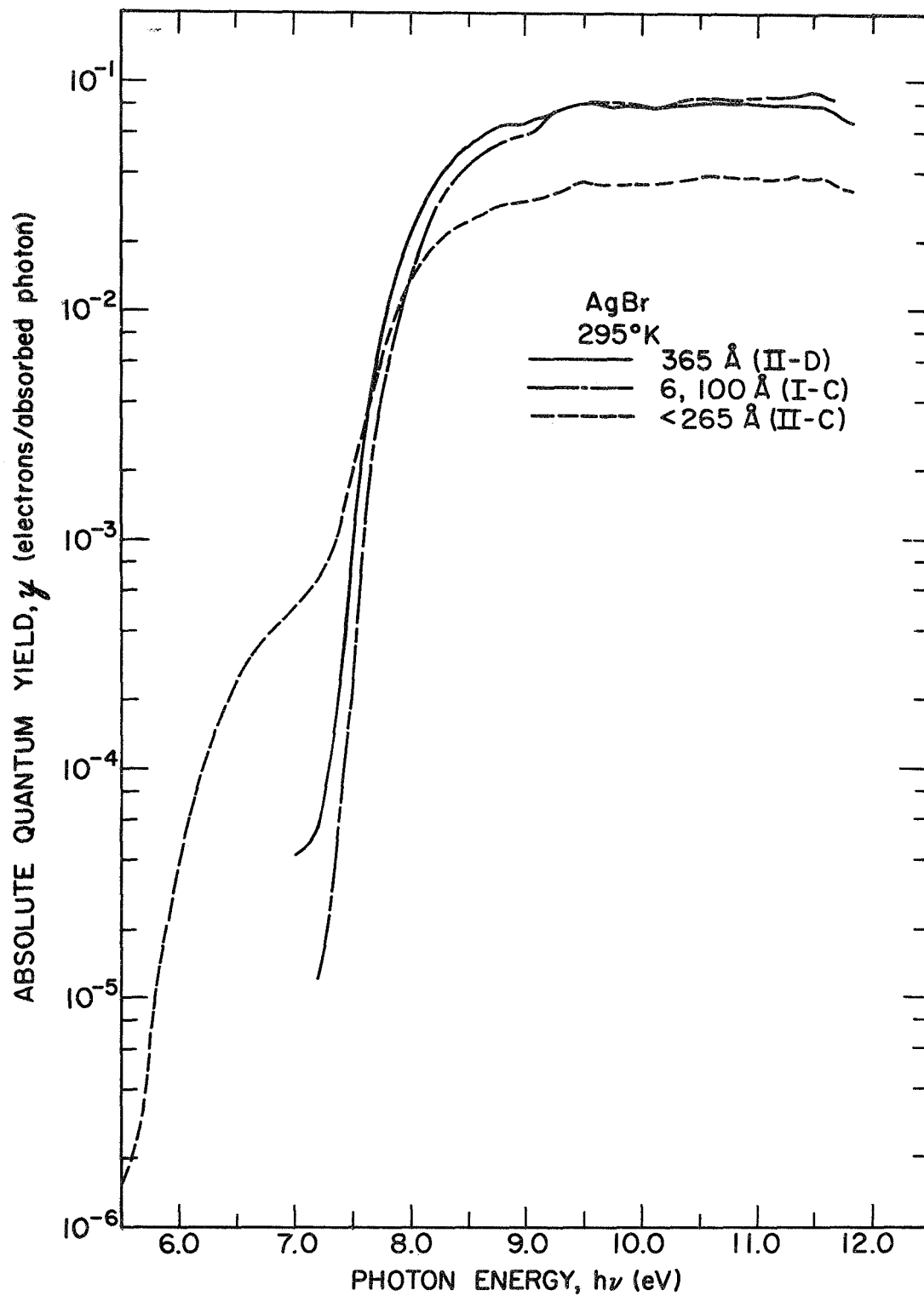
FIGURE 4.24(b). Comparison of the spectral distributions of the yield of electrons photoemitted per absorbed photon from thick and thin AgBr samples at 295°K.

FIGURE 4.25. Comparison of energy distributions normalized to quantum yield (per incident photon) for electrons photoemitted from two AgBr samples at $295^\circ K$ for photon energies of 7.4 and 7.6 eV.

off-scale at 7.6 eV. The same thickness dependence was measured for AgCl . That is, the fundamental photoemission is thickness independent for thin and very thick films as seen in Fig. 4.26. The higher threshold

FIGURE 4.26. Comparison of energy distributions normalized to quantum yield (per incident photon) for electrons photoemitted from thick and thin AgCl samples at 295°K for a photon energy of 10.2 eV.

for the thick sample was due to its deposition on Pt and not its thickness as will be discussed below. Similar to AgBr , photoemission from very thin films shows an additional EDC tail to higher energies due to

substrate photoemission, and this decreases with increasing thickness as shown in Fig. 4.27. The 150 Å measured for the thickness of sample
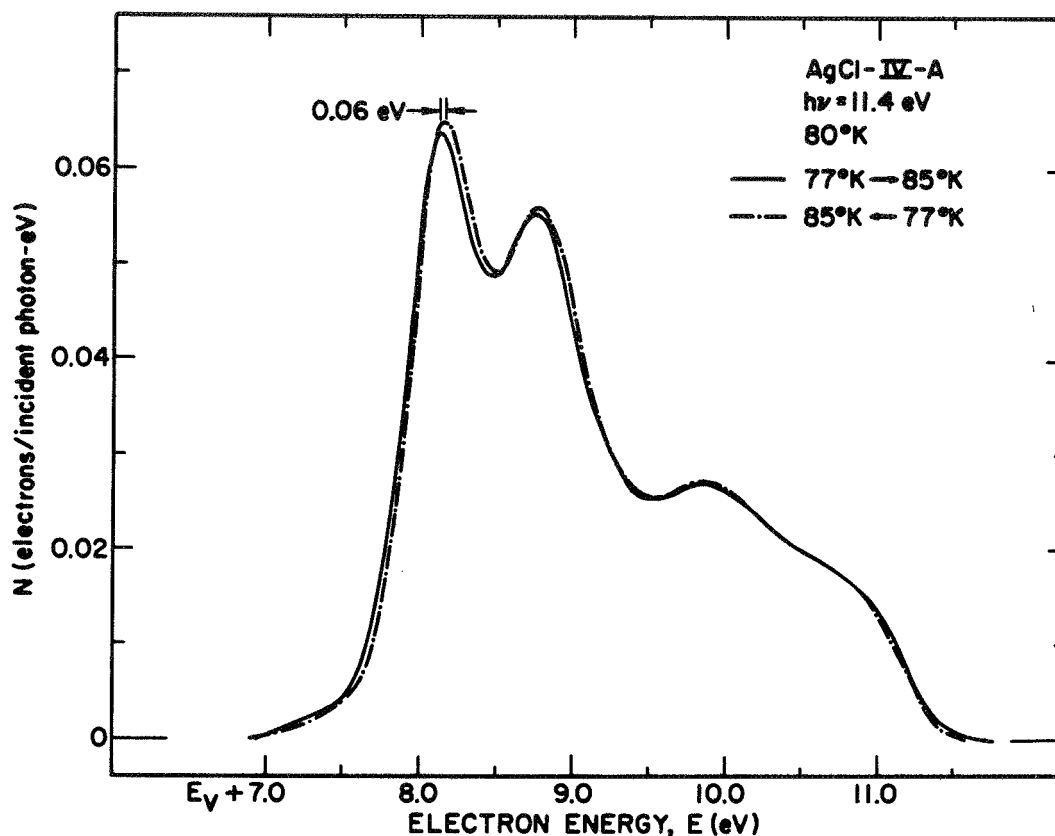

FIGURE 4.27. Comparison of energy distributions normalized to quantum yield (per incident photon) for electrons photoemitted from two AgCl samples at 295°K for a photon energy of 7.7 eV.

I-A is probably erroneous because the quartz crystal monitor used exhibited frequency instabilities.

The thickness independence of the fundamental silver halide photoemission (i.e., Figs. 4.24(a) and 4.26) indicates that the thin films

studied were virtually strain-free. If strain-broadening of the EDCs were postulated, it must occur at room temperature since the EDCs sharpen dramatically upon cooling (e.g., Fig. 2.6). However, one would expect such strain effects to be relieved in thick samples[102] since photoemission takes place over such a small depth near the surface. Since the room temperature EDCs are thickness independent, the effects of thin film strain, if there are any, are negligible. This is consistent with Carrera's findings that no dramatic sharpening in the optical data occurs when special precautions are taken to form low-strain silver halide films.[45]

To determine if any of the EDC characteristics were dependent on the substrate material, AgCl was deposited on both Ag and Pt. The results shown in Fig. 4.28 show that the salient features of the data are unaffected. It is important to realize that the EDCs illustrated in part (a) are independently normalized. The only effect is

FIGURE 4.28(a). Comparison of energy distributions normalized to quantum yield (per incident photon) for electrons photoemitted from AgCl on Ag and Pt substrates at 295°K for a photon energy of 11.8 eV.
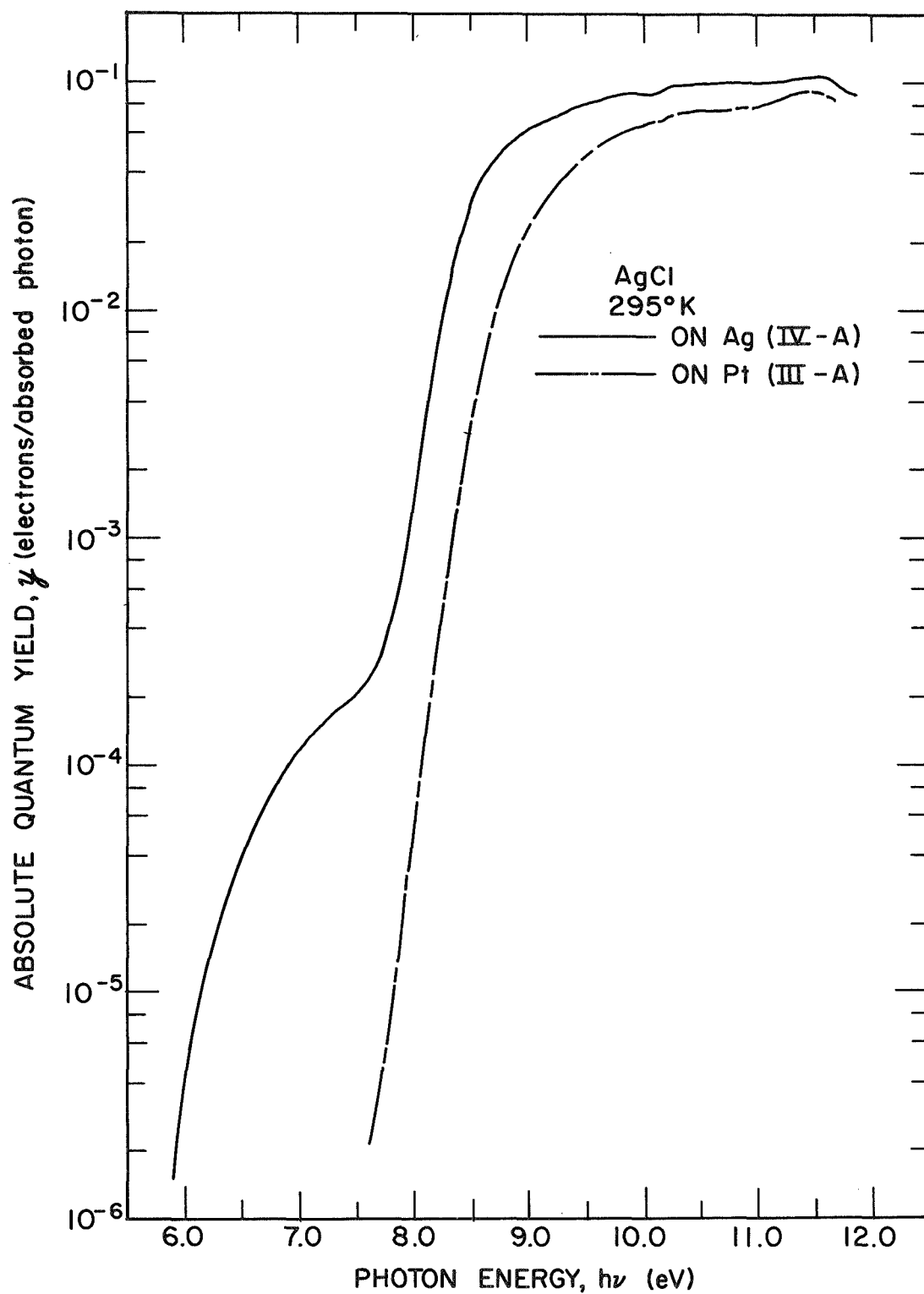
FIGURE 4.28(b). Comparison of the spectral distributions of the yield of electrons photoemitted per absorbed photon from AgCl on Ag and Pt substrates at 295°K.

a higher and less well-defined photoemission threshold for the sample on the Pt substrate. Since the film orientations are the same (see Table IV.2), this may be related to the surface cleanliness of the metals since Pt is very difficult to heat-clean properly[103] compared to Ag .

Since the epitaxial growth of the thin film is dependent on the temperature of the substrate, T_s ,[81] it was important to determine if the EDCs for films grown at different temperatures would show any significant differences. Since the ideal growth temperatures were reported to be from just above room temperature to around $150^{\circ}C$,[81] the range of 22 to $175^{\circ}C$ was sufficient to test for any effects. The results shown in Fig. 4.29 indicate that in this range, the substrate temperature during growth does not significantly effect the EDCs. The need to double the heights of the $T_s = 175^{\circ}C$ EDCs was necessitated by the very thinness of the sample as discussed above [see Fig. 4.24(b)].

In an attempt to perhaps sharpen EDC structure, the films were annealed in the vacuum chamber following deposition. As seen in Fig. 4.30, the only effect of annealing for 12 hours at $100^{\circ}C$ and then 23 hours at $150^{\circ}C$ is to slightly reduce the yield. The features of the EDC structure are not significantly affected.

In an effort to determine the nature of the surface contamination which caused the differences between this and previous work, the chamber was opened to the air for 22 hours and then re-evacuated to simulate transfer of a prepared sample through air to the measurement flange. As can be seen in Fig. 4.31, the EDC threshold is slightly reduced [part (a)] and the yield onset has a bit smaller slope [part (b)]. Though the changes are in the proper direction, these air induced effects are not nearly large enough to explain the large discrepancies between this data and the previous studies discussed in the last chapter.

The depth into the valence band which can be probed with high vacuum photoemission is limited by the cutoff of the LiF chamber window and the photoemission threshold. To increase this energy range, an attempt was made to lower the electron affinity with a surface layer of cesium as has been successful with other solids in the past.[99] The
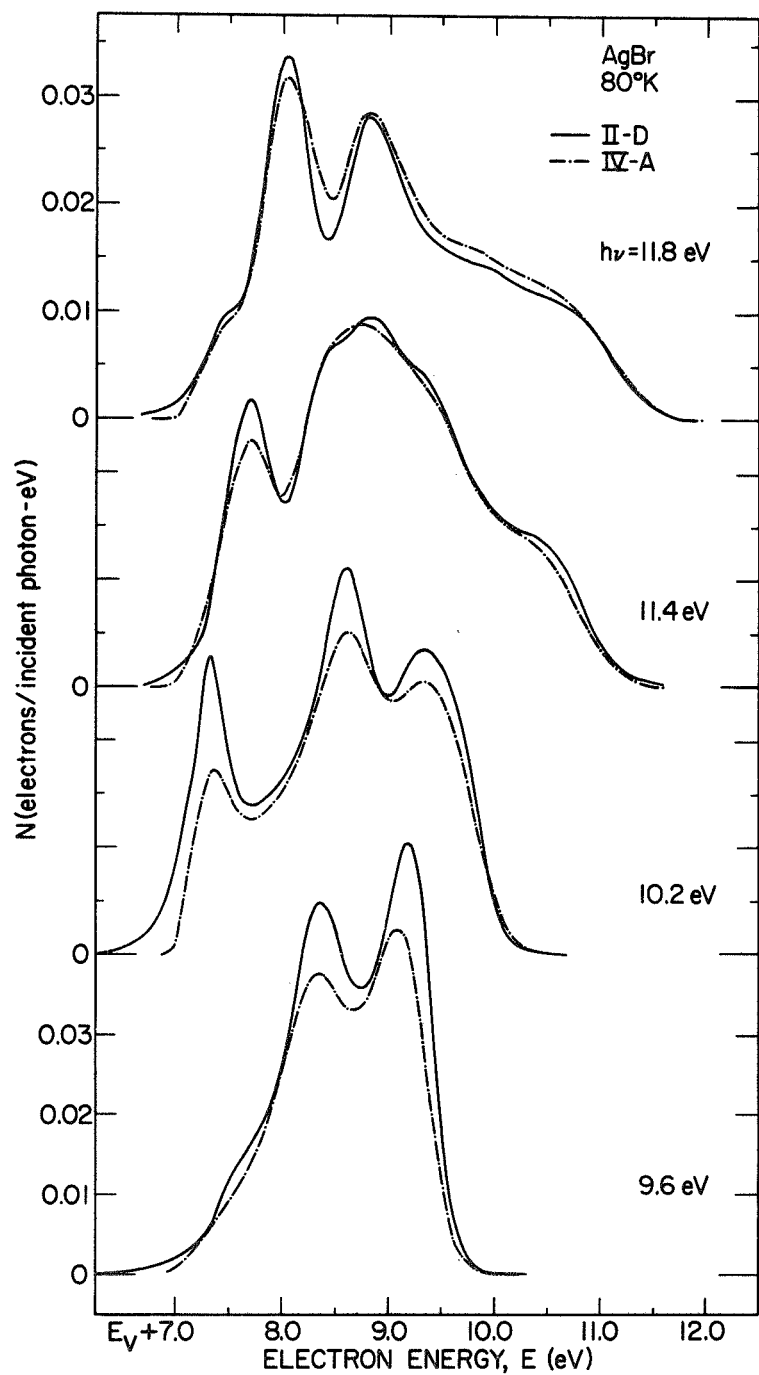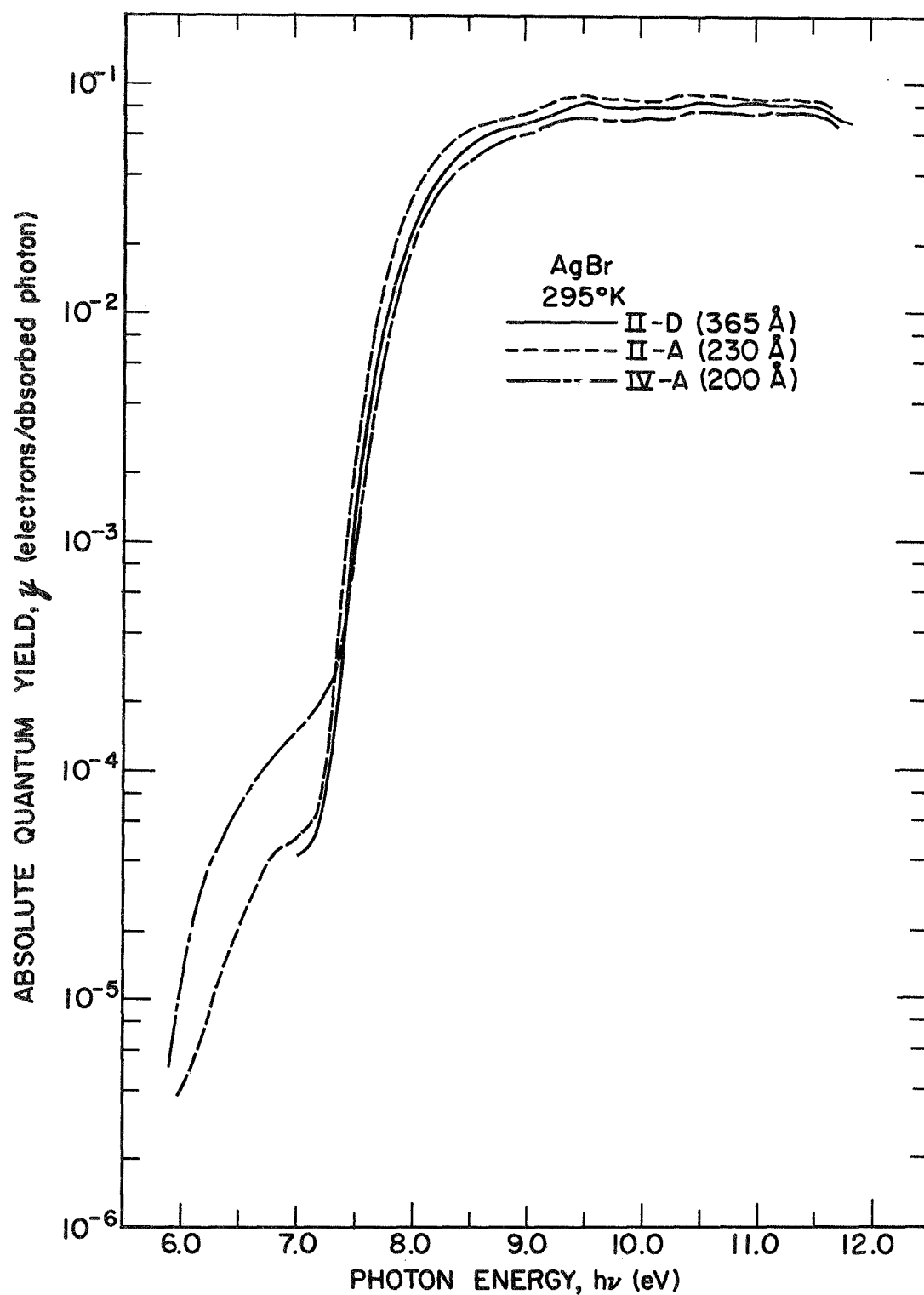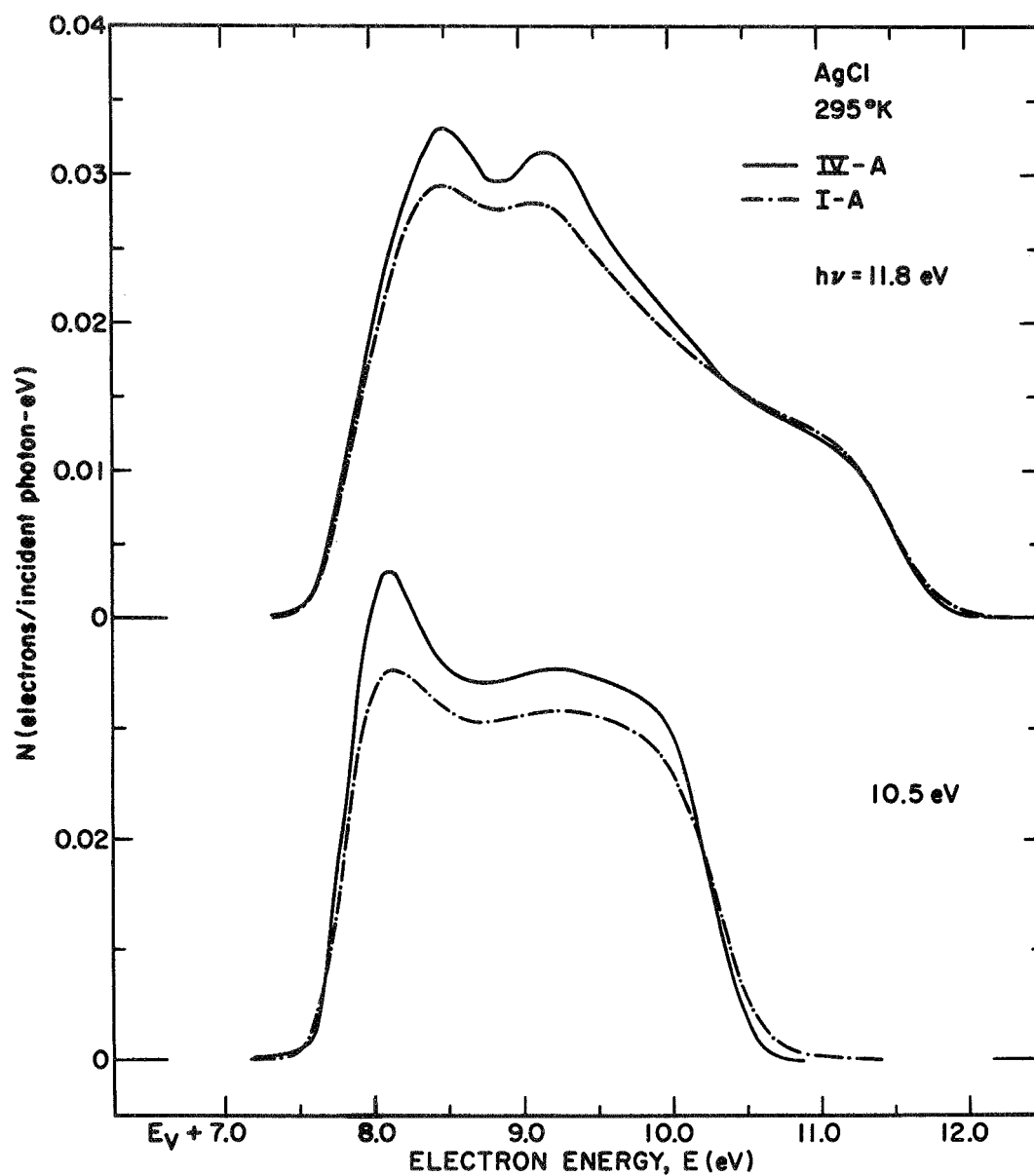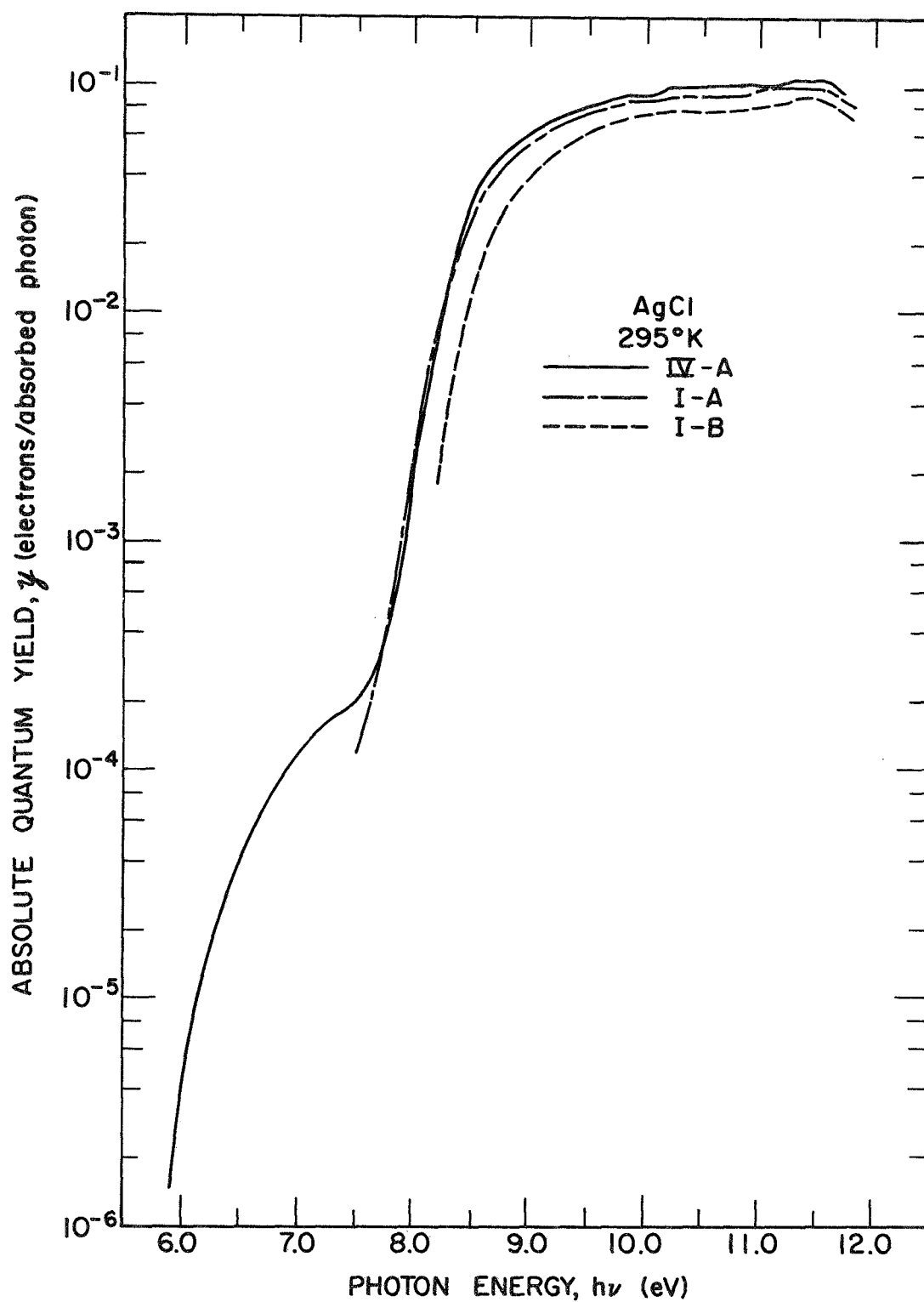
FIGURE 4.29. Comparison of energy distributions normalized to quantum yield (per incident photon) for electrons photoemitted from AgBr samples deposited at four different substrate temperatures, T_s, at $295°K$ for photon energies of 9.6 through 11.8 eV.
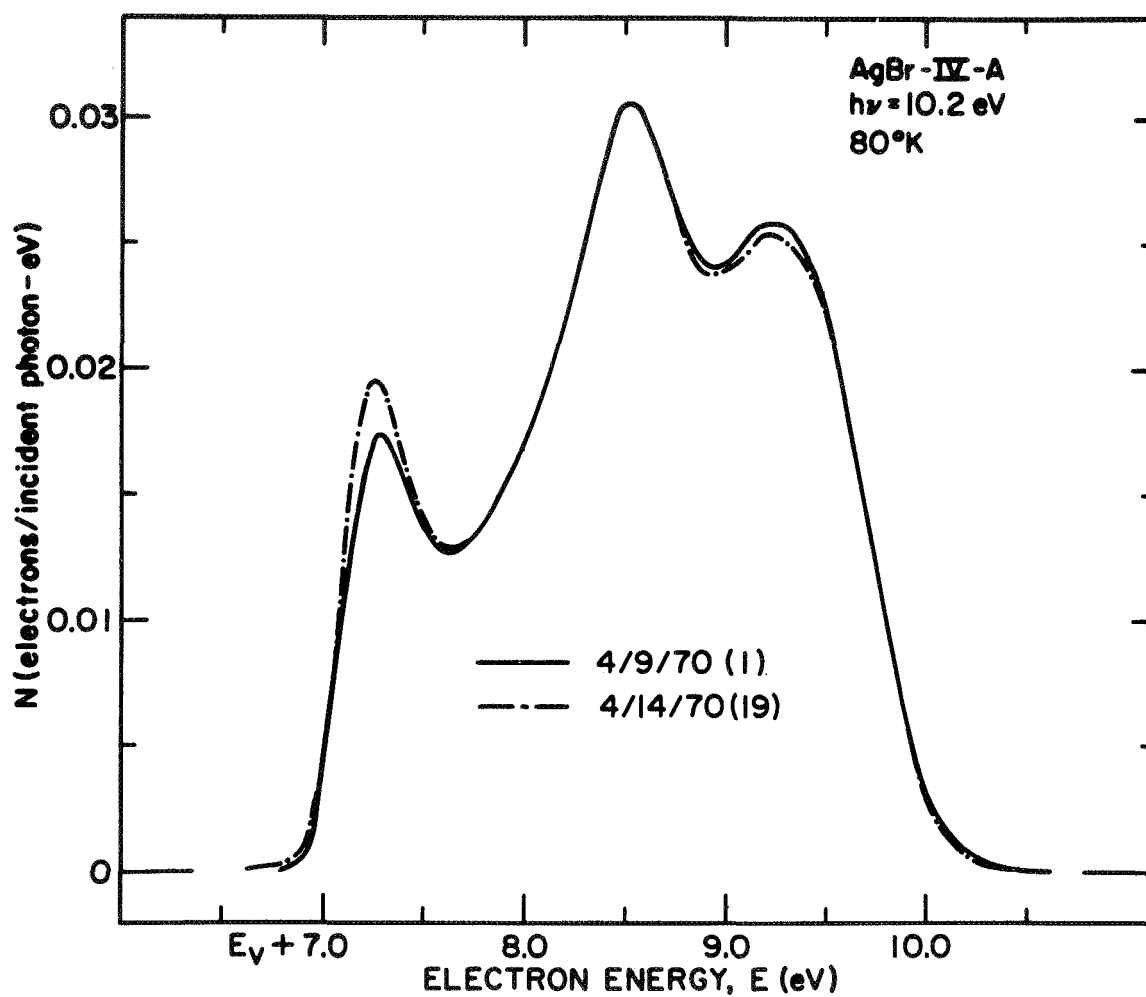
FIGURE 4.30(a). Comparison of energy distributions normalized to quantum
yield (per incident photon) for electrons photoemitted
from a AgCl sample before and after each of two
annealing treatments at 295°K for a photon energy of
11.2 eV.

FIGURE 4.30(b). Comparison of the spectral distributions of the yield
of electrons photoemitted per incident photon from a AgCl sample
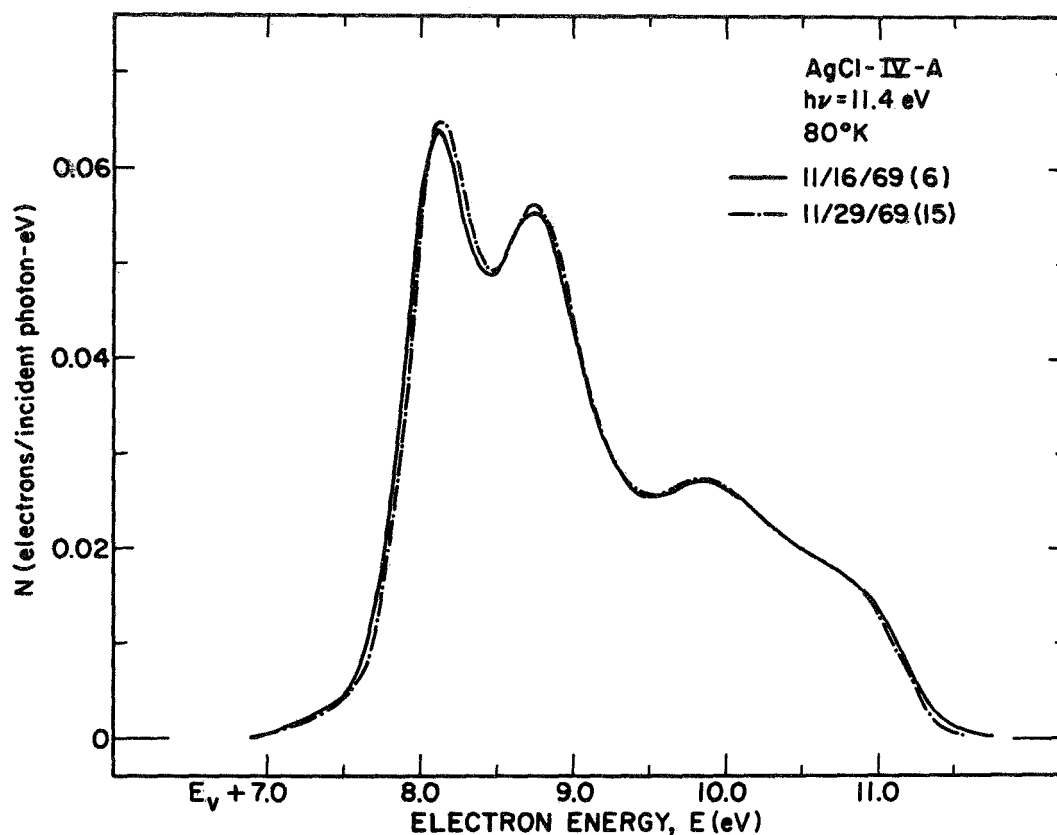before and after each of two annealing treatments at 295°K.

FIGURE 4.31(a).   Comparison of energy distributions normalized to quantum
                  yield (per incident photon) for electrons photoemitted
                  from a AgCl sample before and after air exposure
                  at 295°K for a photon energy of 11.2 eV.
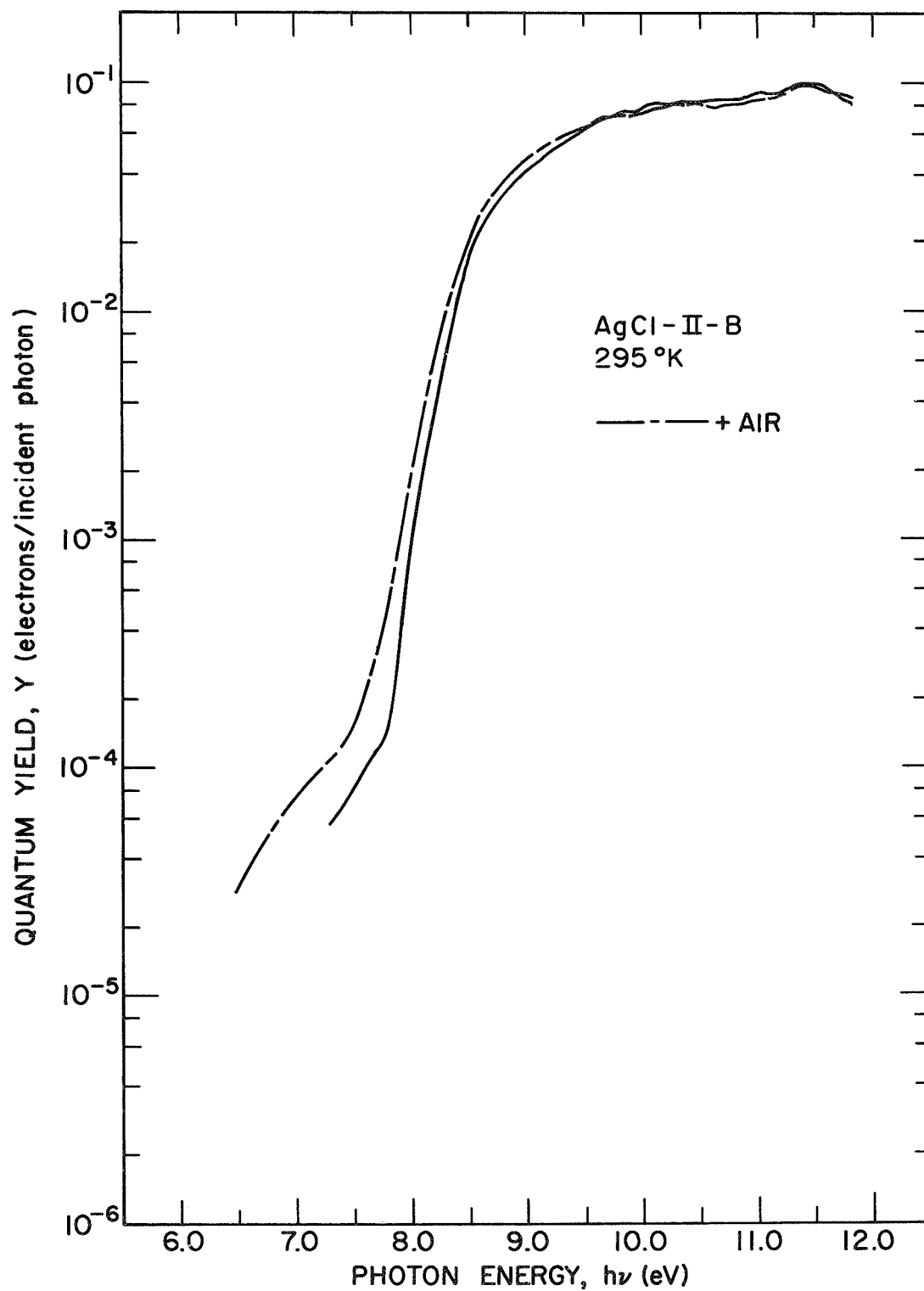
FIGURE 4.31(b). Comparison of the spectral distributions of the yield
of electrons photoemitted per incident photon from a AgCl sample
before and after air exposure at 295°K.

results are shown in Fig. 4.32. Though the threshold is lowered by 4 and 7 Cs exposures [part (a)], the entire character of the EDC structure is changed in the process [part (b)]. It is clear from these curves that the cesium has reacted with the AgCl thus destroying the AgCl features of the data. The LiF window was removed to probe deeper into the valence band (see Chapter VI) but this could only be done at room temperature. The detailed temperature dependence of the silver halide photoemission to be discussed next was thus limited to an energy range of 4.7 eV, 4.2 eV, and 5.2 eV for AgBr, AgCl, and AgI respectively.
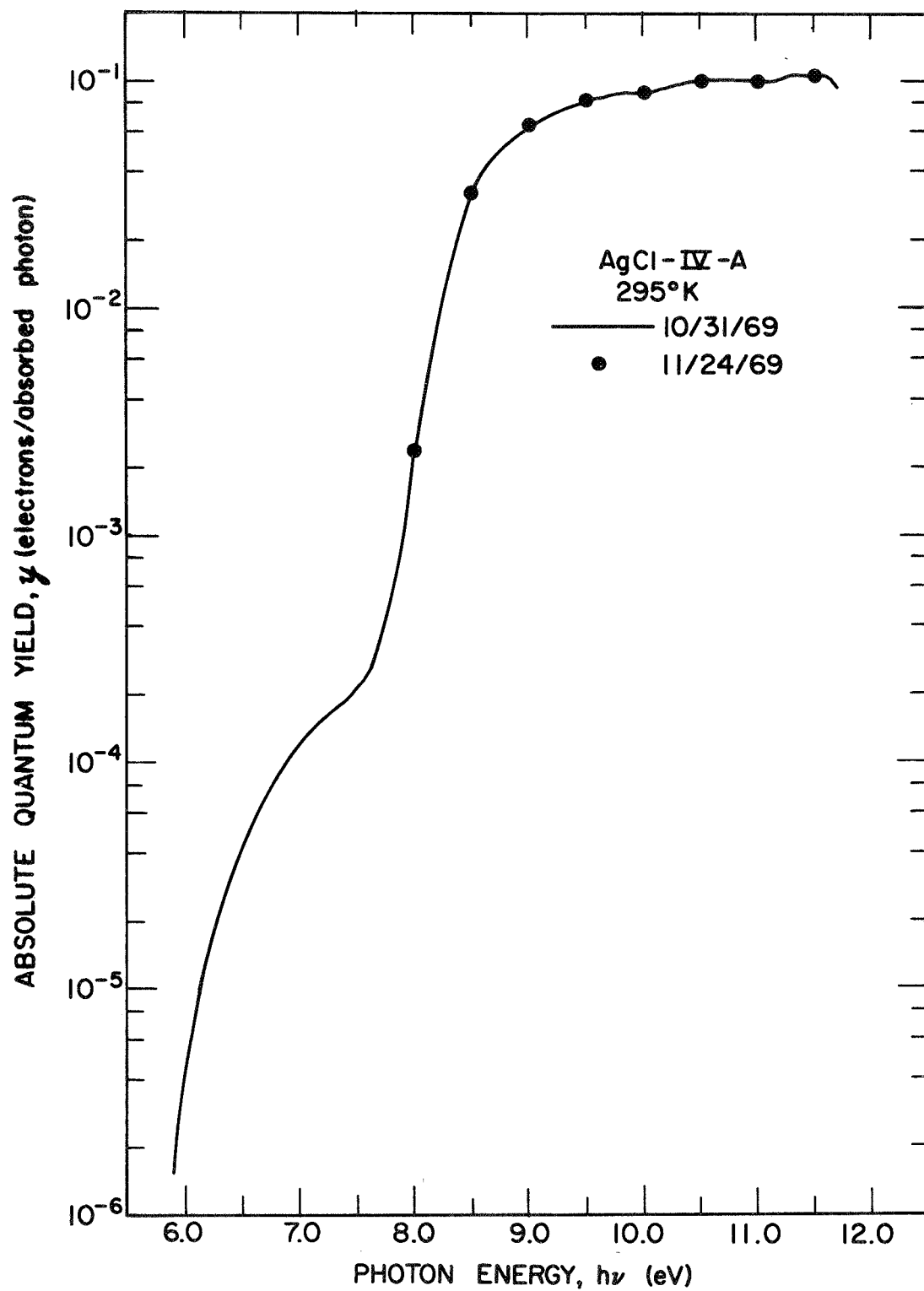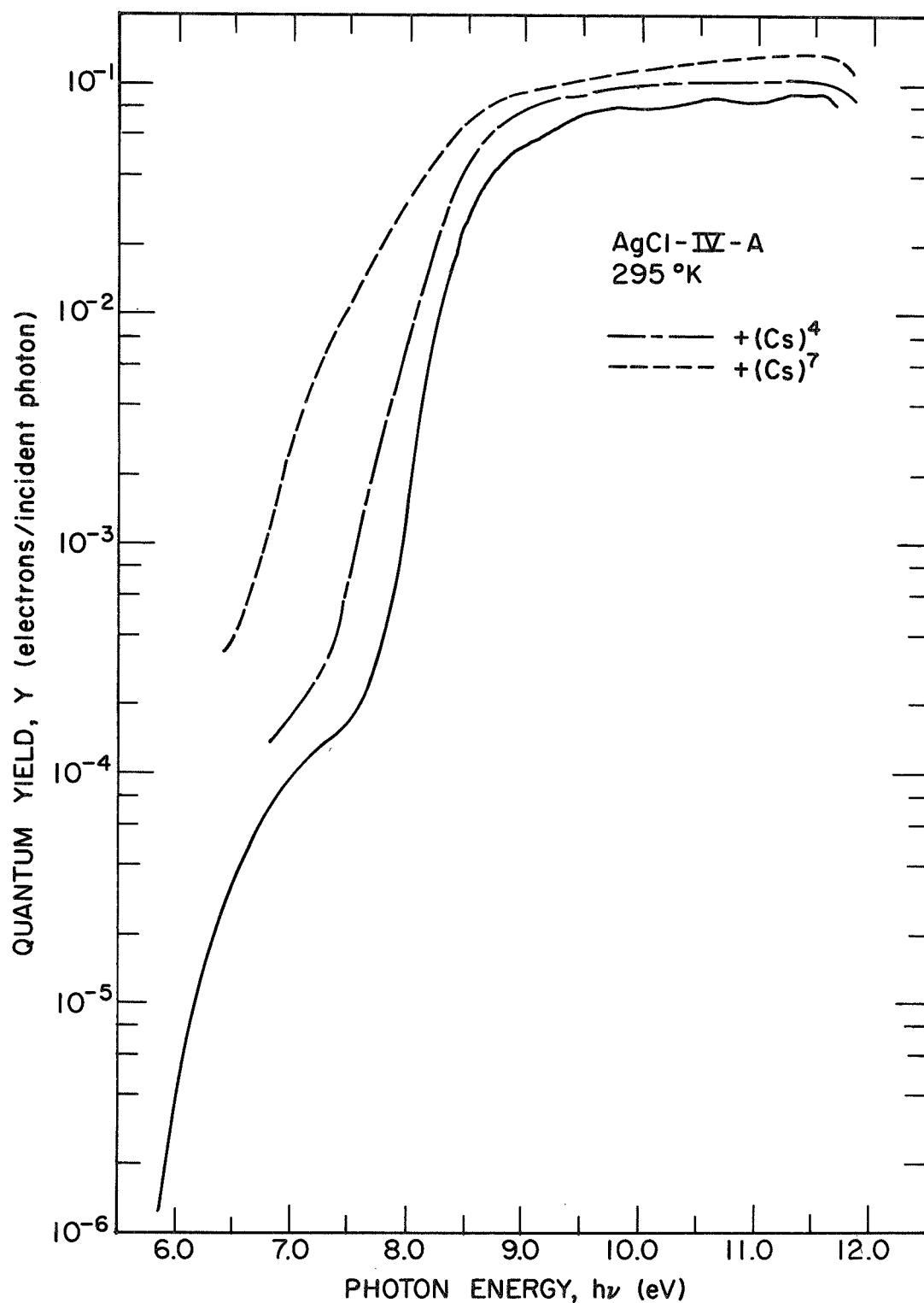
FIGURE 4.32(a). Comparison of the spectral distributions of the yield of electrons photoemitted per incident photon from a AgCl sample before and after each of two cesium treatments at 295°K.
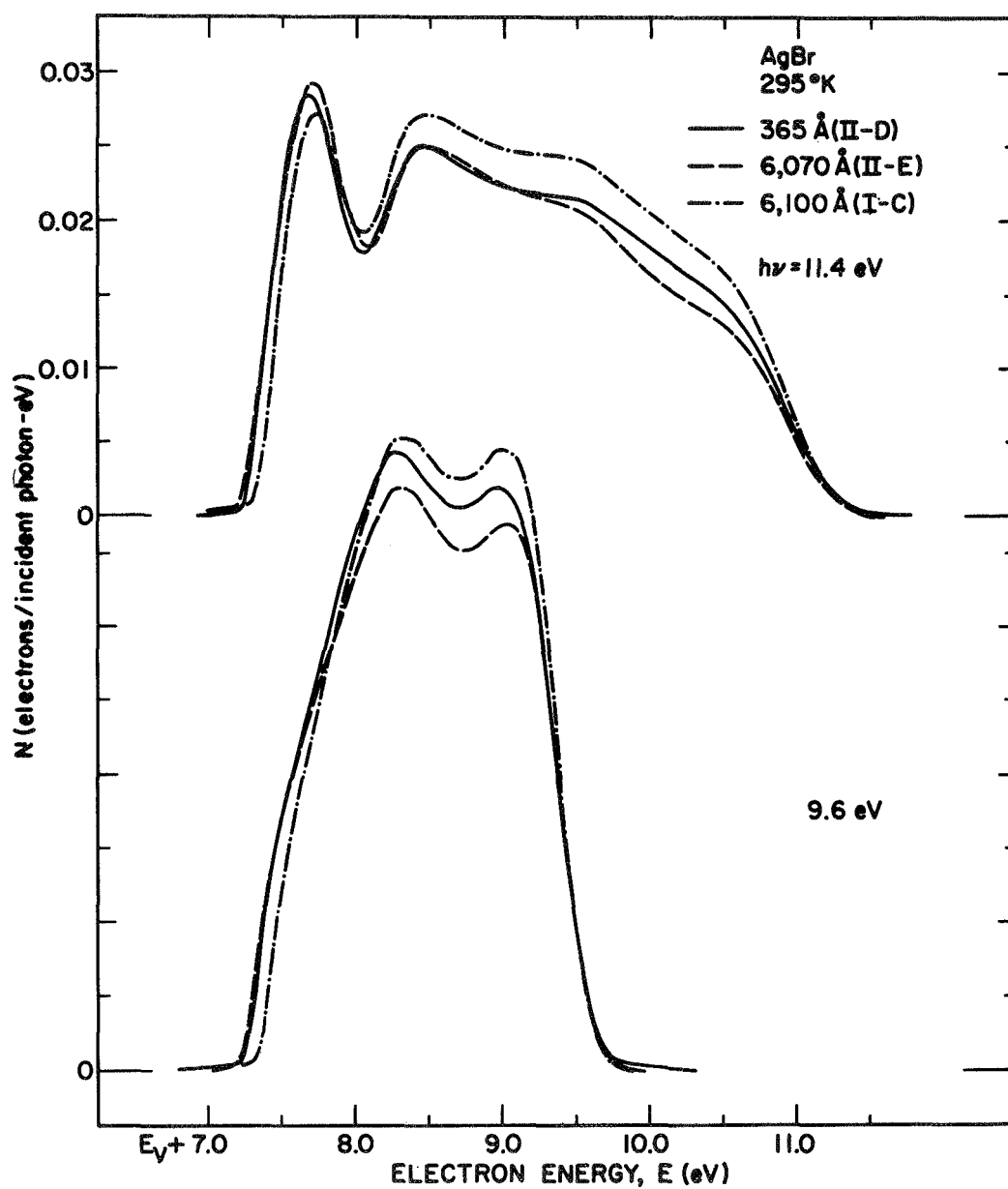
113

FIGURE 4.32(b). Comparison of energy distributions normalized to
quantum yield (per incident photon) for electrons
photoemitted from a AgCl sample before and after
each of two cesium treatments at 295°K for a photon
energy of 11.4 eV.

V. THE HYBRIDIZED HALOGEN p-DERIVED ELECTRONIC VALENCE STATES OF

AgBr and AgCl

The AgBr and AgCl temperature dependent photoemission data[104]
will be examined in detail in this chapter. Following a detailed
presentation of the data, the dynamic hybridization model will be applied
to these halides. It will be shown that such a mechanism predicts energy
level broadening and the temperature dependence of such broadening which
is of the same order of magnitude as that observed in the EDCs. This is
done by using our calculations of the tight-binding AgCl energy bands
and by using the AgBr and AgCl pressure dependent absorption data.
These results can then be used as a method to determine the atomic origin
of the states to which the EDC structure correlates. It should be re-
called that since the energy states of these two halides are so similar,[3,6]
they can be discussed interchangeably, to first order. In addition, the
salient features of the EDC data are the same for both halides. There-
fore, for clarity the experimental results for one of these solids is
discussed fully and similar data for the other halide is presented by
comparison to it.

A. Data

The complete photoemission data for AgBr and AgCl are presented
in this section for the photon energy range where the temperature depen-
dent features are most striking. The discussion will only emphasize
these features. In particular, the temperature dependence of the width
of the structure at some fixed fraction of the height will be seen to
be the most meaningful parameter. The heights of the EDCs must be
compared with caution since they are normalized relative to the incident
rather than the absorbed photon flux. As pointed out in Chapter III,
this is due to the lack of low temperature optical data in this photon
energy range. The behavior of the position and height of EDC structure
with photon energy variation is discussed in Chapter VIII.

115

The AgBr EDCs from 8.8 eV through 9.6 eV are presented at both
room and liquid nitrogen temperatures in Fig. 5.1. At the low photon
energies, the EDCs sharpen only slightly upon cooling. The dramatic
change occurs when a peak emerges on the leading edge of the curve.
Note how dramatic the onset is over such a small energy range of 9.0 to
9.2 eV. It is important that the energy range from the first appearance
of the new structure to its emergence as a peak is much smaller at 80°K
than at room temperature. Consistent with this, there appears to be a
much greater strength in this leading peak at low temperatures as evi-
denced by the reversal in the relative heights of the two peaks. Both
of the peaks appear sharper and more well-defined since the peak-to-
valley ratios are greatly increased and the widths are reduced upon
cooling. These effects are all characteristic of a large change in the
valence states from which these electrons were photoexcited.

Such changes in EDCs are also seen in Fig. 5.2 at higher photon
energies. The onset of the new structure at the trailing edge again
occurs over a smaller energy range at 80°K. This may be somewhat
artificial since the threshold decreases by about 0.1 eV in AgBr upon
cooling. All the structure through 10.4 eV is sharpened considerably
and the peak-to-valley ratios increased. As was pointed out earlier,
the full width at 90% of the height of the central peak at 10.2 eV is
sharpened from 0.6 eV at 295°K to less than 0.3 eV at liquid nitrogen
temperature. The reason for the loss of structure above a final state
energy of about 9.5 eV and the lack of sharpening of this structure
(see hν = 10.6 eV) with sample cooling is discussed in Chapter VII.

It is important to note that the peak-to-peak separations are not
significantly altered by temperature variation. This is particularly
evident when EDCs at intermediate temperatures are included as in
Fig. 5.3. At 9.7 eV where the peak-to-valley ratios are a maximum, the
peaks each sharpen upon cooling with a height modulation that reverses
the ordering of the relative heights of the peaks, but the peak-to-peak
spacing and their absolute positions are unaffected. It is meaningful
to compare positions of peaks since the energy scales were independently
determined for each set of EDCs at a fixed temperature. The sharpening
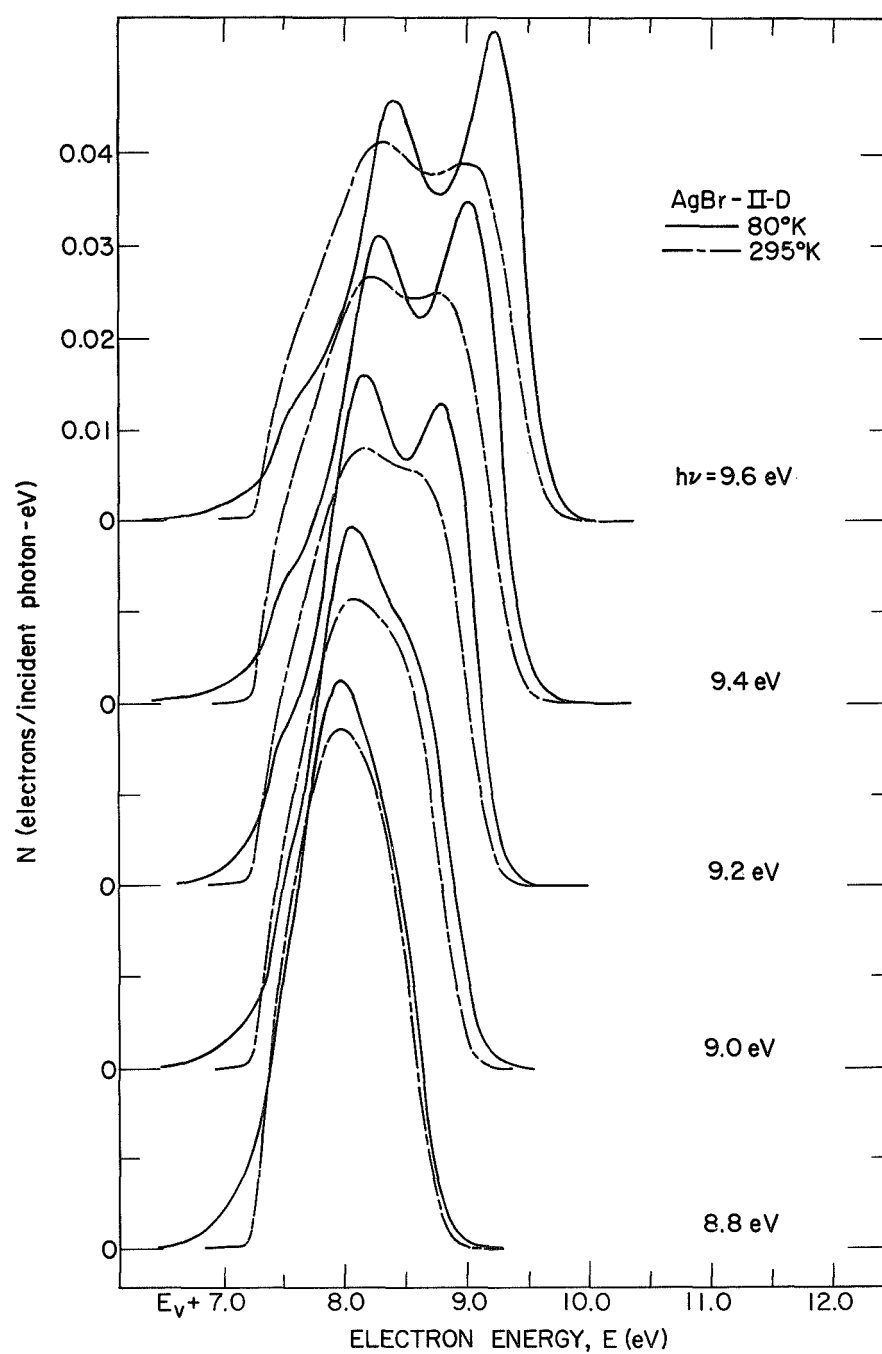
FIGURE 5.1. Comparison of energy distributions normalized to quantum yield (per incident photon) for electrons photoemitted from AgBr at 80 and 295°K for photon energies of 8.8 through 9.6 eV.
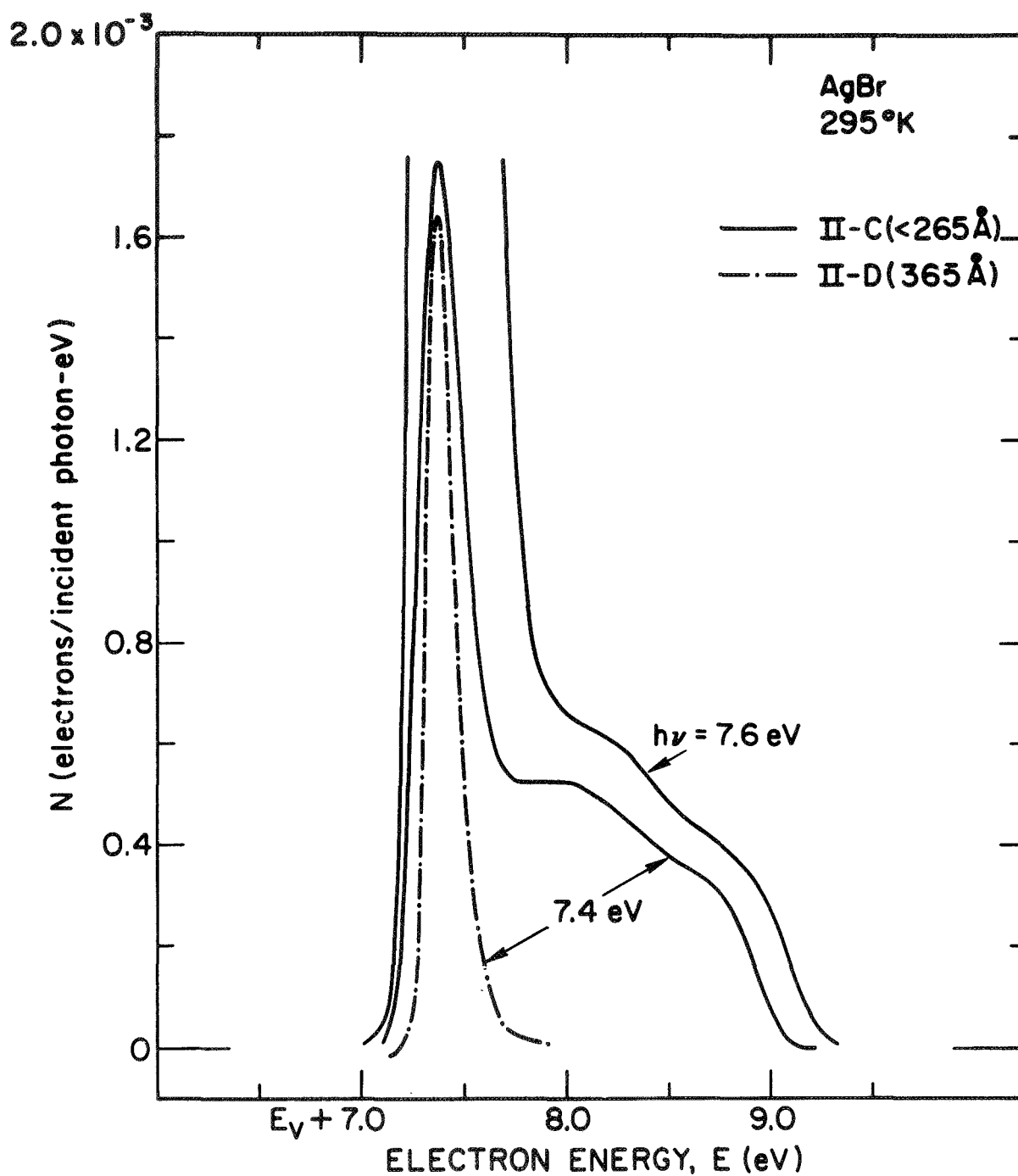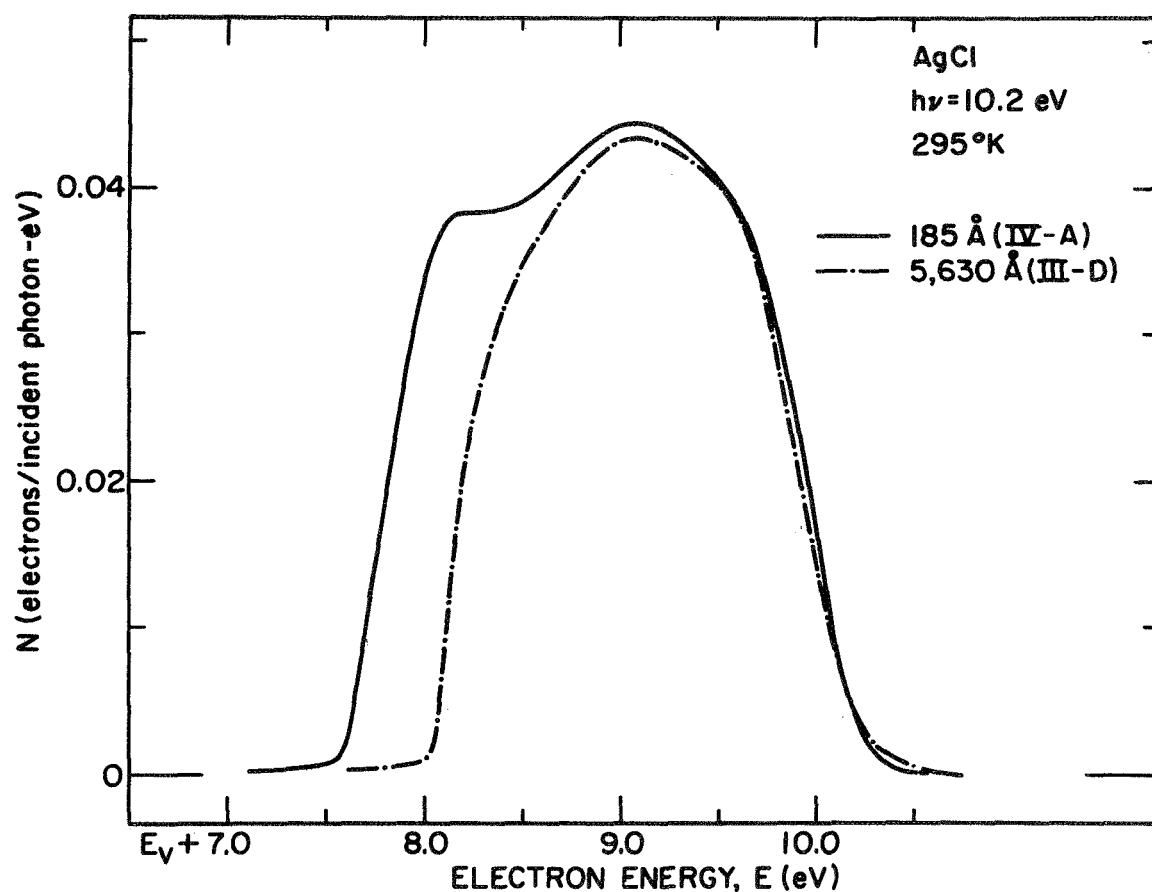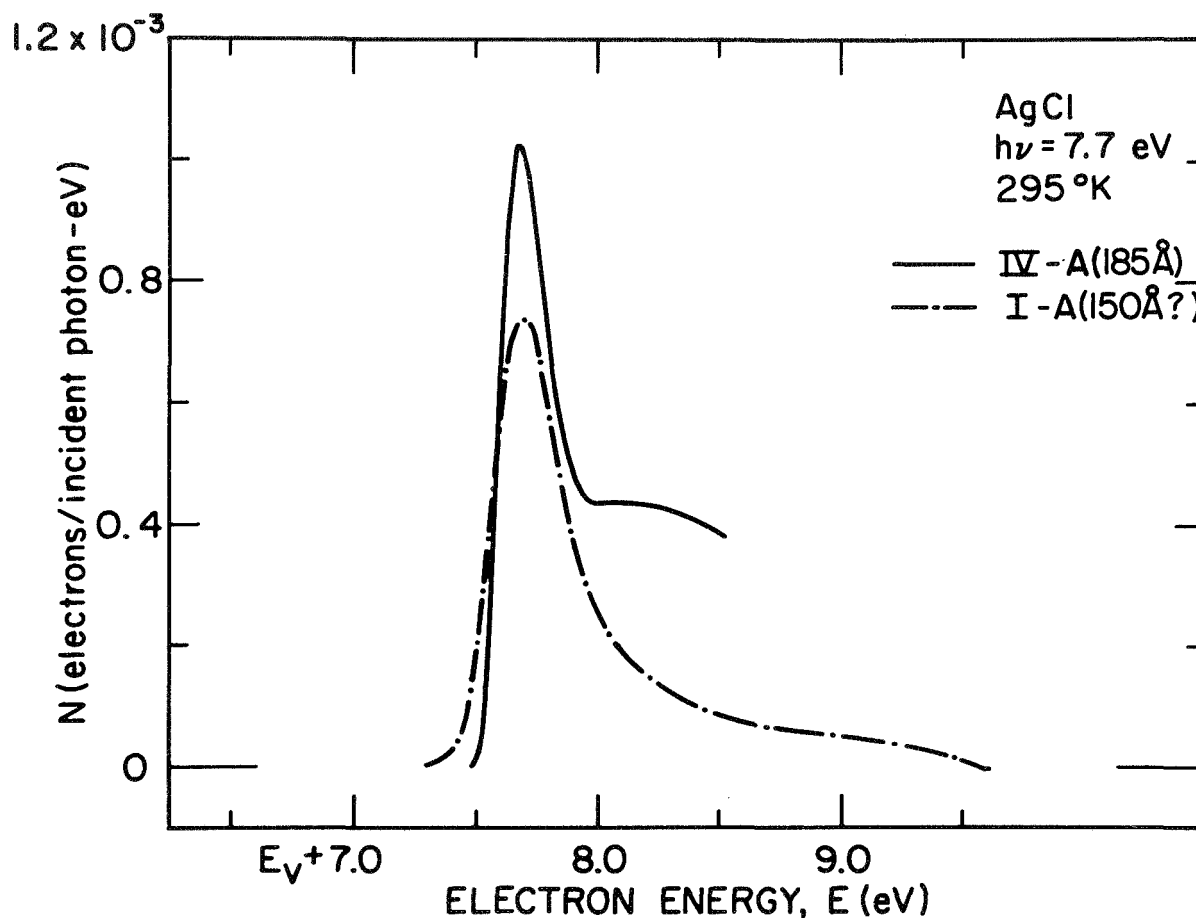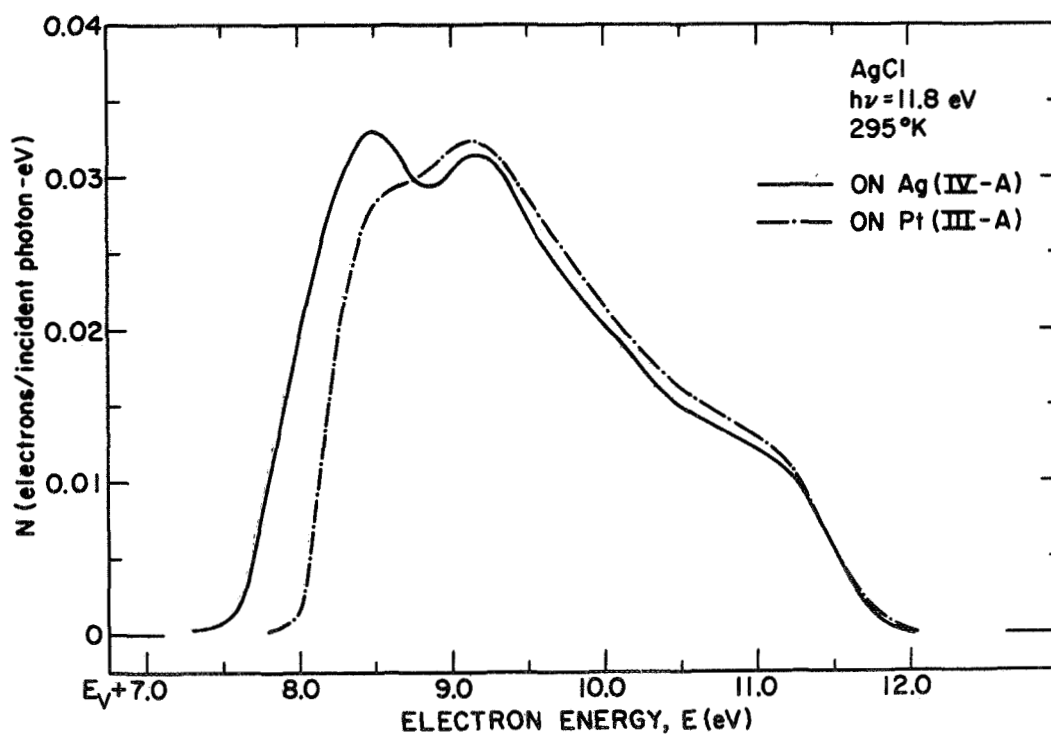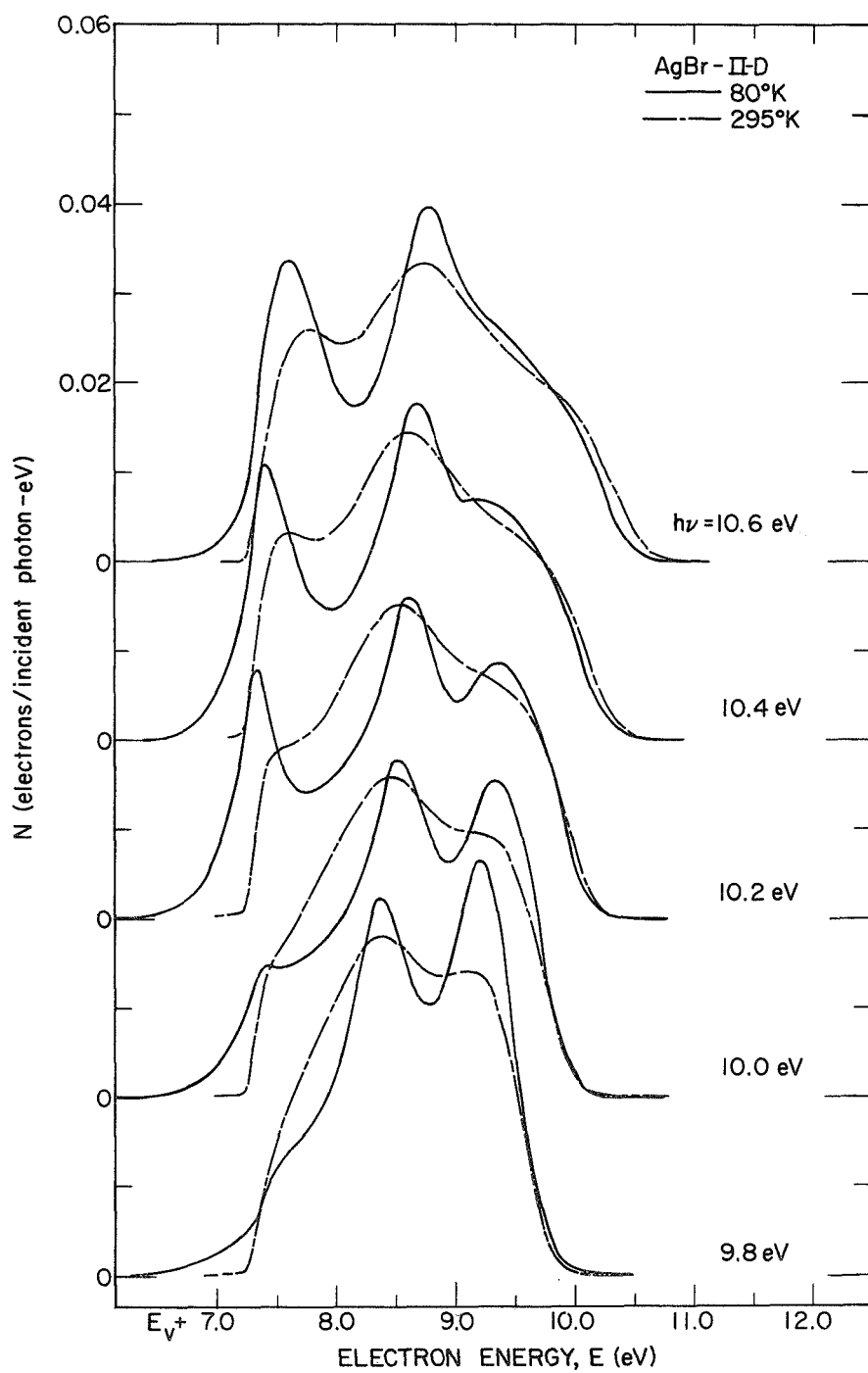
FIGURE 5.2. Comparison of energy distributions normalized to quantum
yield (per incident photon) for electrons photoemitted
from AgBr at 80 and 295°K for photon energies of 9.8
through 10.6 eV.
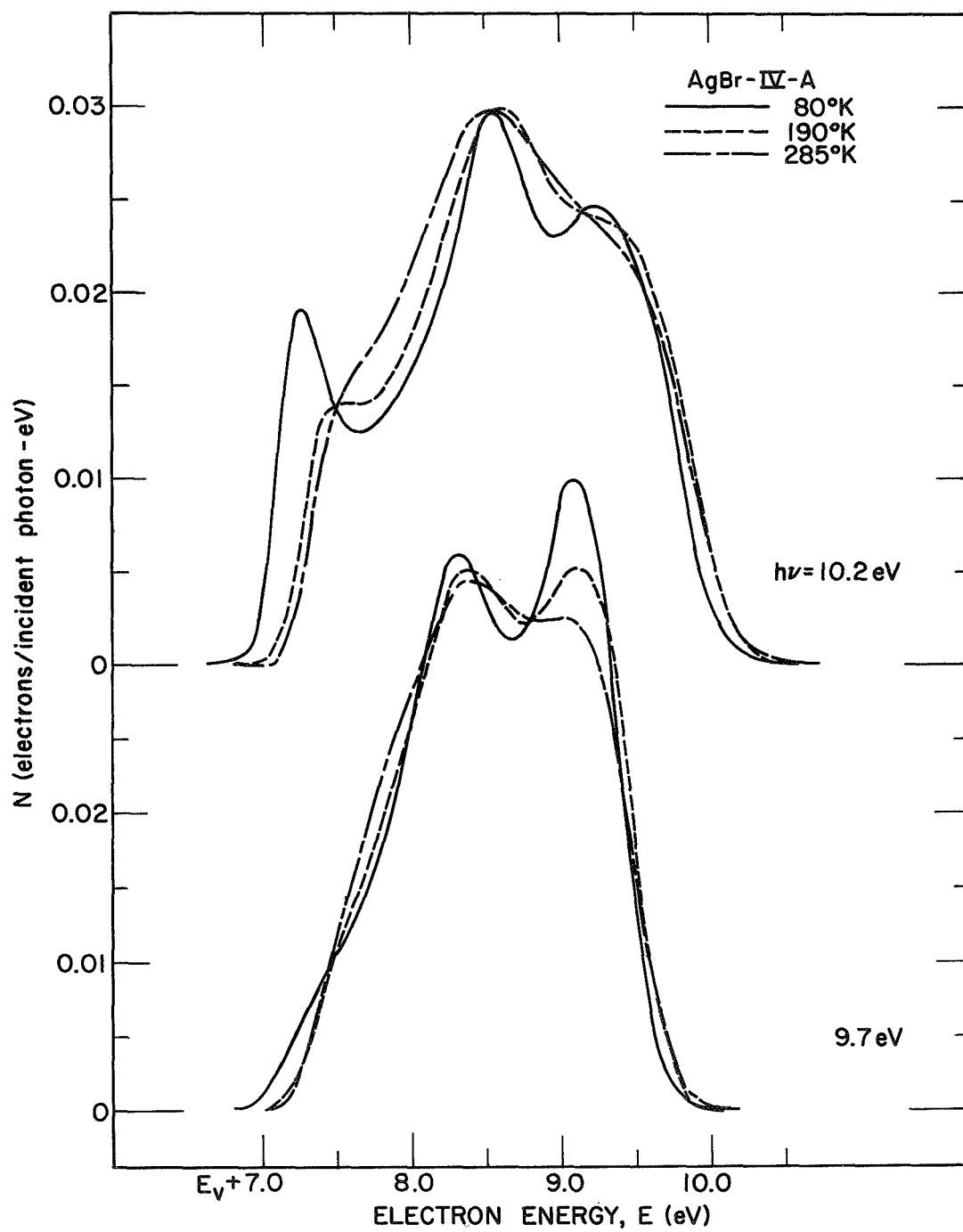
FIGURE 5.3. Comparison of energy distributions normalized to quantum yield (per incident photon) for electrons photoemitted from AgBr at 80 through 285°K for photon energies of 9.7 and 10.2 eV.

of the leading edge with cooling, seen in this figure, is indicative
of a more well-defined valence band maximum. As is seen clearly at
10.2 eV, the striking appearance of a peak at the trailing edge is in
part due to the reduction of the threshold by 0.1 eV upon AgBr cooling
(see Chapter VIII).

Consideration of these curves shows why the quantum yield cannot be
used to understand the effect of cooling on the electronic states. Since
the yield is a measure of the area under the EDC, the total changes in
all the pieces of structure are measured together. Thus, the large
structure changes in an EDC such as those for $h\nu = 10.2$ eV (Fig. 5.3,
top) result in only a small yield decrease as seen in Fig. 5.4. This
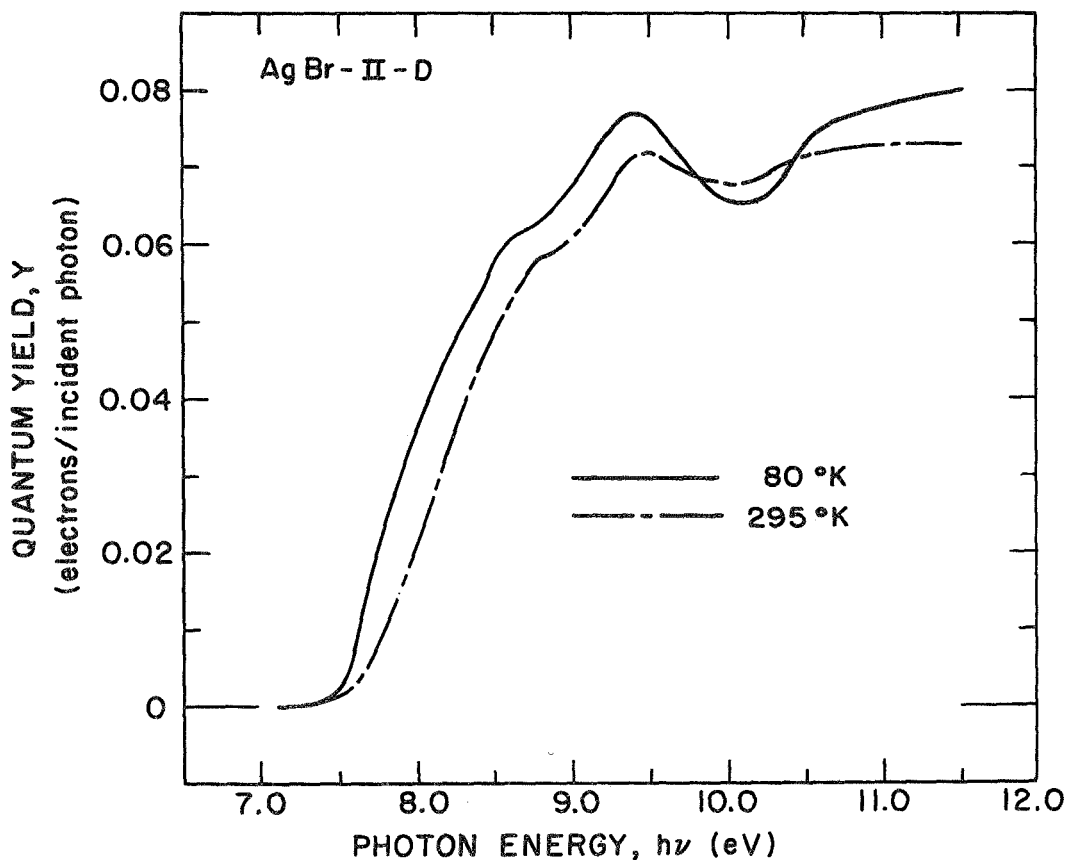
FIGURE 5.4. Comparison of the spectral distributions of the yield of
electrons photoemitted per incident photon from AgBr at
80 and 295°K.

120

yield is plotted on a linear scale to accentuate the saturation region. At each photon energy on these curves, an integrated effect of the states is measured, and thus does not yield any detailed, definitive electronic state information. The dip in the yield at 10.1 eV is enhanced upon cooling and is of some interest. As is seen in Fig. 5.5, the yield peak-to-valley ratio increases gradually with decreasing temperature. Since these yields have not been corrected for sample
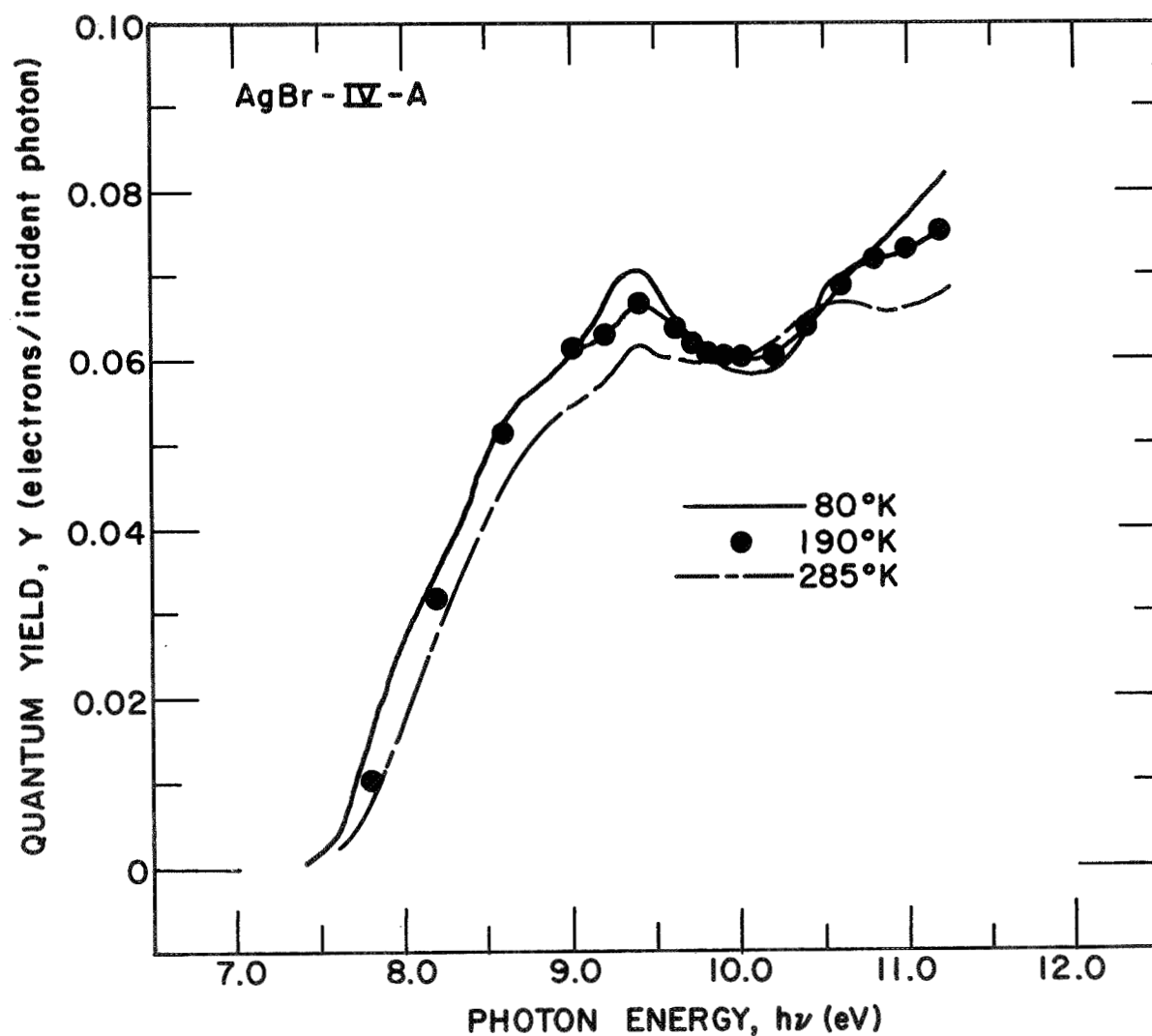
FIGURE 5.5. Comparison of the spectral distributions of the yield of electrons photoemitted per incident photon from AgBr at 80 through 285°K.

reflectivity, there may be some concern that this yield structure is
introduced by the optical properties. At room temperature where the
reflectance has been measured,[55] the yield can be calculated in terms
of the absorbed photon flux as shown in Fig. 5.6. As can be seen, the
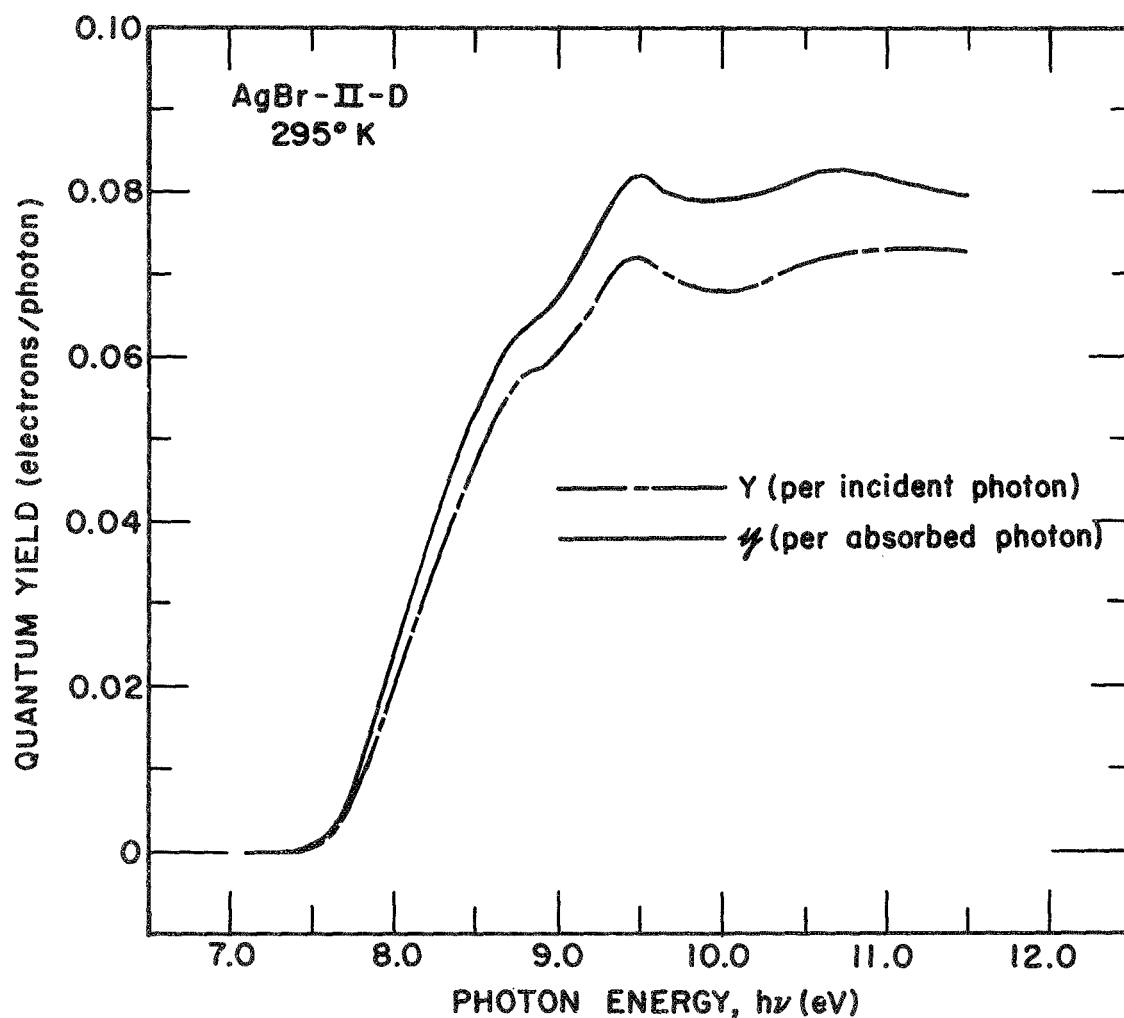
FIGURE 5.6. Comparison of the spectral distributions of the yield of
electrons photoemitted per incident and absorbed photon
from AgBr at $295°K$.

dip in the yield around 10 eV is not removed by correcting for sample reflectance and thus, cannot be due to the optical properties. It is reasonable to assume that its temperature dependence is characteristic of a change in the intrinsic photoemission. The effect of cooling on the electron transport in the silver halides is seen in the yield when it is plotted on a logarithmic scale in Fig. 5.7. The low pnoton energy tail due to electrons excited in the silver substrate is considerably increased upon AgBr cooling. This is probably due to an increased hot electron scattering length in the silver halide at 80°K caused by reduced thermal vibration of the lattice at the low temperature (i.e., freezing out of the optical phonons).

The data for AgCl shows the same characteristics as those discussed for AgBr above. The EDCs in the energy range from 9.2 through 10.0 eV are shown in Fig. 5.8. The peak which appears on the leading edge of the EDC is sharper and somewhat stronger when the sample is cooled. The increased strength of the threshold structure in this figure occurs only over a small range of final state energy and for all structure as it passes through these energies. It will be shown to be due to a temperature dependent final density of states region around 8.1 eV in Chapter VII. This enhancement is especially evident at the higher photon energies shown in Fig. 5.9. Note how the threshold structure becomes so strong at 80°K that it has to be drawn to a reduced scale of 2:3 for ease of comparison. This structure is considerably sharpened by cooling; at $h\nu = 10.8$ eV and 11.0 eV, the trailing peak width at 90% of its height sharpens by about 0.15 eV from 290 to 80°K. The leading edge structure at these energies shows the same reversal in the order of the relative peak heights upon cooling as is seen in AgBr (Fig. 5.1). The leading shoulder is sharpened into a distinct peak much more than the neighboring structure is. This can be seen clearly in Fig. 5.10 when the intermediate temperature data is included. In part (a) at $h\nu = 10.4$ eV , this sharpening is seen to occur gradually. These curves illustrate that the peak-to-peak separation remains relatively independent of temperature in AgCl just as it did in AgBr . Note how the threshold structure strength is so much more enhanced at a final state energy of

123
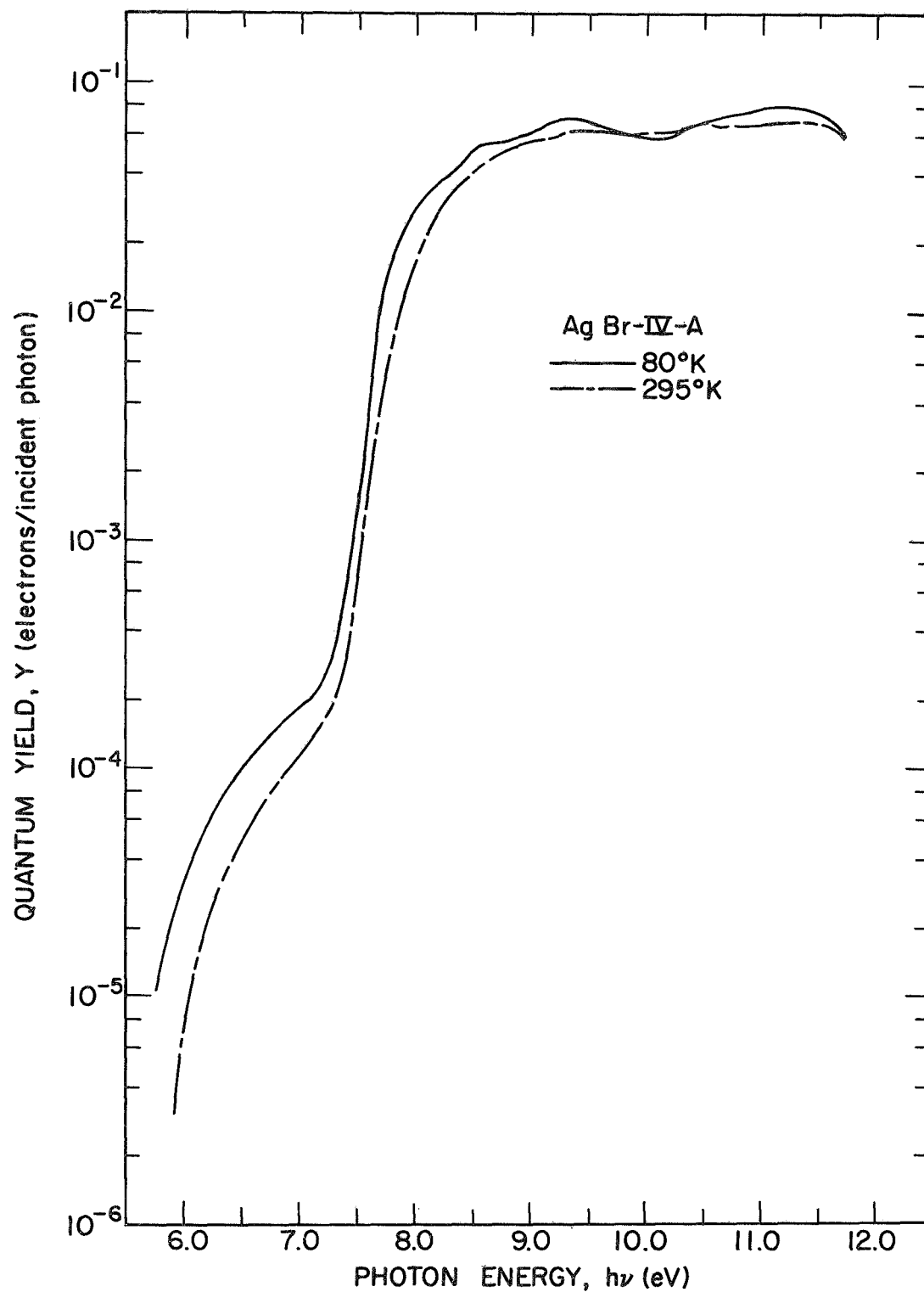
FIGURE 5.7. Comparison of the spectral distributions of the yield
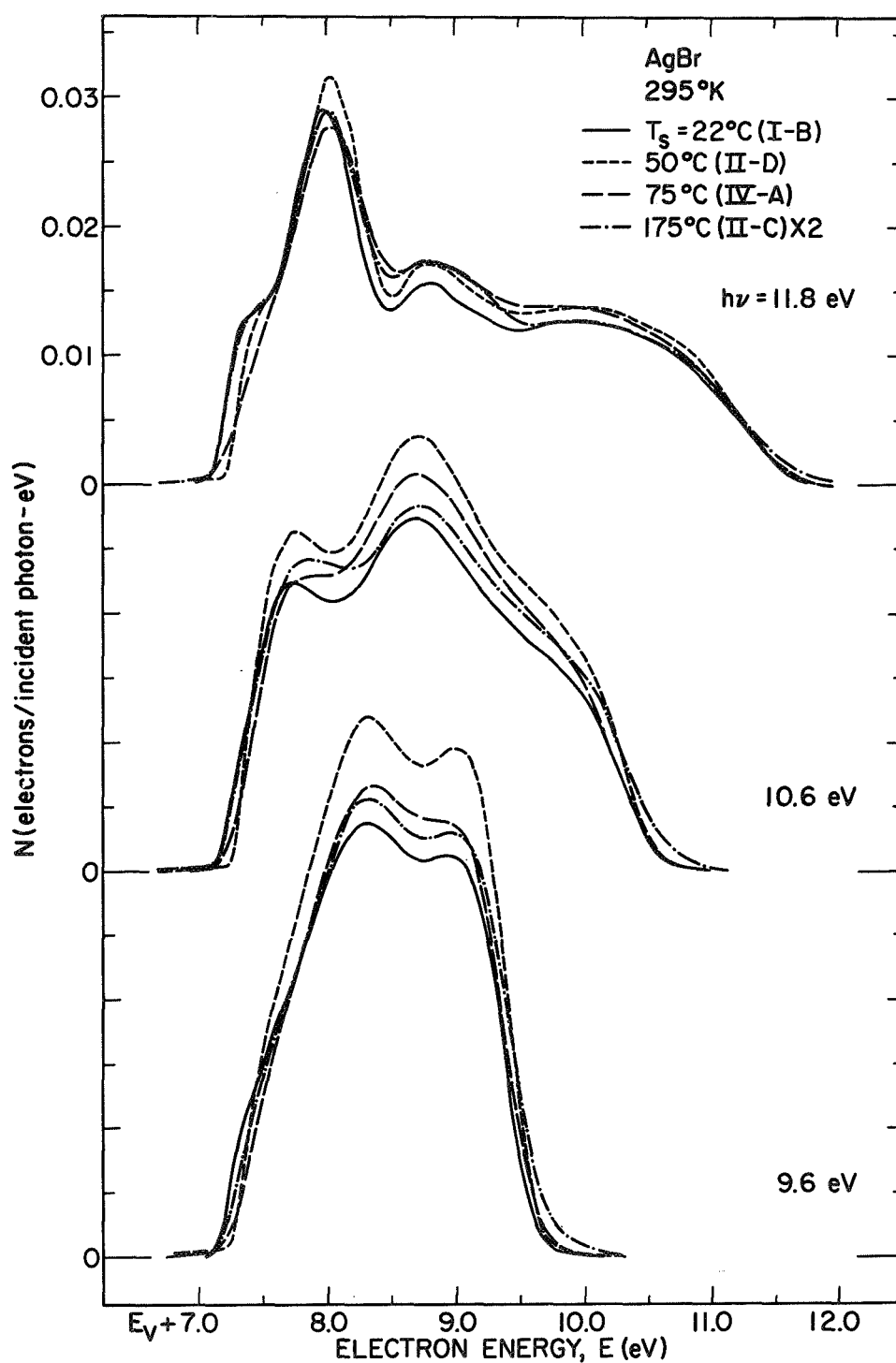of electrons photoemitted per incident photon from
AgBr at 80 and 295°K.

124
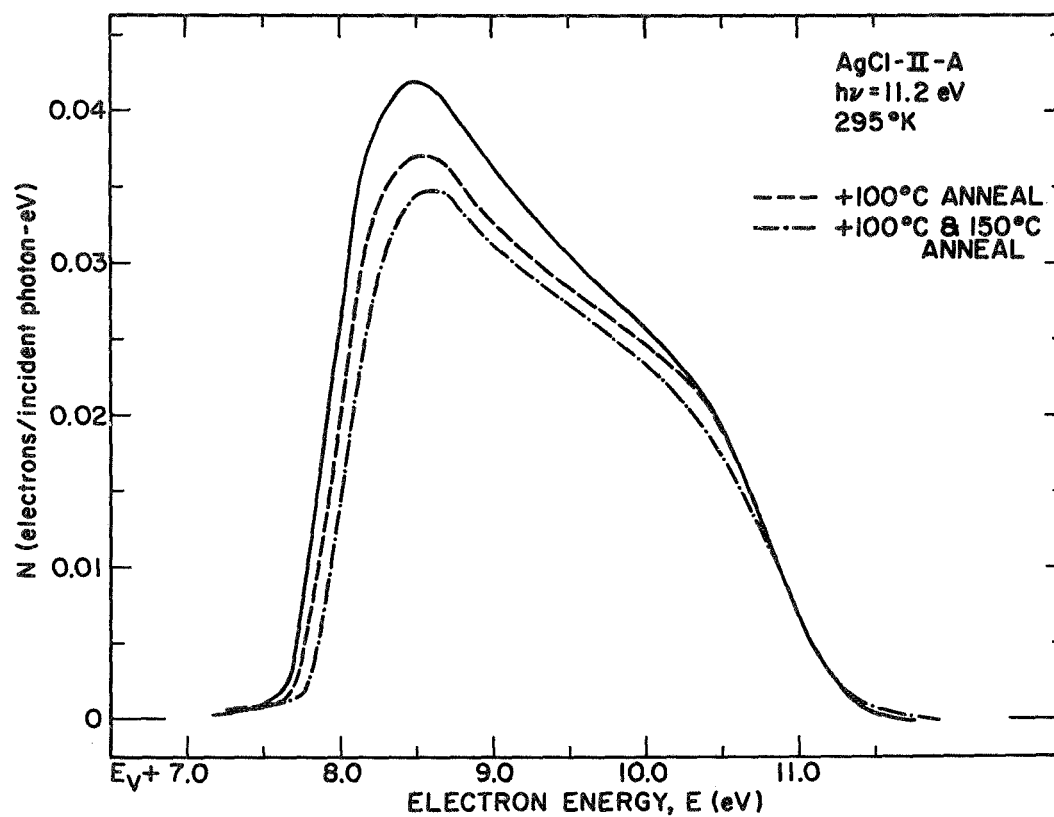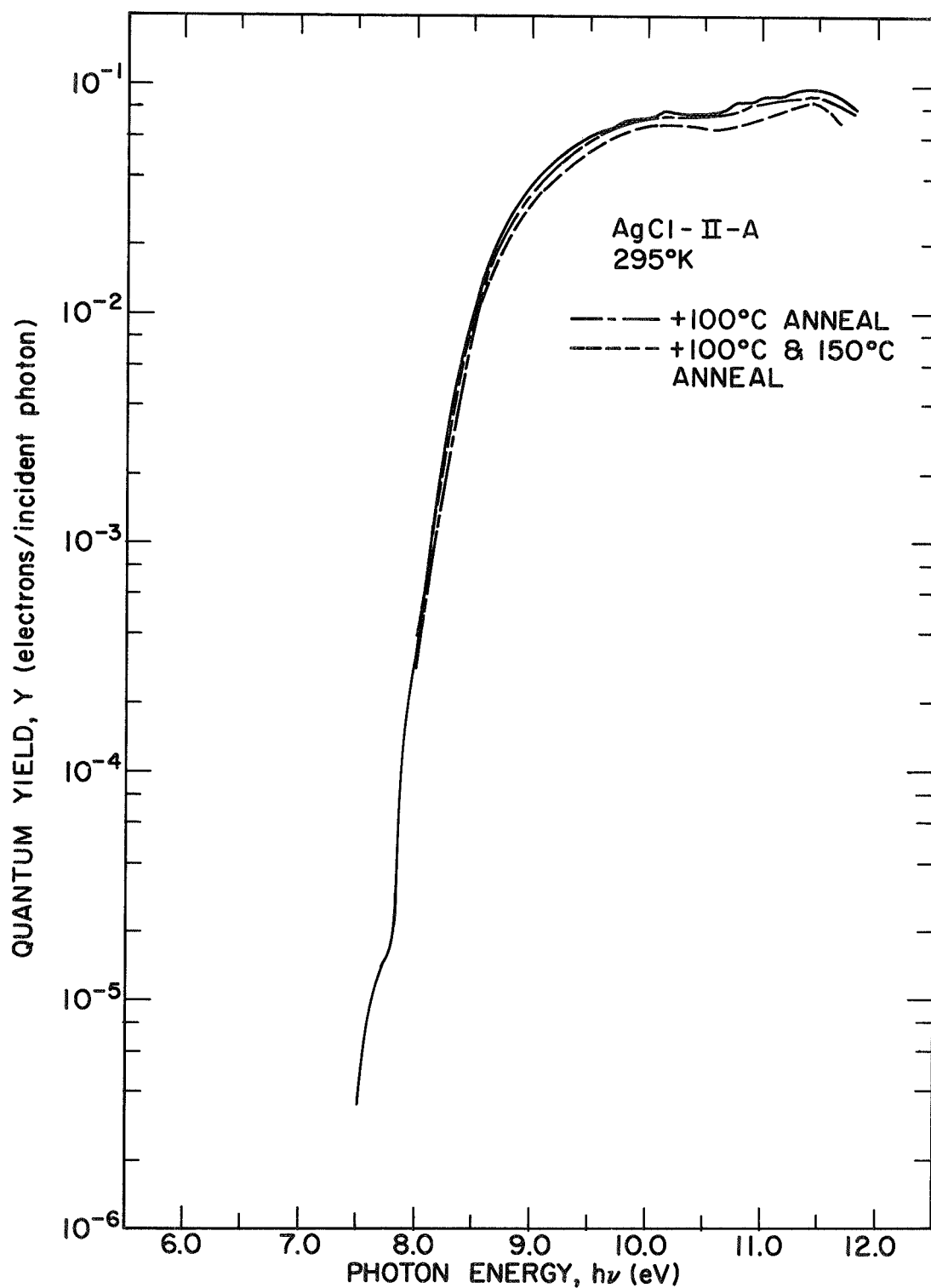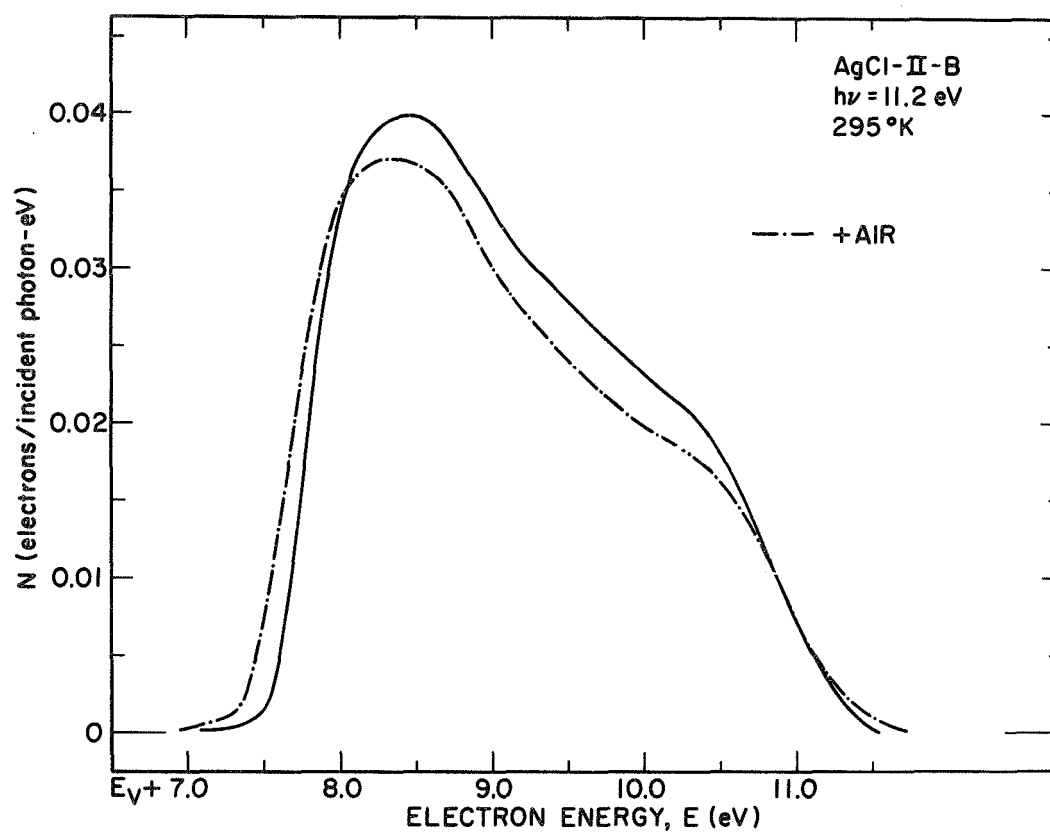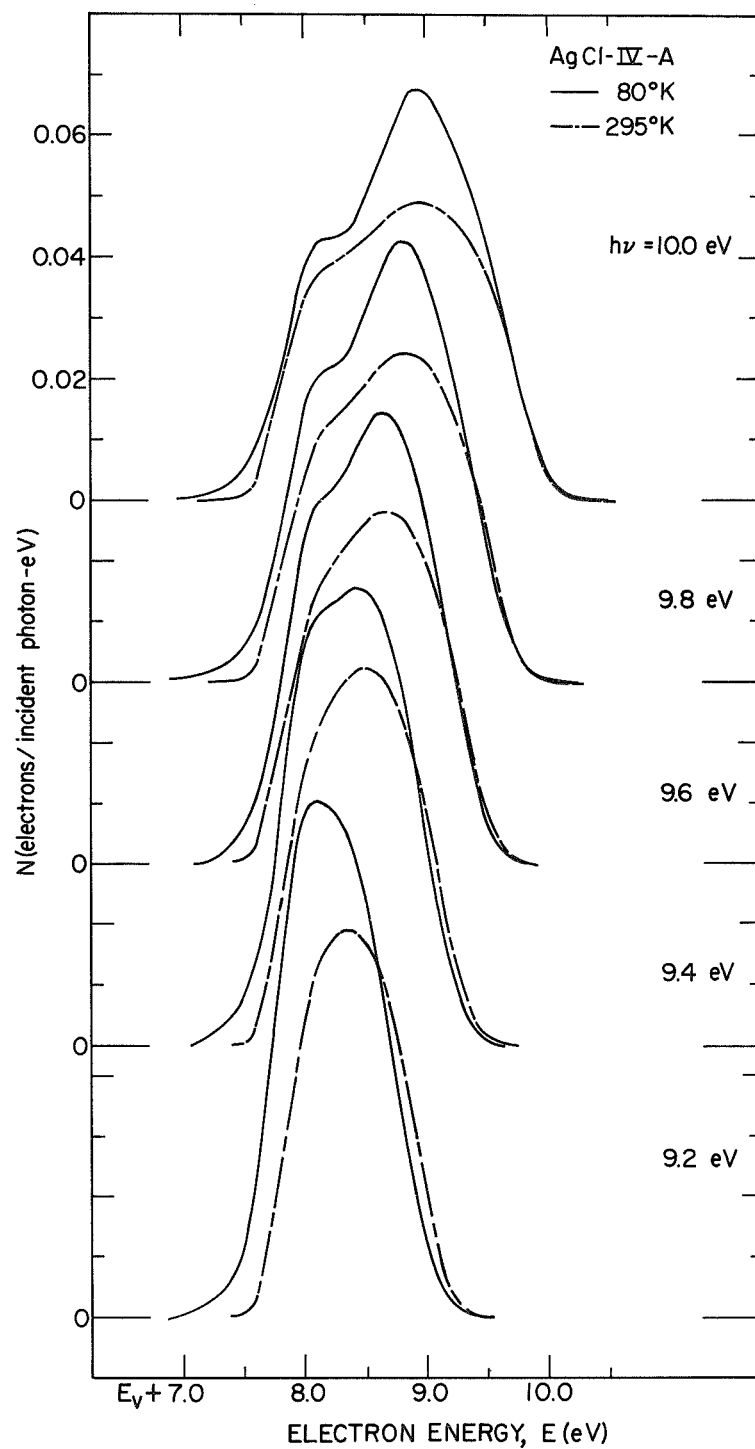
FIGURE 5.8. Comparison of energy distributions normalized to quantum yield (per incident photon) for electrons photoemitted from AgCl at 80 and 295°K for photon energies of 9.2 through 10.0 eV.
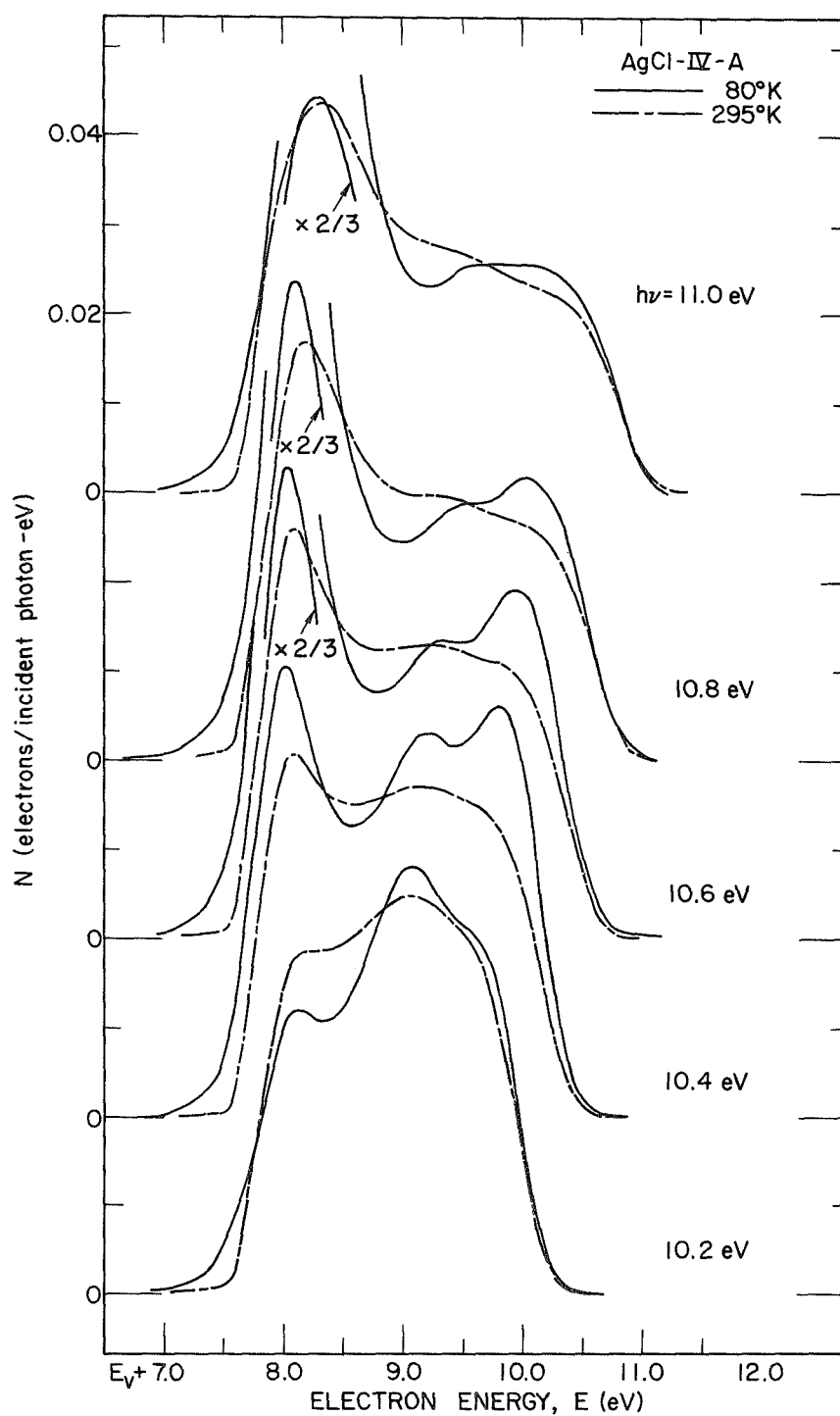
FIGURE 5.9. Comparison of energy distributions normalized to quantum yield (per incident photon) for electrons photoemitted from AgCl at 80 and 295°K for photon energies of 10.2 through 11.0 eV.

126
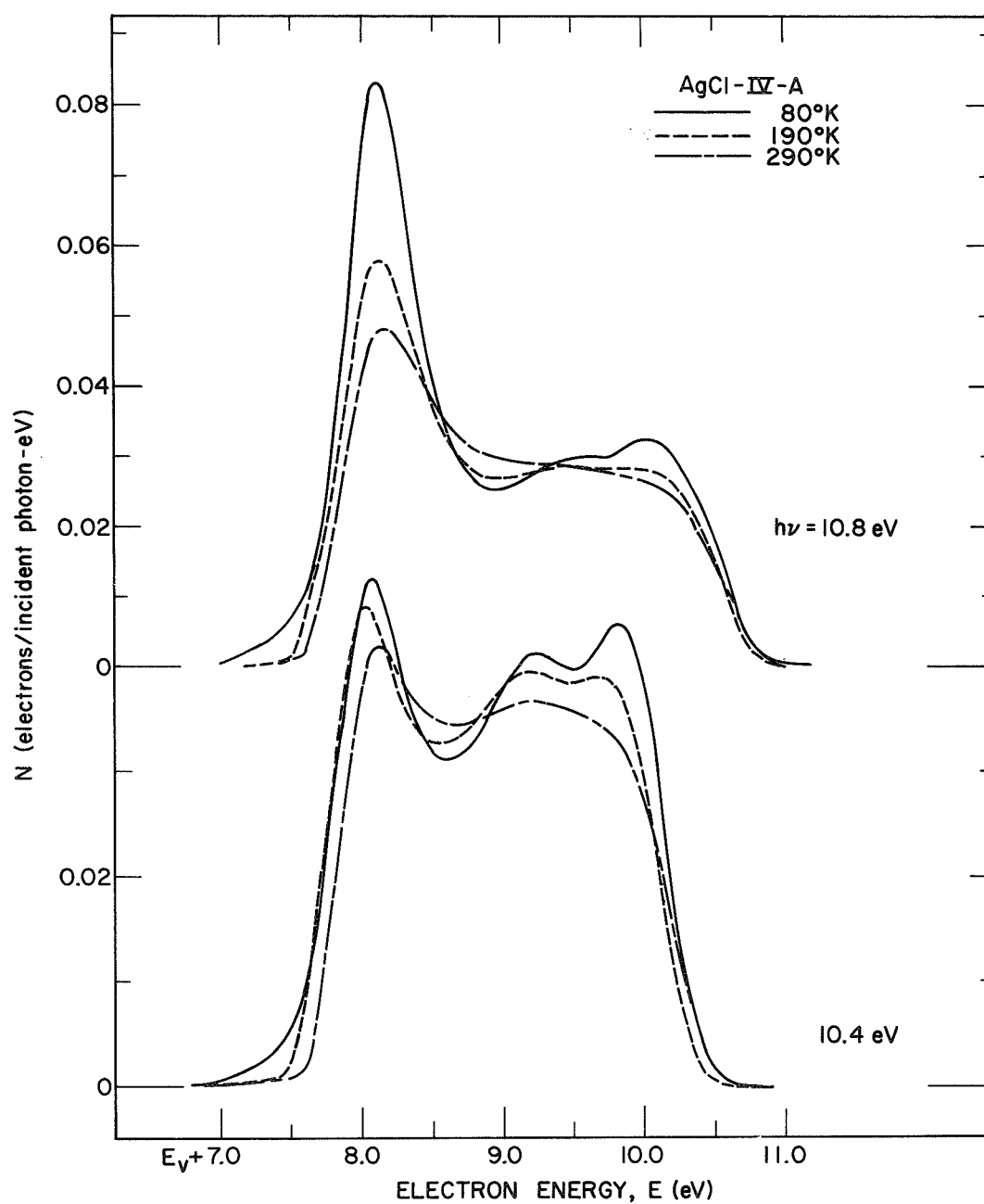
FIGURE 5.10(a). Comparison of energy distributions normalized to quantum yield (per incident photon) for electrons photoemitted from AgCl at 80 through 290°K for photon energies of 10.4 and 10.8 eV.
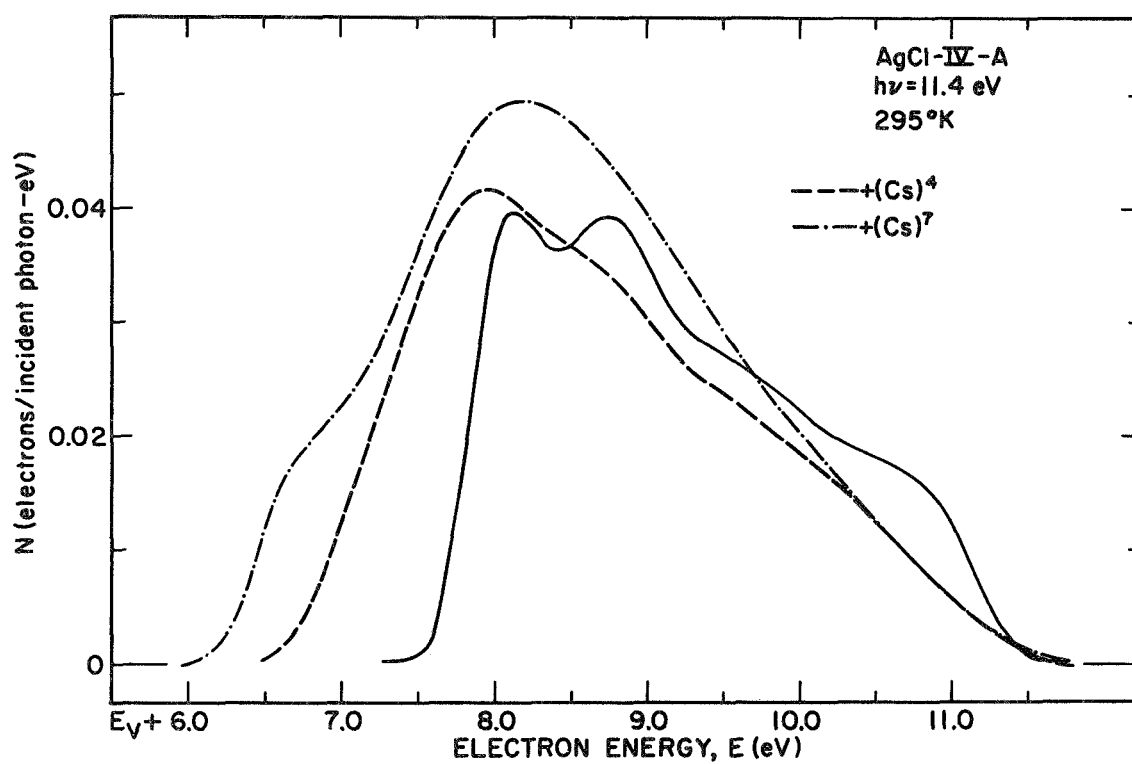
127
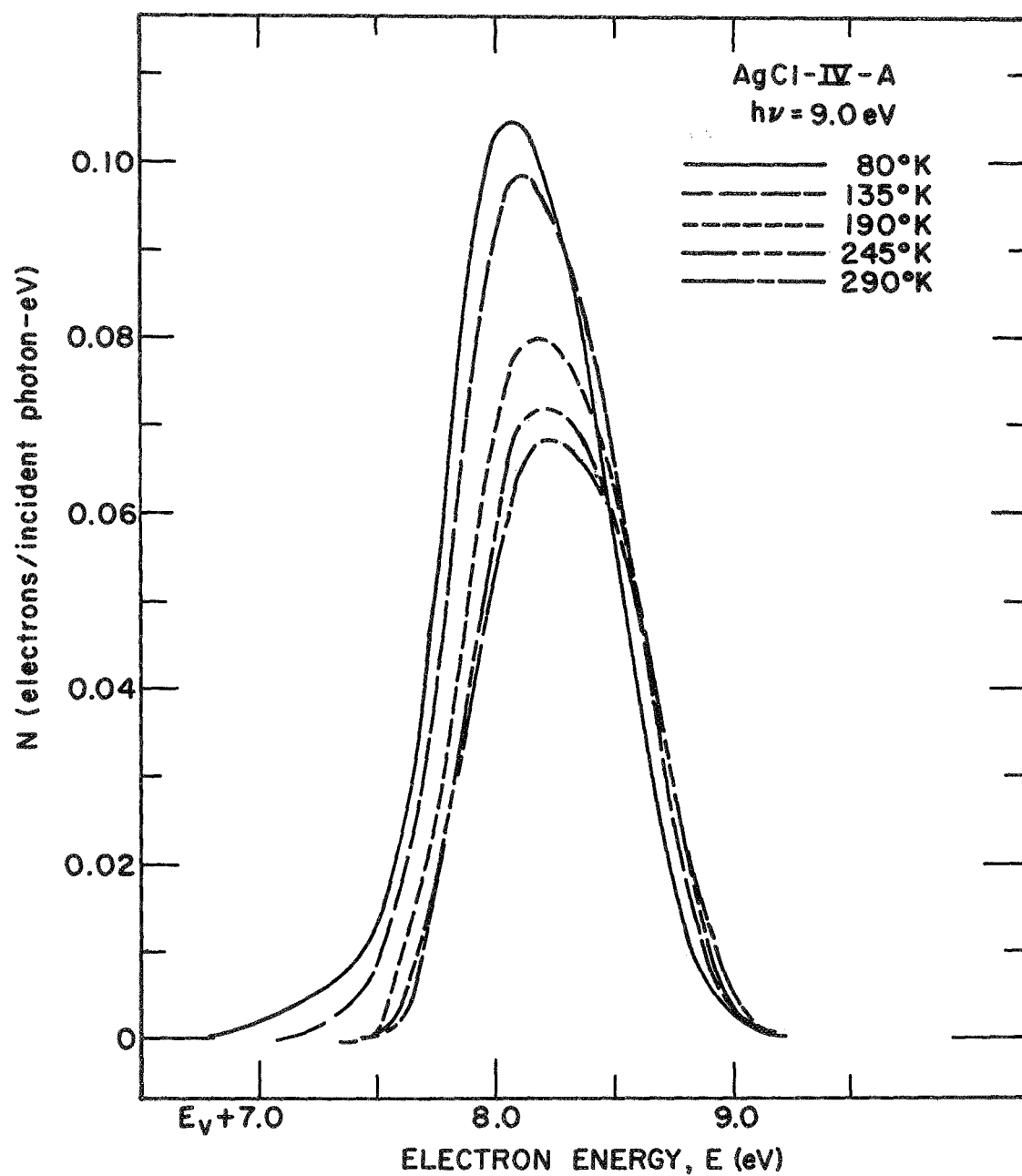
FIGURE 5.10(b). Comparison of energy distributions normalized to quantum yield (per incident photon) for electrons photoemitted from AgCl at 80 through 290°K for a photon energy of 9.0 eV.

128

8.1 eV (hν = 10.8 eV EDC) than at lower energies. This enhanced strength is seen for all structure in this final state energy range as shown in part (b) at hν = 9.0 eV . The apparent shift of this peak from a final state energy of 8.2 to 8.1 eV upon cooling may be further evidence of the effect of a final density of states phenomena: this possibility will be discussed fully in Chapter VII.

The temperature dependent behavior of the quantum yield is also similar for AgCl and AgBr . As seen in Fig. 5.11, the AgCl yield develops a dip around 10.9 eV upon cooling which occurs gradually with decreasing temperature. This is not believed to be caused by the change in optical properties with temperature since, as is seen in Fig. 5.12, accounting for the reflectivity at room temperature[46] does not remove the small dip at this photon energy. From the logarithmic plot of the yield in Fig. 5.13, the reduction in hot electron scattering is seen to cause a significant increase in the yield from the silver substrate. There is also some increase in the absolute yield in the saturation region for AgCl . Based on examination of the EDCs in this energy region, this is probably due to the enhanced photoemission caused by the temperature dependent final density of states region around E = 8.1 eV rather than a transport related phenomenon.

In the photon energy range presented above, there are three EDC peaks which sharpen greatly upon cooling both AgBr and AgCl . As will be seen in Chapter VIII, the corresponding peaks in the two halides change energy with hν variation in the same manner. Thus, the important characteristics of the EDCs are interchangeable for the two halides. In studying the temperature dependence of these silver halide EDCs, the peak sharpening is clearly one of the most important features of the data. The peak strength variations cannot be fully analyzed because the temperature dependence of the reflectance is not known, and the peak positions appear to be relatively independent of temperature. Thus, it is reasonable to focus our attention on the temperature dependence of the width of the AgBr and AgCl EDC structure. The remainder of this chapter will, therefore, be devoted to theoretical calculations of the thermal broadening of the silver halide energy states and a comparison
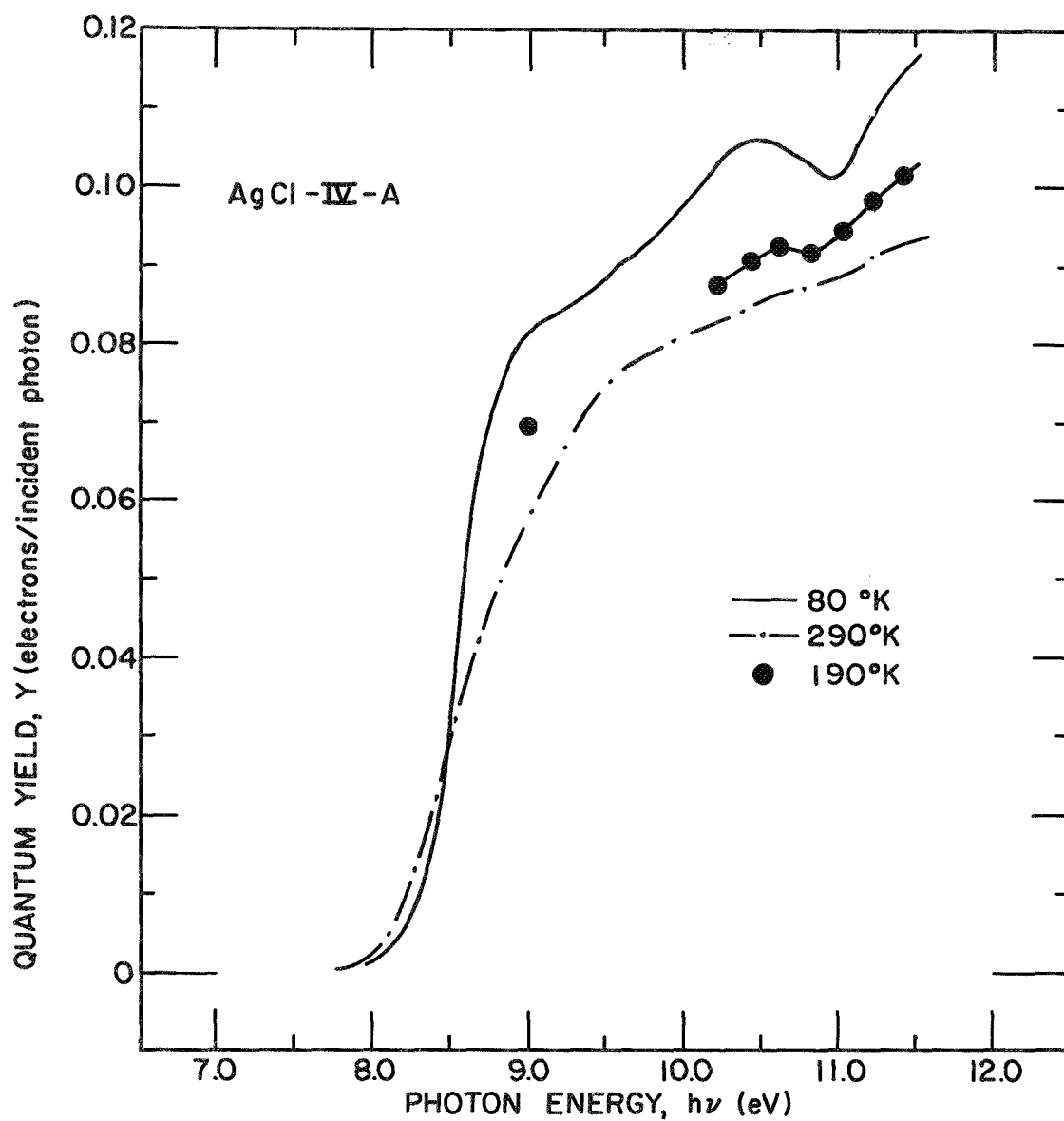
FIGURE 5.11. Comparison of the spectral distributions of the yield
of electrons photoemitted per incident photon from
AgCl at 80 through 290°K.

130
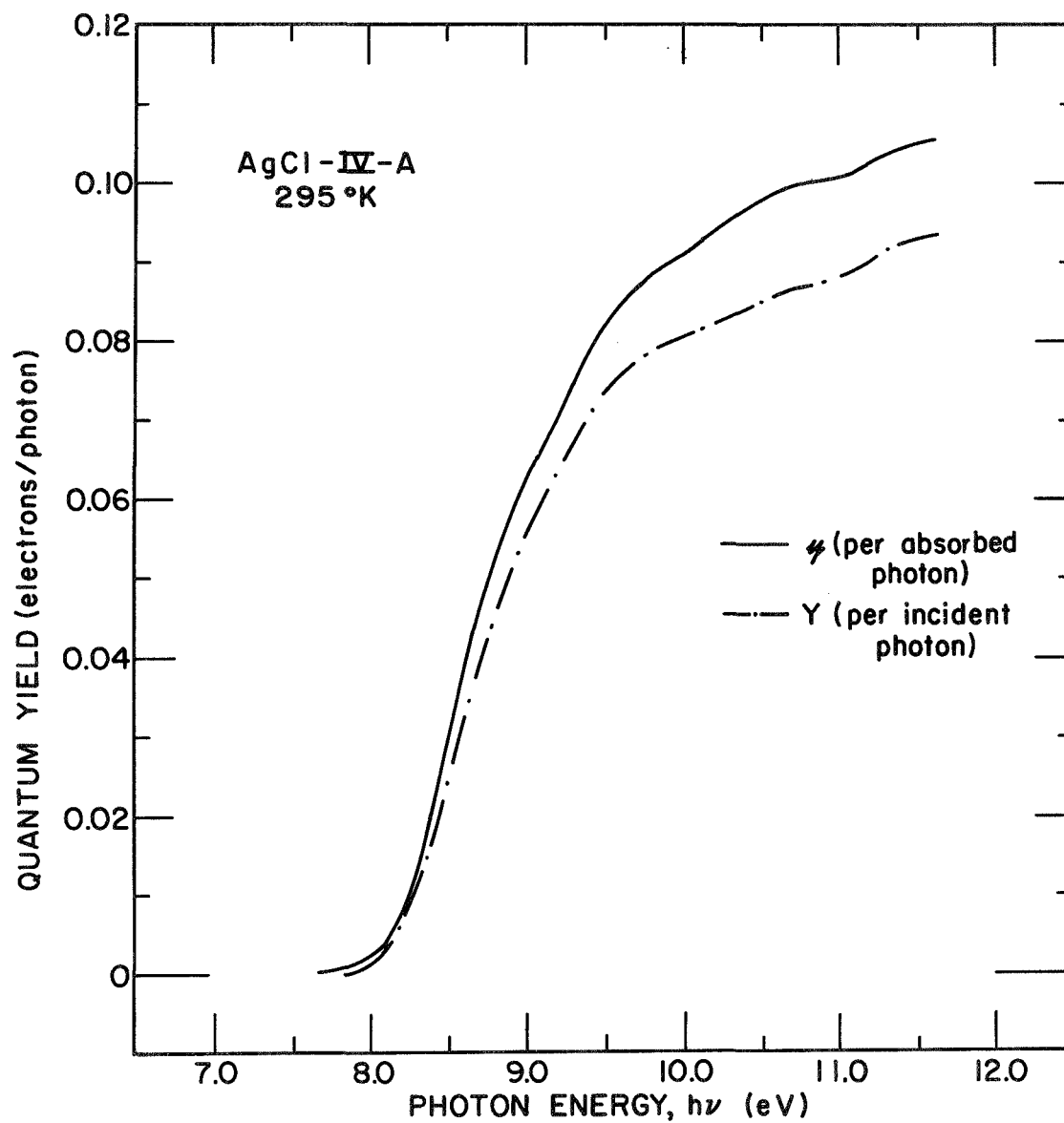
FIGURE 5.12. Comparison of the spectral distributions of
the yield of electrons photoemitted per incident
and absorbed photon from AgCl at 295°K.
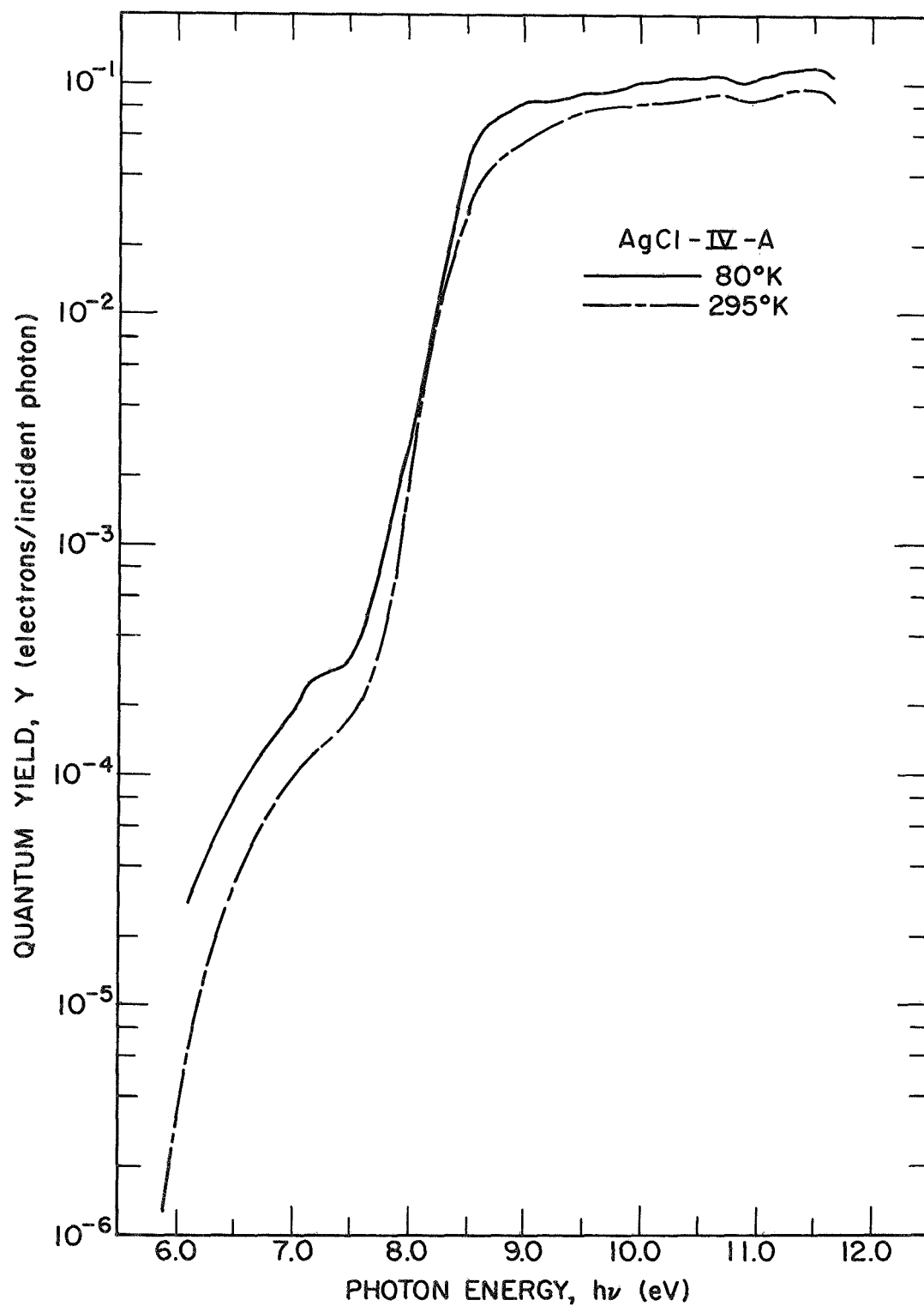
FIGURE 5.13. Comparison of the spectral distributions of the yield
of electrons photoemitted per incident photon from
AgCl at 80 and 295°K.

of these magnitudes to the experimental EDC widths. As will be seen, these computations suggest that dynamic hybridization of the halogen p and Ag 4d wavefunctions is responsible for the EDC broadenings and their temperature dependences.

B. Dynamic Hybridization Calculations in the Tight-Binding Approximation

In Chapter III we discussed the detailed calculation of the valence states of AgCl performed as part of this study, using the tight-binding formalism presented in Chapter II. These calculations showed that of all the terms which are combined to give the energy states in the solid [see Eq. (2.10)], the overlap terms $S_{k,n}$ and $U_{k,n}^{(2)}$, which depend on the p-d mixing, have a most profound influence on the silver halide energy states. Further, these same terms are probably the most dependent on temperature as discussed in Chapter II. We can then use these two hypotheses as a basis for calculating the temperature dependence of the states. The question is thus reduced to considering the effect of the dynamic motion of the lattice on the electron states via its modulation of these two tight-binding overlap terms.

The first part of such a calculation involves accurately accounting for the thermal vibrations of the ions. We have calculated the rms displacement of the ions as a function of temperature using the Debye-Waller theory.[8] From this theory, the mean square amplitude of vibration of each atom in a monatomic solid, with one atom per unit cell of mass m , is given by

$$u^2 = \frac{9\hbar^2 \, T^2}{mk_B \, \Theta_D} \left[\left(\frac{\Theta_D}{2T} \right)^2 + \int_0^{\Theta_D/T} \frac{X}{e^X - 1} \, dX \right] \tag{5.1}$$

The silver halides are, of course, diatomic with two atoms per unit cell, one of each constituent. It has been found that a good first approximation to the calculation of the vibrations of each ion is to assume an equal displacement for the two types of ions and further to assume only one atom per unit cell with a mass which is the mean of the

133

two constituents, $\bar{m}$.[105] Note that using the reduced mass yields a considerably poorer result for the mean square displacement in diatomic solids such as NaCl , InP , and GaP which were used as test cases for this calculation. Using the mean mass, Eq. (5.1) can be used directly to calculate the rms displacement, u , in the silver halides. It is a bit more illuminating to consider the limiting cases of this relation. As $T \to 0$, the second term in Eq. (5.1) becomes very small and the first dominates. Thus, the zero-point displacement of the ions is given by

$$u_0 = \frac{3}{2} \sqrt{\frac{\hbar^2}{\bar{m} k_B \Theta_D}} \quad , \quad T = 0 \qquad (5.2)$$

This is a constant depending only on the Debye temperature and mean mass of the solid. At temperatures above the Debye temperature, the second term dominates and its exponential can be approximated by a power series expansion. Using only the first two terms of this expansion, the integrand is unity and using Eq. (5.2), Eq. (5.1) becomes

$$u = 2u_0 \sqrt{\frac{T}{\Theta_D}} \quad , \quad T > \frac{\Theta_D}{2} \qquad (5.3)$$

It turns out that if the integral is calculated exactly with the first 4 terms in the power series expansion, the first term in Eq. (5.1) is balanced by a nearly equal but negative contribution from the second term thereby making Eq. (5.3) applicable down to around $\Theta_D/2$. Thus, the rms displacement goes as the square root of the temperature above a temperature about half the Debye value. Using Eqs. (5.2) and (5.3), the rms displacement as function of temperature up to 300°K is plotted in Fig. 5.14 for AgCl in part (a) and for AgBr in part (b). The contraction of the lattice constant, a , upon cooling from room temperature to 80°K as determined by Lawn,[28] is shown for each halide for comparison to the vibrational amplitudes. Note that the contraction of the nearest neighbor distance is half this amount. Following these calculations, the rms displacements for each ion in AgCl ,as determined from neutron diffraction measurements, was reported;[106] these are

134
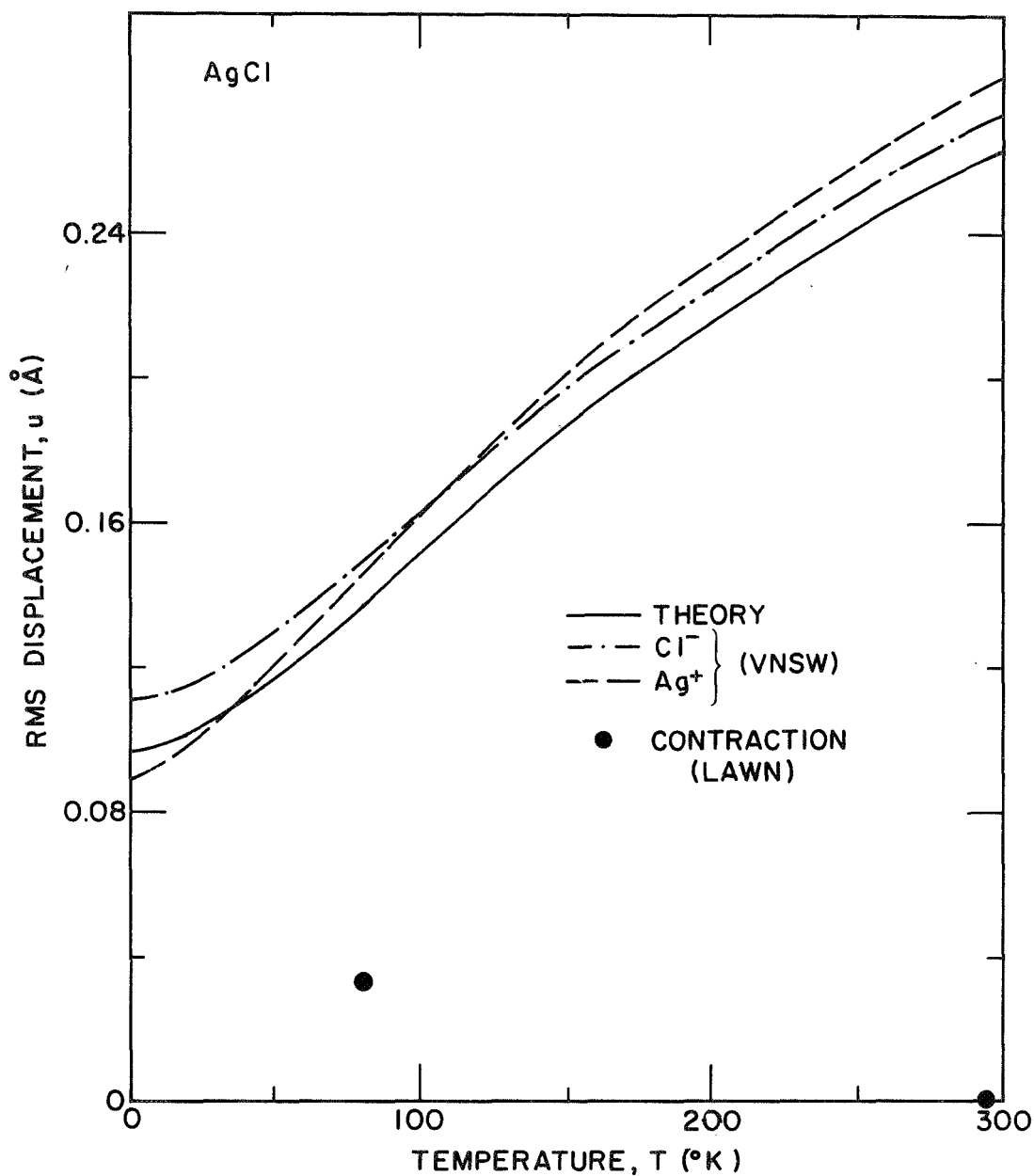
(a)

FIGURE 5.14(a) and (b).

Temperature dependence of the rms displacement of
(a) AgCl and (b) AgBr including the AgCl
measurements of Vijayaraghavan, Nicklow, Smith, and
Wilkinson (VNSW) in part (a) (reference 106). The
contraction of the lattice constant, a , from 295
to 80°K measured by Lawn (reference 28) is included
for comparison.
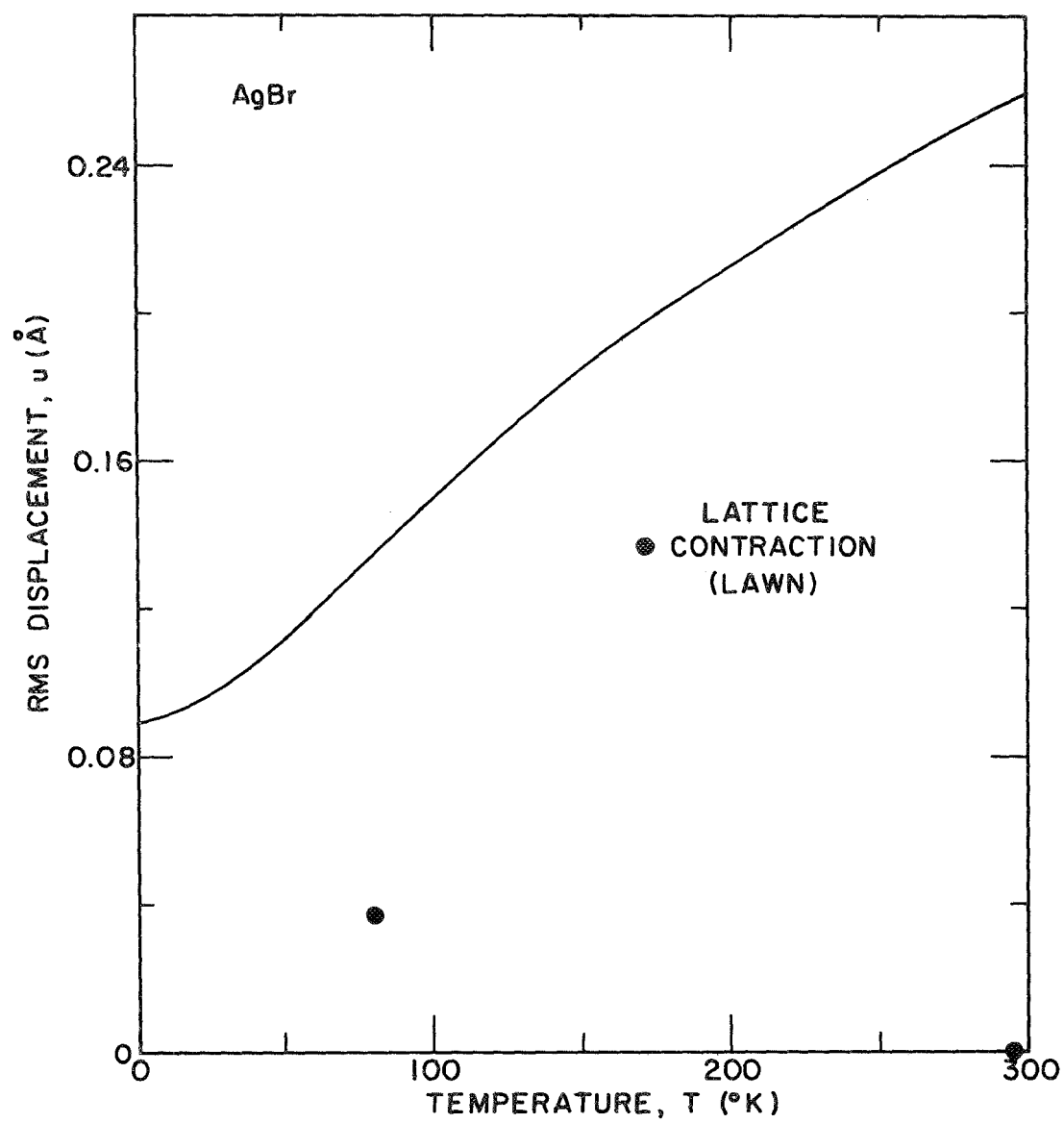
FIGURE 5.14(b)

plotted in Fig. 5.14(a) for comparison to our calculations. As can be seen, the two results are surprisingly close being within 10% and showing the same functional behavior. The important thing to note is that our computed displacements, which are to be used in the calculations discussed below, are at worst lower limits of the actual displacements and certainly are realistic estimates of the dynamic motion of the lattice.

The effect of this ionic motion on the electronic wavefunctions of the solid must now be considered. We will use a very simple approximation of restricting the extent of the interaction to about one nearest neighbor distance and assuming that possible averaging effects are negligible. Further, only the effect of $k = 0$ optical phonons will be considered. In Fig. 5.15, the normalized free atomic wavefunctions, Ψ_n, corresponding to the valence p and d states are drawn to scale for nearest neighbors in the silver halide lattice. These orbitals are taken from the Herman-Skillman tables[5] and represent the actual tight-binding orbitals for the states at Γ as will be made clear below. In the lower part of this figure the distances of interest are presented for comparison. As is seen, the rms displacement, u, of 0.26 Å at room temperature calculated from Eq. (5.3) for both $AgCl$ and $AgBr$, is about 10% of the nearest neighbor distance $a/2$. Further, this displacement is reduced in half when the solid is cooled from 295 to $80^{\circ}K$. Note that the contraction of the lattice upon cooling, $\Delta a/2$, reduces the inter-ionic spacing by about an order of magnitude less than the vibration of the ions. In the adiabatic approximation, the electronic wavefunctions rigidly follow the motion of the ions instantaneously. One can therefore consider the wavefunctions as being displaced relative to each other by the rms displacement of the ions. If the $Ag(4d^{10})$ orbital is held fixed and the halogen p wavefunction is displaced by the rms displacement at $295^{\circ}K$ (shown on the scale at the bottom of the figure), the new position of this orbital is shown by the dashed curves in Fig. 5.15. Since the region of overlap between these wavefunctions is of interest, it is significant to note that the change in the area common to both orbitals (shown shaded in the figure) changes
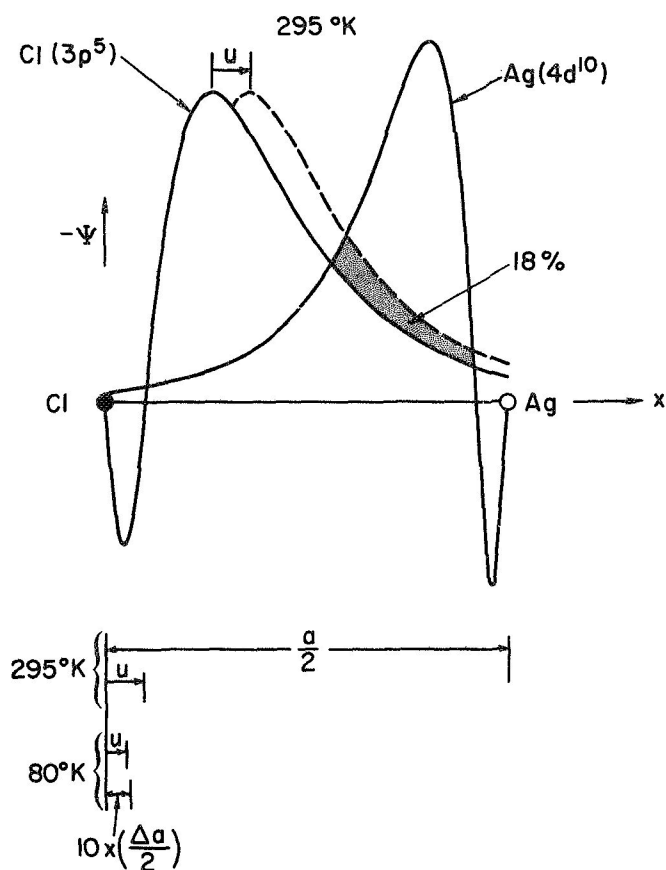
(a)

FIGURE 5.15(a) and (b)

The normalized free atomic orbitals from the Herman-Skillman tables (reference 5) corresponding to the valence p and d wavefunctions at Γ drawn to scale for nearest neighbors in the (a) AgCl and (b) AgBr lattices. The area common to the two orbitals is changed by the shaded region when the interatomic distance is decreased by the room temperature rms displacement. The rms displacements and contractions in nearest neighbor distance due to cooling from 295 to 80°K are shown in the bottom of each part of the figure.

138
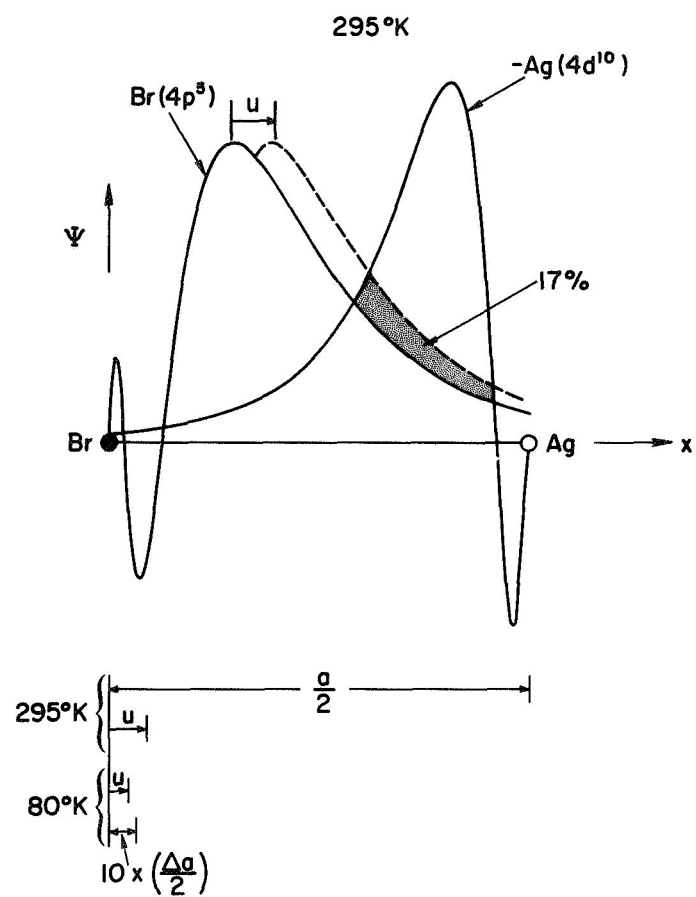
FIGURE 5.15(b)

by 18% in AgCl and 17% in AgBr due to the rms displacement of the ions. Of course, this is not the quantity of interest in determining the energy of the corresponding states. Rather, the product of these wavefunctions (i.e., $S_{k,n}^{(2)}$) and their product including the atomic potential, v (i.e., $U_{k,n}^{(2)}$) are of interest. The latter term is shown in Fig. 5.16 for the halogen p and $Ag(4d^{10})$ orbitals and

295°K

$\Psi_{Cl}^{*} (v_{Cl} + v_{Ag}) \Psi_{Ag}$

Cl ● ————————————— ○ Ag —→ x

$\Delta \int_{U}^{a/2} = 34\%$
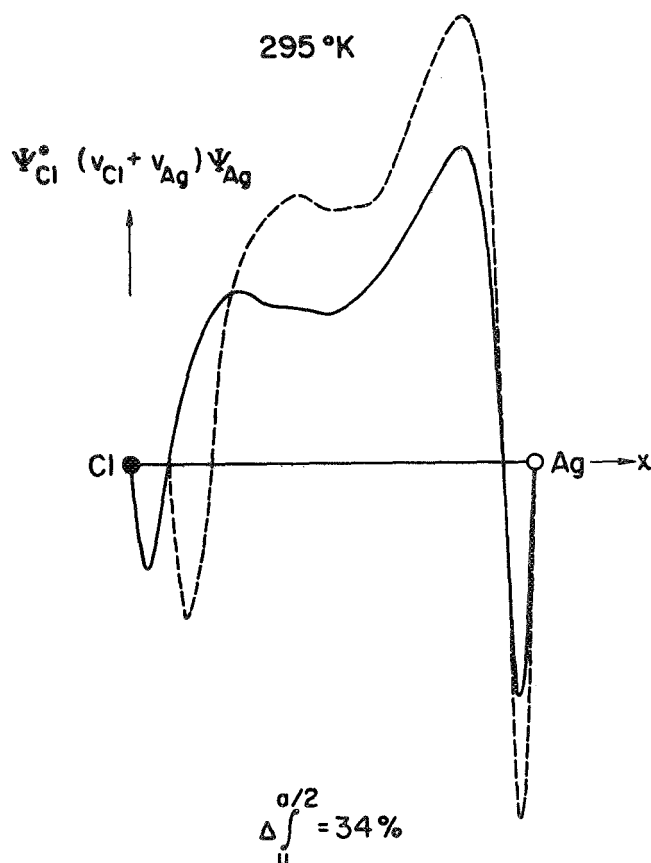
(a)

FIGURE 5.16(a) and (b)

    The overlap terms involving the halogen p and $Ag(4d^{10})$ atomic orbitals and potentials for nearest neighbors in the (a) AgCl and (b) AgBr lattices. These quantities are shown for the equilibrium interatomic separation (——) and for the nearest neighbor distance reduced by the room temperature rms atomic displacement (---) with the difference between the integrals of these quantities shown at the bottom of each part of the figure.
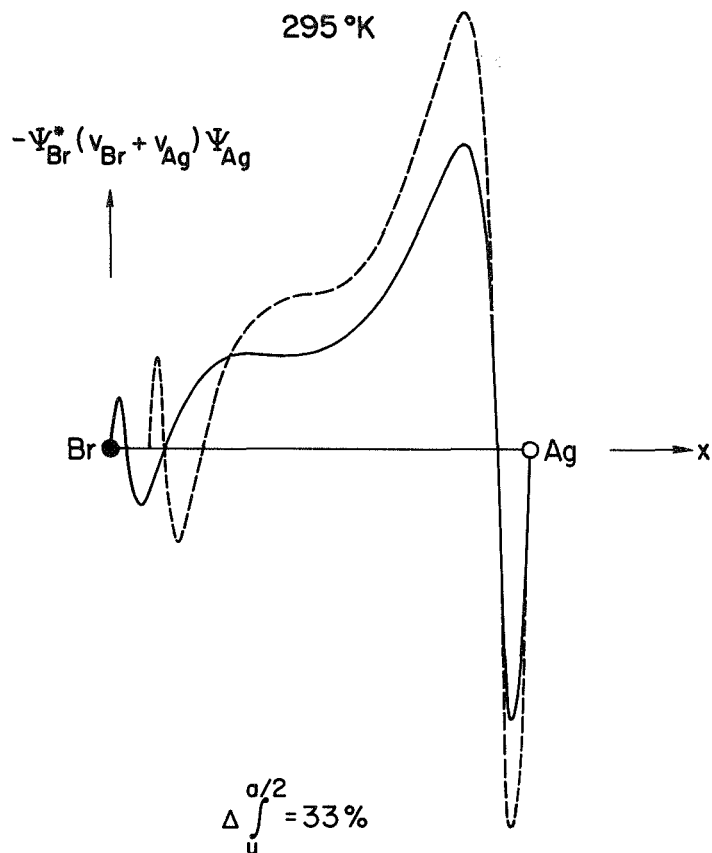
FIGURE 5.16(b)

atomic potentials from the Herman-Skillman tables.[5] It is interesting

to note that no explicit k dependent term has been included in forming

these products. However, since the k-dependence enters into the tight-

binding approximation via the Bloch sum of the orbitals [i.e., Eq. (2.2)],

the k-dependent term $e^{i\vec{k}\cdot\vec{r}_j}$ is just unity at Γ (i.e., at the center

of Brillouin zone where k = 0). Therefore, using unchanged atomic

wavefunctions and potentials is equivalent to carrying out the calcu-

lation at Γ . Again using the adiabatic approximation, we can dis-

place the halogen relative to the nearest neighbor Ag by the rms

displacement and recompute the overlap term; this is shown by the dashed

141

curves for the $295^{\circ}K$ ionic displacement. The energy contribution is simply the integral of this term which is equivalent to the area under the curves in Fig. 5.16. As indicated at the bottom of the figure, this overlap term changes by 34% in AgCl and 33% in AgBr due to the thermal vibrations of the lattice at room temperature. The term which does not involve the atomic potential (i.e., $S_{k,n}$) changes by 27% for AgCl and 26% for AgBr . These changes are quite significant and can be expected to cause a modulation of the energy states at Γ .

Of course, these estimates are only meant to roughly illustrate the physical process by which the energy states are broadened. These terms are not exact because the individual p and d orbitals must be considered and the atomic potential must be correctly screened to yield a meaningful calculation. The computation must be done using the 9 x 9 matrices discussed in Chapter III with the matrix elements of Table III.1 to obtain the contributions to the energy in Eq. (2.10). From calculations made with an unscreened Slater exchange potential in the course of the work of reference 3, Fowler estimates that each of the AgCl two-center integrals (i.e., the parameters like $pd\sigma$ in Table III.1) changes by an average of about 5% upon a 1% change in lattice constant.[107] As a zero order calculation, we will take the calculated rms displacement as an estimate of the maximum and minimum values for the lattice constant. This is the same as considering the vibration of one ion with all the others frozen in their equilibrium positions. It is actually a very conservative estimate since it is equivalent to changing the nearest neighbor spacing (which is half the lattice constant) by only <u>half</u> the rms displacement. We can take account of the ionic displacement by a lattice contraction or expansion since the overlap terms, which are basic to the modulation of the p-d mixing, are quite short range involving primarily nearest neighbors. The separation between these neighbors can be changed by either the thermal displacement of the ions or a change in the lattice constant. Thus, as far as the dynamic hybridization of the wavefunctions is concerned, a contraction or expansion of the lattice is roughly, to zero order, equivalent to the vibration of the ions. Using Fowler's estimate for the resulting effect on the matrix elements,[107]

the two-center $U_{k,n}^{(2)}$ and normalization $S_{k,n}$ contributions to the
energy can be recomputed. We thereby calculate a variation in energy
of the AgCl L_3' valence band maximum state of about 1.1 eV at room
temperature which sharpens to 0.6 eV upon cooling to $80°$K. Though this
p-derived state is not directly related to any measured EDC structure,
its energy provides an order of magnitude estimate for the experimental
broadenings since its large hybridization (i.e., 30% d character[3]
makes it particularly sensitive to ionic separation. The absolute error
in these calculations can be estimated by recalling from Chapter III
that the effects of the lattice vibration on the absorption are "frozen
out" by $4.2°$K. Thus, one would expect any energy broadening calculated
using the zero-point rms displacement of the ions to be erroneous. We
calculate an AgCl L_3' broadening of 0.3 eV at $0°$K. Thus, the corrected
room temperature broadening is 0.8 eV with a sharpening of 0.5 eV upon
cooling to $80°$K. Our simple calculation thus indicates that the lat-
tice vibrational modulation of the overlap produces fluctuations in
the energies of the hybridized states which is of the same magnitude as
the observed broadening of the photoemission EDCs (e.g., 0.6 eV for
AgBr at $295°$K, $h\nu$ = 10.2 eV , seen in Fig. 5.2). These rough calcula-
tions further indicate that the changes of these energy variations upon
temperature reduction are of the same order of magnitude as the measured
EDC temperature dependences (e.g., 0.3 eV for AgBr at $295°$K, $h\nu$ =
10.2 eV , seen in Fig. 5.2). In addition, since the broadening depends
on the amplitude of the ionic vibration, the gradual dependence on
temperature seen in our experiments (Figs. 5.3 and 5.10) is to be
expected. The complete numerical results of these calculations and a
comparison of them to experiment are presented in Tables V.1 and V.2,
respectively, at the end of the next section.

It should be emphasized that these calculations only considered the
dynamic modulation of the overlap contributions to the energy, $S_{k,n}$
and $U_{k,n}^{(2)}$. It has been calculated by Fowler that the Madelung energy,
$E_n^{(M)}$, changes by at least as much as these two terms for a given change
in lattice constant.[27] However, the assumption that the vibrations of
the ions are equivalent to a lattice constant change, is a very poor

approximation for the Madelung energy since it is a long range term. It is formed by taking the sum over many unit cells; when many cells are included in the sum, the dynamic variations of the ions will tend to average to zero. As pointed out above, the overlap terms, on the other hand, are very short range involving primarily nearest neighbors and thus depending quite strongly on local variations in ion position. One can thus assume, to first order, that the dynamic variations of the Madelung term are negligible compared to those of the overlap contributions.

C. Dynamic Hybridization Calculations Using the Pressure Dependence of the Absorption

The dynamic broadening of the energy states can be estimated in another way. The temperature dependent EDC broadening is caused by dynamic variations in the inter-ionic spacing. One can obtain static variations in the same spacing by applying hydrostatic pressure to the solid. Thereby, the dependence of the electronic energy levels on equilibrium ionic separation can be experimentally determined. We can, in fact, use the measurements of Aust for the quasihydrostatic pressure dependence of the direct and indirect absorption edges at $295°K$,[4] to determine the dependence of the valence band maximum energy, E_v, on ionic position for AgBr and AgCl . From this the dynamic broadening effects due to the rms displacement of the ions at elevated temperature can be estimated.

Aust measured the pressure induced shift in the direct exciton absorption, ΔE_{EX}, and found it to be the same for both AgCl and AgBr .[4] In an effort to determine the functional form of its dependence on fractional volume change $\Delta V/V_0$, it was found that the data plotted linearly on a log-log scale as shown in Fig. 5.17. This implies that the exciton shift is related to the volume change by a power law of the form

$$\Delta E_{EX} = \Delta E_{EX}^0 \left(\frac{- \Delta V}{V_0} \right)^{0.77} \tag{5.4}$$
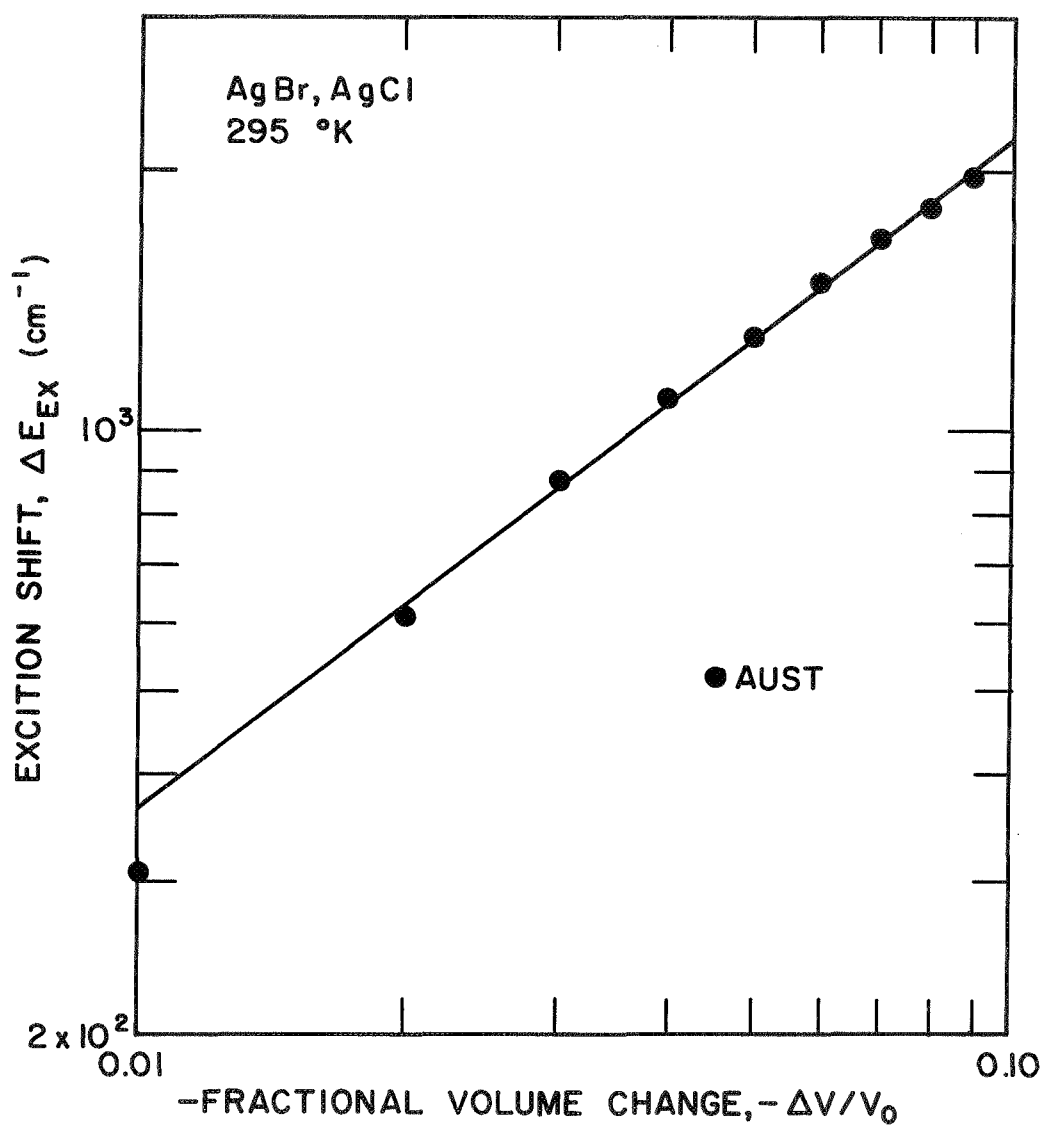
FIGURE 5.17. Pressure dependence of the direct exciton absorption of AgBr and AgCl at 295°K from the work of Aust (reference 4).

as determined by the slope of the linear fit to the data shown in this figure. Aust determined that the energy of the highest valence state at Γ (i.e., Γ_{15}), which is the initial state of this excitonic transition, is unaffected by pressures up to the 50 Kbar limit of his experiment. Thus, the pressure-induced exciton shift is due entirely to the shift of the conduction band minimum, Γ_1 ; the pressure dependence of Γ_1 is thus given directly by Eq. (5.4). This conduction band state is just the final state for the indirect transition from the valence band maximum at L . Further, the shift of the indirect edge is only 10 to 15% as large as the direct exciton but in the opposite direction.[4] Therefore, it can be concluded that the shift of the valence band maximum is in the same direction as and slightly greater than the shift of Γ_1 . Thus, Eq. (5.4) is also the general form for the pressure dependence of the energy of the valence band maximum, E_v , to within 10 to 15%. Using the E_v shifts measured at 8.5% volume decrease by Aust,[4] the zero pressure constants in Eq. (5.4) can be determined for both AgCl and AgBr . We then have the experimentally deduced valence band maximum dependence of

$$\Delta E_v = \left(\frac{-\Delta V}{V_0}\right)^{0.77} \times \begin{cases} 1.86 \text{ eV} & , \quad \text{AgCl} \\ 1.72 \text{ eV} & , \quad \text{AgBr} \end{cases} \tag{5.5}$$

If we assume, as in section B, that in the dynamic hybridization model, the rms displacement, u , is roughly equivalent to an equal change in lattice constant, the fractional volume change is just

$$-\frac{\Delta V}{V_0} = \left(\frac{u}{a}\right)^3 + 3\left(\frac{u}{a}\right)^2 + 3\left(\frac{u}{a}\right) \tag{5.6}$$

Using the temperature dependence of the rms displacement given in Eq. (5.3), a total energy variation of the valence band maximum at room temperature of about 0.8 eV in AgCl and 0.7 eV in AgBr is deduced using Eqs. (5.6) and (5.5). This broadening is comparable to both the calculated and experimental values presented in the first two sections.

Consistent with our other findings, it is reduced by 0.3 eV for both halides upon cooling to $80°K$. It should be noted that the broadening calculated for the zero-point motion of the AgCl and AgBr lattices are not reasonable estimates for the error of these calculations. This is because Eq. (5.5) will grossly overestimate the broadening for small volume changes as is clear from the deviation of the data from the linear fit in Fig. 5.17.

In Table V.1, the results are summarized for the dynamic hybridization calculations of the total energy variation of the hybridized halogen p-derived valence band maximum (i.e., ΔE_v) using both the tight-binding approximation (i.e., BANDS) and the pressure dependence of the optical absorption (i.e., α). This table includes the uncorrected

TABLE V.1. Values calculated for the temperature dependences of the rms displacement ("u") and total broadening of the valence band maximum ("ΔE_v") of AgCl and AgBr . The latter was computed using both the tight-binding, AgCl electronic energy bands ("BANDS") and the pressure dependence of the optical absorption ("α").

T (°K)	u (Å)	AgCl ΔE_v (eV) BANDS	AgCl ΔE_v (eV) α	AgBr u (Å)	AgBr ΔE_v (eV) α
295	0.26	1.13	0.82	0.26	0.73
272	0.25	1.08	0.80	0.25	0.71
245	0.24	1.03	0.77	0.23	0.68
217	0.22	0.97	0.73	0.22	0.64
190	0.21	0.90	0.70	0.21	0.62
162	0.19	0.83	0.66	0.19	0.58
135	0.18	0.76	0.61	0.17	0.54
107	0.16	0.68	0.56	0.15	0.50
80	0.14	0.59	0.50	0.13	0.44
0	0.10	0.31		0.09	

calculations not only at room and liquid nitrogen temperatures, but also the changes which occur upon cooling between these values. The rms displacements are calculated using Eqs. (5.2) and (5.3) with $\bar{m}$ = 71.7 amu and 93.9 amu and Θ_D = 162°K and 144°K for AgCl and AgBr respectively. Since both a positive and negative displacement of the ions from equilibrium must be considered, the energy changes represent this total broadening. The broadenings are calculated from the tight-binding AgCl bands as described in section B and from the pressure dependent absorption Eqs. (5.5) and (5.6) above. The energy entries include more digits than are significant; however, they are included to show the functional dependence of the energy from 80 to 295°K. These calculations are compared to the experimental full widths of the EDC peaks at 90% of their maximum height in Table V.2. The tight-bidning entries have been

TABLE V.2. Comparison of the temperature dependences of the 90% EDC width and the computed broadening of the valence band maximum ("ΔE_v") of AgCl and AgBr . The calculations used both the tight-binding bands ("BANDS") and the pressure dependence of the absorption ("α") for both the rms displacement ("u") and the contraction of the lattice (Δa) upon cooling from room to LN$_2$ temperature.

	T (°K)	90% EDC WIDTH[†] (eV)	u (Å)	ΔE_v (eV)		a* (Å)	ΔE_v (eV)	
				BANDS	α		BANDS	α
AgCl	295	0.5	0.26	0.8	0.8	5.550	0	0
	80	0.3	0.14	0.3	0.5	5.517	< 0.1	< 0.1
	295 → 80	0.2	0.12	0.5	0.3	0.033	< 0.1	< 0.1
AgBr	295	0.6	0.26		0.7	5.774		0
	80	0.3	0.13		0.4	5.737		< 0.1
	295 → 80	0.3	0.13		0.3	0.037		< 0.1

[†]AgCl: IV-A, $h\nu$ = 11.6 eV, -2.65 eV peak (2 × right half-width) (Fig. 6.3).

AgBr: IV-A, $h\nu$ = 10.2 eV, direct peak (Fig. 5.18).

*Reference 28.

148

corrected for the computed broadening at $T = 0^{\circ}K$ in accordance with the discussion in section B. The calculated broadenings can be compared to these measured 90% widths since they are a sort of "half-width" energy having been computed using the rms rather than the amplitude of the ionic displacement from equilibrium. On the right side of this table, calculations to determine the effect of the lattice contraction are presented. As can be seen, the contraction produces shifts of less than 0.1 eV upon cooling from 295 to $80^{\circ}K$ and, of course, no change in broadening. The calculations using the rms ionic displacement, on the other hand, are always of the same order of magnitude as and are as large or larger than the observed quantities. It is thus the changing amplitude of vibration of the ions which causes the temperature dependent broadening rather than the lattice contraction. It is clear from Table V.2 that the predictions of our dynamic hybridization model for the magnitudes of both the dynamic broadenings and the changes upon cooling of these broadenings are quite comparable to the corresponding EDC magnitudes when computed either from purely theoretical considerations or by extension of other experimental results.

One of the significant conclusions we can make from the success of this dynamic hybridization model is that all the structure in the EDCs which exhibits a large dependence on temperature must correspond to electronic states which are highly hybridized. Since all the AgCl and AgBr EDC structure examined in section A is temperature dependent, the upper filled states in these solids are formed from hybridized mixtures of halogen p and silver 4d orbitals. These states are clearly p-derived since the p states are increased in energy while the d's are reduced upon mixing the two species.[3] This is quite significant since it is the first direct experimental measurement of the halogen p state origin of the valence band maximum.

The EDC broadenings we have discussed are many times greater than the thermal energy, $k_B T$, and there may be some question as to how this can occur. The principle which governs such considerations is that the maximum energy which can be transferred to the electronic states is the energy in the vibrating lattice. The important thing is that this

is true for all the states in the solid taken together. When a p-derived
state is increased in energy due to the ionic motion, the net energy of
the d-derived states with which it mixes will decrease by nearly the same
amount. Thus, the individual hybridized states may be shifted by a much
greater amount than $k_B T$. This occurrence for the hybridization of
electronic states is equivalent to the more familiar crystal field
splitting case where the average energy of the split levels is equal to
the energy of the unperturbed state when the degeneracy of the levels is
taken into account.

D. Functional Dependence of the EDC Broadening

The discussion in this chapter has emphasized the mechanism pro-
ducing the EDC broadening which is more than an order of magnitude
greater than $k_B T$. In order to study the detailed dependence of this
broadening on temperature, the peak width at 90% of the maximum height,
W , must be closely examined. This width is shown on the 10.2 eV
AgBr EDCs in Fig. 5.18. The very interesting experimental observation
is that these widths plot linearly against temperature on a semi-
logarithmic scale as shown in Fig. 5.19. This means that the 90% width,
W , depends exponentially on temperature, T :

$$W = W_0 \exp[C(T/\Theta_D)] \tag{5.7}$$

where $C = 0.47$ for the data of Fig. 5.18. Unfortunately, there are
very few EDC peaks which have 90% widths characteristic of only one
piece of structure over the range of temperature variation. In fact,
the right end of the 285°K width in Fig. 5.18 is nearly measuring the
influence of the neighboring shoulder. Of the peak widths that can be
measured at 90% of the height, this exponential dependence [Eq. (5.7)]
occurs for a number of peaks in both AgCl and AgBr ; their constants
W_0 and C are summarized in Table V.3. The EDC peaks whose 90% widths
were measured are identified by their origin in the density of valence
states (i.e., -3.7 and -2.65 eV) or by the nature of the optical excita-
tion process (i.e., direct transition - "D") if the peak does not

FIGURE 5.18. Comparison of energy distributions normalized to quantum yield (per incident photon) for electrons photoemitted from AgBr at 80 through 285°K for a photon energy of 10.2 eV. The width of the center "direct" transition peak at 90% of its maximum height is shown in each curve.
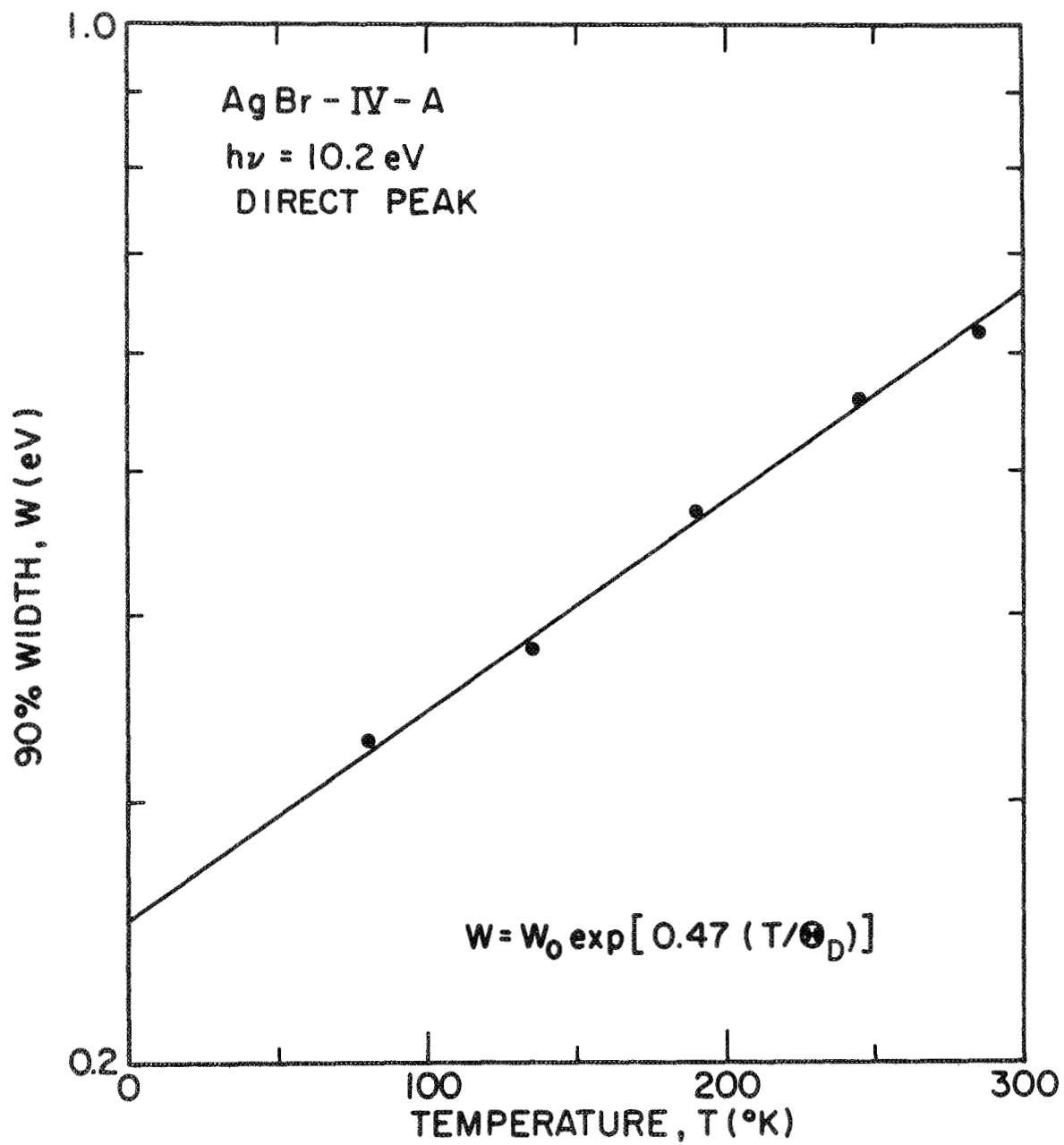
FIG. 5.19.   Temperature dependence of the AgBr , 10.2 eV 90% EDC
             width presented in Fig. 5.18.

TABLE V.3. Parameters which define the exponential temperature dependence of the AgBr and AgCl 90% EDC peak widths, W , given by Eq. (5.7): W_0 is the frozen lattice, EDC width and C is a measure of the temperature dependence.

	EDC PEAK[*]	hν (eV)	W_0 (eV)	C
AgBr (IV-A)	-3.7	11.8	0.24	0.13
	-3.7	11.4	0.25	0.12
	D	10.8	0.32	0.33
	D	10.2	0.25	0.47
	D(ℓ)	9.7	0.15	0.27
	D(ℓ)	9.2	0.14	0.32
AgCl (IV-A)	-2.65(r)	11.8	0.14	0.35
	-2.65(r)	11.6	0.11	0.47
	-2.65(r)	11.2	0.13	0.28
	-2.65	11.0	0.31	0.28
	-2.65[†]	10.8	0.15	0.43

[*]D = Direct

ℓ = Left Half-Width

r = Right Half-Width

[†]E = 8.1 eV

originate from one initial state energy for all photon energies; these identifications are discussed in detail in Chapter VIII (see Figs. 8.1 and 8.3). In some cases, only the half-width could be measured over the large temperature range, and these are indicated by an "ℓ" or "r" for left or right half-width. The W_0 is a measure of the EDC width at $T = 0°K$ if there were no significant zero-point vibration, while the slope, C , is a measure of the dependence of the width on temperature. It is quite important to note that the average parameters for the halogen p-derived structure are nearly identical for AgBr and AgCl . For the AgBr "D" structure, W_0(full) = 0.29 eV and C = 0.35

while for the AgCl "-2.65" eV structure, W_0(full) = 0.27 eV and C = 0.34 ; the $h\nu$ = 10.8 eV AgCl data is neglected because it is effected by the E = 8.1 eV final state region as will be discussed in Chapter VII. These nearly equal temperature dependences for AgBr and AgCl (C $\cong$ 1/3) emphasize the similarities between the data for the two halides and may be indicative of a fundamental constant describing this effect. The -3.7 eV AgBr structure will be discussed in the next chapter.

This observed dependence on temperature is quite significant. Doniach has taken a Green's function approach to explaining the dynamic hybridization.[108] This theory, which takes into account random variations in tight-binding overlaps induced by the ionic motion, predicts that to first order, the dependence of the width of density of states structure, w , on temperature should be of the form,[108]

$$w = w_0 \exp[C'(T/\Theta_D)] \qquad (5.8)$$

This is precisely the form [Eq. (5.7)] we deduced from experiment for the EDC width dependence. If C' in Eq. (5.8) should be a constant, then the deviation of C , in Eq. (5.7), from C' may be a quantitative measure of the amount of hybridization of the electronic states corresponding to the particular EDC peak. This prediction of Eq. (5.8) by Doniach's theory gives further credence to the dynamic hybridization model for the temperature dependence of silver halide photoemission.

VI. THE "PURE" Ag 4d ELECTRONIC VALENCE STATES OF
AgBr AND AgCl

The large hybridization of the halogen p states with the silver 4d states has been the object of our discussion thus far. It is this mixing which creates the complex valence electronic structure (Chapter III) and causes the very large temperature dependence of the EDC structure (Chapter V). There are also a large number of Ag 4d states whose wavefunctions are highly localized on the silver sites and do not significantly mix with the neighboring halogen orbitals.[109] Our temperature dependent photoemission EDCs offer a unique method for unambiguously measuring these "pure" states. Since the energy of such "pure" states does not depend on wavefunction overlap, one expects from the dynamic hybridization model that the energy of these states will not be greatly affected by the vibrations of the lattice. Hence the photoemission from these states will exhibit a much smaller temperature dependence than for the hybridized states. Therefore, structure which exhibits virtually no change upon cooling probably corresponds to the Ag states with almost pure 4d symmetry. In this chapter, we will examine the EDCs of AgBr and AgCl for such structure. To test this hypothesis, the LiF window was removed from the chamber so the entire AgBr valence band could be probed at room temperature. The results of these studies are discussed in part B of the chapter.

It is important to realize at the outset that there are, of course, hybridized silver states which would be expected to exhibit a temperature dependence. As was pointed out in the last chapter, the energy of the silver states are decreased when they mix with the halogen p's . This means that they should occur deeper in the valence band than the "pure" silver states. As will be seen in the data presented in section A, the threshold in both halides is such that at 11.8 eV we can only probe a few tenths of an eV below these pure states and therefore were unable to observe the temperature dependence of the hybridized d states.

155

A. Temperature Independent EDC Structure

In the representative EDCs presented in Fig. 6.1 for AgBr , it
is seen that only certain transitions sharpen drastically upon cooling
the sample. The structure which emerges on the trailing side of the
11.0 eV EDC from -3.7 eV in the valence states shows no significant
change upon temperature variation. This is in marked contrast to the
tremendous sharpening of the next highest peak when it was near thresh-
old at 10.2 eV (see Fig. 5.2). Note that this structure in Fig. 6.1
neither sharpens nor does its peak-to-valley ratio increase when the
sample is cooled to 80°K. This is the exact converse of that which was
observed for all the AgBr structure below 10.6 eV (see Chapter V).
This near constancy with temperature variation of the -3.7 eV peak is
especially evident when the intermediate temperatures are included in
Fig. 6.2. Note that this data was measured for a different sample from
the one used for Fig. 6.1; this again emphasizes the reproducibility of
the silver halide photoemission. In part (a) of the figure, the tempera-
ture independence of the trailing peak at 11.4 eV is particularly strik-
ing. It is even more significant when one realizes that each EDC was
independently normalized and the energy scales were chosen independently
for each set of EDCs at a fixed temperature. In part (b) of the figure
the changes in the hybridized p-derived EDC structure is shown for
comparison at 10.8 eV. At the limit of the measurement, $h\nu = 11.8$ eV ,
the trailing -3.7 eV peak, which was discussed in Fig. 6.2(a) at 11.4 eV,
is still temperature independent compared to the other structure. This
is not only evident from visual inspection of the EDC data but also from
numerical analysis of the data characteristics. The slight dependence
of the peak's width on temperature was found to fit the exponential
relation of Eq. (5.7) with characteristic parameters W_0 and C inclu-
ded in Table V.3. The important thing to note is that even though the
zero width, W_0 , of 0.24 eV is comparable to the 0.28 eV average value
found for the hybridized p-derived EDC structure for both AgBr ("D")
and AgCl ("-2.65"), the temperature dependence, C , of 0.12 for the
-3.7 eV peak is considerably less than the $\approx 1/3$ average value found

FIGURE 6.1. Comparison of energy distributions normalized to quantum yield (per incident photon) for electrons photoemitted from AgBr at 80 and 295°K for photon energies of 10.8 through 11.8 eV.

157
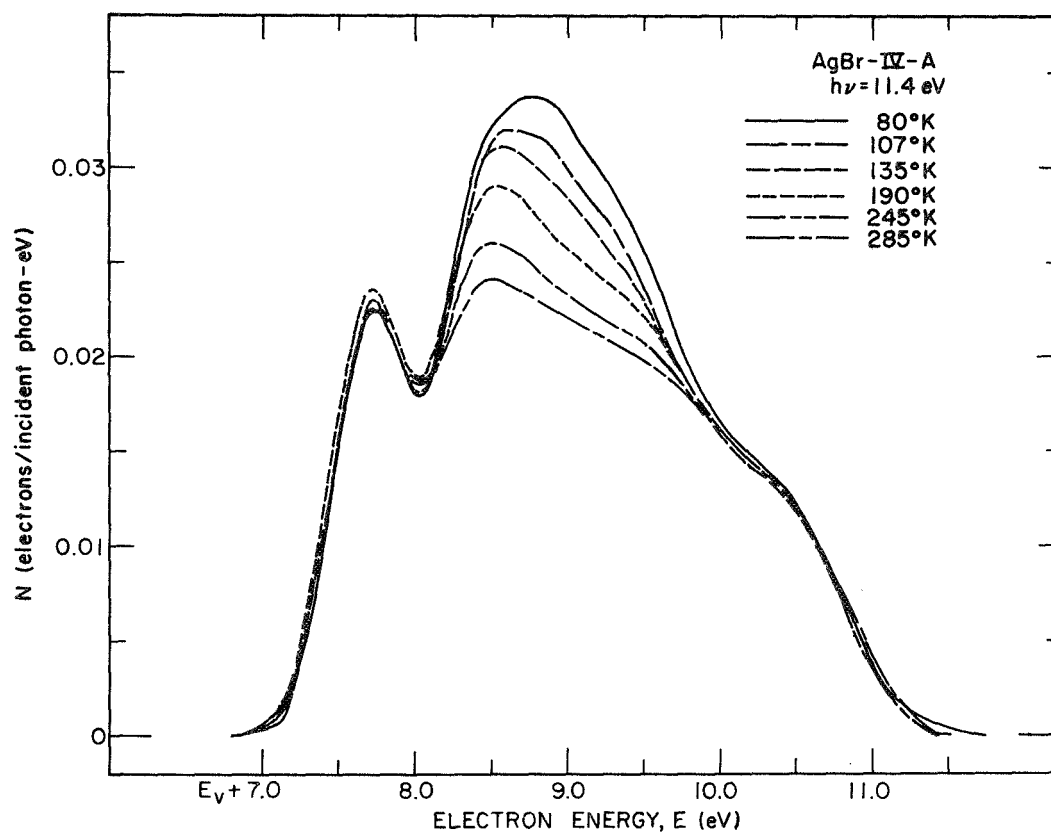
FIGURE 6.2(a). Comparison of energy distributions normalized to
quantum yield (per incident photon) for electrons
photoemitted from AgBr at 80 through 285°K for a
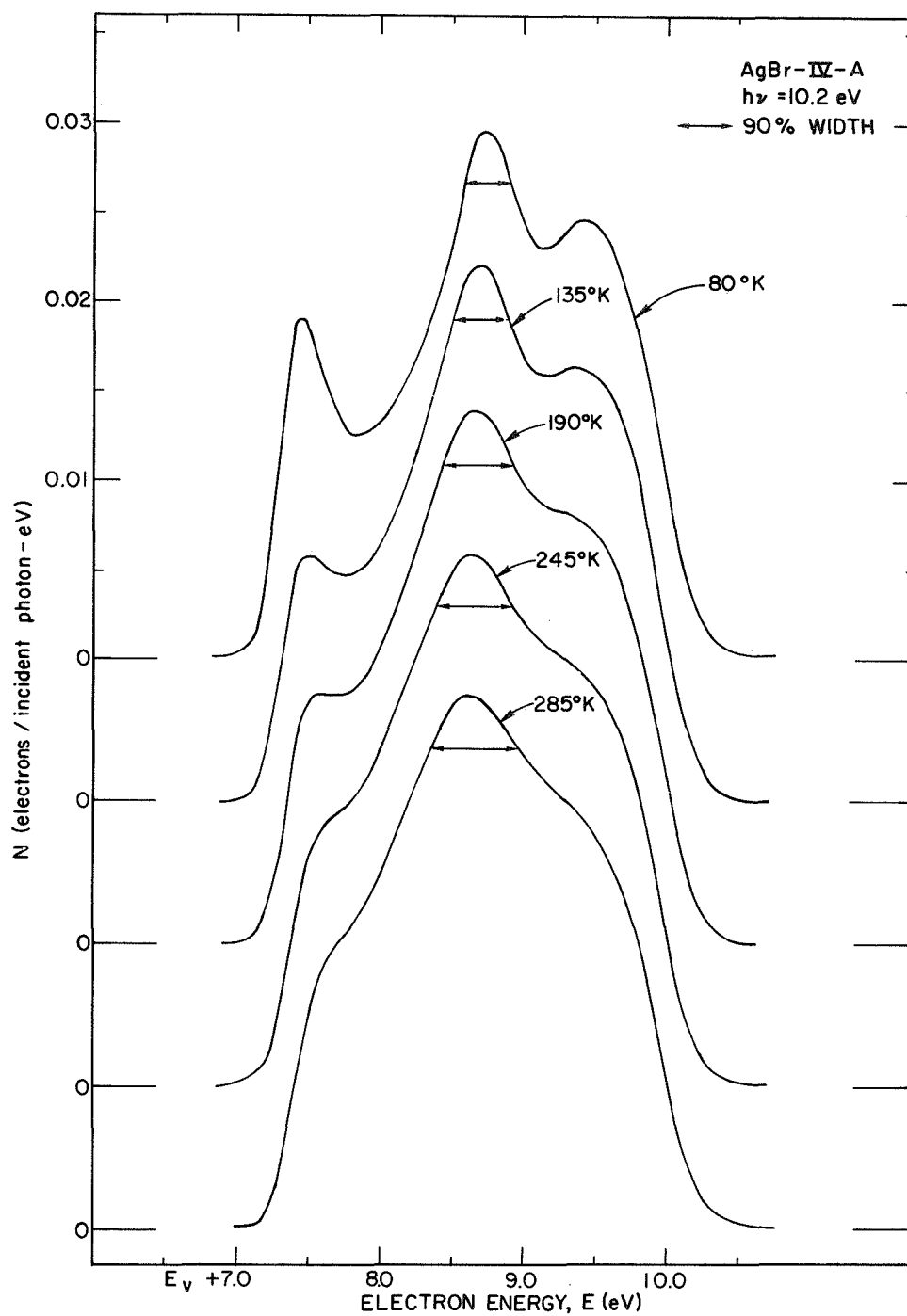photon energy of 11.4 eV.
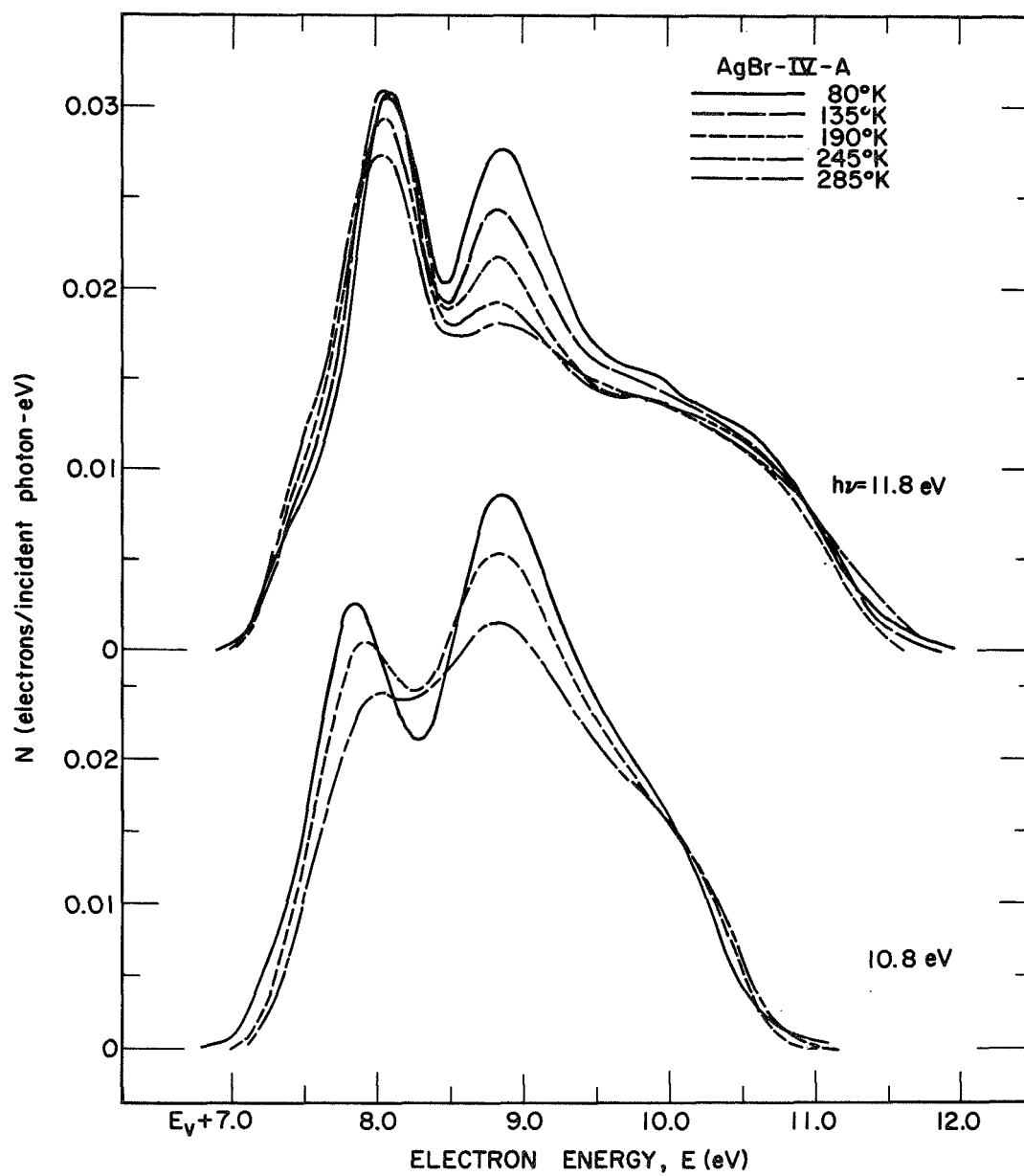
FIGURE 6.2(b). Comparison of energy distributions normalized
to quantum yield (per incident photon) for
electrons photoemitted from AgBr at 80 through
285°K for photon energies of 10.8 and 11.8 eV.

159

for the p-derived structure. If it is further realized that this 0.12 value is only about a factor of two greater than the precision with which the width can be measured, it is reasonable to conclude that the temperature dependence of the -3.7 eV AgBr peak is characteristically different from that measured for the hybridized p-derived structure.

It is interesting to note that since the width and peak-to-valley ratios are relatively unaffected by temperature variation, there is reason to expect that the heights should be nearly constant when the reflectivity of the sample is corrected for. Since the heights of this peak are already constant with temperature without taking the optical properties into account for both samples shown, one can conclude that the AgBr reflectance is relatively temperature independent from 11.0 eV to 12.0 eV. The lack of sharp structure in all EDCs above a find state energy of $E \approx 9.5$ eV and the temperature independence of this structure is probably due to a different effect and will be discussed fully in the next chapter.

From the similarity of the AgCl and AgBr EDCs, a peak in the AgCl valence band density of states can be identified as being relatively temperature independent. The corresponding peaks in the AgCl EDC data occur for electrons excited from -3.3 eV in the valence states, though their temperature independence is somewhat difficult to observe because of final state effects. This peak emerges on the trailing side of the 11.1 eV EDC as seen in the high photon energy curves of Fig. 6.3. This difficulty in observing its temperature independence occurs because of the enhancement of all the structure on the low energy side of the EDCs. As was pointed out in the last chapter, there appears to be a temperature dependent high final density of state region around 8.1 eV which causes all structure at this energy to be enhanced at $80^{\circ}K$. This is better illustrated when the intermediate temperature data is included in Fig. 6.4. The important thing to note in this data is the behavior of the EDC structure when it moves to energies above $E = 8.1$ eV . The second peak in these EDCs ("-2.65" in Table V.3) sharpens and is increased in height by about the same amount at both $E = 8.8$ eV and 9.2 eV (i.e., $hV = 11.4$ eV and 11.8 eV, respectively). By contrast, the

FIGURE 6.3. Comparison of energy distributions normalized to quantum yield (per incident photon) for electrons photoemitted from AgCl at 80 and 295°K for photon energies of 11.1 through 11.8 eV.

161

FIGURE 6.4. Comparison of energy distributions normalized to quantum yield (per incident photon) for electrons photoemitted from AgCl at 80 through 290°K for photon energies of 11.4 and 11.8 eV.

trailing -3.3 eV peak height increases from 290 to 80°K by more than
either of these when $E = 8.1$ eV (i.e., $h\nu = 11.4$ eV) but is enhanced
noticeably less when its final state energy is 8.5 eV (i.e., $h\nu = 11.8$ eV).
Thus, when the effects around $E = 8.1$ eV are taken into account, the
trailing EDC structure photoexcited from -3.3 eV in the valence band
appears to be more independent of temperature than the peak excited from
-2.6 eV. This is true for both the widths and peak-to-valley ratios of
these peaks. To perhaps show this more clearly, the heights of the
-3.3 eV peaks at 80°K are adjusted to be equal to the corresponding
heights at 295°K in Fig. 6.5. As can be seen in these EDCs, the widths
and peak-to-valley ratios are much more temperature independent for the
trailing peak than the neighboring one. Note that any changes which may
occur in this -3.3 eV peak upon cooling happens on its right side where
the temperature changes of the neighboring peak will influence its shape.
The temperature independence of the width and peak-to-valley ratio of
this -3.3 eV EDC structure is most similar to the -3.7 eV structure in
the AgBr data. It is thus reasonable to conclude that both of these
valence band density of states regions have similar characteristics and
origins.

From the above discussion it is evident that there is a peak in the
EDCs of both AgBr (i.e., -3.7 eV) and AgCl (i.e., -3.3 eV) which
exhibits a substantially smaller dependence on temperature than the three
higher energy pieces of structure identified with the halogen p-derived
valence states in the last chapter. In order to determine the origin of
these new peaks, it is helpful to make use of published estimates of the
electronic structure. As was discussed in detail in Chapter III, there
is a large amount of theoretical evidence that the Ag 4d states lie
lower in energy than the halogen p-derived states in both AgBr and
AgCl.[3,6,27] As will be shown in Chapter VIII, the regions under con-
sideration in both AgBr and AgCl lie precisely where the very flat
Ag 4d states have been placed in the work of Bassani, Knox, and
Fowler.[3] Even though this region has too high an energy in the calcu-
lation of Scop,[6] the discrepancy with our experimental peaks is the same
for both halides ($\approx 21\%$). Because these are the only band estimates
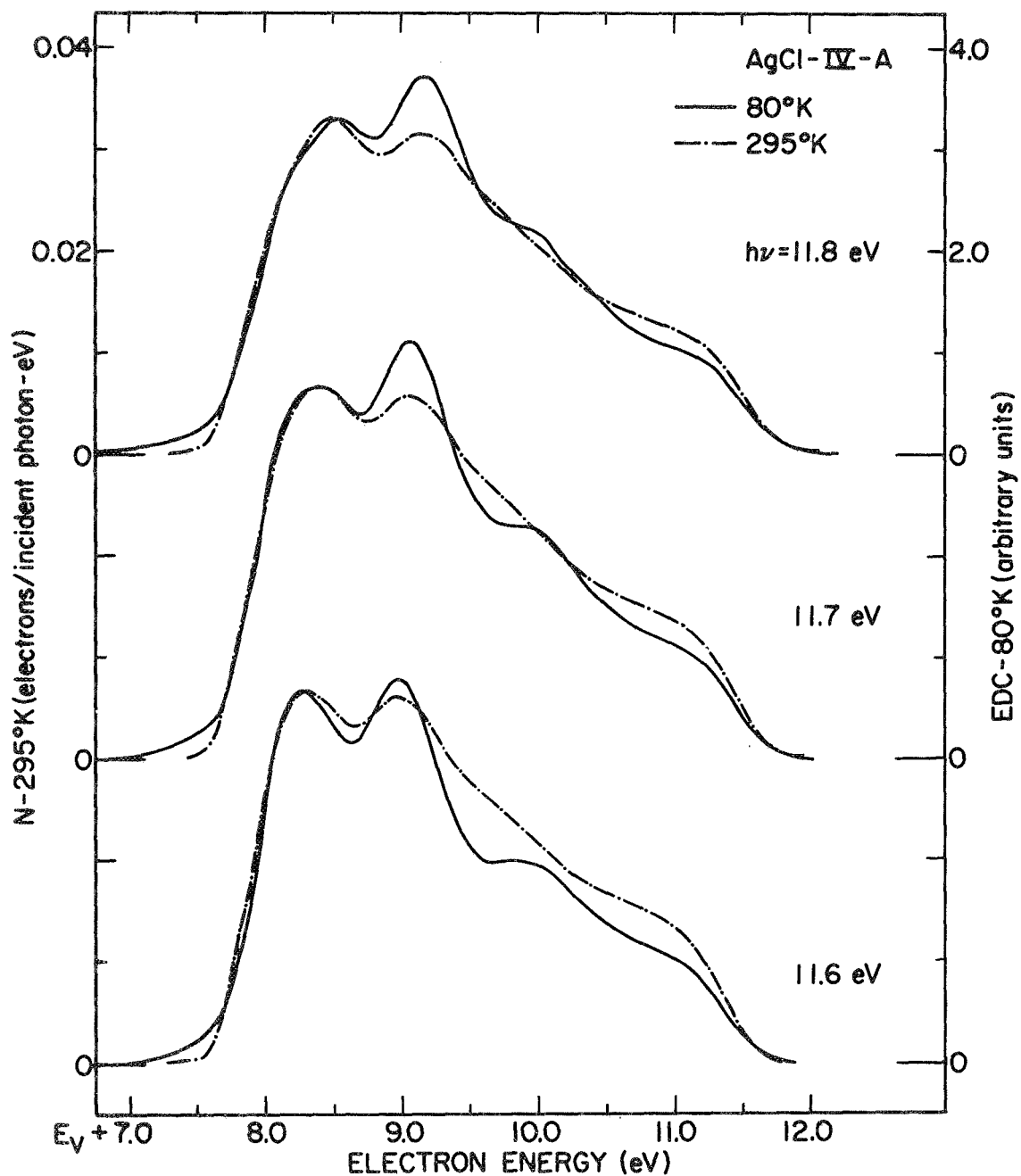
FIGURE 6.5. Comparison of energy distributions for electrons photoemitted from AgCl for photon energies of 11.6 through 11.8 eV at 295°K (normalized to quantum yield per incident photon) and 80°K (un- normalized with the -3.3 eV peak height adjusted to the value of the corresponding 295°K peak).

which are the result of detailed calculations, it is useful to examine the characteristics of this very narrow, virtually k-independent flat band region. These bands all lie within a range of 0.26 eV for both halides[109] thereby producing a high density of states. The EDC structure corresponding to such states should originate from the same initial energy for all $h\nu$. This can be easily tested by subtracting the photon energy from the final state energy to form a plot of the EDCs as a function of initial state energy. This is done for some of the AgBr data of Fig. 6.1 in Fig. 6.6. As can be seen, the largely temperature independent EDC peak appears to originate at -3.7 eV for all the curves. Further, the zero temperature width of 0.24 eV determined for this peak (see Table V.3) is quite close to the calculated 0.26 eV width of the flat band states.[109] Over 3/4 of the states within this range have greater than 90% d-character in both AgCl and AgBr .[109] Thus, the flat band states are primarily unhybridized Ag states with almost pure 4d symmetry. As noted in the introduction to this chapter, the EDC structure corresponding to such states would be expected to be largely temperature independent by the dynamic hybridization model. Thus, the characteristics of the data are consistent with the properties of the silver halide flat band region,[109] which occurs at the same energy as the experimental peaks in energy band estimates based on the measured optical properties of these solids.[3] It is therefore reasonable to associate the -3.7 eV peak in AgBr and -3.3 eV peak in AgCl with photoexcitation from Ag states with almost pure 4d symmetry. The small number of hybridized states which occur at this same energy[109] could account for the very small temperature dependence measured for this structure in AgBr (see Table V.3). The EDC structure from valence states higher than these energies corresponds to excitation from hybridized, p-derived halogen states.

B. AgBr EDCs for Photon Energies Above 11.8 eV

It is very useful to be able to probe the entire valence band not only to determine more electronic state features but also to substantiate the assignments of the ultrahigh vacuum EDC structure. The EDC strength
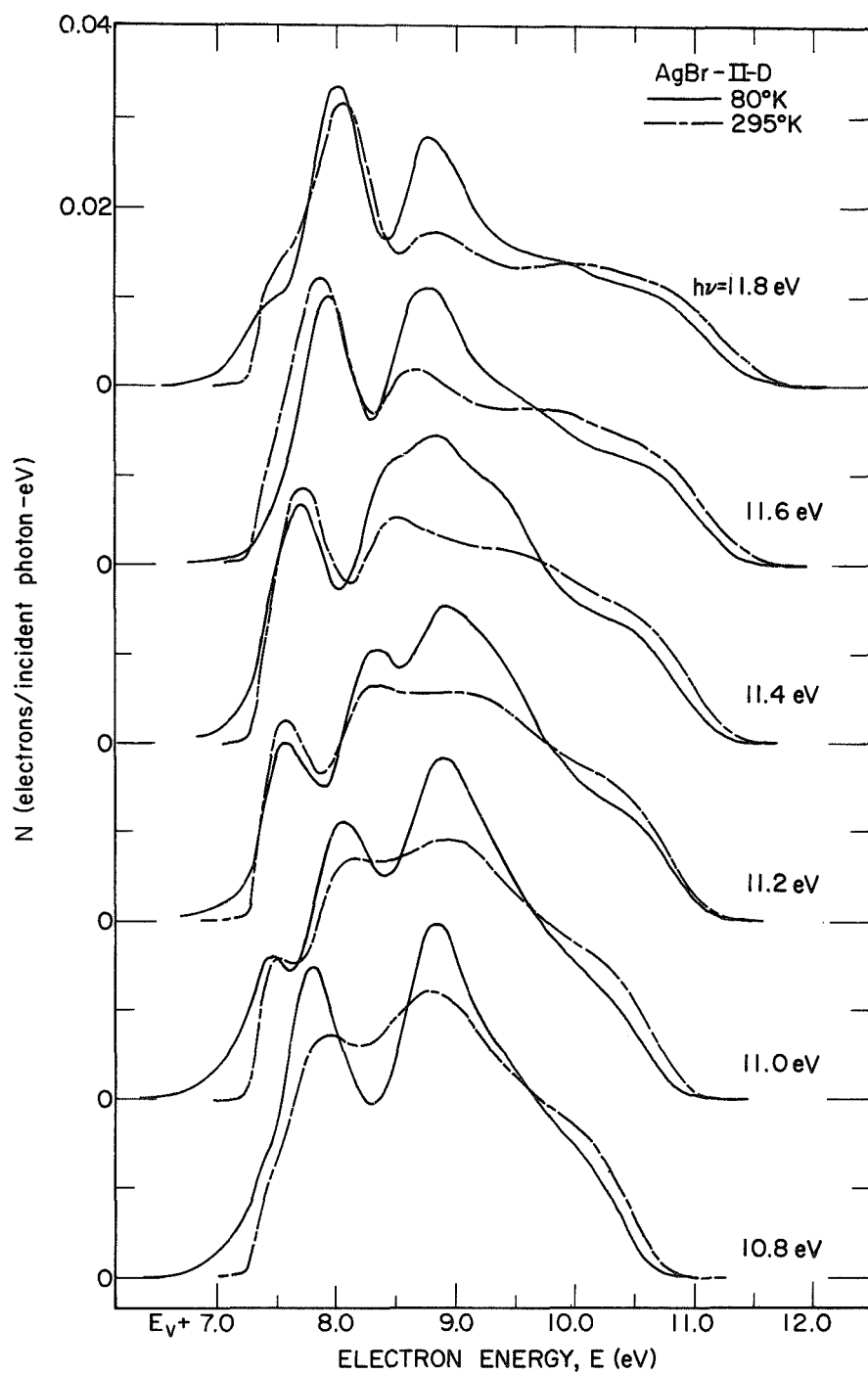
165
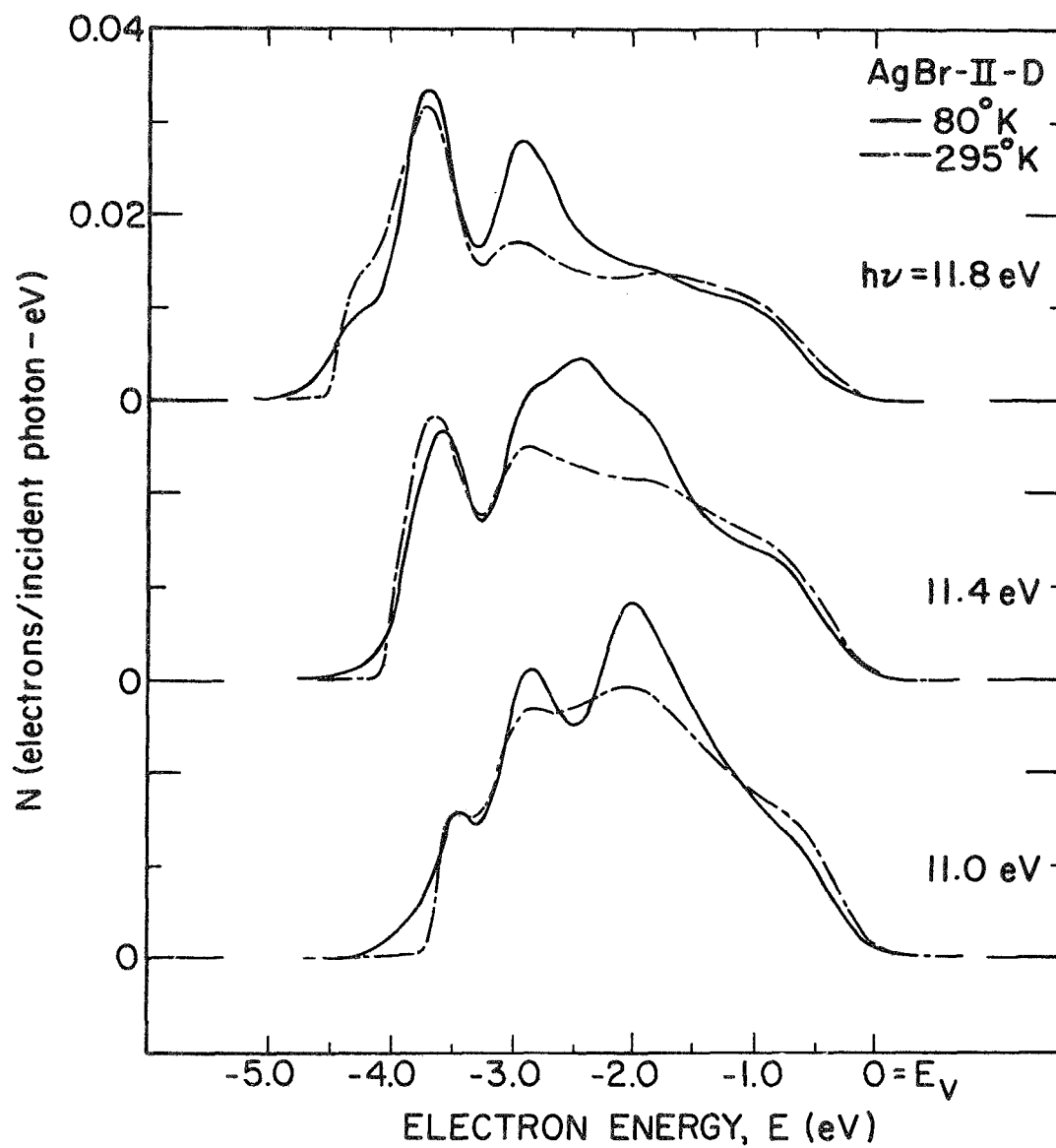
FIGURE 6.6. Comparison of energy distributions normalized to quantum yield (per incident photon) for electrons photoemitted from AgBr at 80 and 295°K for photon energies of 11.0 through 11.8 eV.

of various regions of the band structure can be studied, and the behavior of the structure with hν variation can be examined over a greater photon energy range. The depth of the band which can be probed is limited by the sum of the electron affinity and bandgap of the silver halide and the LiF chamber window cutoff. As discussed in Chapter IV, the attempts to lower the threshold by covering the surface with a monolayer of cesium failed because the cesium reacted with the silver halide sample [see Fig. 4.32(b)]. Therefore, the photon energy range of measurement was increased by removing the LiF window from the chamber while it was attached to the monochromer. This was done by having the window mounted on a thin-walled glass tube (0.002" thick) and then using a blade mounted on a linear motion[1] to break the window off the chamber. (For details, see reference 35.) The major shortcoming of this procedure is that the sample could not be cooled below room temperature because of the adsorption of oil and other contaminants from the poor monochromer vacuum. If the ultra-high vacuum results are compared to the windowless data below 11.8 eV in Fig. 6.7, it is clear that this vacuum environment lowers the threshold for photoemission and causes scattering of the high energy electrons which leads to smeared out structure above about $E = 9$ eV . The important thing is that the EDC structure all correlates in the two sets of data as is seen in the figure. It should be noted that the energy scales were determined independently for each set of data and for the entire set of curves rather than each curve individually. By removing the window, we could take advantage of higher energy lines in the gas spectra. In particular, H_2 has nearly a continuum up to around 14.0 eV. Neon has its strongest transitions at 16.8 eV with a very weak line around 14.7 eV. By reducing the pressure of Ne in the lamp by an order of magnitude, some of the oscillator strength is transferred into a higher energy 26.8 eV transition.[110] This was the first time this high energy line was used in this laboratory. Helium has a very strong line at 21.2 eV with a much weaker one at 23.1 eV. N_2 has transitions around 18.5 eV but these are weak and the discharge is difficult to stabilize. The relative strength of these weaker lines is 9:3:1.5:1 for 23.1 eV:26.8 eV:18.5 eV:14.7 eV; it
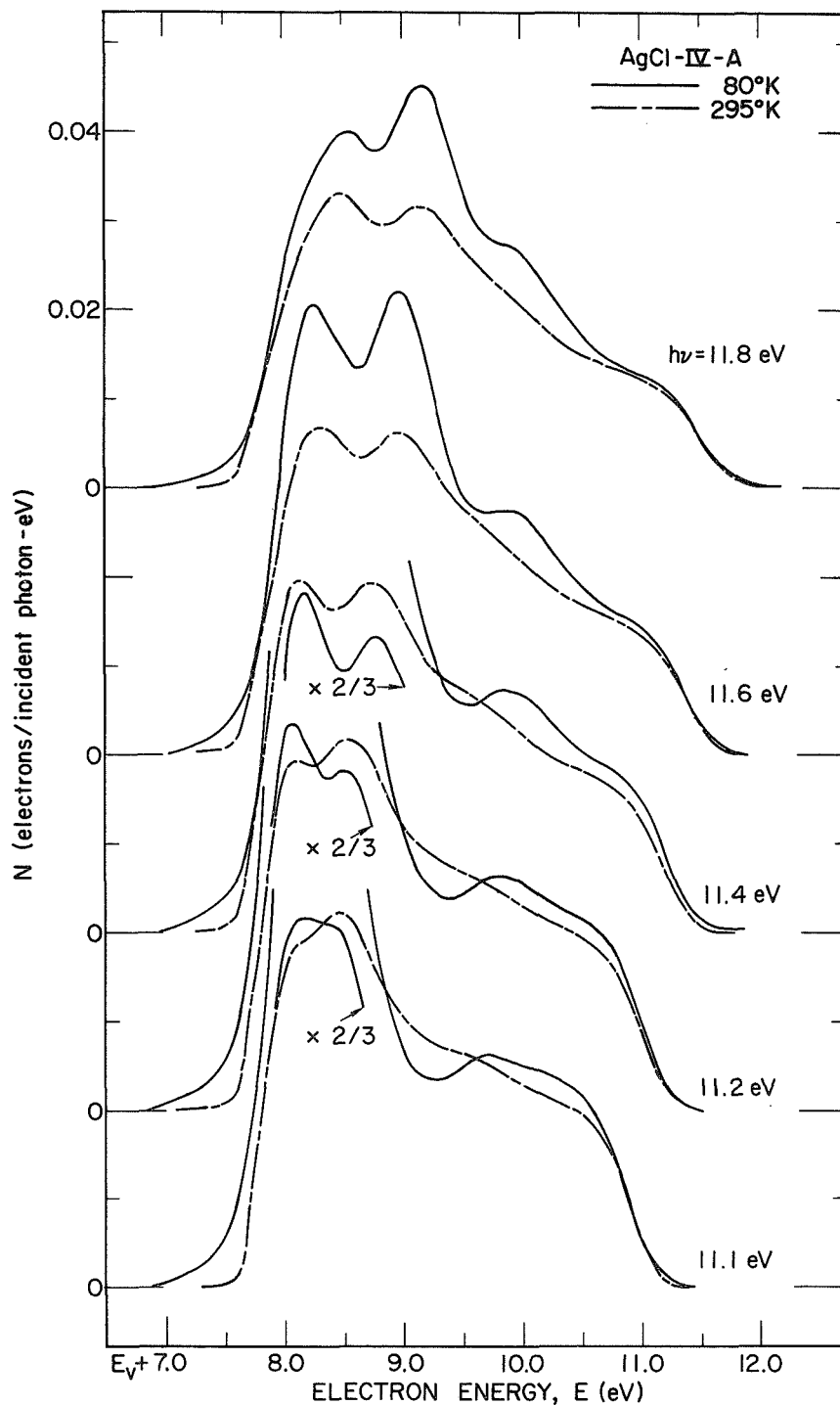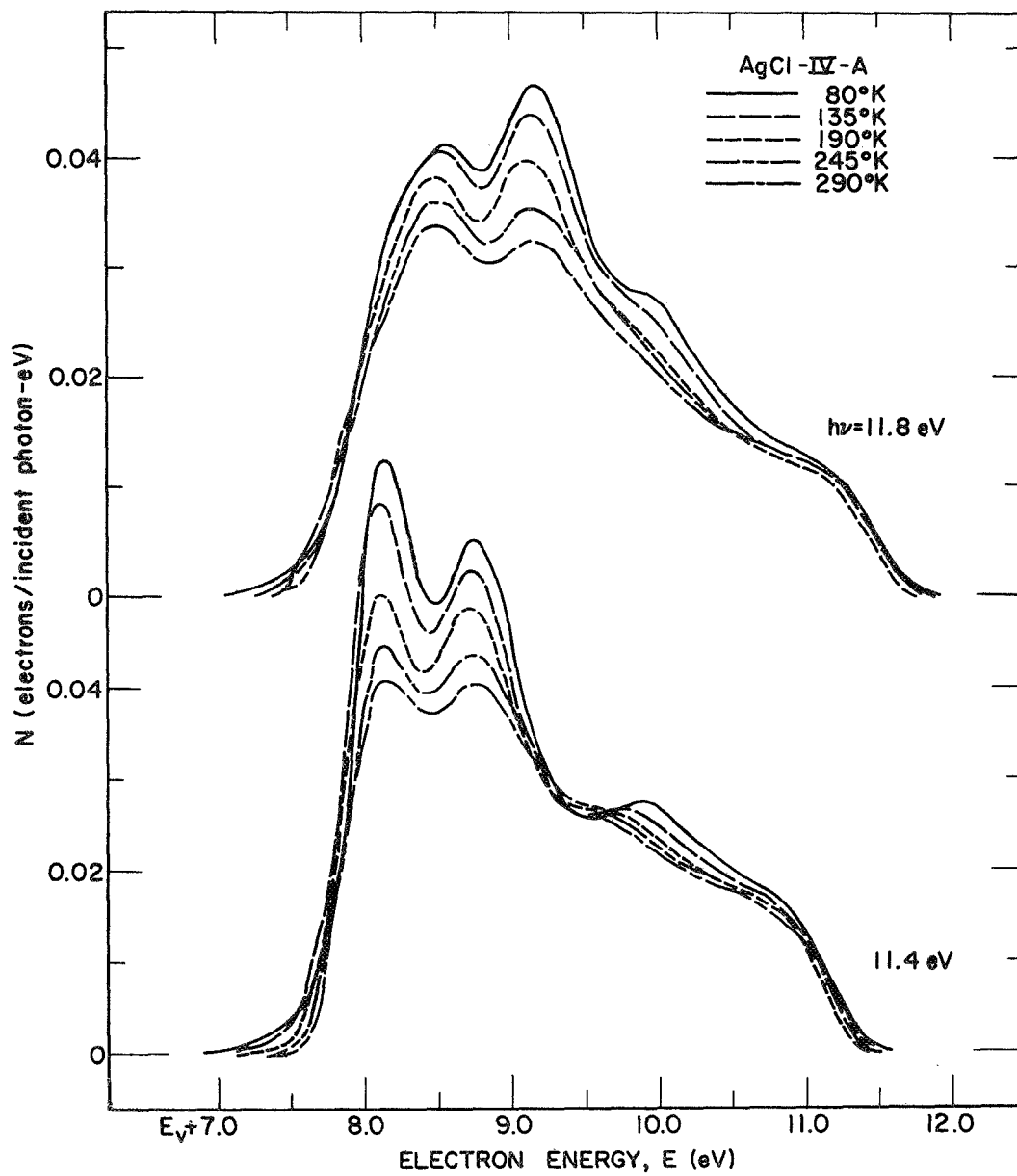
167

FIGURE 6.7. Comparison of energy distributions normalized to quantum yield (per incident photon) for electrons photoemitted from a AgBr, ultrahigh vacuum sample (II-D) and one exposed to the monochromator vacuum (IV-A) at 295°K for photon energies of 10.2 and 11.8 eV.

is difficult to obtain meaningful EDCs with the weakest two of these lines.

One of the first things we can study with these high energy AgBr EDCs is the behavior of the -3.7 eV peak, discussed in section A, over a wide range of energies; this un-normalized data is presented in Fig. 6.8. A dashed line has been drawn at the -3.7 eV energy which was the origin for this peak in the low energy, temperature dependent data of Fig. 6.6. As can be seen, the peaks are all located on this line for all photon energies until the peak becomes a shoulder due to scattering. The behavior of this EDC structure can then be explained quite well by having a high density of states at -3.7 eV in the AgBr valence band. This is consistent with this structure originating from relatively unmixed states which should not produce temperature dependent EDC structure and therefore consistent with the assignment of it to Ag states with almost pure 4d symmetry.

The peak which emerges on the left side of the EDCs in Fig. 6.8, also appears to originate from one energy in the valence band for all photon energies, once it has emerged from the influence of the threshold; this is apparent in the higher energy un-normalized data of Fig. 6.9. We can thereby identify another region of high electronic state density at -5.0 eV. It should be noted that this energy band structure would not have been identified without these windowless measurements. The peak which emerges on the left side of these EDCs is due to scattered electrons emerging above the threshold. This will be clear from the higher energy data to be presented next.

By going to much higher photon energies, the entire valence band can be seen directly; such data is presented in Fig. 6.10. The very strong peak on the left side of the EDCs is just the scattering peak which we first noted at 13.5 eV in Fig. 6.9. It can be identified with the electron-electron scattering since it always appears at threshold.[36] The other structure, which was expanded in the original data and is reproduced here, is due to excitation from the entire Br 4p and Ag 4d derived valence band (see Fig. 3.1). The peak in this part of the EDCs occurs at precisely -5.0 eV in all these high energy curves. If we
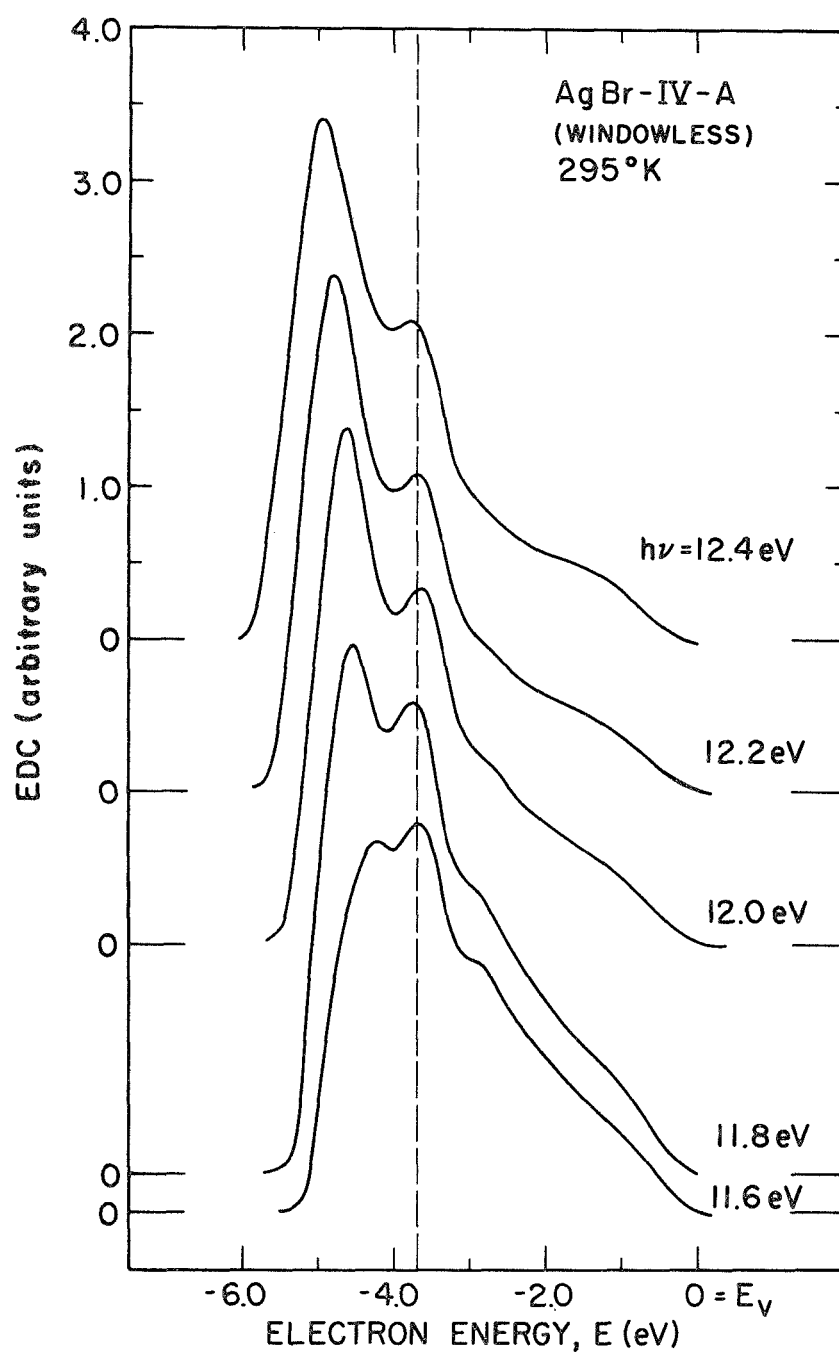
FIGURE 6.8. Comparison of un-normalized energy distributions for electrons photoemitted from AgBr at 295°K for photon energies of 11.6 through 12.4 eV. A line is shown at an electron energy of -3.7 eV.

170
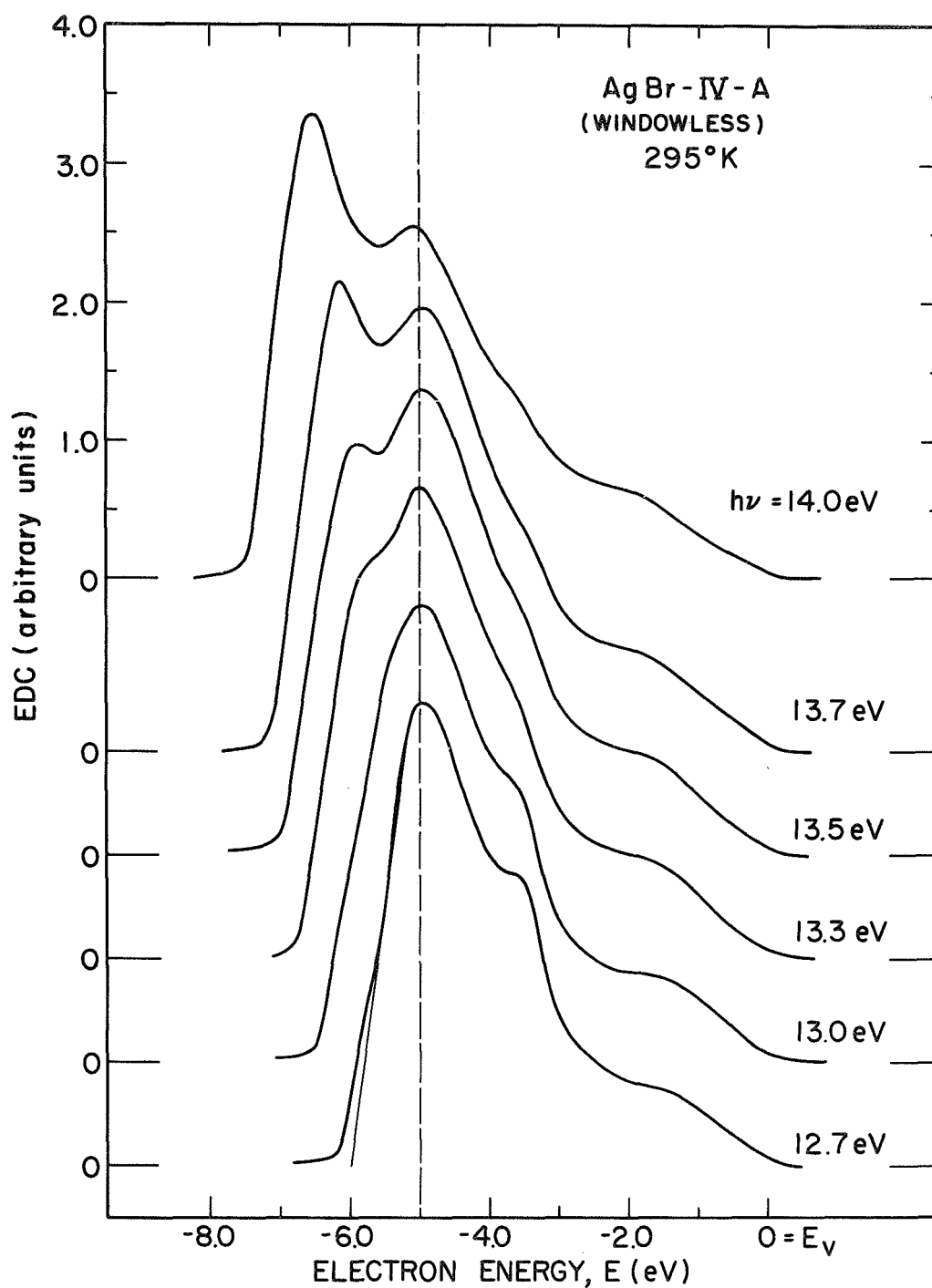
FIGURE 6.9. Comparison of un-normalized energy distributions for electrons photoemitted from AgBr at 295°K for photon energies of 12.7 through 14.0 eV. A line is shown at an electron energy of -5.0 eV.
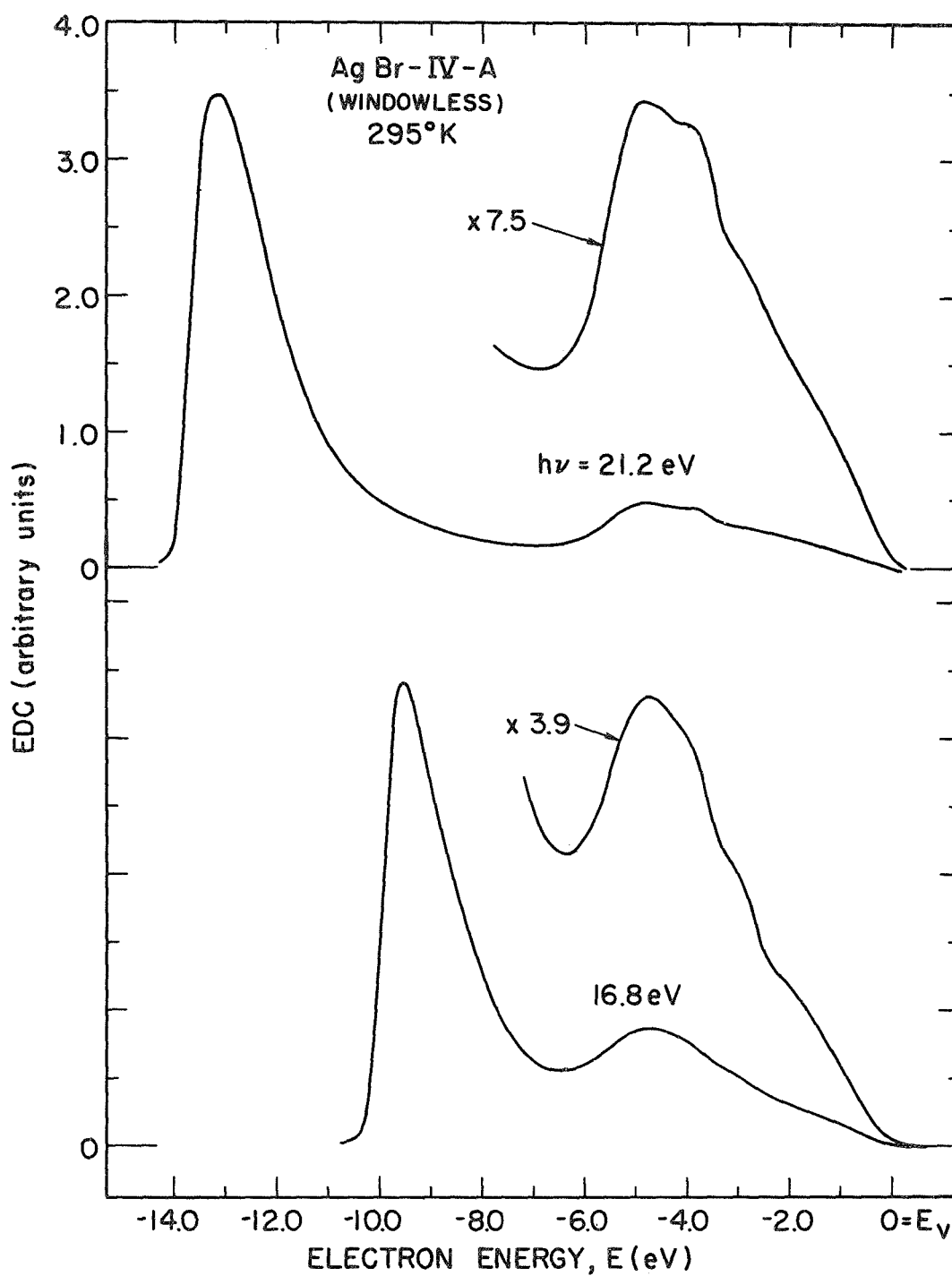
FIGURE 6.10(a). Comparison of un-normalized energy distributions for photoemitted from AgBr at 295°K for photon energies of 16.8 and 21.2 eV. Part of each curve is expanded by the factor shown.

172
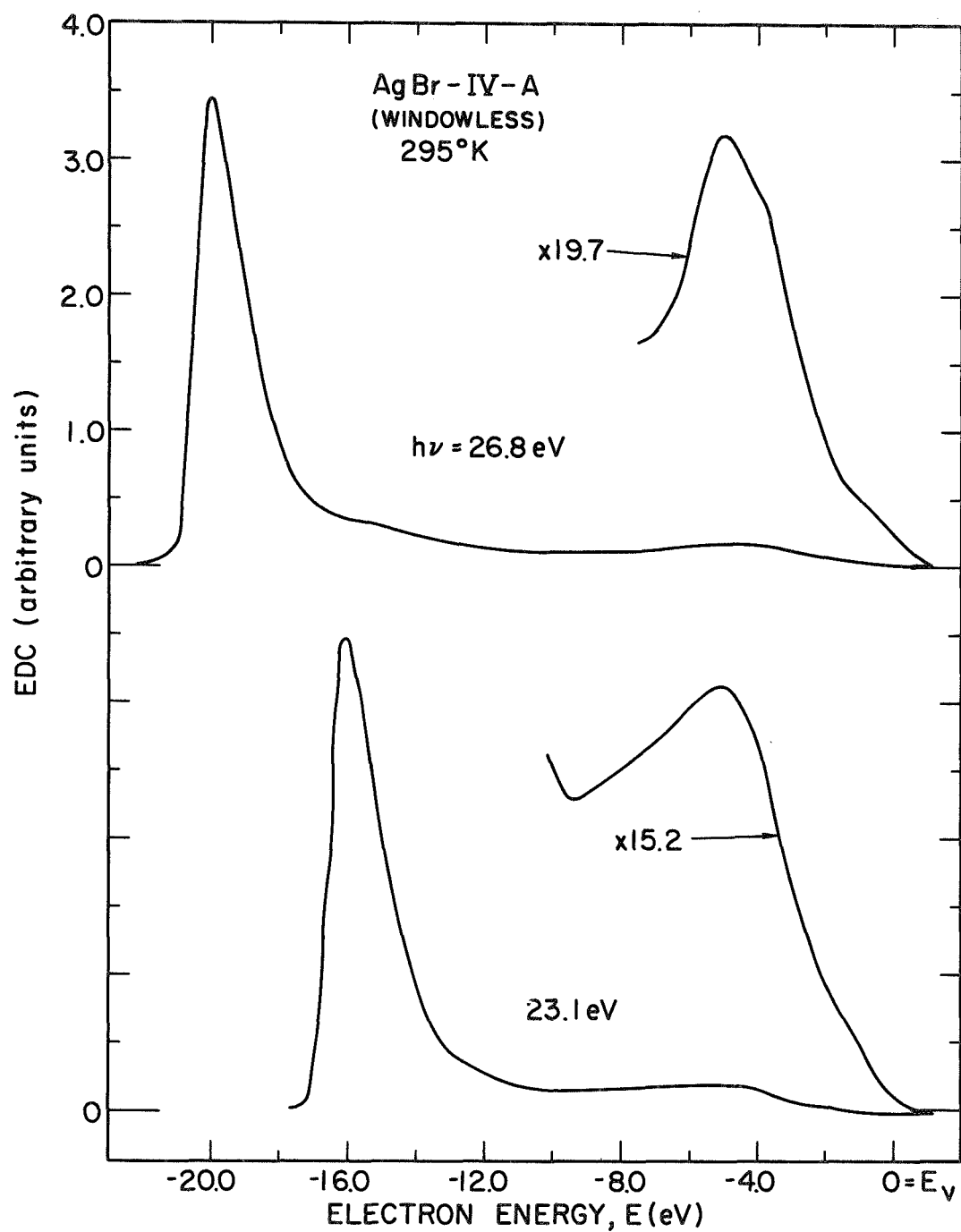
FIGURE 6.10(b). Comparison of un-normalized energy distributions for electrons photoemitted from AgBr at 295°K for photon energies of 23.1 and 26.8 eV. Part of each curve is expanded by the factor shown.

examine part (a) in detail, a second piece of structure occurring at -3.7 eV is clearly evident at $h\nu = 21.2$ eV . These -5.0 and -3.7 eV structures are the regions of high state density determined from the previous two figures. It is important to note that the area under these two pieces of structure in part (a) is more than half the total area under this part of the EDC. This is significant because in the high photon energy data, the EDC structure originating from Ag d states may be stronger than the Br 4p derived structure. Such a strength ratio is expected since the matrix elements of the d states should increase with the increased photon energy, and also there are four more d than p electrons.[111] Thus, we expect the -3.7 eV AgBr structure to originate from the silver d states because of its strength at high photon energies (e.g., $h\nu = 21.2$ eV) as well as its temperature independence at lower $h\nu$. The -5.0 eV structure would also appear to correspond to d state excitations by such considerations. These states are probably hybridized with the halogen p orbitals since the d states which mix with the halogen p's are decreased in energy relative to the pure Ag d states[3] which we located at -3.7 eV in section A. It is interesting to note that this -5.0 eV structure was just being seen near threshold at $h\nu = 11.8$ eV in the ultrahigh vacuum data of Figs. 4.20(a), 4.29, and 6.1. This is further evidence that the windowless measurements are characteristic of AgBr .

As can be seen in Figs. 6.10(a) and (b), this -5.0 eV peak is the last structure which is characteristic of the valence states of AgBr . It can, therefore, be extrapolated to yield an estimate of the valence band width. This is shown by the straight line on the left side of the 12.7 eV EDC in Fig. 6.9. From this we can deduce that the valence band is about 6.0 eV wide in AgBr . The widths of the high energy EDC expansions in Fig. 6.10(a) also indicate that the valence band is approximately 6.0 eV wide. We have placed particular emphasis on part (a) of Fig. 6.10(a) since, as noted above, the photon energiesof 16.8 and 21.2 eV are due to very strong lines in Ne and He ; thus, the EDCs taken at these energies and displayed in part (a) were virtually noise free. On the other hand, the second order 23.1 and 26.8 eV lines were at least

174

two orders of magnitude less intense than these lines and the raw EDCs corresponding to part (b) were very noisy. The EDCs of part (b) therefore serve only to show that the characteristics at 16.8 and 21.2 eV are also present at higher energies.

These windowless studies were only performed for AgBr because of the expense of the "one-shot" LiF window, the time and expense involved in having to completely clean the chamber and flange from oil contamination following each experiment, and the time necessary to do such additional experiments. The important information which was determined for AgBr can be used as a further justification that the nearly temperature independent structure for all the silver halides is due to transitions from Ag states with almost pure 4d symmetry and to thereby further support the dynamic hybridization model for silver halide photoemission.

VII. THE ELECTRONIC CONDUCTION STATES OF

AgBr AND AgCl

In the previous two chapters, we discussed the most predominant
features of the temperature dependent data. In Chapter V, the dynamic
hybridization model was used to explain the strong temperature depen-
dence of EDC peak widths, and this structure was shown to be due to
excitations from hybridized halogen p-derived states. This was extended
in Chapter VI to locate the Ag states with almost pure $4d$ symmetry
by the temperature independence of the corresponding EDC structure.
These features of the data have all been characteristic of the complex
valence band structure and were used to understand these electronic
states. There are two other major features of the silver halide data
which are related to the characteristics of the conduction band states
and have only been alluded to in the previous discussions. The apparent
occurrence of temperature dependent final density of states structure
and the weakness and temperature independence of all EDC structure with
high final state energies will be examined in detail in this chapter in
sections A and B, respectively.

A. The Halogen d-Derived Conduction States

In both AgBr and AgCl there appears to be EDC structure which
occurs at a fixed final state energy only at 80°K. The appearance of
structure upon cooling is particularly striking in the AgBr high
photon energy data of Fig. 6.1; a portion of this data is reproduced in
Fig. 7.1. This is the same as Fig. 6.6 only plotted as a function of
the final state energy of the electrons. A dashed line has been drawn
at a final state energy of about 8.8 eV to show the enhancement of all
EDC structure with this energy at low temperatures. Perhaps the most
dramatic imanifestation of this is the occurrence of an additional peak
at 80°K for $h\nu = 11.4$ eV ; for 11.8 eV, this enhancement appears as
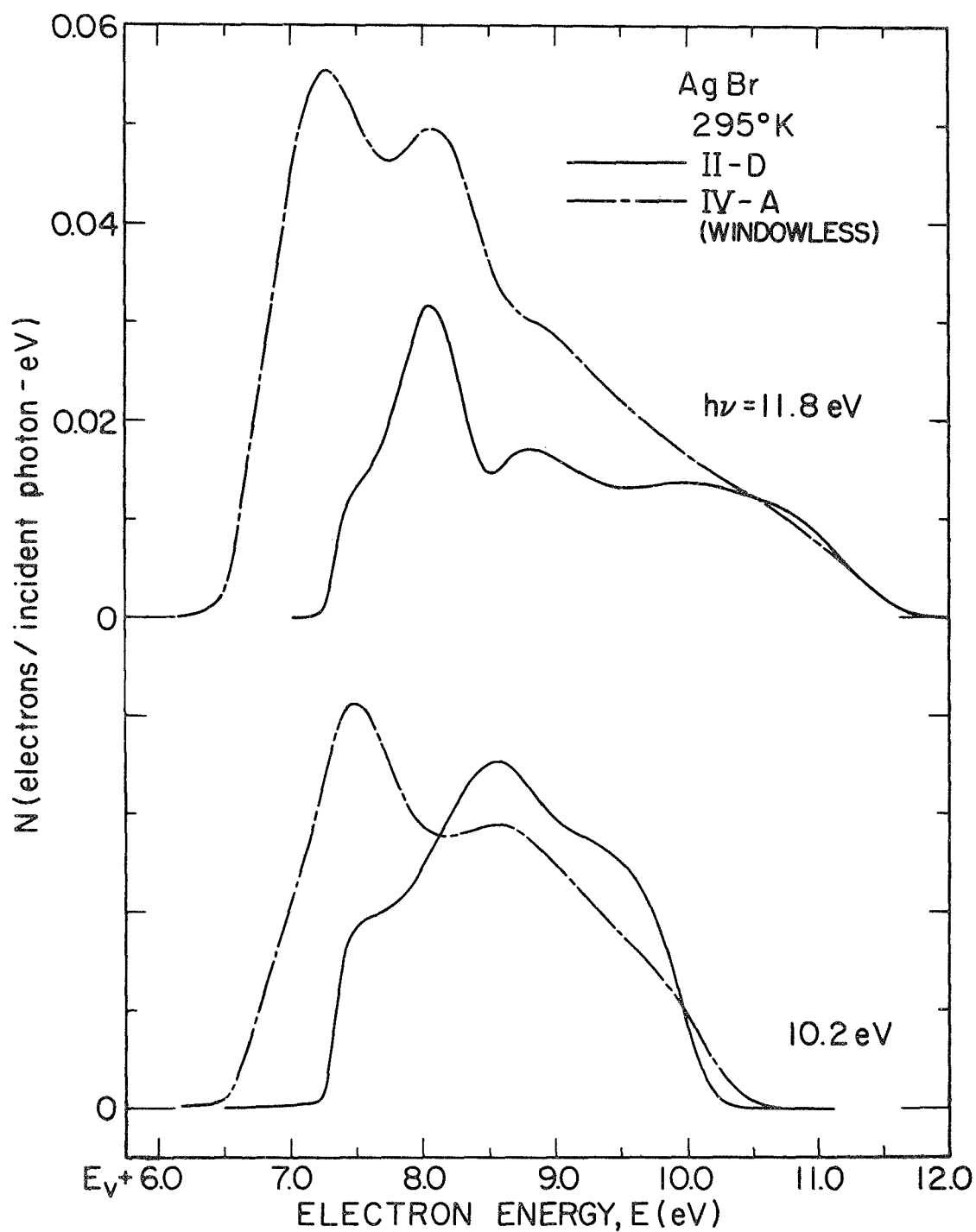an enlargement of a peak which is present at 295°K and is the only

FIGURE 7.1. Comparison of energy distributions normalized to
quantum yield (per incident photon) for electrons
photoemitted from AgBr at 80 and 295°K for
photon energies of 11.0 through 11.8 eV. A line
is shown at an electron energy of about 8.8 eV.

temperature dependent change of the EDC. It is clear that these changes are due to the appearance of a new final density of states region by examining the detailed temperature evolution of the new 11.4 eV peak from a valley at 295°K; such data was presented in Fig. 6.2(a) and is reproduced here as Fig. 7.2 for easy reference.

FIGURE 7.2. Comparison of energy distributions normalized to quantum yield (per incident photon) for electrons photoemitted from AgBr at 80 through 285°K for a photon energy of 11.4 eV.

The center peak with two side shoulders at $80°K$ is not as clear for this sample as it was for others. A comparison with sharper data was shown in Fig. 4.20(a) where the slight broadening of sample IV-A is evident; however, the trend of what is occurring is still quite clear for the data of Fig. 7.2. In warming just $55°$ above $80°K$ the low-temperature peak has lost most of its strength so that what had been the left shoulder is now the EDC peak. By very carefully adjusting the temperature halfway between these two values ($107°K$), both of these pieces of structure are clearly evident as is seen in Fig. 7.2. This new $80°K$ structure, which is only a shoulder at $135°K$, completely disappears when the temperature is raised above the Debye temperature ($\Theta_D \approx 144°K$) to $190°K$.

In order to understand this dramatic temperature change in the conduction band density of states, the electronic structure must be examined in detail. Based on the dynamic hybridization model, one can hypothesize that this is caused by a high density of hybridized states which occurs at a final state energy of 8.8 eV when the lattice is frozen but is so considerably broadened at elevated temperatures that no distinctive EDC structure is observed above Θ_D. Unfortunately, the bands for the silver halides have not been calculated at such high energies so this hypothesis cannot be tested in detail. It can be estimated, however, that the halogen d states and the Ag $5p$ states, which have higher energies, both lie around 9 eV above the highest filled states in AgBr (see references 3 and 41). To determine how such states would look in the band structure, we can make an analogy to the conduction states of LiCl calculated by Kunz[112] and shown in Fig. 7.3. The atomic designations refer to the orbitals from which the states at Γ and the bands emanating from this point are derived. As in the case of the silver halides, the circumstance exists where the metallic p band [in this case Li (2p)] lies just a bit higher than the halogen d band [in this case Cl (3d)]. The important thing to note is that this is completely analogous to the p and d valence states of the silver halides in that the orbitals are of the proper species and close enough in energy to significantly mix and produce hybridized states. Then by

179

LiCl (KUNZ)
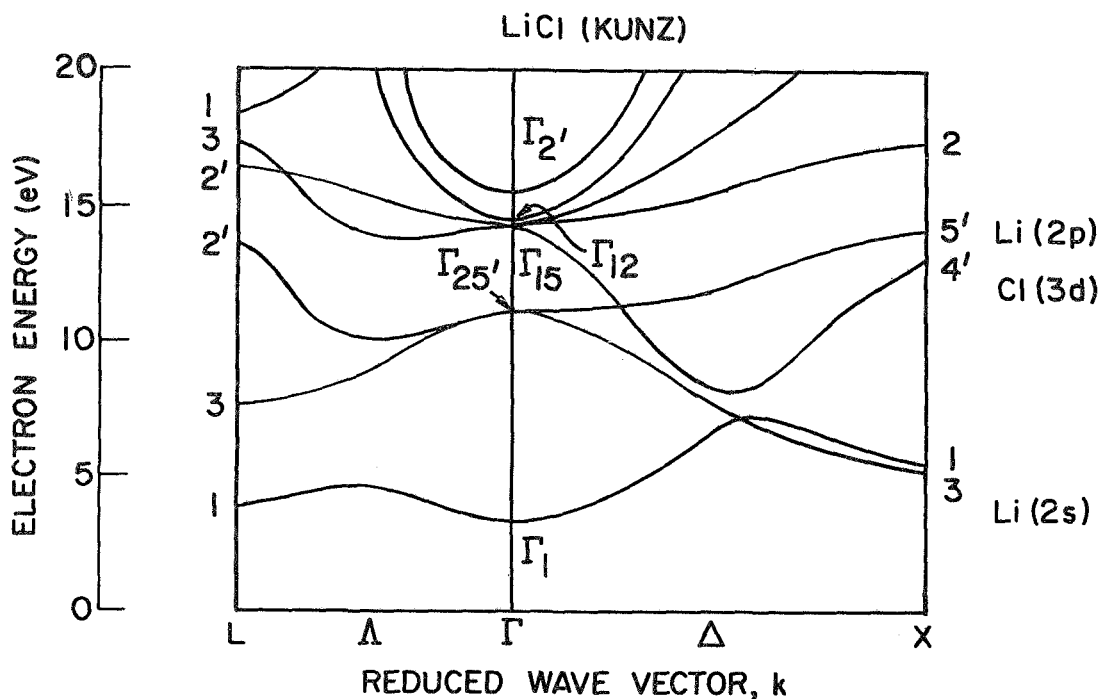
FIGURE 7.3. The electronic conduction band structure of LiCl calculated by Kunz (reference 112). The atomic designations are the orbitals from which the states at Γ are derived.

the dynamic hybridization model first discussed in Chapter II, the energies of these conduction states will be very dependent on the vibrations of the lattice and hence the temperature of the solid. As seen in Fig. 7.3 for LiCl , this p-d mixing produces a large number states which converge in a small energy range (around 14 eV) at Γ . It is important to realize that these states do not contribute strongly to the photoemission since the density of states goes to zero at Γ . The bands which move away from Γ can form a large number of states over a small energy range and thus lead to a large density of states region. Since most of the states which compose this region are hybridized, when the temperature is near enough the Debye value to cause significant

lattice vibrations, they will broaden considerably and not necessarily uniformly about the same energy. Thus, they may very well lead to a very broad continuum density of final states at room temperature and not produce any distinctive EDC structure effects at elevated temperature. Though much of this is speculative, it is based on the known general character of the silver halide conduction states and seems to be the most plausible explanation for the observed EDC characteristics.

As has been pointed out in the previous two chapters, a temperature dependent final density of states also affects the AgCl EDCs significantly at $E \approx 8.1$ eV . These EDCs are summarized over a wide energy range in Fig. 7.4. If the peak which first appears near the threshold of the 10.3 eV EDCs (i.e., -2.65 eV) is examined, one can see that its strength at 80°K is significantly enhanced over the 295°K height when $E = 8.1$ eV (i.e., for $h\nu = 10.8$ eV); when its final state energy is below 8.1 eV (i.e., $h\nu = 10.3$ eV) or above this value (i.e., $h\nu = 11.3$ and 11.8 eV), the increase upon cooling is much less. (The modulation of this particular peak as it moves through $E = 8.1$ eV can be examined in detail in Fig. 5.9 with intermediate temperatures included in Fig. 5.10(a).) The temperature dependence of this -2.65 eV peak modulation can clearly be seen to be simply a height change by analysis of the peak width by Eq. (5.7). The $h\nu = 10.8$ eV parameters in Table V.3 are characteristic of this AgCl peak when its final state energy is 8.1 eV. They indicate that the temperature dependence, C , is within the range of values determined for this peak at all $h\nu$ but the zero temperature width, W_0 , appears to be considerably reduced at this energy. These characteristics of the parameters are indicative of having increased the peak height so that the width at a fixed fraction of that height (i.e., 90%) will be less but yet will exhibit the same dependence on T as found for all other final state energies and thereby being characteristic of the valence states.

The second peak which emerges at 11.3 eV in Fig. 7.4 (i.e., -3.3 eV) similarly shows an increased 80°K height only at the same 8.1 eV final state energy; this can be seen by its decrease at $h\nu = 11.8$ eV . (This peak's temperature dependent behavior over a finer photon energy grid
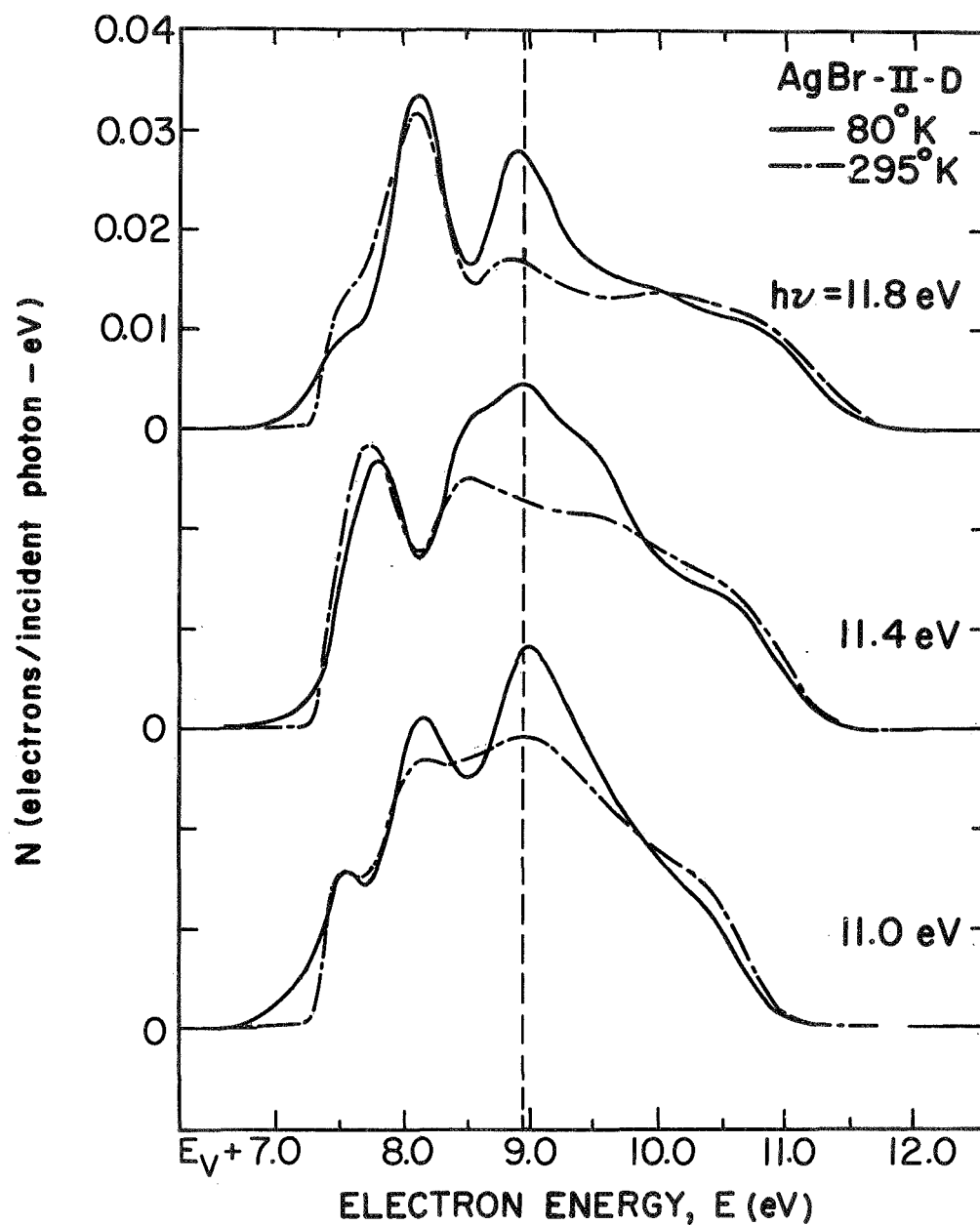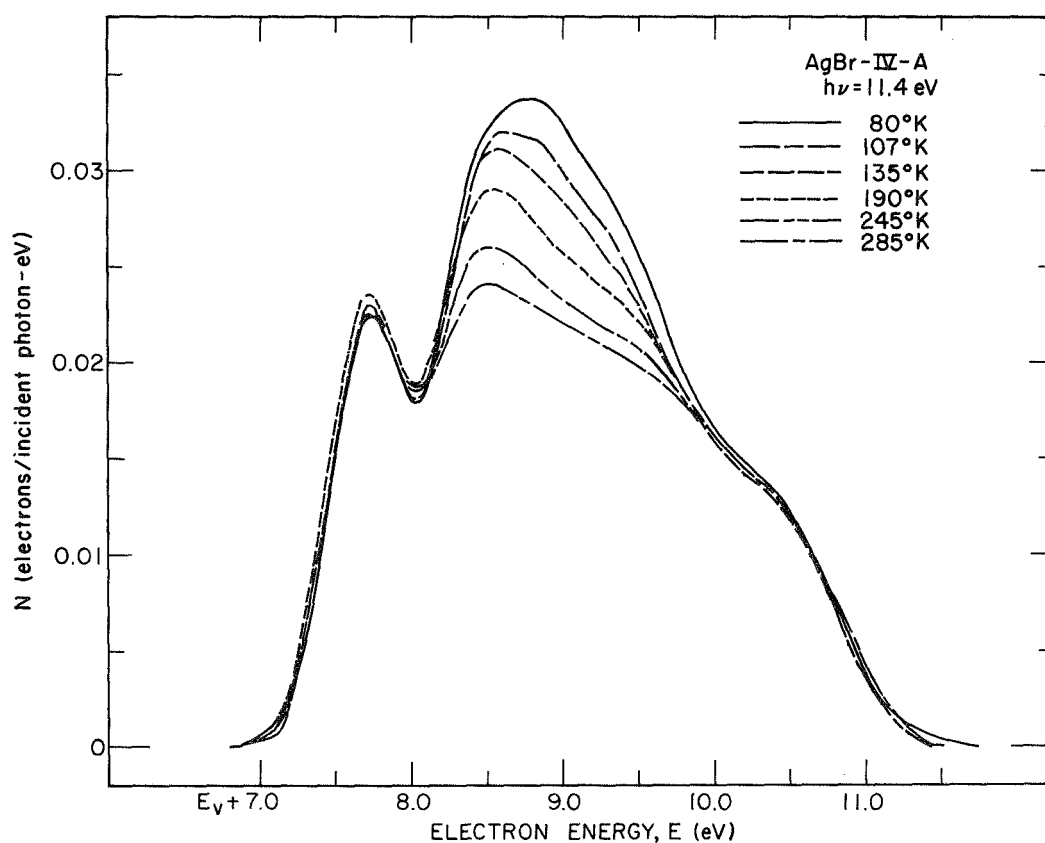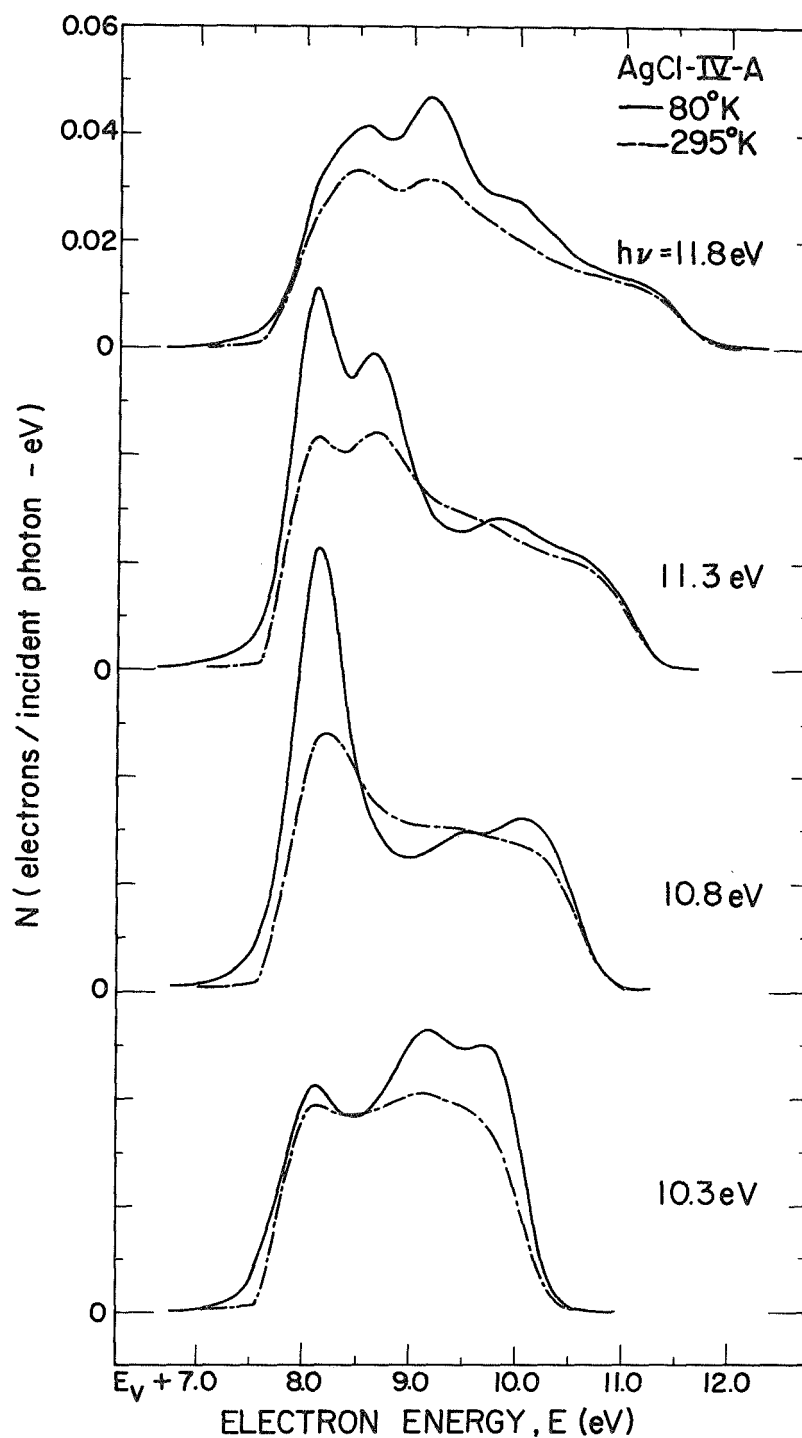
FIGURE 7.4. Comparison of energy distributions normalized to quantum yield (per incident photon) for electrons photoemitted from AgCl at 80 and 295°K for photon energies of 10.3 through 11.8 eV.

was presented in Fig. 6.3 with intermediate temperatures included in Fig. 6.4.) In contrast to the -2.65 eV peak discussed above, this particular "pure" d piece of structure does not show any sharpening or peak-to-valley ratio changes with temperature at any final state energy (see Chapter VI). This is a further indication that the localized height changes are characteristic of conduction state changes since the other -3.3 eV peak parameters are T independent and thus character- istic of the valence states. This final state region of 8.1 eV can also produce shifts in the peak positions upon cooling as was seen for the low photon energy structure in Fig. 5.10(b). This shifting accompanied the peak height enhancement (Fig. 5.8) as would be expected. It is reasonable to assume that this 8.1 eV region is composed of hybridized halogen d-derived states (Cl 3d) which are mixed with the Ag 5p empty states as was similarly hypothesized for AgBr above.

It should be noted that we have already observed that the strength of the density of hybridized states can be temperature dependent. This was found to be the case for the filled valence states of both AgBr and AgCl in Chapter V. It was seen that the EDC structure on the leading side of the EDCs would undergo a reversal in their relative heights upon cooling to 80°K. This was most evident for AgBr at about $h\nu = 9.6$ eV as shown in Fig. 5.1 and for AgCl at 10.4 eV as depicted in Fig. 5.9. This temperature dependence of the density of states height occurred gradually as was seen in Figs. 5.3 and 5.10(a) for AgBr and AgCl , respectively. Thus this temperature dependent peak height modu- lation, which was characteristic of the valence states, is the same occurrence as the temperature dependent final density of states we have been discussing in this section. It is thus reasonable that similar mechanisms based on the dynamic hybridization model should explain both phenomena, as we hypothesized.

B. The Ag 5p-Derived Conduction States?

There is still one major feature of the EDCs of both halides which we have not discussed. As can be easily seen at high photon energies in Figs. 6.1 and 6.3 for AgBr and AgCl , respectively, there appears

to be two distinct final state energy regions over which the character
of the structure and its temperature dependence are quite different.
At low energies, there is strong structure (i.e., peaks), which sharpens
by varying amounts while at higher final state energies, the structure
is characteristically weak (i.e., shoulders) and shows virtually no
change with temperature variation. The transition between these two
regions is really quite distinct. There is a sharp peak on the leading
side of the EDCs at $80^\circ K$ which over just a 0.2 eV photon energy increase
abruptly becomes a shoulder. As seen in Fig. 5.2, this occurs for AgBr
between $h\nu = 10.2$ and 10.4 eV for structure originating -0.8 eV in
the valence states. We can thus conclude that at a final state energy
of 9.5 eV there is a change in the AgBr EDCs. As can be seen at
higher photon energies in Fig. 6.1, all the structure at energies, E ,
higher than this is weak and temperature invariant. In a similar manner
for the AgCl data displayed in Fig. 5.9, strong structure originating
-0.7 eV in the filled states becomes weak between $h\nu = 10.8$ and
11.0 eV. Further, all the AgCl structure above E = 10.2 eV (see
Fig. 6.3) is independent of temperature and weak no matter what its
character or behavior was at lower final state energies. We have thus
far in the thesis only discussed the EDC data in the low E region. It
is the purpose of this section to examine the causes for this weakening
effect on the EDCs.

The most reasonable explanation which comes to mind for the presence
of two final state energy regions over which the character of the struc-
ture and its temperature dependence are different, is that it is a fea-
ture of the optical excitation process. It was pointed out in section A
that the high energy final states in the silver halides are derived from
Ag 5p orbitals mixing with lower energy halogen d states. The hybrid-
ized d states probably produced the temperature dependent final density
of states structure at 8.6 eV in AgBr and 8.1 eV in AgCl . The
conduction states above these energies would then be mainly p-like in
character. Furthermore, in Chapter V we determined that the filled
states were derived from halogen p orbitals to a depth of about 3.3 eV
in AgBr and 3.0 eV in AgCl (see Chapter VI). Recalling that dipole

transitions between two p orbitals are forbidden by symmetry, it is
clear that optical transitions between these two regions of p-derived
states are only possible between those parts of one set of hybridized
states which have d character and the predominant p symmetry parts
of the other set of states. Since the hybridized states' d character
represents only a small fraction of the total joint density of states
in this transition energy range, such a mechanism would seem to explain
the weakness and relative, temperature insensitivity of the valence
p-derived EDC structure at high photon energies. From these considera-
tions, it would be concluded that the conduction states are primarily
of Ag 5p origin and symmetry above 9.5 eV in AgBr and 10.2 eV in
AgCl up to at least 11.8 eV, the limit of the ultrahigh vacuum measure-
ments. Since the final states below these energies of 9.5 and 10.2 eV
(AgBr and AgCl , respectively) are thought to be of s and d
character, one would expect considerably more allowed optical transi-
tions from the same hybridized p valence states and therefore the
stronger EDC structure which is seen.

From the windowless AgBr experiments discussed in the last
chapter, there is additional data available which both supports and
casts doubt on such conduction state assignments. When the -5.0 eV d
electrons are excited to a final state energy of 11.8 eV in the
$h\nu = 16.8$ eV EDC of Fig. 6.10(a), the peak is quite strong compared to
the structure due to excitations from the p-derived states to this same
final state energy in Fig. 6.1. These strengths are consistent with
the transitions being to Ag 5p-derived states at E = 11.8 eV . On
the other hand, at lower photon energies when the -3.7 and -5.0 eV
d-derived structures are excited to the E = 9.5 eV energy where these
Ag 5p states should begin, both peaks lose strength in the same manner
as the p-derived structure did (see Figs. 6.8 and 6.9). This, of course,
could not happen if we were simply dealing with d → p transitions.
This casts some doubt on the Ag 5p assignment. However, this data
does show some contradictions, as pointed out above, and exhibits other
anomalies when H_2 was used as the light source at high photon energies.

Thus, we will speculate that the two final state regions over which the ultrahigh vacuum EDC behavior is clearly different is due to the occurrence of Ag 5p-derived states at energies above 9.5 eV in AgBr and 10.2 eV in AgCl though other effects on the optical excitation process may be the cause.

VIII. THE ELECTRONIC STATES AND OPTICAL EXCITATION PROCESS IN AgBr AND AgCl DETERMINED FROM THESE STUDIES

We have discussed in great detail many different features of the photoemission data and in each case used these to determine the nature of the electronic states involved in the optical transitions. It is the purpose of this chapter to summarize all of this information in a concise form so one can easily use the results of these studies and also gain a perspective on the features which are characteristic of the silver halide electronic structure. They are compared to estimates of the band structure in section B; in section D they are compared to the cuprous halide room temperature characteristics determined by Krolikowski[1] to study the effect of changing the noble metal constituent. The importance of conserving crystal momentum, k , in the optical transitions is examined in section C since some question exists as to the nature of the excitation process in the silver halides as well as the cuprous halides. These solids are particularly interesting in this regard since they are intermediate between classic wide band gap, tightly bound insulators, where transitions may be predominantly non-direct, and narrow gap, covalent semiconductors in which transitions are direct.[113]

A. The Electronic States of AgBr and AgCl

A large amount of photoemission data has been presented in the previous chapters. It was divided according to the characteristics of the electronic states which could be determined from a particular part of the data. In this manner all of the EDC data for AgCl and AgBr has been depicted except near threshold. The omitted data is presented in Appendix D for completeness and future reference. It is not presented in the main text since it does not contain any characteristics which have not already been examined and can be used much more efficiently as structure plot data to be presented below. The major

characteristics of the EDC data discussed in the last three chapters are
summarized along with the suggested interpretations in Table VIII.1.

TABLE VIII.1. Summary of AgBr and AgCl photoemission
EDC characteristics

FINAL STATE ENERGY[*] (eV)		EDC STRUCTURE		SUGGESTED INTERPRETATION
AgBr	AgCl	CHARACTER	$295 \rightarrow 80^\circ K$	
< 9.5	< 10.2	Strong	3 Highest Peaks Sharpen	Hybridized halogen p-derived valence states
			No sharpening of lowest peak	Pure Ag 4d-derived valence states
> 9.5	> 10.2	Weak	No sharpening	Forbidden halogen p → Ag 5p transitions?
8.3	8.1		Enhanced strength; Some new structure	Hybridized halogen d-derived conduction states

[*]$0 = E_v$

The table is divided according to the final state energy of the elec-
trons to attempt to separate the EDC effects characteristic of the con-
duction states from those of the valence states. The characteristics of
the filled states were all determined at low final state energies as
shown by the first line of this table.

In order to determine the detailed origin of this structure in the
electron states, it is very useful to summarize the EDC information by
plotting the final state energy of each peak and shoulder as a function
of photon energy. (This method was first used extensively by Eden.[99])
This is done for AgBr at room and liquid nitrogen temperature in
Fig. 8.1. We have also included, the ectrapolations of the EDC's
leading and trailing edges to the base line in these "structure plots".

FIGURE 8.1(a). Spectral distribution of the AgBr EDCs' structure and edges at 295°K. Unit and zero slope lines, with their electron energy-axis intercepts, are shown fit to appropriate data.

FIGURE 3.1(b). Spectral distribution of the AgBr EDC' structure
and edges at 80°K. Unit and zero slope lines, with
their electron energy-axis intercepts, are shown fit
to appropriate data.

It should be noted that very vital information on the strength and width variations of the EDC structure has been discarded in forming such a plot. However, the systematics of the variation of the structure with variation of the photon energy can be easily determined by this method of data presentation. This is very important since transitions from regions of high density of states in the valence band produce structure in the EDCs which changes position with increments of energy equal to the changes in photon energy. Such structure should thus be described by a line of unit slope on the structure plot; the energy of the high density of states region is given by the electron energy-axis intercept of such a line. As can be seen by Fig. 8.1, at both 295 and 80°K, regions of high density of states are predicted by this method to be 0.8, 2.9, and 3.7 eV below the AgBr valence band maximum. From Table VIII.1 where the temperature dependences of the widths of this structure are summarized in the first line, we conclude that the -0.8 and -2.9 eV peaks are Br 4p-derived hybridized valence states while the -3.7 eV structure is derived from the localized Ag valence states with almost pure 4d symmetry.

It should be emphasized at this point that these unit slope lines and this interpretation for the Ag 4d state origin were used in setting the energy scales for all the EDC data. The highest point of the leading edge extrapolation should correspond to excitation from the highest filled state. (The method of extrapolating the data and the less than 0.1 eV error of this process was discussed in Chapter IV, part D.) Thus if the valence band maximum, E_v , is taken to be the zero of energy, the final state energy of electrons photoexcited from these states would just be equal to the photon energy, $h\nu$. Thus, we can set the energy axis by fitting a unit slope line corresponding to $E = h\nu$ to the highest leading edge points as was done in Fig. 8.1. There may be some question as to the temperature dependence of this energy scale since we have determined that the energy of the highest filled states will be broadened with temperature variation (see Table V.1). Fortunately, there is a somewhat independent check on the energy scale. Since we determined in Chapter VI that the "pure" Ag 4d states

should not be dependent in any way on temperature, the absolute energy which we determine from the EDCs for these states relative to the valence band maximum should be temperature independent. As can be seen by comparison of parts (a) and (b) of the figure, if the $E = h\nu$ line is located at the highest leading edge points, the energy determined for the temperature independent EDC structure is the same -3.7 eV value at 295 and 80°K. This temperature independence of the energy scale is important since as can be seen, the leading edge does deviate from the $E = h\nu$ line a bit more at 80°K than at room temperature.

Regions of high conduction band density of states structure can also be determined from the structure plots. Transitions to such high density of states regions produce EDC structure which is independent of the photon energy. Therefore, such structure is described by a line of zero slope whose E-axis intercept is the origin of the final density of states region. It is quite interesting to note that no EDC structure is characteristic of a high density of conduction states at room temperature [see part (a)] but at 80°K [part (b)] there is clearly a peak which has a fixed final state energy of 8.8 eV. This is a graphic demonstration of the temperature dependent Br 4d-derived conduction state density examined in detail in the last chapter. Note that the structure which originates -0.8 eV in the valence band does not appear to be influenced by this final state region. It would thus appear that these conduction states only occur over a restricted portion of the Brillouin zone, and the excitations from valence states above about -3.0 eV (i.e., 11.8 - 8.8 eV) conserve crystal momentum. The optical excitation process will be examined in detail in section C. There is some evidence for a 9.3 eV conduction band peak at 80°K as can be seen for the -0.8 eV structure as it moves to this final state energy and the behavior of a few shoulders originating deeper in the valence states [see part (b)]. However, it should be noted that the peaks are also diminishing in strength eventually becoming a shoulder at $h\nu = 10.5$ eV . Therefore, this change in movement of the -0.8 eV structure with $h\nu$ variation is believed due to the influence of the change in EDC structure character beginning around 9.5 eV as was pointed out in the last chapter (see also Table VIII.1).

It is important to realize that we have not made any assumptions about the optical excitation process in locating these high density of state regions. If k conservation is not an important selection rule, then the structure corresponding to these density of states regions will behave in the manner described above due to conservation of energy. If k is conserved, then this behavior can occur for transitions between the high density of states region and a sharply changing band in the same region of the Brillouin zone. Thus, the assignments made for EDC structure which follows either a unit or zero slope line on the structure plot are independent of the nature of the optical excitation process.

The zero slope line which fits the position of the trailing edge extrapolation is a good measure of the vacuum level. It is interesting to note that the AgBr photoemission threshold is reduced by 0.1 eV upon cooling to 80°K. This was also observed in the AgBr yield presented in Chapter V (see Fig. 5.7).

All of the AgBr electronic structure information is summarized in Table VIII.2. The energies were determined as discussed above from

TABLE VIII.2. Summary of information determined for the electronic states of AgBr .

ENERGY ($\pm$ 0.1) (eV)	ORIGIN	DEGREE OF MIXING[*]
> 9.5	Ag (5p) ?	H
8.8	Br (4d)	H
7.15	Vacuum Level	
0	Valence Band Maximum	
- 0.85	Br (4p)	H
- 2.9	Br (4p)	H
- 3.3	Bottom of Br (4p) Band	
- 3.7	Ag (4d)	P
- 5.0	Ag (4d)	H
- 6.0	Bottom of Valence Band	

[*]H = Hybridized, P = Pure

the structure plots of many sets of data. To show the reproducibility
of not only the data but the energies determined from it, the structure
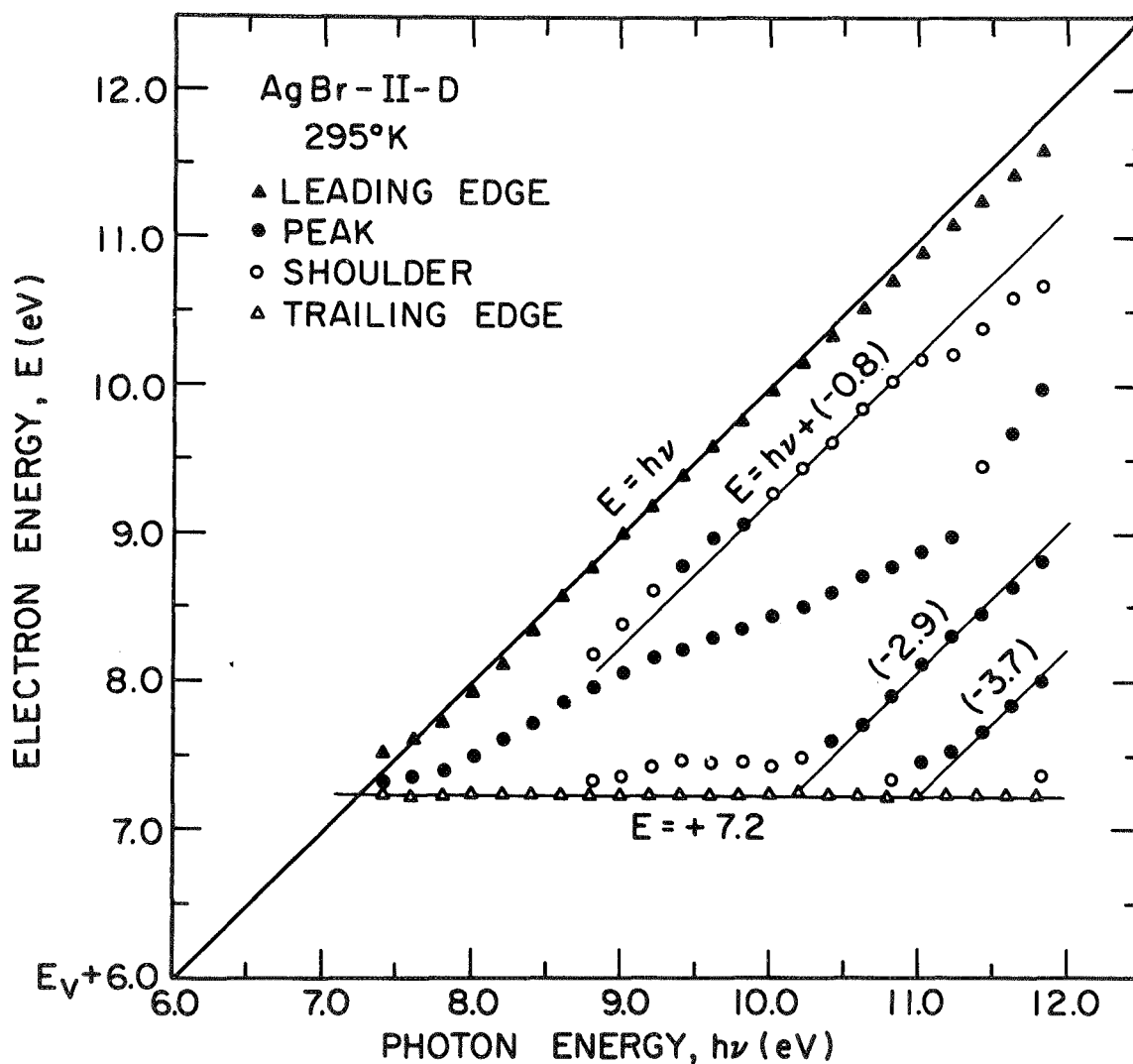plot for another AgBr sample at room temperature is shown in Fig. 8.2.
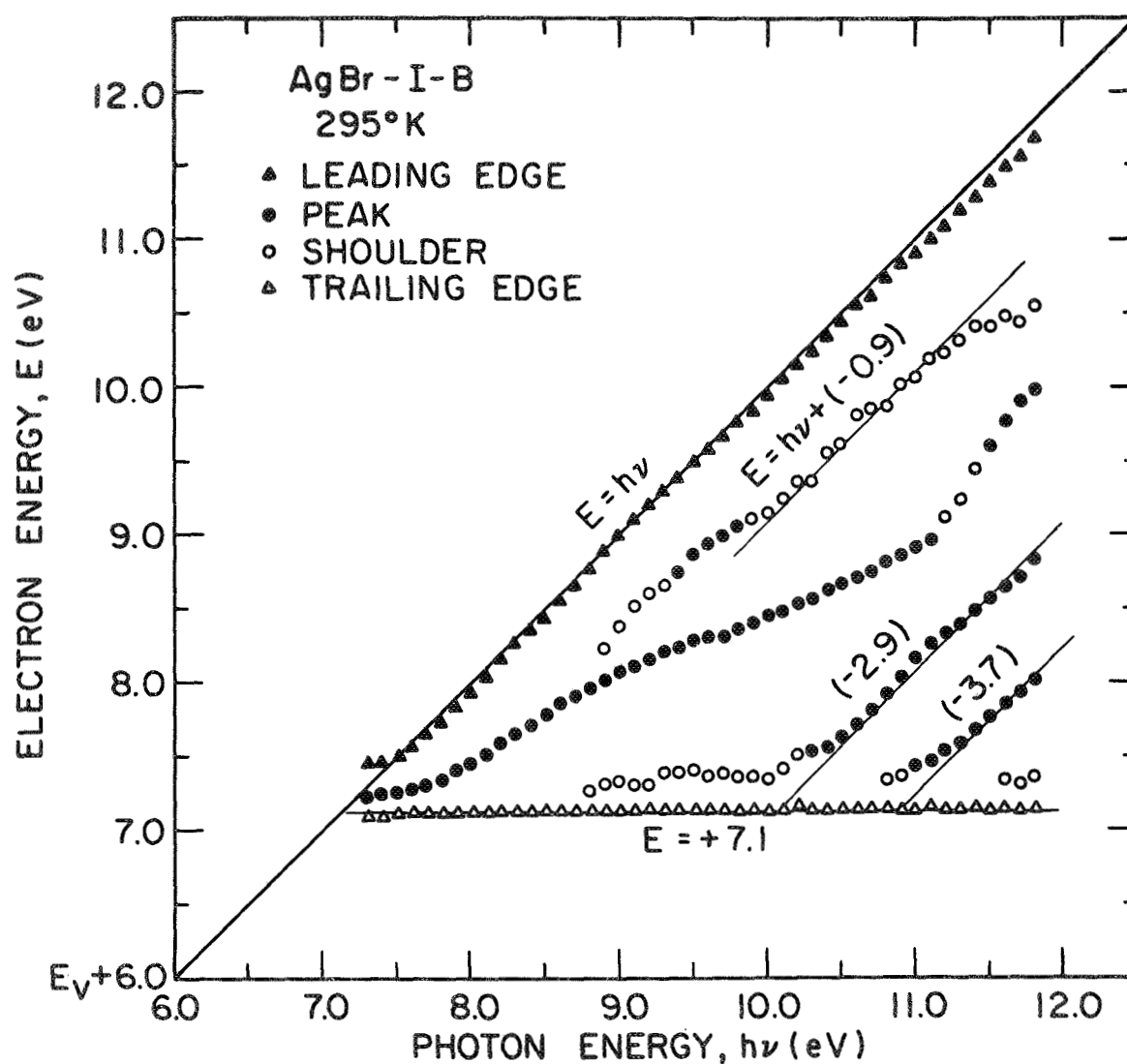
FIGURE 8.2. Spectral distribution of the AgBr EDCs' structure
and edges at 295°K. Unit and zero slope lines, with
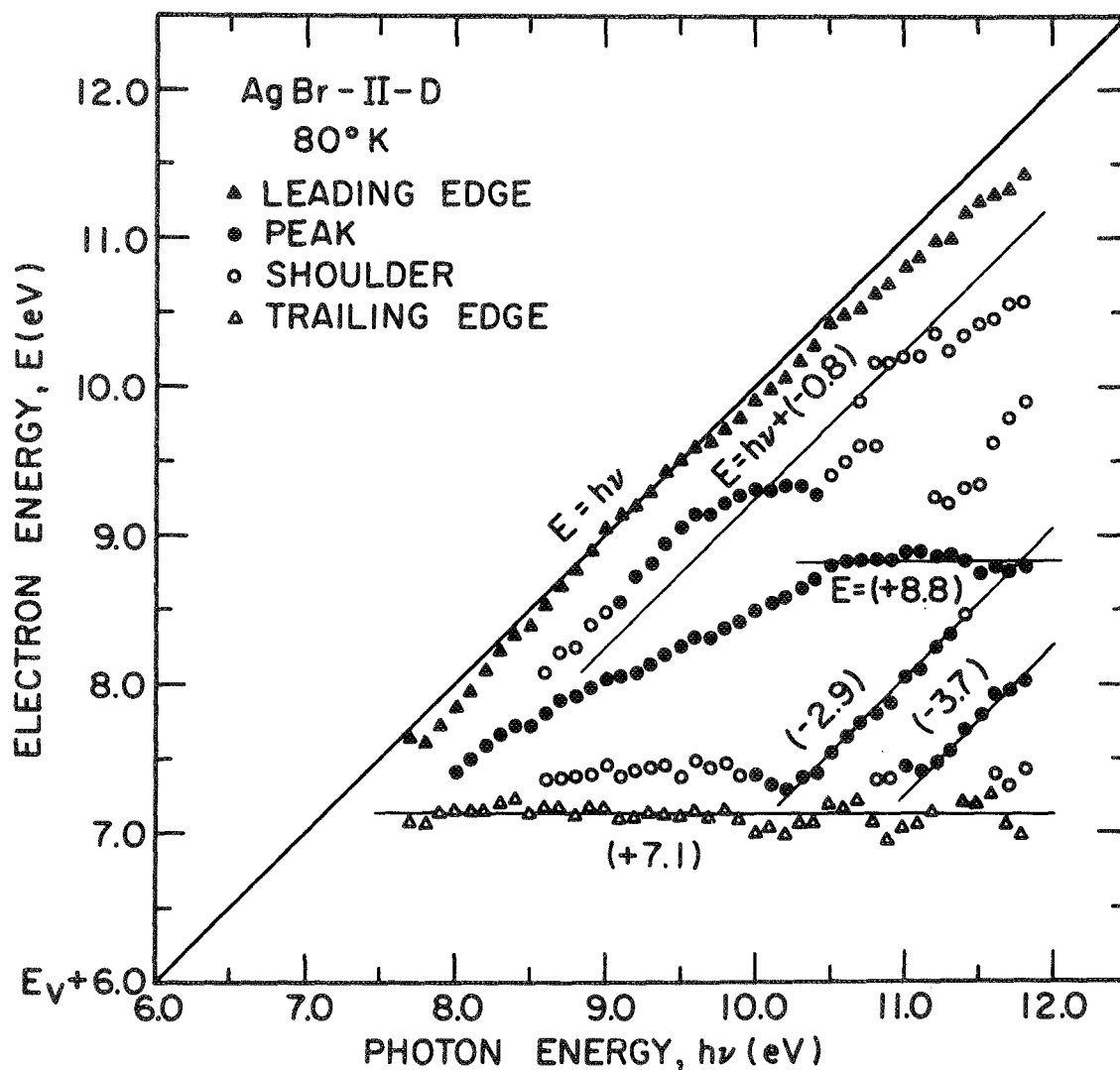their electron energy-axis intercepts, are shown fit
to appropriate data.

Noting the high reproducibility of the data and the errors discussed in Chapter IV, it is believed that these energies are known to ± 0.1 eV. The atomic origin of the various density of states structure is indicated in the table along with the extent of the wavefunction mixing associated with the states. This information on the detailed origin of the structure was determined in the last three chapters.

The EDCs of AgCl can also be analyzed using structure plots to observe the systematic variation of their structure with changing photon energy. Such plots are shown at 295 and $80°K$ in Fig. 8.3. Regions of high density of states can be located at -0.7, -2.6, and -3.3 eV in the AgCl valence band. It is important to note that the temperature independent structure originating at -3.3 eV remains constant in energy even though the leading EDC edge departs significantly from the E = hν line at $80°K$ for low photon energies. The final density of states region at 8.1 eV, which was discussed extensively in the last chapter, is clearly evident on these plots. It is interesting that it affects the AgCl EDCs at both room and liquid nitrogen temperatures in contrast to the AgBr 8.8 eV structure which is only seen at $80°K$ (see Fig. 8.1). The vacuum level is constant with temperature at 7.6 eV in AgCl . The reproducibility of this data and the energy locations is shown by the structure plot of Fig. 8.4 for another sample at $295°K$. These AgCl energies can be summarized in Table VIII.3. As in the case

TABLE VIII.3. Summary of information determined for the electronic states of AgCl .

ENERGY (± 0.1) (eV)	ORIGIN	DEGREE OF MIXING[*]
> 10.2	Ag (5p) ?	H
8.1	Cl (3d)	H
7.55	Vacuum Level	
0	Valence Band Maximum	
- 0.8	Cl (3p)	H
- 2.65	Cl (3p)	H
- 3.0	Bottom of Cl (3p) Band	
- 3.3	Ag (4d)	P

[*]H = Hybridized, P = Pure
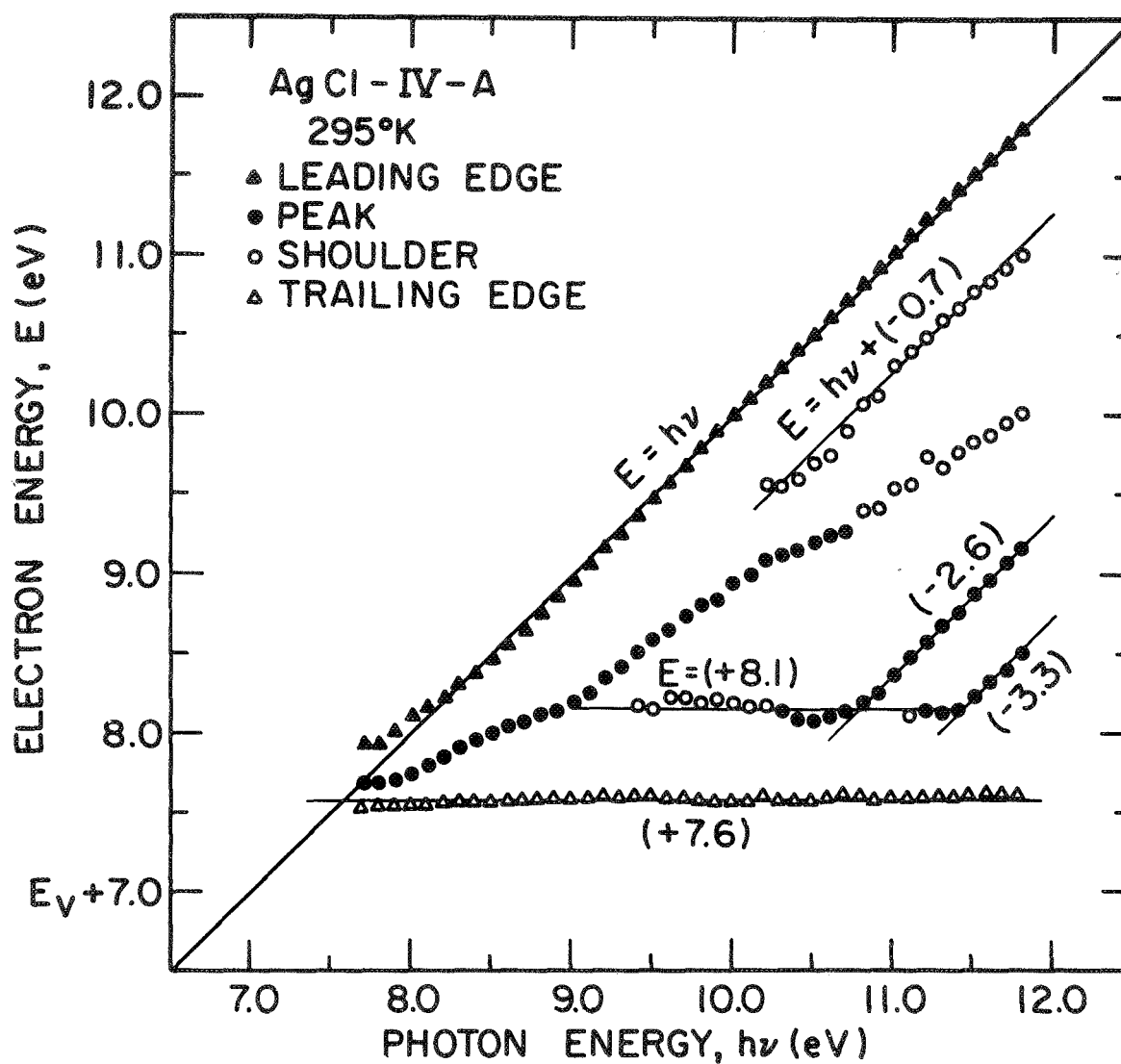
FIGURE 8.3(a).   Spectral distribution of the   AgCl   EDCs'
structure and edges at 295°K.   Unit and
zero slope lines, with their electron
energy-axis intercepts, are shown fit to
appropriate data.
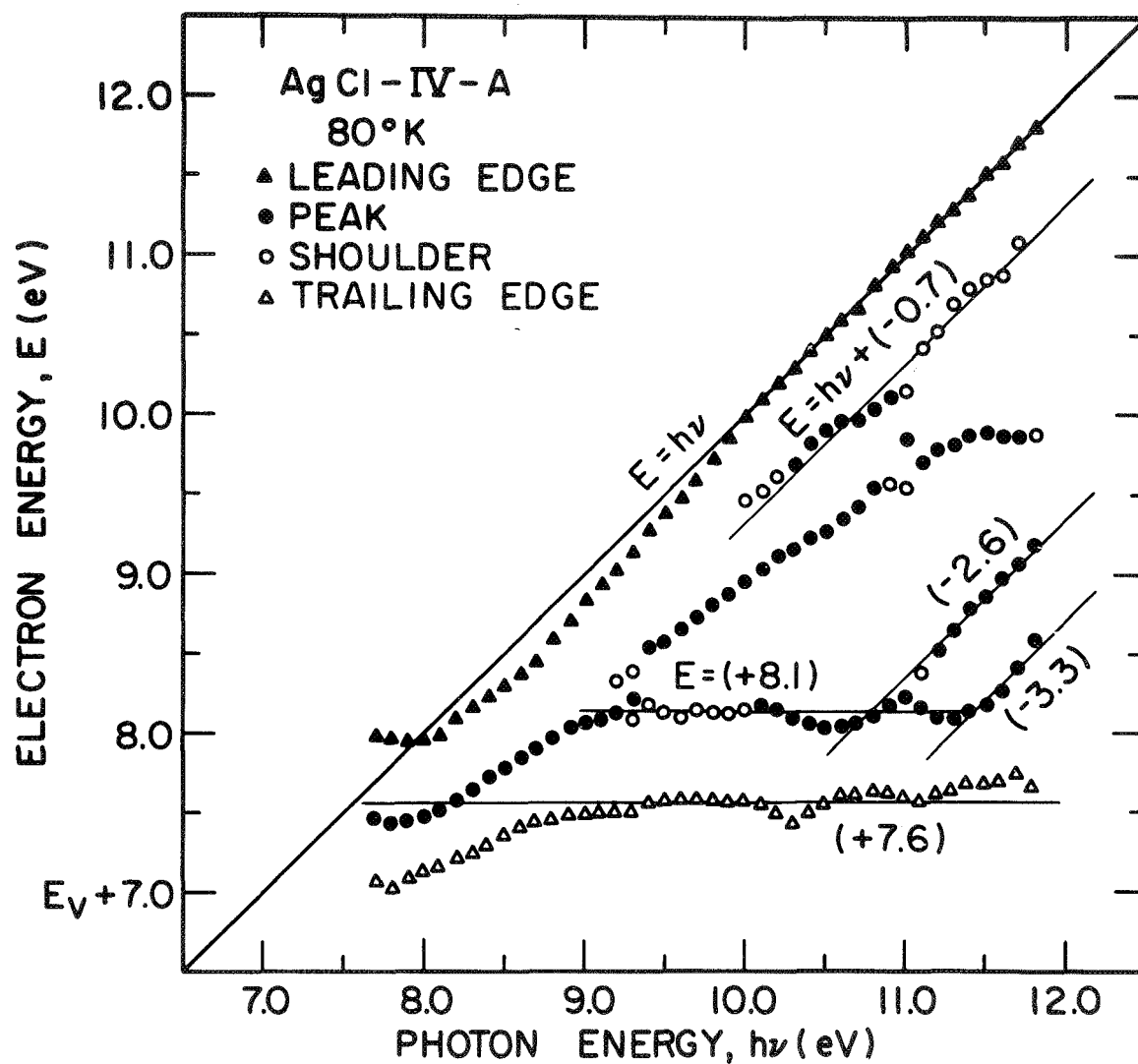
FIGURE 8.3(b). Spectral distribution of the AgCl EDCs'
structure and edges at 80°K. Unit and
zero slope lines, with their electron
energy-axis intercepts, are shown fit to
appropriate data.
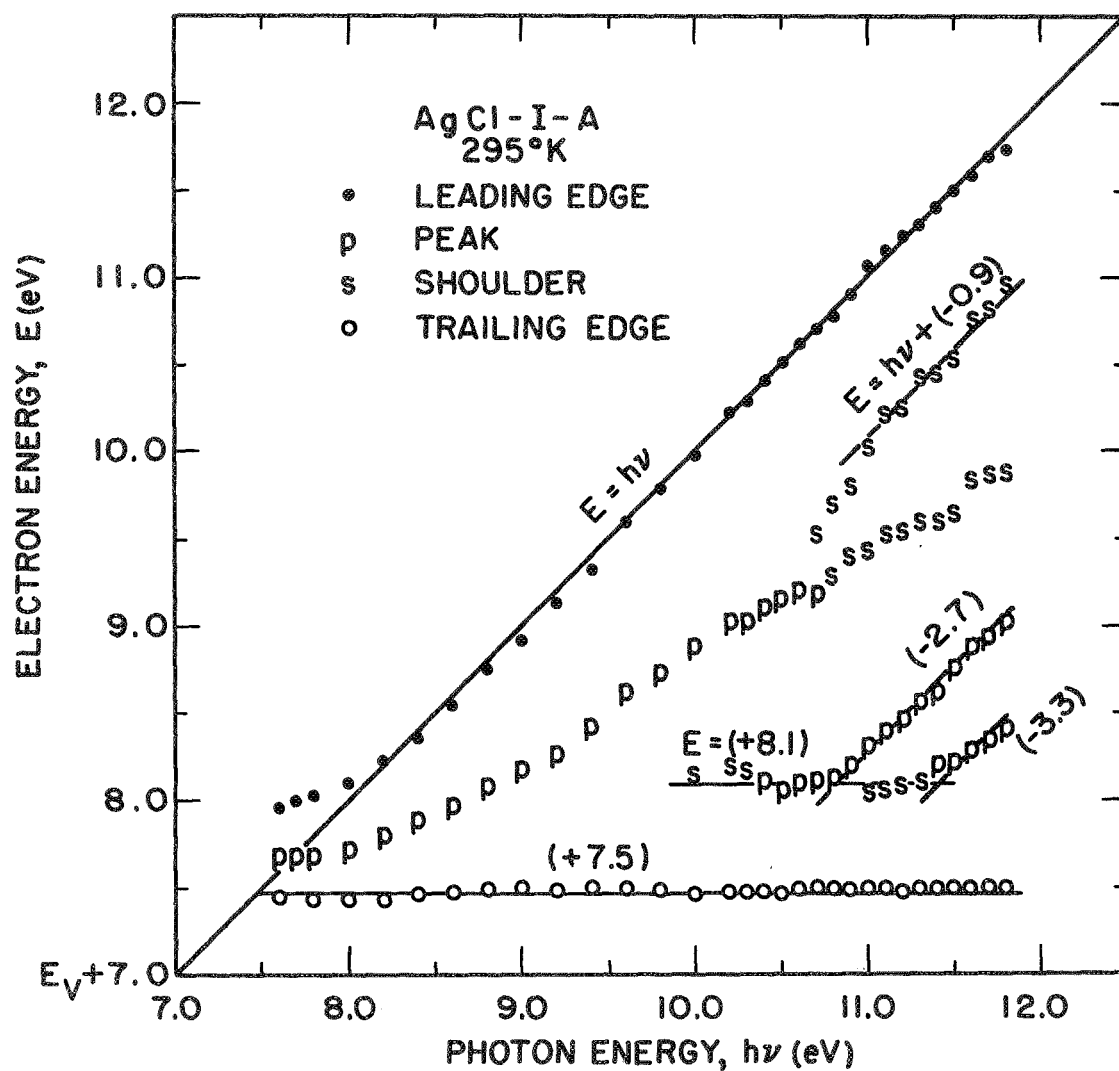
FIGURE 8.4. Spectral distribution of the AgCl EDCs'
structure and edges at 295°K. Unit and
zero slope lines, with their electron
energy-axis intercepts, are shown fit to
appropriate data.

of AgBr , we have included the atomic origin and degree of mixing of
the states corresponding to these energies as determined in the last
three chapters.

B. Comparison to Energy Band Structures

It is helpful in evaluating both the validity of these assignments
and the calculations of the energy bands to compare the results sum-
marized in section A to the band structures which are reported in the
literature. As pointed out in Chapter III, the APW calculations of
Scop[6] do not yield any reasonable agreement in energy with our findings
and will thus not be discussed here. On the other hand, the speculative
band structures of Bassani, Knox, and Fowler[3] (hereafter referred to as
BKF) agree surprisingly well with our results even though they are only
based on calculations of the AgCl valence band and measured silver
halide optical properties. Their estimate for the AgBr band structure
is reproduced in Fig. 8.5. The estimate of Seitz for the separation of
the Ag 5p and 5s states in the silver halides,[41] is included with
these bands as an estimate of the location of the Ag 5p-derived states.
The regions of high density of states determined by these photoemission
studies (see Table VIII.2) are shown by the shaded areas superimposed on
the bands. It should be noted that the atomic designations on the right
side of the figure refer to the orbitals from which the BKF states at
Γ and the bands emanating from this point are derived. Since they are
not interpretations of our data, it is significant that the origin
determined from the photoemission data correctly corresponds to these
labels in every case. The -3.7 eV region, which was related to the Ag
states with almost pure 4d symmetry, lies precisely where the very
flat Ag 4d bands have been placed by BKF. It should be recalled that
these flat bands are composed of localized states which are not signi-
ficantly hybridized.[109] The -5.0 eV structure occurs in a high density
of hybridized Ag 4d states in the bands as we found it should. The
other valence structure lies in the Br 4p-derived region of the bands
as we predicted. One can see that there is room here for adjustment of
the calculation to better fit our data. For example, the highest Δ_6

AgBr

FIGURE 8.5. The electronic band structure of AgBr as speculated by
Bassani, Knox, and Fowler (reference 3) with the estimate for the
Ag (5p) states by Seitz (reference 41). The atomic designations are
the orbitals from which the states at Γ are derived. The vacuum
level (---), possible beginning of the Ag(5p) states (— - —), and
regions of high density of states (shaded) determined from these
studies are superimposed on these bands.

200

band could be lowered into the range of the -0.8 eV experimental density of states region. The calculated conduction states substantiate the basic assignments made in the last chapter. The broken line shown at 9.5 eV is the experimentally determined starting energy for the Ag 5p-derived conduction states (see Table VIII.2). This is in accord with the general computed locations for the Ag 5p and Br 4d states. The 8.8 eV Br 4d-derived density of states was predicted to be near the energy where many states merge at Γ to obtain the proper temperature dependence of the corresponding EDC structure. Not only are the BKF bands in this energy range clearly Br 4d-derived in agreement with our predictions, but even the Γ'_{25} energy is consistent with our interpretations of Chapter VII. In fact, this location in the region of Γ is consistent with the lack of observed EDC effects for direct transitions to this energy from -0.8 eV valence states which are seen in Fig. 8.5 to lie between the center and boundaries of the zone (e.g., Δ and Σ).

The data is compared to the AgCl electronic band structure of BKF[3] in Fig. 8.6. The Ag 5p states are again located in the energy bands using the estimate of Seitz for the Ag 5s to 5p separation in the silver halides.[41] Carrera has estimated the locations of the three Γ energy states above Γ_1 by comparison of his recent AgCl far UV optical studies to the measurements of KCl .[45] These are included in the band structure also. The effect of these new estimates are to lower the Cl 3d-derived Γ'_{25} level a few tenths of an eV towards the location of our high density of states at 8.1 eV. However, the experimentally located structure would still occur at L rather than at Γ , as it did for AgBr (Fig. 8.5). This non-negligible L state density may be the difference which allows the halogen d-derived states to be observed at 295°K in AgCl but only at 80°K in AgBr (compare Fig. 8.3 to 8.1). Further, the experimental location of the beginning of the Ag 5p-derived states at 10.2 eV is consistent with the theoretically estimated states in Fig. 8.6. The coincidence of the -3.3 eV density of states with the nearly flat Ag 4d states is totally consistent with our temperature independent EDC structure predictions of Chapter VI. The

FIGURE 8.6. The electronic band structure of AgCl as speculated by Bassani, Knox, and Fowler (reference 3) with the estimates for the Ag (5p) states by Seitz (reference 41) and the conduction states at Γ by Carrera (reference 45). The atomic designations are the orbitals from which the states at Γ are derived. The vacuum level (– – –), possible beginning of the Ag (5p) states (— - —), and regions of high density of states (shaded) determined from these studies are superimposed on these bands.

higher hybridized Cl 3p-derived structure lies in the proper energy
range as determined by BKF. These valence p state results provide a
1 eV estimate for the error of the calculated highest valence Δ_1 state.
It should be noted that there are relative maxima such as this calculated
at other points in the Brillouin zone (i.e., Σ_4 by reference 3) which
probably also contribute to a density of states at about -0.8 eV in both
AgCl and AgBr.

These comparisons serve to substantiate the electronic structure
results determined by our studies. Since these assignments were made
on the basis of the temperature dependence of the EDCs as interpreted
using the dynamic hybridization model, this agreement is further evi-
dence for such a description of silver halide photoemission. These
results can now be used as a basis for more refined calculations of the
electronic band structure of the silver halides.

C. The Optical Excitation Process

We have already considered in Chapter VII one selection rule for the
optical excitations which is of major importance to the EDCs. It was
found that since the halogen valence p-derived states and the Ag 5p-
derived conduction states were of the same parity, dipole transitions
between them were forbidden by symmetry. The other major selection rule
of importance in determining the characteristics of the EDCs is the re-
quirement of conserving crystal momentum, k , in an optical transition.
As was pointed out clearly by Shay and Spicer,[114] one of the necessary
conditions for non-conservation of k (i.e., "nondirect" transitions)
is that the position of the EDC structure either be independent of photon
energy or change energy by increments equal to the $h\nu$ variation. This
is equivalent to requiring the EDC structure to follow a unit or zero
slope line on a structure plot. As is quite clear from the plots of
Figs. 8.1 and 8.3, there is one piece of structure which moves through
the entire set of both AgBr and AgCl data with a locus which is
considerably different from either of these test slopes. One can readily
conclude that k-conservation is important for transitions from the hybrid-
ized halogen p-derived states which correspond to this EDC structure;

this is the structure which was referred to as "DIRECT" in Tables 5.2 and 5.3. The other structure all satisfies the necessary nondirect condition so we must examine two additional properties.

If the transitions are non-k conserving, then by conservation of energy one would expect the EDC structure to first become noticeable when the photon energy was high enough to bring it above the vacuum level. In other words, if there were no peculiar structure or characteristics of the conduction states, then structure should not suddenly appear in the middle of the EDC if only energy conservation is important. The -0.8 eV structures in both AgBr and AgCl do "pop" into the EDC on the leading edge. This can be seen in Fig. 5.1 for AgBr where the onset at 80°K is very sharp between $h\nu = 9.0$ eV and 9.2 eV. For AgCl, the structure is not as sharp; however, in Fig. 5.8 there is clearly structure at 80°K which is first observed between $h\nu = 9.2$ and 9.4 eV at the leading edge of the EDC. On the basis of these observations, we can conclude that optical excitation from -0.8 eV in the valence states of AgBr and AgCl conserve crystal momentum in the transition.

The other criterion which can be used in evaluating the k-conservation selection rule is the height modulation of the EDC structure. One must be careful, however, since the heights can only be compared if the curves are normalized to the absorbed photon flux. As was pointed out in Chapter III, this can only be done at room temperature since the optical properties of the silver halides have not been measured at low temperatures in this photon energy range. The room temperature EDCs of AgCl , corrected for sample reflectivity using the data of White,[46] are presented in Fig. 8.7. There curves were normalized with yield based on the 11/66 calibration of the Cs_3Sb F-7 standard by Koyama; therefore, the EDCs are uniformly too high by about 30% (see Appendix C). As can be seen by close study of this data, the only height modulation occurs after all the structure emerges above the threshold, and it is simply a continuous loss of strength as the structure goes to higher final state energies. This is really not very valuable since such an effect can just be explained by simple conservation of energy and assuming a conduction density of states with decreasing magnitude as the energy increases. Physically
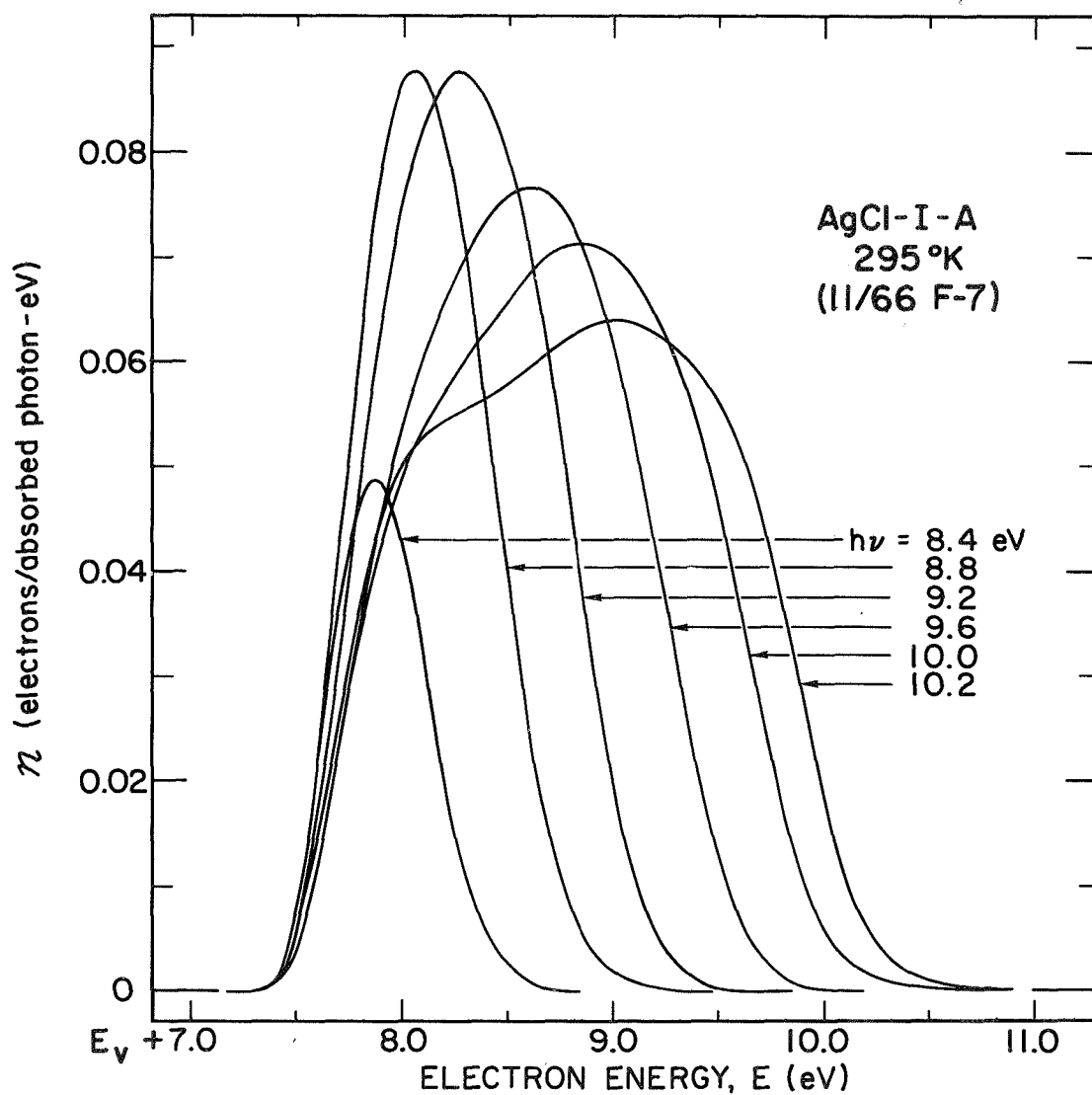
FIGURE 8.7(a). Comparison of energy distributions normalized
to absolute quantum yield (per absorbed photon)
for electrons photoemitted from AgCl at $295°K$
for photon energies of 8.4 through 10.2 eV.
This normalization is based on the 11/66
calibration of the Cs_3Sb standard F-7, and
the curves are thus uniformly too high by 29%
at all photon energies (see Appendix C).
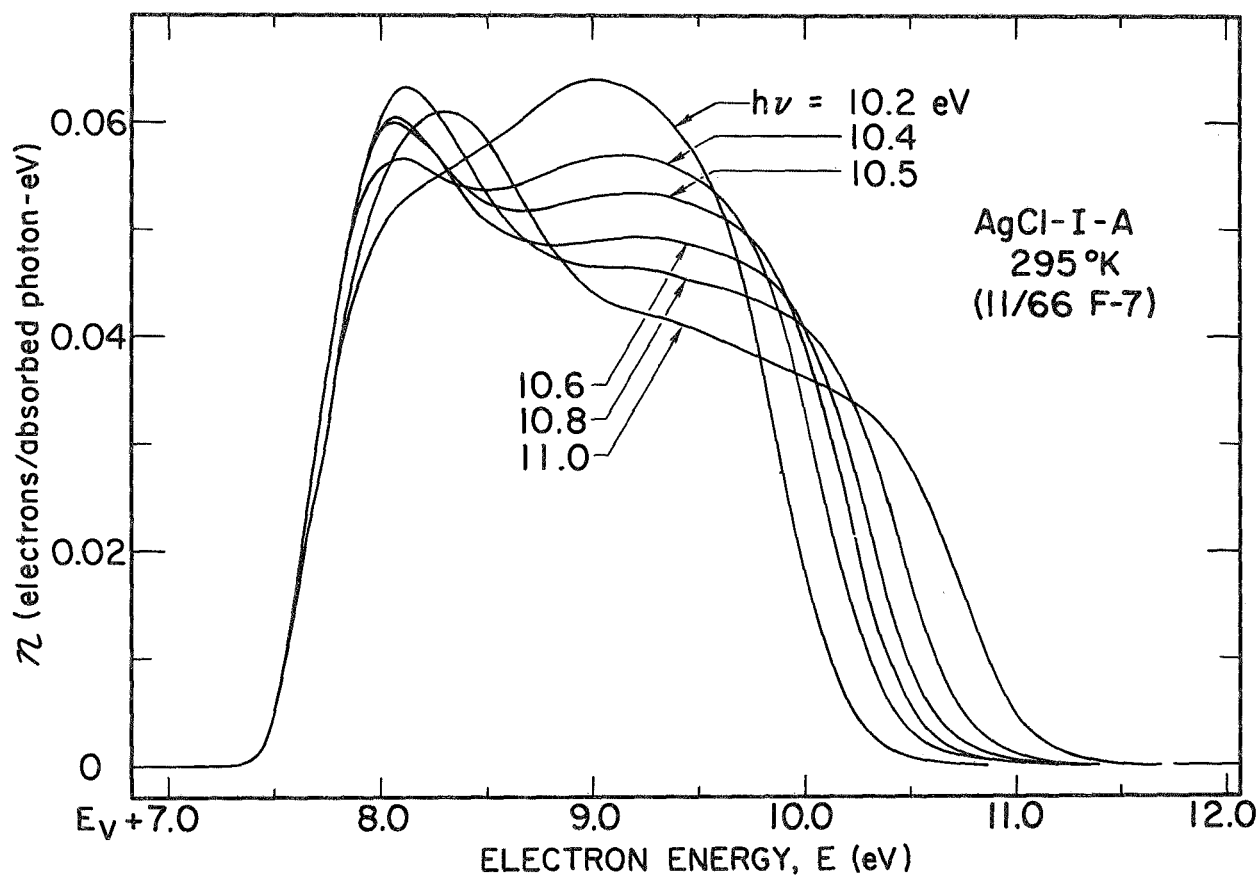
FIGURE 8.7(b). Comparison of energy distributions normalized to absolute quantum yield (per absorbed photon) for electrons photoemitted from AgCl at 295°K for photon energies of 10.2 through 11.0 eV. The normalization is based on the 11/66 calibration of the Cs_3Sb standard F-7, and the curves are thus uniformly too high by 29% at all photon energies (see Appendix C).
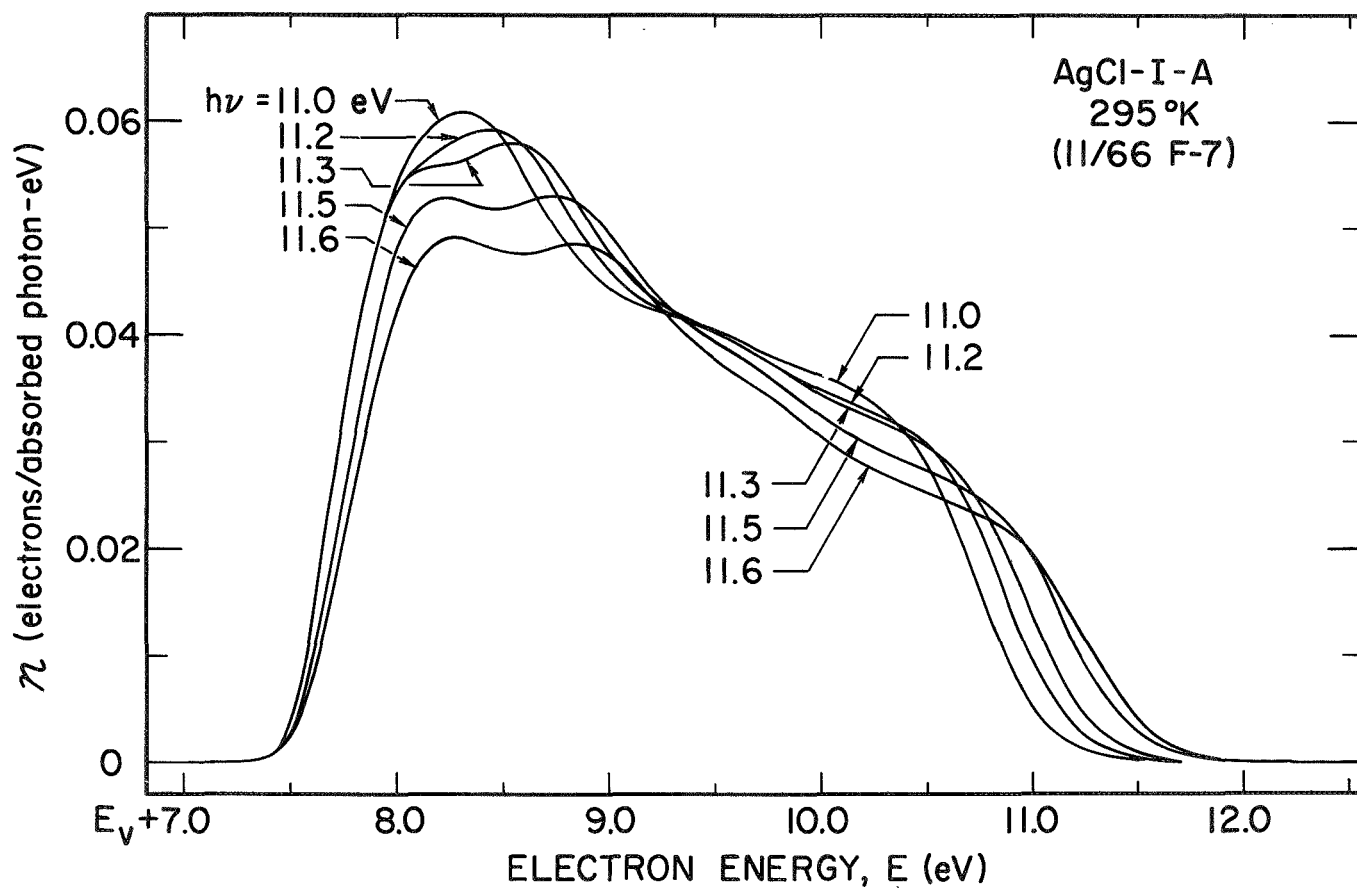
FIGURE 3.7(c). Comparison of energy distributions normalized to absolute quantum yield (per absorbed photon) for electrons photoemitted from AgCl at 295°K for photon energies of 11.0 through 11.6 eV. This normalization is based on the 11/66 calibration of the Cs$_3$Sb standard F-7, and the curves are thus uniformly too high by 29% at all photon energies (see Appendix C).

such an assumption is reasonable since the hybridized d conduction states will have more p character as the energy approaches the Ag 5p-derived state range; therefore, the transitions from the valence halogen p-derived states should become weaker at higher final state energies.

We consequently have no evidence for the remaining two pieces of EDC structure of each halide that k need be conserved in the optical transitions. It should be noted that the lower structure (-3.7 eV in AgBr and -3.3 eV in AgCl) corresponds to Ag states with almost pure 4d symmetry. Thus, the energy bands are very flat and k is not a very good indexing parameter for these energy states. The question of k-conservation is really not meaningful for transitions from such electronic states. We therefore conclude that for the four predominant EDC features associated with the AgBr and AgCl valence states: (1) transitions from the highest two sets of states appear to conserve crystal momentum, (2) there is no reason to believe that k is or is not conserved in transitions from -2.9 eV in AgBr and -2.6 eV in AgCl, and (3) the question of whether conserving k is an important selection rule is not meaningful for the -3.7 eV AgBr states or the -3.3 eV AgCl states. It is important to note that conclusion (1) is consistent with the observation made in section A of the effect of the 8.8 eV AgBr conduction state structure on the "direct" but not the -0.8 eV valence structure (see Fig. 8.1).

D. Comparison of Silver and Cuprous Bromide and Chloride
   Photoemission

Because of the basic similarities between the noble metal halides, this study and that by W. F. Krolikowski of the cuprous halides[1] should reinforce each other and lead to a better understanding of each. The resemblances in photoemission from the silver and cuprous halides are quite striking. Comparing the results of this study, just summarized above, with the room temperature data of Krolikowski,[1] it is seen that there is considerable structure in the EDCs of the silver halides which varies in both magnitude and position with $h\nu$ variation in the same

manner as structure for the corresponding cuprous halide. Such simi-
larities between the bromides are well illustrated by the highest energy
structure in the 11.5 eV EDCs shown in Fig. 8.8. The leading part of

FIGURE 8.8. Comparison of energy distributions for electrons
photoemitted from AgBr (normalized to quantum
yield per absorbed photon) and CuBr (un-normalized)
from the work of Krolikowski (reference 1) at 295°K
for a photon energy of 11.5 eV. Part of the CuBr
curve is expanded by the factor shown. Note that the
electron energy scales are different for the two curves.

the CuBr EDC is expanded for easier comparison. This structure reaches its maximum as a peak at a photon energy of about $h\nu = 9.5$ eV at room temperature for both AgBr (see Fig. 5.1) and CuBr . The EDC structure, which shows common features for the two materials, lines up in energy quite well when the E-axis is linearly scaled. The necessity for scaling is to be expected when it is recalled that in addition to the difference of Ag and Cu , these noble metals give rise to different crystal structures for the silver (cubic-NaCl) and cuprous (cubic-ZnS) halides. This coincidence in scaled energy of the similar structure also occurs for the chloride compounds as depicted at $h\nu = 11.6$ eV in Fig. 8.9. Again for CuCl the leading part of the curve is expanded for easier comparison. It should be recalled that the structure which we associate with the Ag 4d-derived states is the farthest peak on the left side of the silver halide EDCs of Figs. 8.8 and 8.9. In addition, the structure which Krolikowski associated with the Cu 3d states of the cuprous halides is the very strong peak on the left side of these EDCs. The close correlation of these two peaks in the figures and the other similarities of EDC structure serves to substantiate the d state locations in both sets of halides. This coincidence in scaled energy of the noble metal d state structure is quite significant not only because it locates these states but also because it supports the assignment of the highest filled states to the halogen p-derived orbitals. The atomic origin of the valence band maximum has been the subject of speculation in the cuprous as well as silver halides for decades (see reference 1 for a historical discussion).

It is important to note that for both sets of halides, the Cu 3d EDC structure originates deeper in the valence states than the Ag 4d structure does even though the Cu 3d states lie higher in energy for the noble metals. This reversal in relative position of the two sets of d-states would seem to imply that the noble metal d-halogen p mixing is stronger in the cuprous halides than it is in the silver salts. One can thereby understand why only three pieces of structure occur in the cuprous halide EDCs presented in Figs. 8.8 and 8.9 while four are observed for the silver halides at the same photon energies. It should
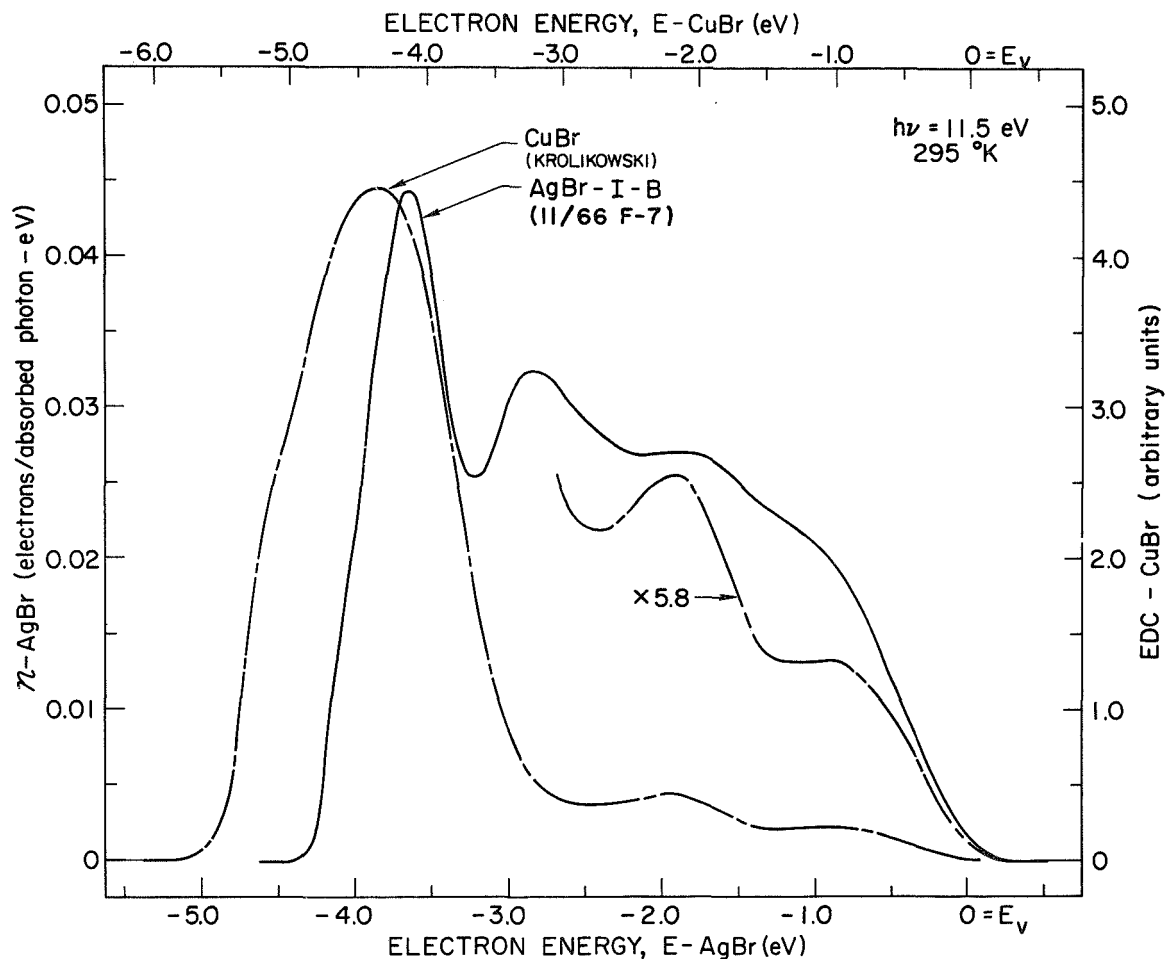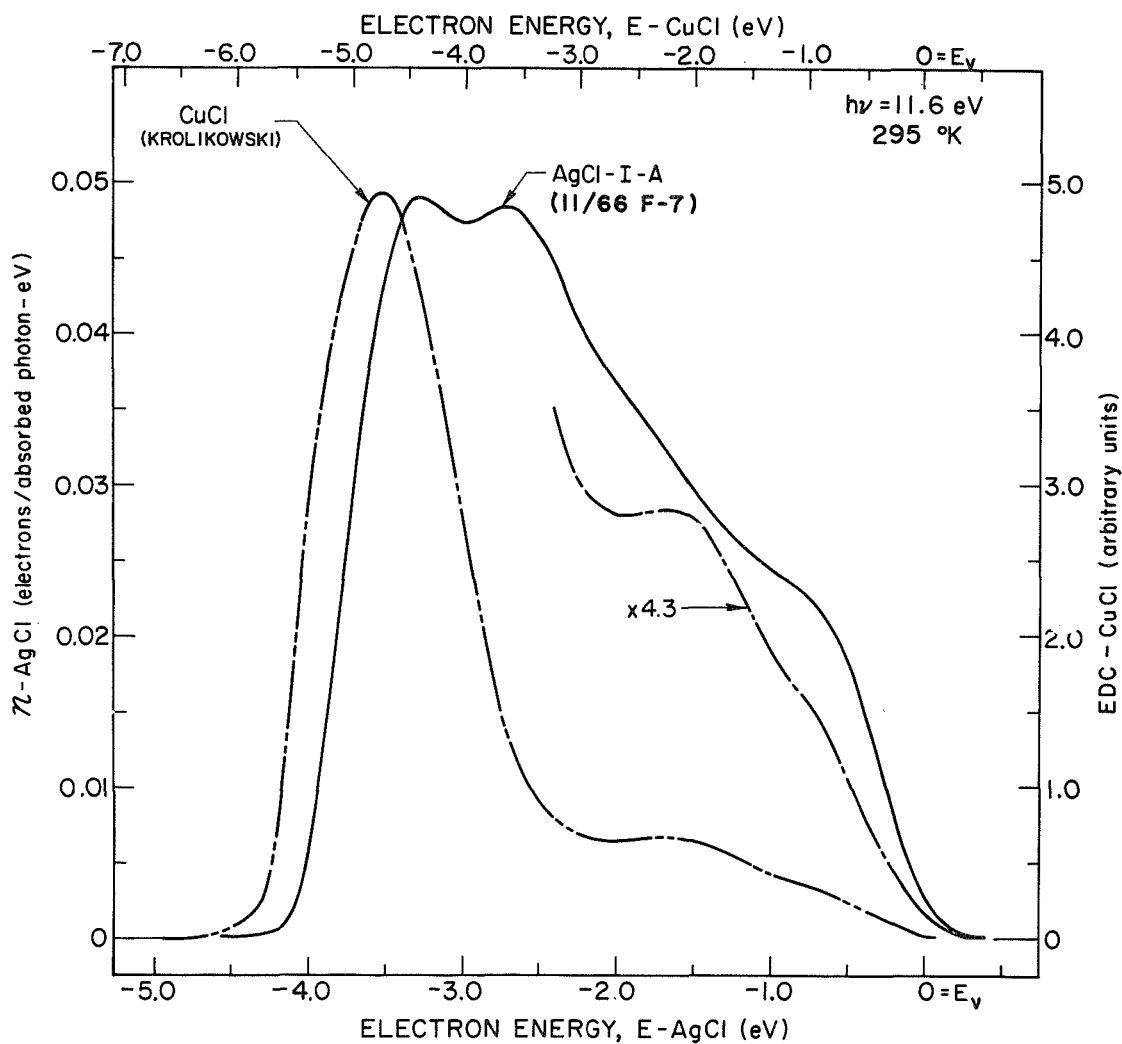
FIGURE 8.9. Comparison of energy distributions for electrons
photoemitted from AgCl (normalized to quantum
yield per absorbed photon) and CuCl (un-normalized)
from the work of Krolikowski (reference 1) at 295°K
for a photon energy of 11.6 eV. Part of the CuCl
curve is expanded by the factor shown. Note that the
electron energy scales are different for the two curves.

be noted that this absence of structure occurs in the region of the halogen p-derived states of the silver halides and above the energy of the structure corresponding to the Cu 3d-derived states of the cuprous halides. It is thus reasonable to hypothesize that the p states are so highly hybridized and widely spread in energy that the large peak on the left side of the cuprous halide EDCs contains not only Cu 3d-derived states but also hybridized halogen p-derived states. It follows from this large p-d mixing of the cuprous halide valence states that the hybridized levels should be significantly modulated by the vibrations of the lattice. If the left peak were derived from Cu states with almost pure 3d symmetry, then, as we saw for the silver salts in Chapter VI, this EDC structure would be independent of temperature. On the other hand, if it also contained hybridized p states as speculated above, then this peak's width would be temperature dependent. The temperature dependence of cuprous halide photoemission would therefore be a most powerful tool in testing this hypothesis.

It is interesting to note that if the structure which is not seen in the cuprous halide data is neglected, the structure plots of the corresponding silver and cuprous halides are essentially identical in character. Such a comparison leads to an important observation. The motion of the central cuprous halide structure with hv variation is such that it appears very much like the superposition of the lower two hybridized p-derived structures in the silver halides. Therefore, one might conclude that the p-d mixing is less in the cuprous halides leading to a narrower p-derived band. As should be evident, a complete comparison of the temperature dependent cuprous halide photoemission to silver halide photoemission would be extremely informative in interpreting the structure plots. One thing that can be concluded from comparing just the room temperature plots which are available is that there is a significant amount of cuprous halide EDC structure which is characteristic of k-conserving optical transitions. In particular, there is some structure which, like the -0.8 eV silver halide structure, emerges on the leading side of the EDCs. It is reasonable to conclude from the resemblances of these noble halide EDCs that Krolikowski's basic nondirect

assumption for <u>all</u> optical transitions in the cuprous halides is probably incorrect. Cooling the cuprous halides should even accentuate these direct transition effects more. Much of the conduction density of states structure which Krolikowski postulated to explain these effects are probably artificial and not representative of the bulk properties of the cuprous halides.

IX. THE ELECTRONIC STATES OF AgI

The electronic states of AgBr and AgCl have been the only
silver halides discussed extensively thus far. As pointed out in
Chapter I, AgI is examined separately because of its differing crystal
structure and the considerably lesser amount of knowledge of its prop-
erties. Because of this lack of information, one of the prime methods
of anlayzing the AgI results will be to compare its photoemissive
properties and their temperature dependences to those of the other
halides which have been interpreted above. This will lead to perhaps
the first definitive estimate for the composition of the AgI elec-
tronic states.

A. Experimental

1. Sample Characteristics

Most of the details concerning the preparation of AgI samples
were included in the discussion of Chapter IV. The evaporation condi-
tions for each of the samples studied are included in Table IV.1. One
of the important considerations which was not discussed fully was the
crystalline modification of the thin films studied. AgI has three
phases at normal pressure.[115] The stable phase below about $115^{\circ}C$ is
cubic (ZnS) and it is referred to as the γ phase. Between 115° and
$126^{\circ}C$ AgI is stable in an hexagonal (wurtzite) structure which is
identified as the β phase. Above this temperature a very complex
α phase exists which is referred to as the AgI lattice. Of these,
only the γ and β modifications exist at room temperature.[116] The
room temperature phase of the films used for these studies was deter-
mined by X-ray diffraction of thick samples ($\approx$ 0.3 μm) which were
removed from the experimental chamber for analysis. The principle dif-
fraction peaks lie at almost the same angle for both the γ and β
phases; therefore, one must analyze higher order directions. The X-ray
results for two films are shown in Fig. 9.1 where the intensity is plotted

as a function of the diffraction angle. As can be seen there is no
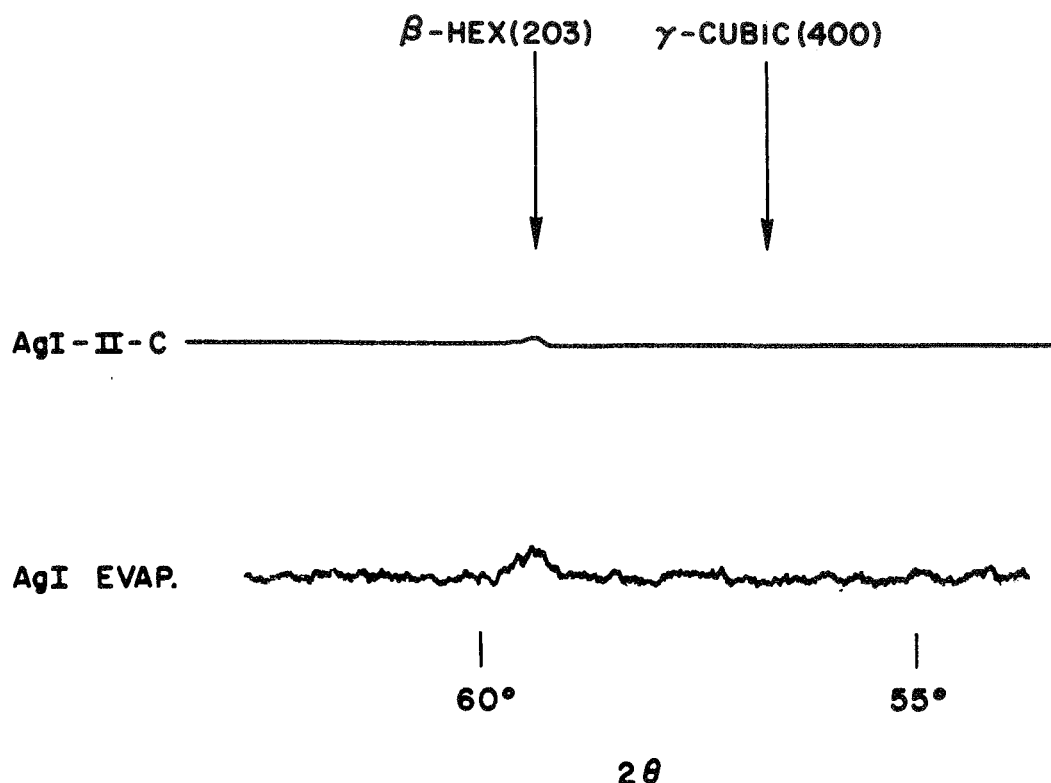
FIGURE 9.1. The angular distribution of the diffraction of X-rays
by two AgI samples. Structure is predicted for the
β and γ phases of AgI at the positions indicated
by the arrows.

evidence for the γ phase but the β-hexagonal modification is clearly
present. This is interesting because this phase is not stable at room
temperature. However, the rate with which the unstable β phase trans-
forms to γ must be negligible since none of the latter phase was ob-
served after many days had elapsed between evaporation and X-ray dif-
fraction analysis of the film. Cardona[116] and Bottger and Geddes[88] also
found that the AgI thin films which they studied were in the wurtzite
modification. Our X-ray studies show that the films used in these in-
vestigations were characteristic of polycrystalline pure AgI which is

215

highly oriented in the (002) direction with a particle size of about
800 Å (see Table IV.2). The sample designations on the data to be
presented in this chapter are followed by a "β" to emphasize the AgI
phase to which the results apply.

The AgI photoemission data was reproducible among the samples
studied. This is shown in Fig. 9.2 for two samples at $80°K$. It should
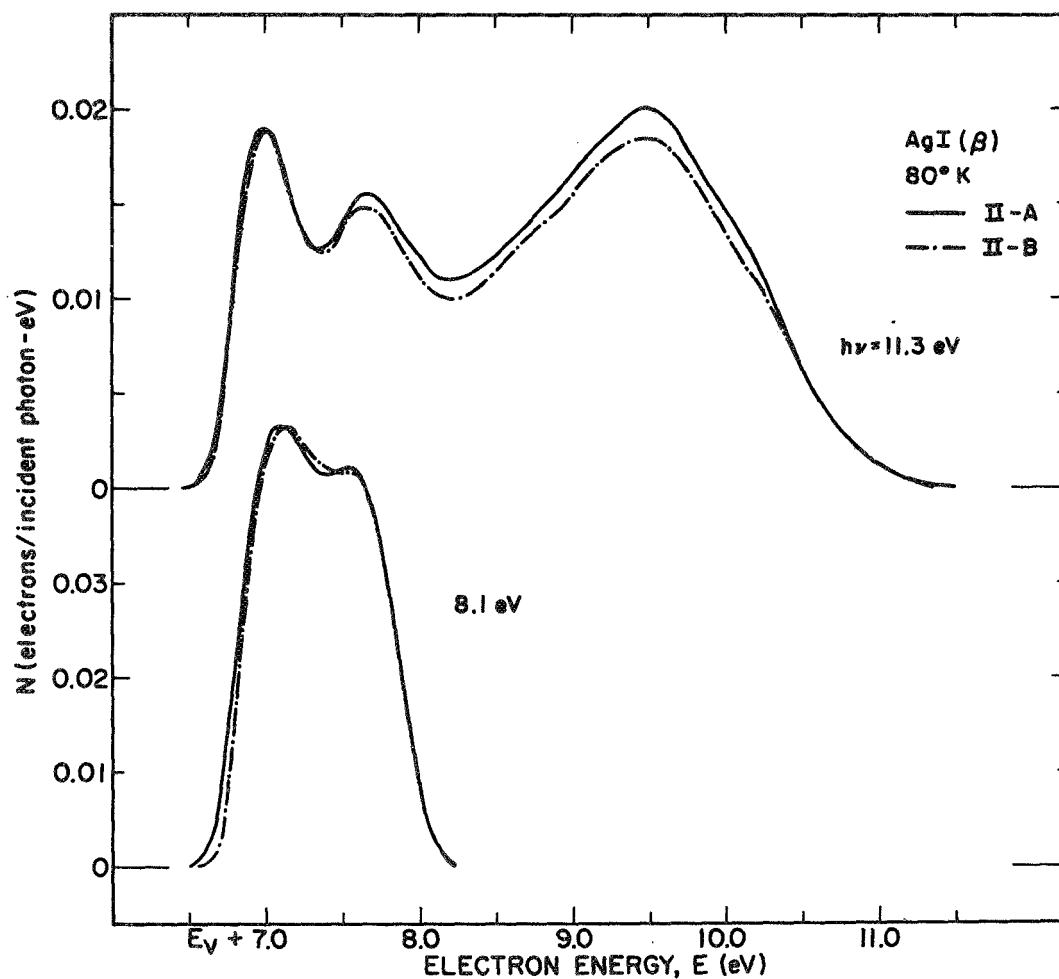
FIGURE 9.2. Comparison of energy distributions normalized to
quantum yield (per incident photon) for electrons
photoemitted from two AgI (β) samples at $80°K$
for photon energies of 8.1 and 11.3 eV.

be emphasized again that the two sets of curves are individually normalized to their own yield and have their energy scales independently determined. As will be discussed in section C, the peaks which appear at about $E = 7.6$ eV in these EDCs are quite distinctive temperature dependent characteristics. Therefore, the excellent agreement at 80°K is a very sensitive test of the reproducibility of the data.

The EDCs are also reproducible following numerous temperature cycles between room and liquid nitrogen values as shown by Fig. 9.3. The number of times that the sample was cooled to 80°K is indicated in parentheses. Since the two curves taken 20 cycles apart are independently normalized, the stability of the yield is also seen to be quite good. This figure also illustrates the stability of the samples with time. Over a period of more than two weeks, no significant changes in the AgI EDCs occurred. Note also that if photolytic decomposition was significant in these thin films, one would expect a slow degradation of the EDCs with increasing exposure to UV radiation. Thus, the data of Fig. 9.3 shows that light-induced chemical reactions are not significant for the AgI samples studied.

Electron microscopy[81] and optical[116,88] studies have established that evaporated thin films are good model systems for the study of bulk AgI properties. In order to determine if the very thin film used in these studies are "good" films, a very thick film was evaporated under the same conditions (e.g., evaporation rate and substrate temperature). As noted above, the X-ray diffraction study of this film showed it to be highly oriented pure polycrystalline AgI (β) . In addition, it was found that at room temperature the photoemission from the very thin film (220 $\overset{\circ}{A}$) was the same as that measured from very thick films (0.30 μ) as shown in Fig. 9.4. Though there are slight changes in the EDC structure, all the salient features of the data appear independent of thickness. Since these EDC's are independently normalized, the yield is also seen to be thickness independent in the range. Unfortunately, the thick films could not be measured at LN_2 temperature because of their high resistance. We can conclude from these considerations that the very thin films are representative of bulk AgI photoemission. As discussed in detail in
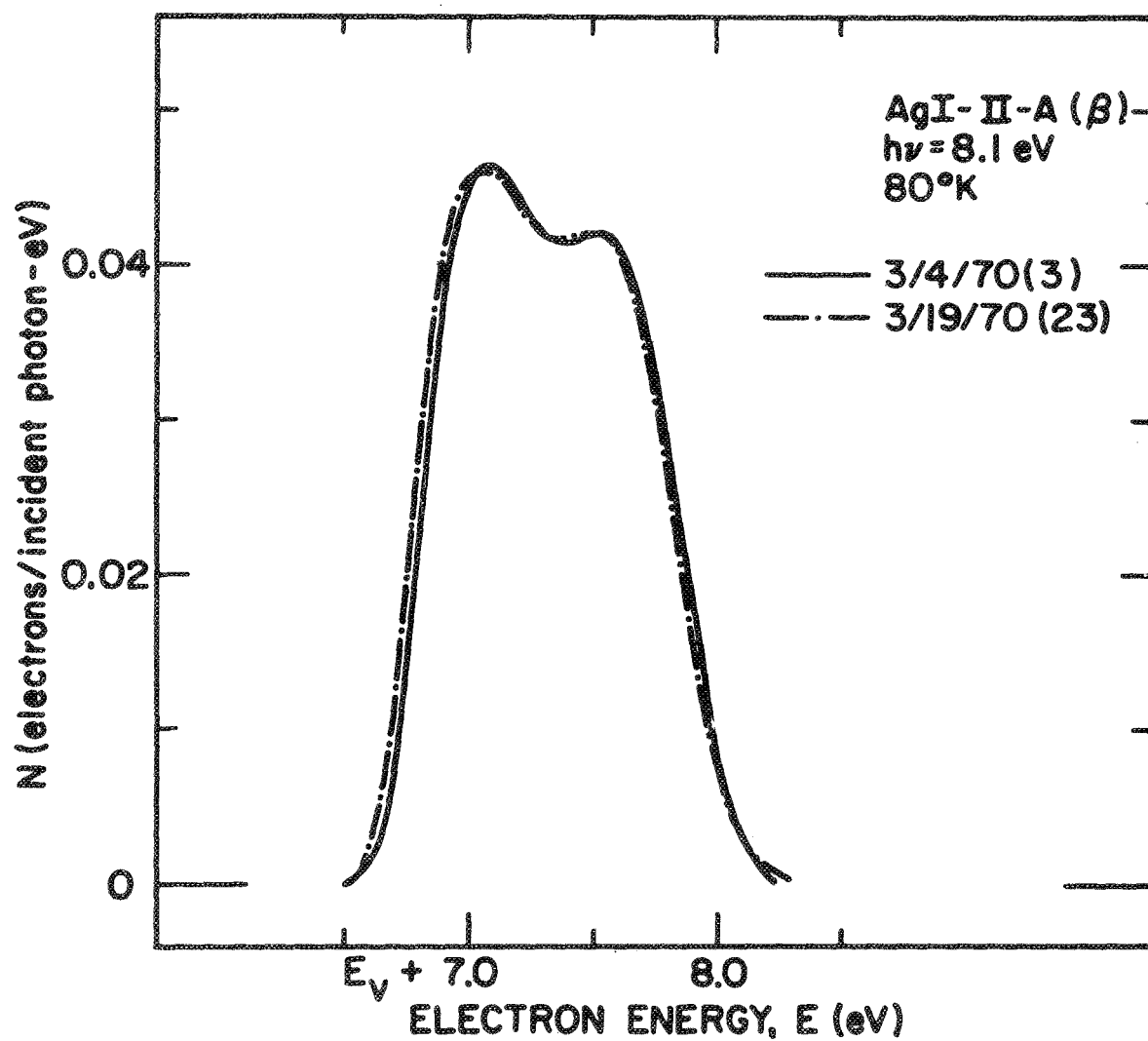
FIGURE 9.3. Comparison of energy distributions normalized
to quantum yield (per incident photon) for
electrons photoemitted fifteen days and twenty
cooling cycles apart from AgI (β) at 80°K
for a photon energy of 8.1 eV.

218

FIGURE 9.4. Comparison of energy distributions normalized to
quantum yield (per incident photon) for electrons
photoemitted from thick and thin AgI (β) samples
at 295°K for a photon energy of 11.3 eV.

Chapter IV, the thickness independence of the photoemissive properties
indicates that the thin films studied were virtually strain-free.

2. Photoemission Data Characteristics

The only work reported on the photoemission from AgI has been
concerned exclusively with the quantum yield. A comparison of the
yield measured in this study and the previous work of Peterson[77] and
Fleischmann[74] is made in Fig. 9.5. The break in our yield at about
6.7 eV and the lower energy region is due to electrons photoemitted
from the silver substrate through the sample film (as discussed in
Chapter IV) and should be neglected for the purposes of the present

219
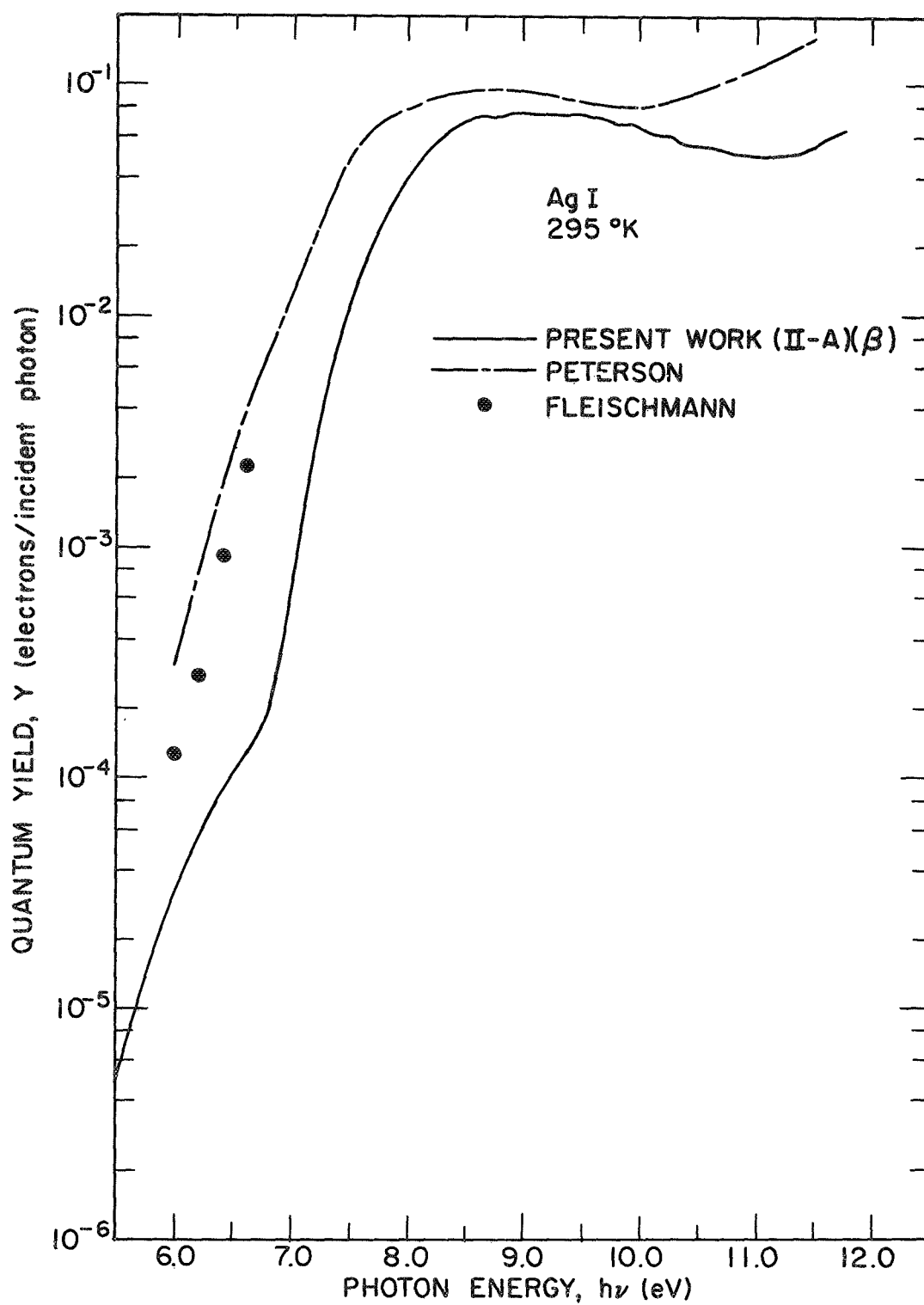
FIGURE 9.5. Comparison of the spectral distributions of the yield of electrons photoemitted per incident photon from AgI at 295°K from this work and the works of Peterson (reference 77) and Fleischmann (reference 74).

discussion. The previous yield has a bit higher value in the saturation region above threshold but the differences of interest are in the threshold region. As was the case for the measurements of the other silver halides by these same workers (see Chapter III), their yield near threshold has a smaller slope and has a lower onset by over 1 eV than does the quantum yield measured in the present work. If we take into account our detailed analysis in Chapter III of these differences in yield as well as EDCs of AgBr and AgCl , we must conclude that the AgI differences occur because the earlier data is dominated by surface contamination effects. Their questionable sample handling and preparation procedures,[48] lead us to believe that this investigation is the first measurement of photoemission representative of bulk AgI properties.

There is actually only a very small amount of literature on the electronic states and optical transitions in AgI . Our studies are the first measurement of EDCs for AgI. The optical properties in the UV have only been studied to a photon energy of 8.2 eV; measurements of the β phase of AgI are only reported up to 3.9 eV.[116] It is interesting to note that the salient features of the absorption spectrum of the γ-cubic phase show no large sharpening effects upon cooling from 297 to 80°K for hν between 4.1 and 8.2 eV.[116]

One of the things which makes it so difficult to analyze the data for this silver halide is that no calculations have been reported for the electronic states of AgI . Therefore, the similarities of the AgI temperature dependent photoemission data of those of the other silver halides is the most definitive method available for estimating the nature of the AgI states. To obtain an overall view of the data characteristics, the structure plots for AgI are presented in Fig. 9.6 at 295°K [part (a)] and 80°K [part (b)]. All the general features of the structure plots discussed in the last chapter are present in AgI plus one new effect. The -1.7 eV valence state structure does not occur throughout all the data so it would appear to be a k-conserving transition. The -4.4 eV density of states peak is temperature independent in position even with the considerable modulation of all the other data, including the leading edge. This type of behavior of the AgI EDC
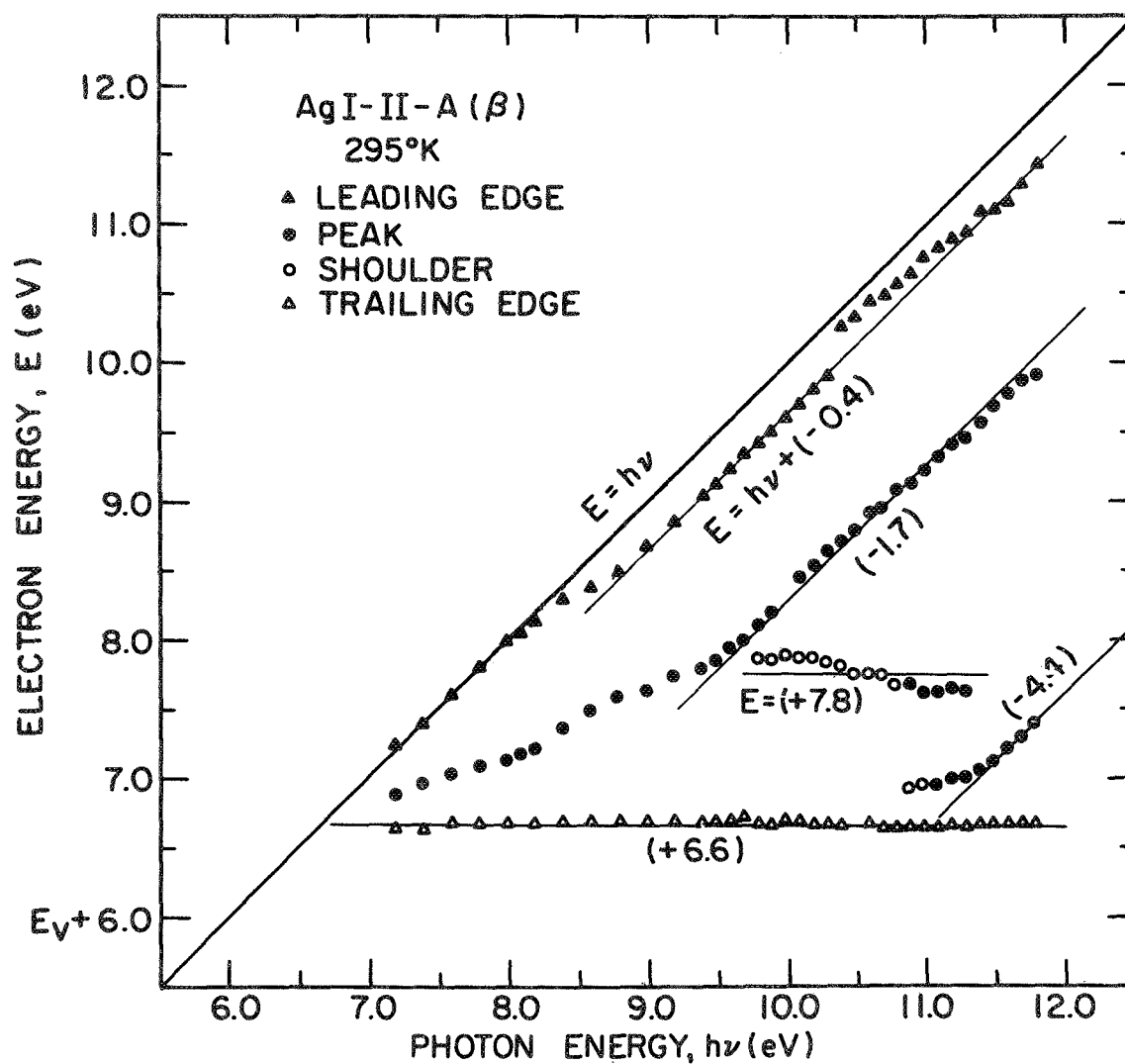
FIGURE 9.6(a). Spectral distribution of the AgI (β) EDCs' structure
and edges at 295°K. Unit and zero slope lines, with
their electron energy-axis intercepts, are shown fit
to appropriate data.
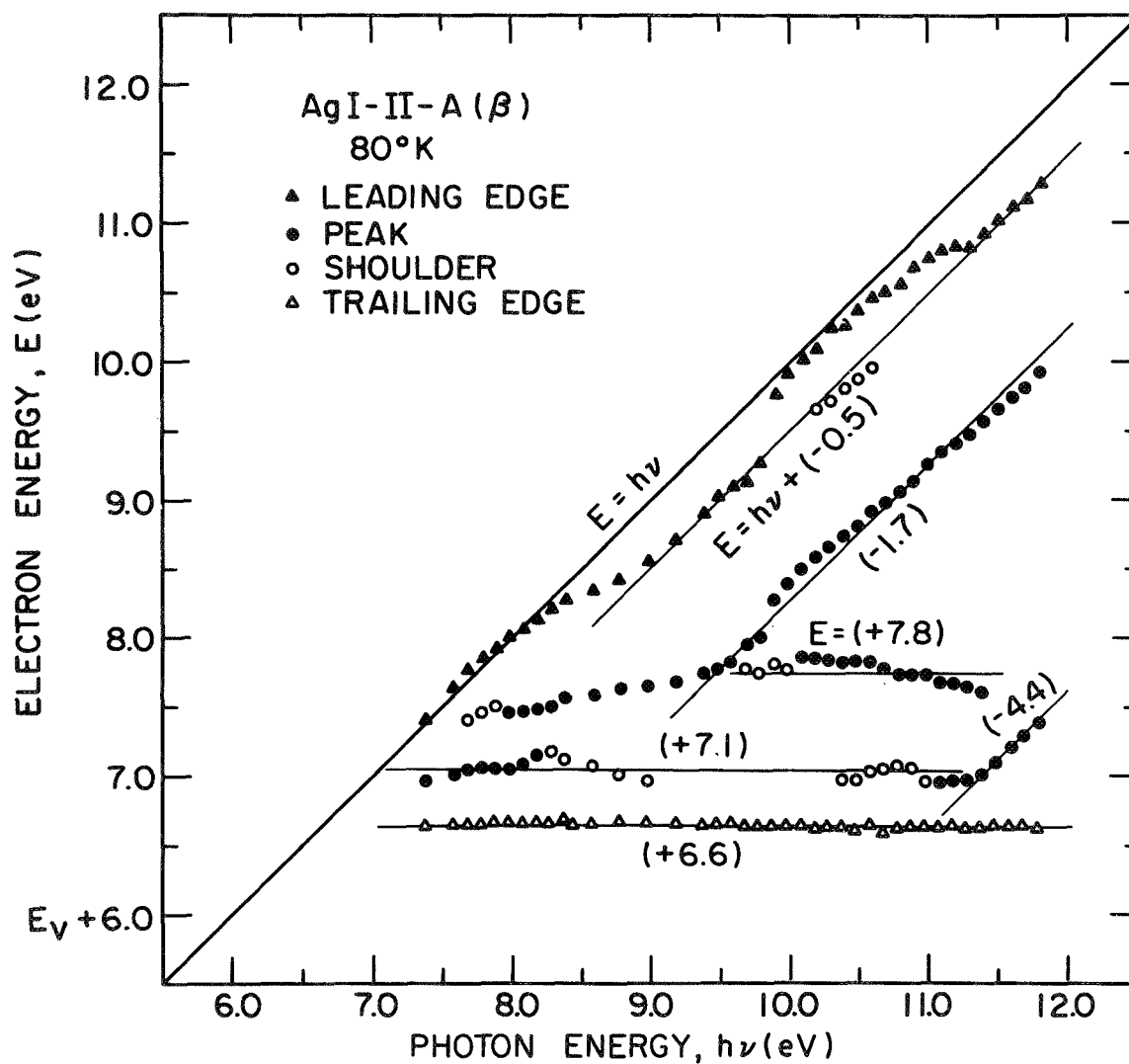
FIGURE 9.6(b). Spectral distribution of the   AgI (β)   EDCs' structure
and edges at 80°K. Unit and zero slope lines, with
their electron energy-axis intercepts, are shown fit
to appropriate data.

223

leading edge with hν variation was not observed for AgBr or AgCl .
As can be seen at both room and liquid N_2 temperature, the leading
edge extrapolation follows two distinctively different loci on the
structure plot. This cannot be due to simple error of the extrapola-
tion process because at 80°K there is evidence for the -0.5 eV line in
the structure of the EDCs (i.e., shoulders). The conduction states show
both of the effects observed in the other silver halides. There are two
high density of states regions in the conduction band which are tempera-
ture dependent. The one at 7.8 eV produces effects in the EDCs at 295
and 80°K (as in AgCl at 8.1 eV) while the 7.1 eV structure is only
observed at low temperatures (as in AgBr at 8.8 eV). With this very
general overview as an introduction, the data corresponding to each of
these features will be examined in detail to better understand its
complete characteristics and perhaps to estimate its origin in the
electronic states. It is important to note that the room temperature
structure plot for CuI ,[1] shows very little if any similarity to the
AgI plot at 295°K. Thus, comparison of silver to cuprous iodide is not
very fruitful.

B. The Hybridized I 5p-Derived Electronic Valence States

The -1.7 eV valence band structure and nature of the valence band
maximum will be discussed in this section. The EDCs which show the
characteristics of this structure are presented in Fig. 9.7 for photon
energies from 9.8 through 10.8 eV. As was the case for the -0.8 eV
structure of AgBr and AgCl , the EDC structure which originates at
-1.7 eV in the AgI valence states can be seen to come into the EDCs
on the leading edge over a relatively small photon energy range. Equally
important, this structure sharpens considerably upon cooling to 80°K.
It should be recalled that by the dynamic hybridization model only those
states whose wavefunctions involve significant p-d mixing will exhibit
a temperature dependence many times the change in k_BT . In fact, the
temperature dependence of this peak width obeys the same functional
relation, Eq. (5.7), as the halogen p-derived structure of AgBr and
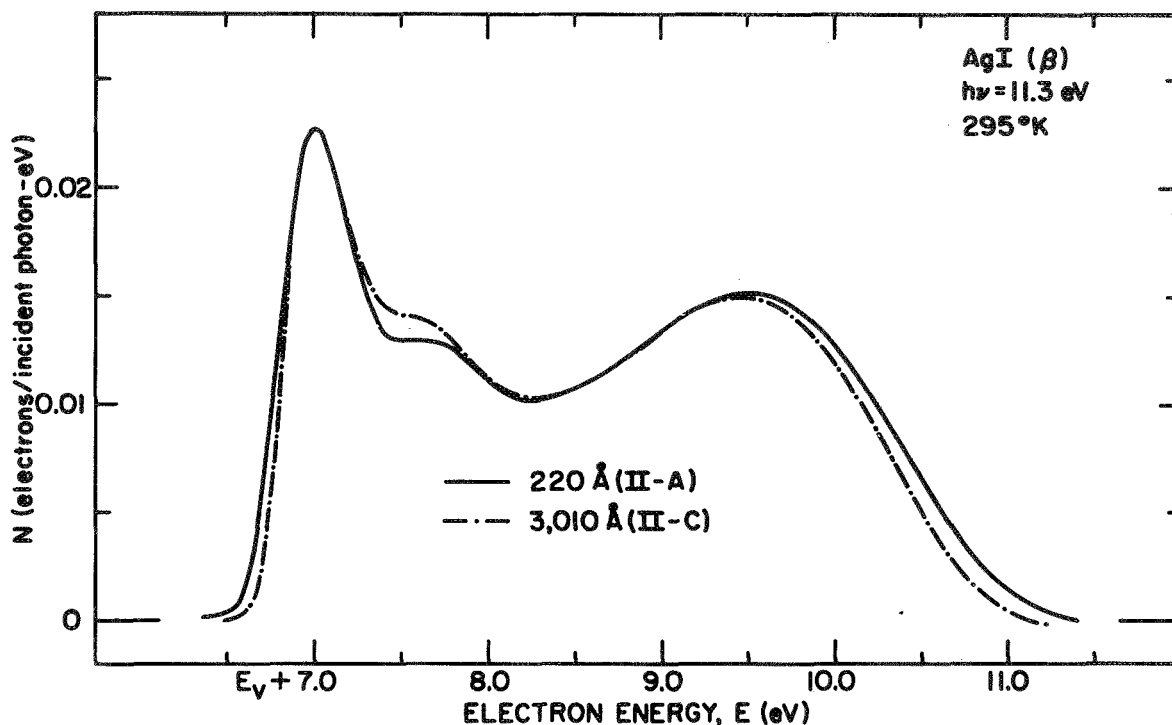AgCl . This was measured for the AgI peak in question at two photon

FIGURE 9.7. Comparison of energy distributions normalized to
quantum yield (per incident photon) for electrons
photoemitted from AgI (β) at 80 and 295°K for
photon energies of 9.8 through 10.8 eV.

225

energies and was found to be virtually the same at both. (This is summarized in Table IX.1 that is to be presented in the last section.) It seems reasonable, from this structure's temperature dependence and its similarity to AgBr and AgCl structure, that its -1.7 eV origin is composed of hybridized I 5p-derived states. In addition, transitions from these states appear to conserve crystal momentum in the optical excitation process because of its abrupt onset.

The behavior of the EDC leading edge with photon energy variation is quite striking as seen on the structure plots of Fig. 9.6. The rapid change in position around 10.0 eV is clearly depicted in Fig. 9.7; the 80°K EDC leading edges are particularly interesting. Between $h\nu$ = 9.8 eV and 10.2 eV a distinctive shoulder emerges on the long structureless EDC nose. This reaches a maximum at about 10.4 eV and then becomes merged with the leading side of the neighboring -1.7 eV peak at $h\nu$ = 10.8 eV . The EDC's leading edge really is quite different at this photon energy compared to its shape at 9.8 eV. Such an observance has been noted before for the highly covalent group IV and III-V semiconductors (Ge is a particularly fine example of this).[31] In each of these cases the onset of the structure was associated with direct optical transitions from the valence band maximum. The weakness of this EDC structure and the calculated energy bands available for these solids indicated that these highest valence states were at Γ . All that we have to analyze for AgI is the strength and behavior of the EDC structure. On the basis of the comparison to these semiconductors, the weakness of this AgI valence band maximum structure points to the highest valence states occurring at Γ . It should be noted that the strength of the exciton absorption spectrum of AgI led Cardona to predict the occurrence of direct allowed transitions, originating from I p-derived states at the center of the zone.[116] Thus, the optical properties also suggest that the valence band maximum occurs at Γ .

One can further estimate that the second, lower energy ($\approx$ -0.45 eV) position of the leading edge (see Fig. 9.6) corresponds to a different group of states in the valence band which are also derived from the I 5p orbitals. If the assumption of direct transitions from Γ is

valid for the highest leading edge positions, then it would follow that the absence of such transitions between $h\nu = 8.3$ and 10.0 eV [see Fig. 9.6(b)] probably implies a lack of conduction states at Γ in this energy range. Since this region occurs for nearly 2 eV, it would follow that the states which are seen about 0.5 eV below the highest ones occur in a region away from the center of the Brillouin zone. The absence of $E = h\nu$ transitions for some 2 eV may also be due to conduction states at Γ whose symmetry is such that optical transitions from p states are unallowed; however, this explanation seems less likely. We can therefore estimate the location in the zone where the -0.45 eV AgI valence structure is probably not located.

C. The Electronic Conduction States of AgI

At the end of the last section it was pointed out that the nature of the conduction states could be estimated using the assumed Γ symmetry of the highest valence states and the assumed importance of k-conservation as a selection rule for transitions from these states. It would follow that the absence of transitions from these p-derived states in the region from 8.3 to 10.0 eV [see Fig. 9.6(b)] was due either to the absence of conduction states at Γ in this range or to the final states at Γ having such a symmetry (e.g., p-like) so as to cause the transitions to be unallowed. This is somewhat speculative but is included as basis for future analysis of this data.

The conduction state region at 7.8 eV is strongly temperature dependent between 295 and 80°K. This is depicted in Fig. 9.8 where the 9.0 and 9.2 eV EDCs had to be reduced by 20% to be presented on the same scale as the other two sets of curves. This peak is roughly stationary at $E = 7.8$ eV . Its width variation follows the same functional relation [Eq. (5.7)] as the p-derived valence structure; the parameters for this exponential behavior are included in Table IX.1 in section E below for the $h\nu = 9.2$ eV EDCs. This 7.8 eV conduction state structure is quite noticeable in the higher photon energy EDCs of Fig. 9.9. The center structure which disappears between $h\nu = 11.4$ and 11.6 eV can be seen to remain stationary at about 7.8 eV in the EDCs. At these high

FIGURE 9.8. Comparison of energy distributions normalized to
quantum yield (per incident photon) for electrons
photoemitted from AgI (β) at 80 and 295°K for photon
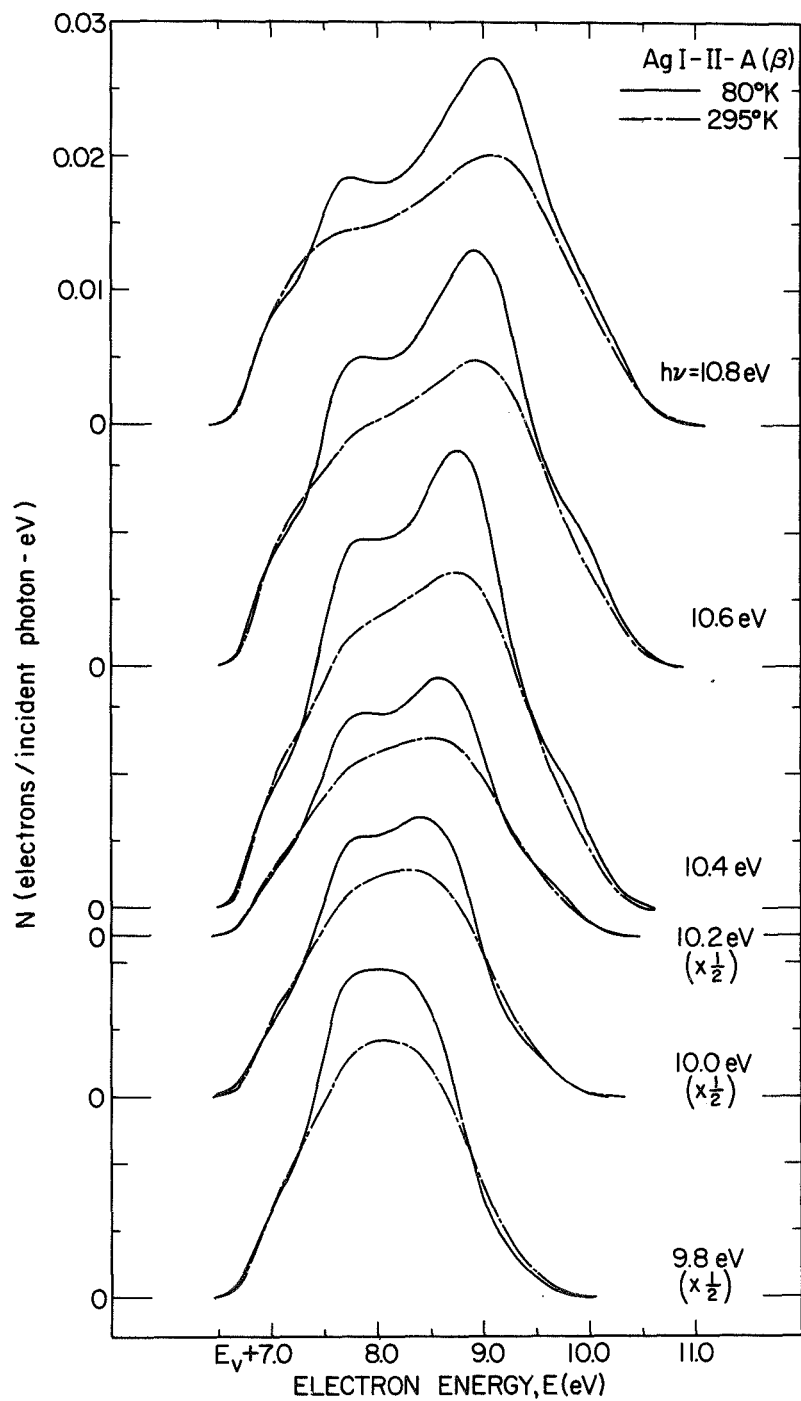energies of 9.0 through 9.6 eV.

FIGURE 9.9. Comparison of energy distributions normalized to
quantum yield (per incident photon) for electrons
photoemitted from AgI (β) at 80 and 295°K for
photon energies of 11.0 through 11.8 eV.

energies this structure is quite temperature dependent as seen when the intermediate temperatures are included in Fig. 9.10. At both $h\nu = 11.3$ and 10.6 eV the $E \approx 7.8$ eV structure sharpens from a shoulder at room

FIGURE 9.10. Comparison of energy distributions normalized to quantum yield (per incident photon) for electrons photoemitted from AgI (β) at 80 through 285°K for photon energies of 10.6 and 11.3 eV.

temperature to a peak at 80°K in a continuous manner. This strong temperature dependence and its functional behavior for the conduction

structure is highly suggestive of states whose orbitals are significantly hybridized.

The temperature dependences of the conduction state structure at both 7.8 and 7.1 eV are both quite dramatically seen and their characteristics can be compared at low photon energies as shown in Figs. 9.11(a) and (b). In this energy range, the p-derived valence electrons are being excited into the 7.1 eV conduction states at about $h\nu = 7.4$ eV until it passes through and out of these final states into the 7.8 eV states at around 8.6 eV. As was shown in Fig. 9.8, the EDC peak then remains stationary at 7.8 eV until the -1.7 eV structure clearly emerges at photon energies beyond $h\nu = 9.8$ eV . The presence of these two distinct conduction state regions is dramatically seen when they sharpen at $80°K$. In Fig. 9.11(a) and (b), one sees two peaks at $h\nu = 8.0$ and 8.2 eV as the valence states move between the two regions. Note that the photon energy difference between when the excitation is primarily to one or the other of the conduction state regions is around 0.6 eV (8.4-7.8 eV) which is nearly the exact separation of the two final state peaks. The temperature dependence of these two conduction state regions is distinctly seen when the intermediate temperatures are included for the EDC at the photon energy in the center of this range, $h\nu = 8.1$ eV ; this is depicted in Fig. 9.12. Note that the one peak at $295°K$ is divided into two peaks at $80°K$ which are at energies different from the original one. The temperature dependence of the 7.8 eV region alone is seen at $h\nu = 9.2$ eV in this figure (characteristics are given in Table IX.1). It is interesting that even though this higher energy region appears more temperature dependent by these EDCs, the 7.1 eV region is only clearly locateable at $80°K$ as shown by the structure plots of Figs. 9.6(a) and (b). Therefore, it is difficult to distinguish any major differences between the temperature dependences of the two regions. We can only estimate that the 7.1 eV region probably has the same general hybridized characteristics as the 7.8 eV region. The 7.1 eV region may be mixed to a lesser extent or just is of lesser strength than the 7.8 eV structure since the latter is so much more prominent in the EDCs.
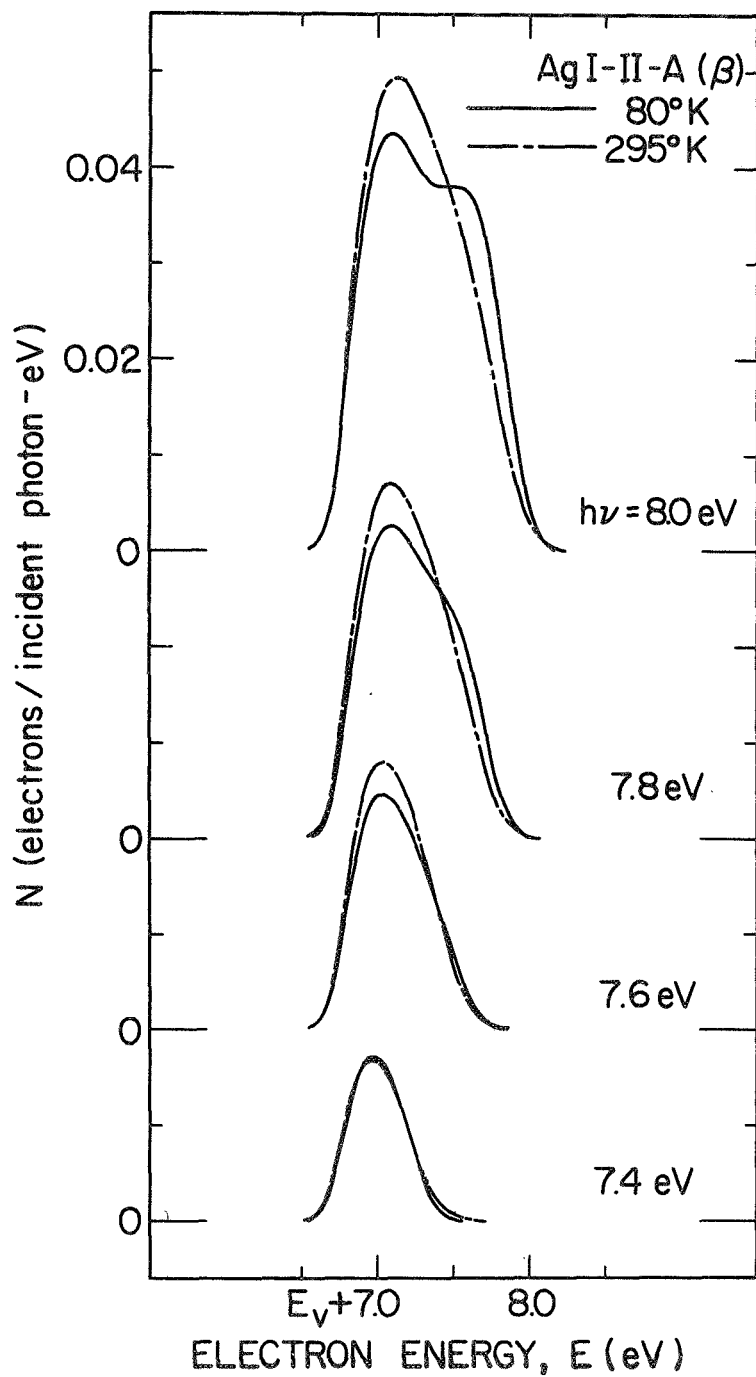
FIGURE 9.11(a). Comparison of energy distributions normalized to quantum yield (per incident photon) for electrons photoemitted from AgI (β) at 80 and 295°K for photon energies of 7.4 through 8.0 eV.
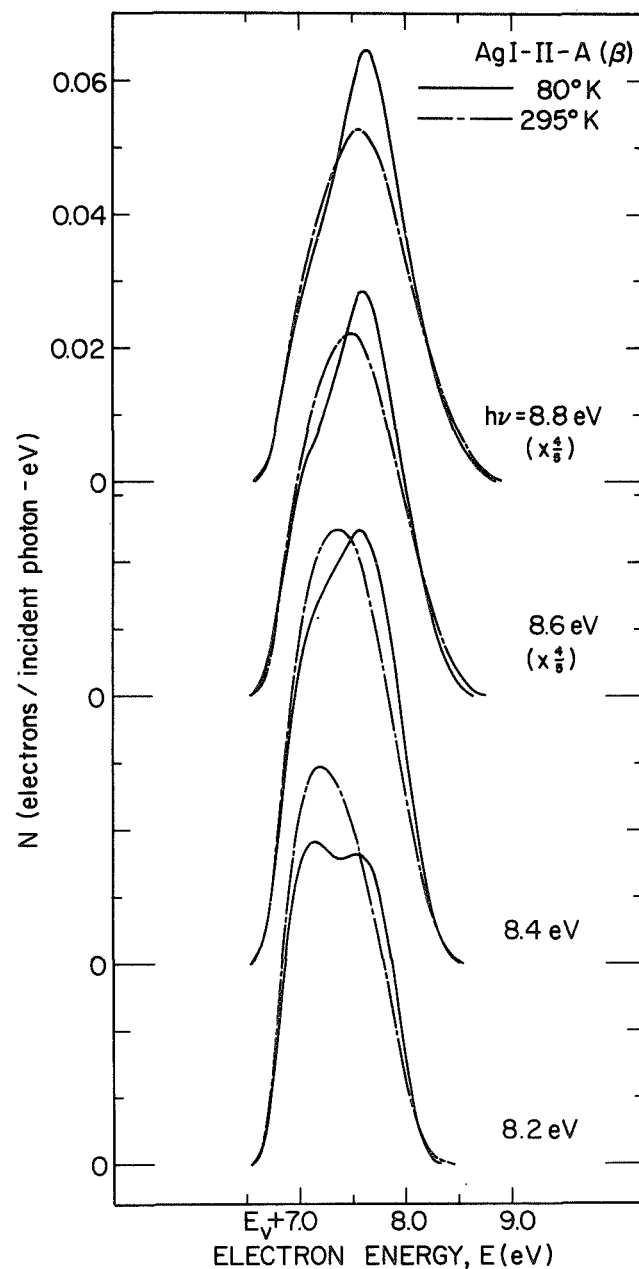
FIGURE 9.11(b). Comparison of energy distributions normalized to quantum yield (per incident photon) for electrons photoemitted from AgI (β) at 80 and 295°K for photon energies of 8.2 through 8.8 eV.

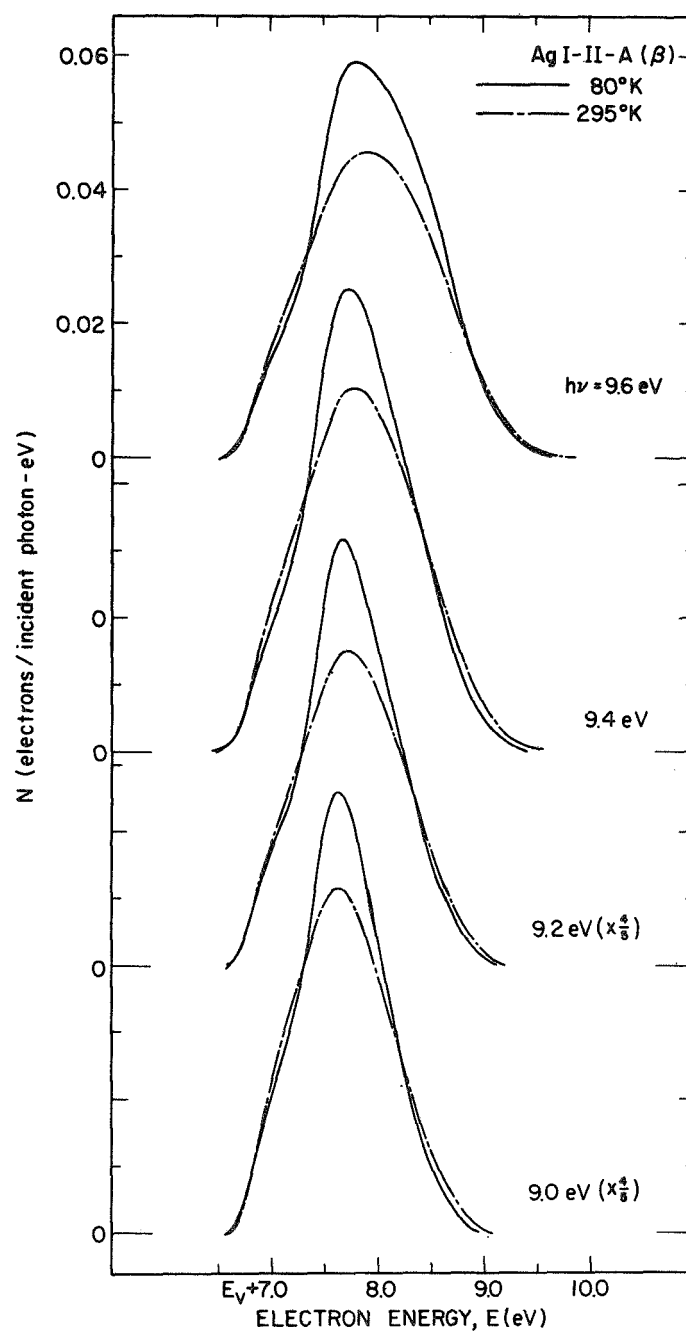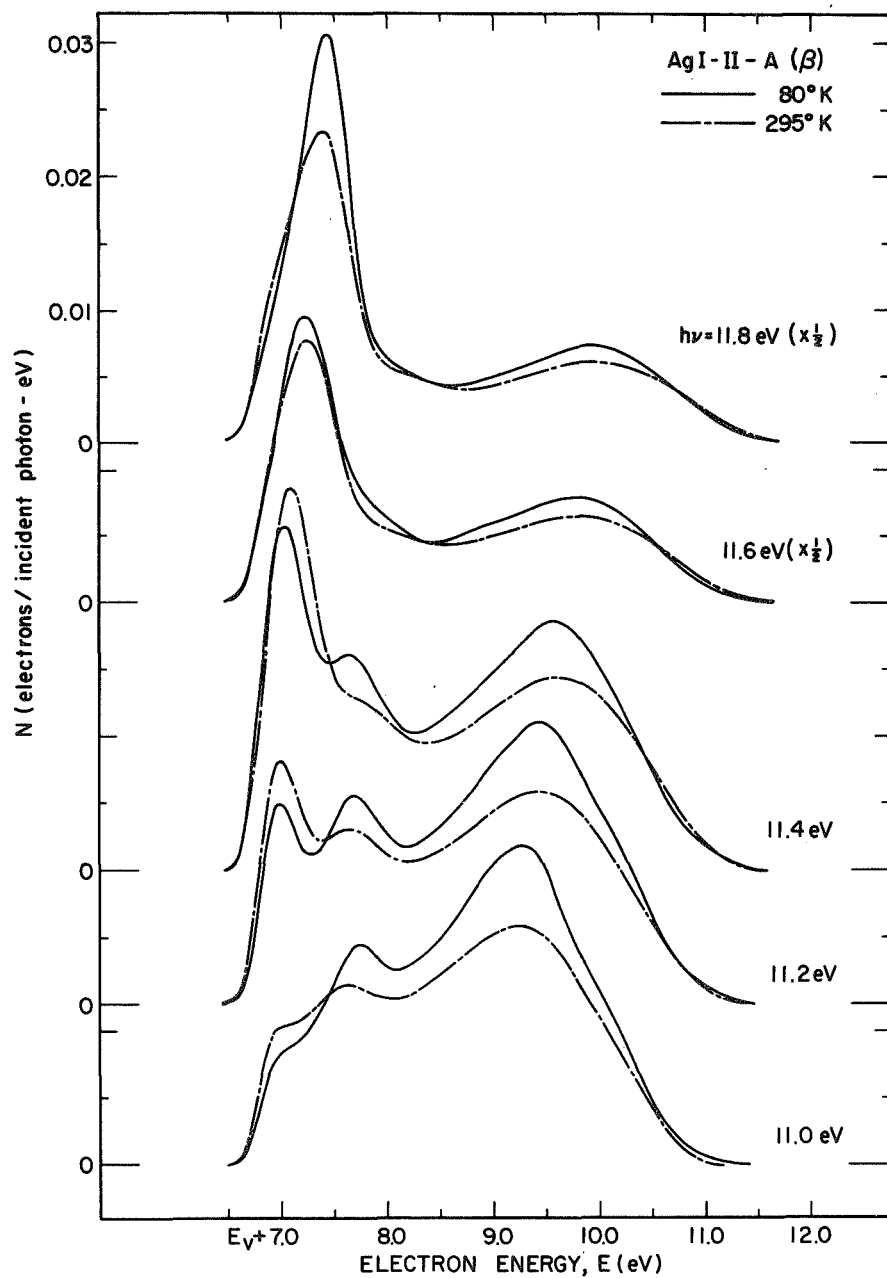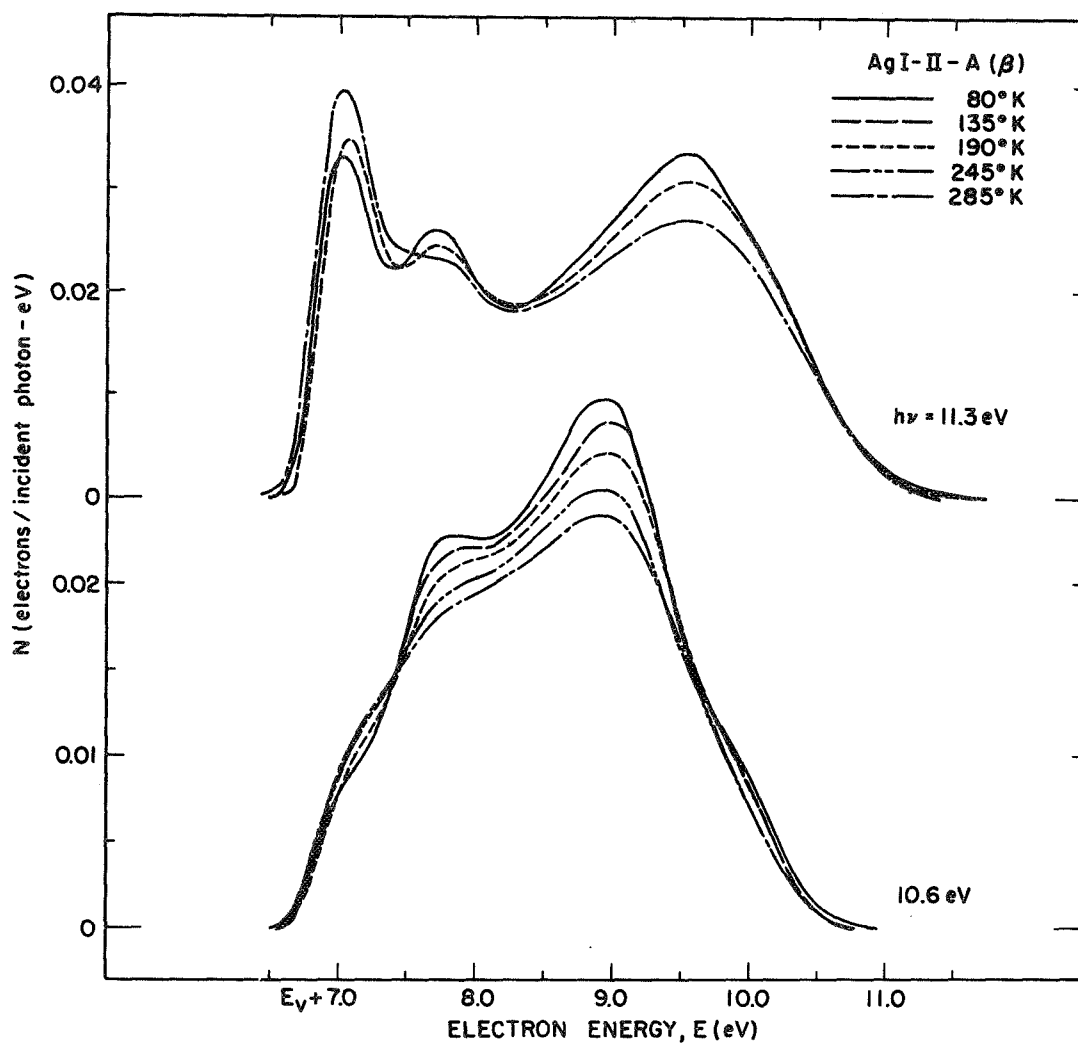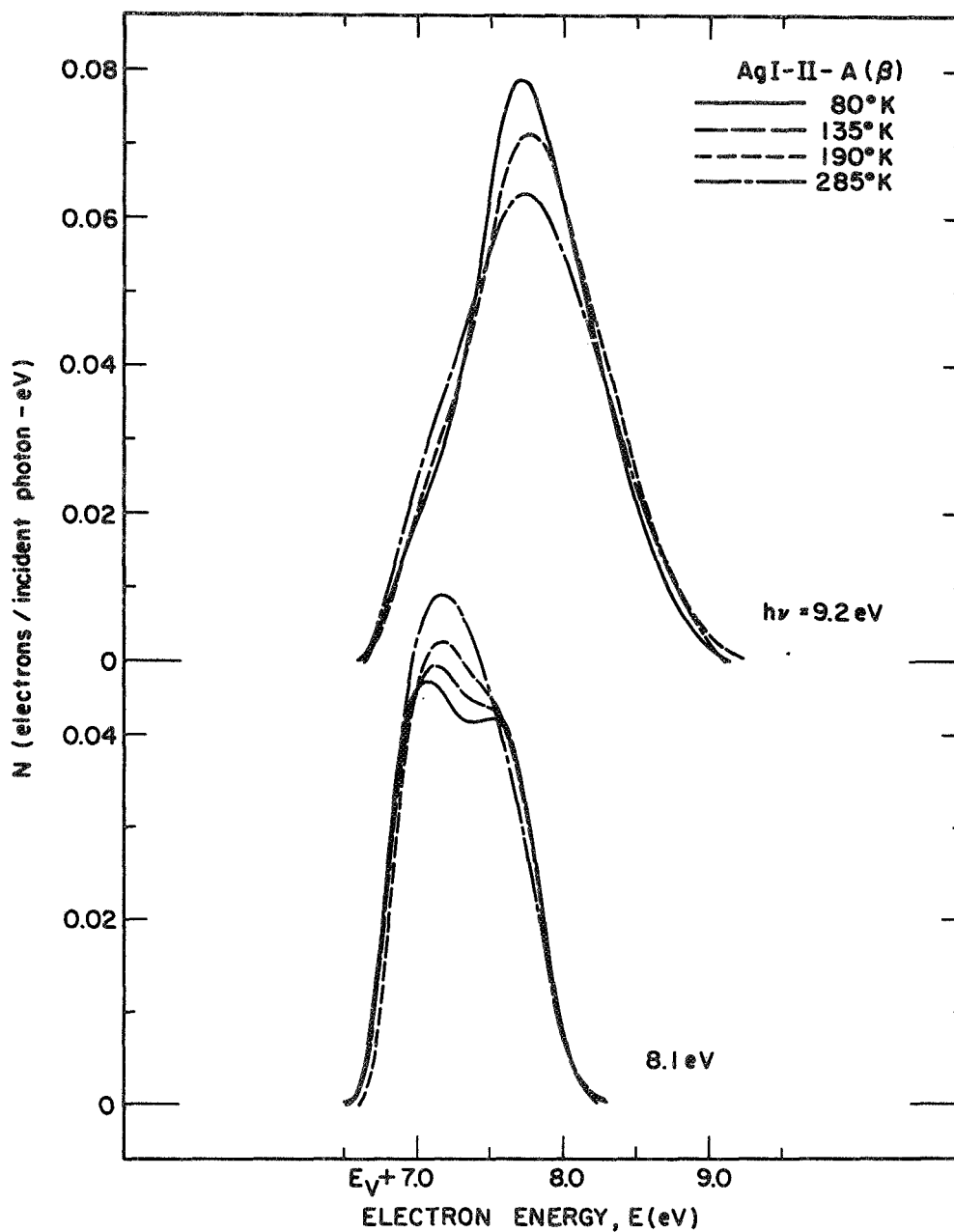FIGURE 9.12. Comparison of energy distributions normalized
to quantum yield (per incident photon) for
electrons photoemitted from AgI (β) at
80 through 285°K for photon energies of 8.1
and 9.2 eV.

From our experience with the other halides (see Chapter VIII) it is reasonable to believe that these conduction state regions are I 5d-derived involving significant mixing with Ag 5p states. As will be seen in the next section, transitions from the valence states with an estimated pure d symmetry are quite strong up to E = 7.4 eV (this occurs at the limit of our measurements hν = 11.8 eV). This strength may be due to the final states being such that the transitions are allowed by symmetry. By these considerations, the regions would appear to be Ag 5p-derived states with significant I 5d mixing instead of the converse. Thus, the two assignments seem equally likely. Note that the 7.1 eV region could not be p-derived and the 7.8 eV d-derived since these conduction states are normally ordered in the opposite way in the silver halides.[41,3,6] A Ag 5s origin seems least likely since one does not expect significant hybridization for such orbitals.[3,112]

D. The "Pure" Ag 4d Electronic Valence States

At a photon energy of around 11.1 eV, a new peak emerges on the trailing side of the EDC which dominates the curves. This is seen by the curves in Fig. 9.9. This is the structure originating -4.4 eV in the valence states as shown on the structure plots of Fig. 9.6. The huge strength of this peak is demonstrated by the necessity for reducing the higher energy 11.6 and 11.8 eV EDCs by 50% in order to fit them on the same scale as the rest of the curves. Further, the yield shows a dramatic increase when this structure does emerge above threshold at 11.1 eV as seen in Figs. 9.13(a) and (b). In Fig. 9.13(a) the only temperature dependence of the yield is seen above the threshold region. On the linear scale of part (b) of the figure, this dependence of the yield on temperature is seen to be gradual. The -4.4 eV EDC peak shows some height variation in Fig. 9.9, but the peak width is found to be temperature independent. This can be seen in Fig. 9.10 at hν = 11.3 eV . The left peak is actually reduced in height upon cooling at this photon energy. However, the width at 90% of its maximum height does not change upon cooling. This temperature independence is entered in Table IX.1 below for completeness. As was discussed fully in Chapter VI, the
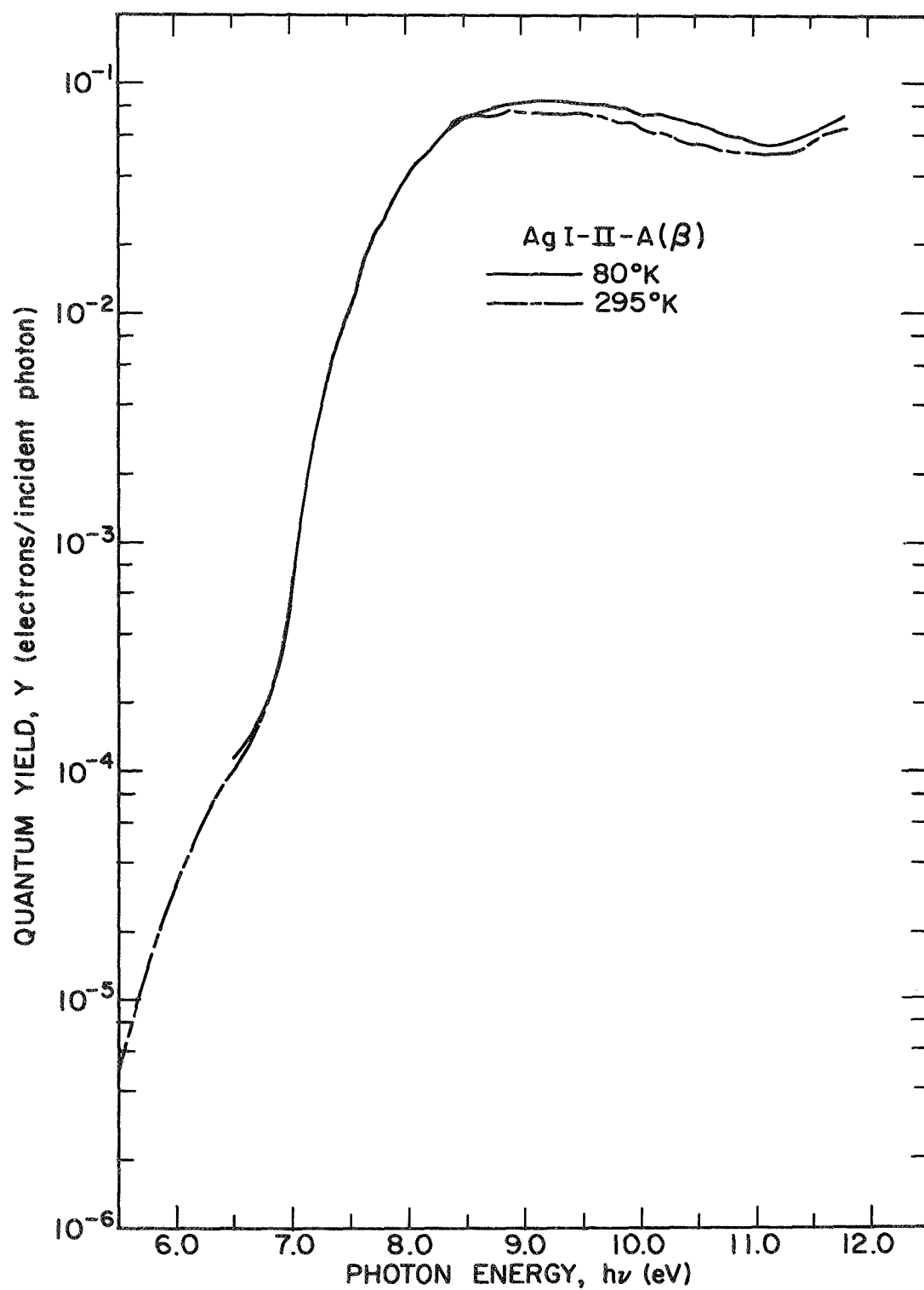
FIGURE 9.13(a). Comparison of the spectral distributions of the yield of electrons photoemitted per incident photon from AgI (β) at 80 and 295°K.
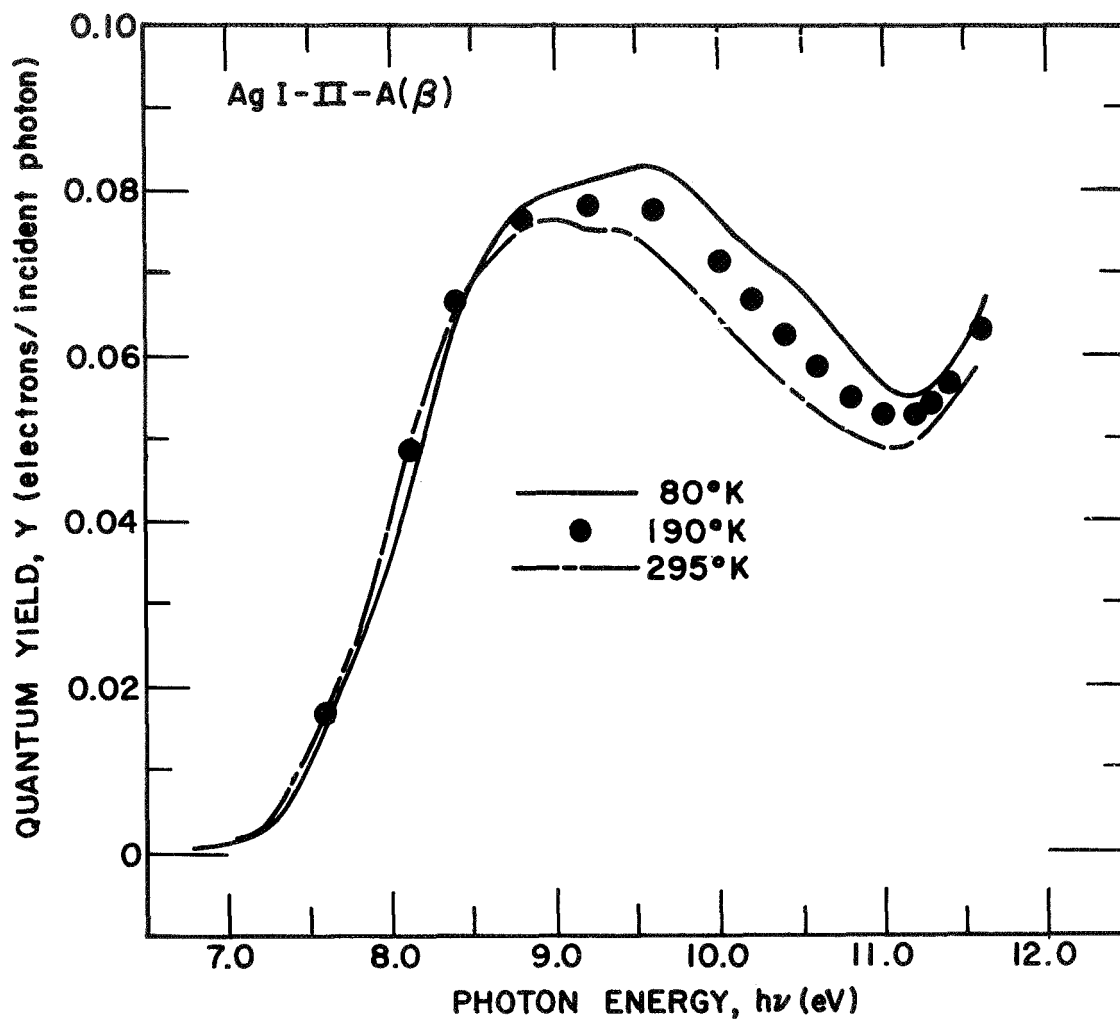
FIGURE 9.13(b). Comparison of the spectral distributions of the yield
of electrons photoemitted per incident photon from AgI (β) at 80
through 295°K.

temperature independent data can be related to the states which are not

formed from hybridized mixtures of two or more orbitals. That is, the

states corresponding to such EDC structure has almost the pure symmetry

of one type of orbital. It was found for AgBr and AgCl that the most

reasonable association to make, based on preliminary band calculations,

was that these states were Ag states with almost pure $4d$ symmetry.
Comparing the AgI results, which also show a temperature independent
peak below the valence band maximum, it is reasonable to assign the
-4.4 eV valence band density of states peak to Ag states with almost
pure $4d$ symmetry.

E. Summary

As was pointed out above, of the five AgI EDC peak widths whose
temperature dependences could be measured, all of them obey the same
exponential dependence on temperature as that deduced for AgBr and
AgCl in Chapter V. The constants of Eq. (5.7) which characterize
these dependences are summarized in Table IX.1.

TABLE IX.1. Parameters which define the exponential temperature
dependence of the AgI (β) 90% EDC peak width, W ,
given by Eq. (5.7): W_0 is the frozen lattice, EDC
width and C is a measure of the temperature dependence.

	EDC PEAK[*]	$h\nu$ (eV)	W_0 (eV)	$\frac{C}{\Theta_D} \times 100$ $(^\circ K^{-1})$
	-4.4	11.3	0.23	0
AgI (β) (II-A)	-1.7	11.3	0.47	0.19
	-1.7	10.6	0.49	0.15
	$D^\dagger$	9.2	0.29	0.13
	$D^\ddagger(\ell)$	8.1	0.14	0.12

[*]D = Direct

ℓ = Left half-width

[†]E = 7.8 eV

[‡]E $\approx$ 7.1 eV

The EDC peaks whose 90% widths were measured are identified by their
origin in the density of valence states (i.e., -4.4 and -1.7 eV) or by
the nature of the optical excitation process (i.e., direct transition -
"D") if the peak does not originate from one initial state energy for

238

all photon energies. At hν = 8.1 eV only the left half-width of the peak could be measured over a large temperature range, and this is indicated by an "ℓ". Recall again that W_0 is a measure of the EDC width at T = 0°K if there were no significant zero-point vibration of the ions. Since this dependence was predicted by Doniach using a first order Green's Function calculation based on the dynamic hybridization model [i.e., Eq. (5.8)],[108] it is reasonable to assume that this description of the temperature dependence of the photoemission is as valid for AgI as it was for the other silver halides.

The information which was determined for the electronic states of AgI is summarized in Table IX.2.

TABLE IX.2. Summary of information determined for the electronic
                states of AgI in the hexagonal (β) phase.

ENERGY (±0.2) (eV)	ORIGIN	DEGREE OF MIXING*
8.3 → 10.0, 10.6 → > 11.8	Γ p States or No Γ States	
7.8, 7.1	Ag (5p) or I (5d)	H
6.6	Vacuum Level	
0	Γ , Valence Band Maximum	
-0.45	I (5p), Not @ Γ	H
-1.7	I (5p)	H
-4.4 ± 0.1	Ag (4d)	P

*H = Hybridized,   P = Pure

At each of the energies listed, some definite feature in the EDC structure can be identified; these were pointed out in the discussion above. Because the positions deviate from straight line loci on a structure plot much more for AgI than the other two halides (compare Fig. 9.6 to Figs. 8.1 and 8.3), the uncertainty in these energies is believed to be ±0.2 eV except for the -4.4 eV structure as noted in the table. The

origin and explanations which have been made and seem reasonable should only serve as suggestions to guide future analysis of the AgI electronic states since so very little is known about them at the present time.

X. CONCLUSIONS

A. The Electronic States and Electron-Lattice Interaction in the Silver Halides

The major new feature of this work is the discovery of a temperature dependence of certain structure in the energy distributions of photoemitted electrons which is an order of magnitude greater than the change in thermal energy, $k_B T$. This probably represents the first observation of what may prove to be a whole new class of effects in solids which satisfy the general criteria listed at the end of Chapter II. It is believed due to a very strong interaction of the electrons with the lattice, very much like the Jahn-Teller effect but many times stronger. A model referred to as "dynamic wavefunction hybridization" has been proposed in a very general sense to describe the manner in which the vibrations of the ions may effect the energies of the electronic states so strongly. Applying this model in a very general way, the silver states with almost pure $4d$ symmetry could be located by experiment with reasonable certainty for the first time; these locations were 3.7, 3.3, and 4.4 eV below the highest filled states in AgBr, AgCl, and AgI respectively. By using a very simple approximation of $k = 0$ optical phonons and restricting the extent of the interaction to about one nearest neighbor distance, the proposed model was applied to the AgCl energy bands and pressure dependent optical absorption data. These computations demonstrate its plausibility by predicting the proper magnitudes for density of states peak broadenings and their temperature dependences. Of course, it must be emphasized that the physics is really much more complex. As in the case of the Jahn-Teller effect, the frozen-lattice approximation is not valid, and one must really consider wavefunctions of the entire solid (e.g., vibronic states) rather than separate electronic and nuclear parts. This further implies that the entire concept of an energy band structure is quite suspect. There is, therefore,

much work to be done to theoretically account for such many-body interactions accurately. As was noted in Chapter V, Doniach has begun a Green's function calculation of the problem which takes into account the randomness of the ionic motion.[108] His first results indicate that the dynamic hybridization picture is, in general, a proper representation for the physical phenomenon. Besides this basic conclusion and the probable location of the "pure" Ag 4d states, the other interpretive results of this thesis must be considered only first order attempts at explaining many complex data features. It is believed that the photoemission data itself, which was carefully and laboriously taken using newly developed techniques, is quite accurate. It should serve as a good storehouse of information for the many fascinating questions which remain to be answered.

B. Suggestions for Future Work

There is obviously a great deal of theoretical work to be done to fully understand all the details of the data presented in this thesis. However, we shall only suggest in this section the experimental studies which seem valuable extensions of the present work.

As was seen in Chapter VI, there is a great deal of interesting EDC structure at energies above the 11.8 eV cutoff of the LiF window. In particular, the hybridized Ag 4d states can be probed for the first time at these higher photon energies. It would be most valuable to be able to study the temperature dependence of this structure as well as all the valence band structure. Because of the poor quality of the monochromator vacuum, it is impossible to make meaningful photoemission measurements at low temperatures without the LiF window. It would therefore be most valuable to make the necessary equipment modifications to measure temperature dependent photoemission over the widest possible energy range.

There are many interesting fundamental questions which could be answered by studies of the alloys of the silver halides. For example, pure AgBr and AgCl have optical absorption features which are indicative of direct transitions. It has been suggested by Joesten and Brown[57]

that k-conservation is not strictly valid for the homogeneous alloys of these two silver halides. It would be most interesting to see if the EDC structure which may be due to direct transitions in the pure materials (e.g., the -0.8 eV structure in both halides) changes upon alloying. The effect of alloying on the location of the d-peaks, which are separated by 0.4 eV in the pure silver halides, would be most informative.

As discussed in Chapter IX, AgI exists in two phases at room temperature. One can actually control the modification of the film obtained by proper adjustment of the substrate temperature, T_s , during evaporation. We found in this study that for $T_s = 75^{\circ}C$, the film is in the β-hexagonal phase at room temperature and below. It has been reported by Cardona that if $T_s = 147^{\circ}C$, AgI condenses in the α phase but upon cooling to room temperature, it transforms to the stable γ-ZnS phase and remains as such at reduced temperatures.[116] It would be very interesting to study any difference which may occur between the EDCs for AgI in the two phases and also their temperature dependences.

It was pointed out throughout this thesis that the optical properties of the silver halides in the vacuum UV have not been measured at low temperatures. Having found the large temperature dependence of the photoemission, it should prove very valuable to study the temperature dependence of the optical properties of these solids. Not only is this important for its own sake, but it will also allow us to normalize the low temperature EDCs to the absorbed photon flux. This will make comparison of the EDC structure heights meaningful.

The temperature dependence of photoemission EDCs can be a powerful new technique for studying the electronic states and electron-lattice interaction in solids which satisfy the criteria imposed by the dynamic hybridization model (see the end of Chapter II). These include solids which have more than one type of valence orbital involved in the bonding. For example, the Ag 4d states must be considered along with the halogen p states in the silver halides. (This question of bonding in solids with "extra" electrons is being investigated by G. Lucovsky, the

author, and others at the Xerox Palo Alto Research Center.) Among the
solids included in this group are the cuprous and thallous halides. As
emphasized many times in Chapter VIII, the temperature dependence of
cuprous halide photoemission would provide invaluable information about
its own properties and also those of the silver halides. The thallous
halides are particularly interesting since they are relared to the noble
metal halides and also because very little is known about their elec-
tronic states at the present time. By combining the work from these
groups of materials, a much more complete picture should be obtained
for the electron-lattice phenomena which is involved in this new effect
as well as for the electronic states of each of the classes of solids.

APPENDIX A. THE OPTICAL CONSTANTS OF AgCl AT 295°K DETERMINED BY THE KRAMERS-KRÖNIG ANALYSIS

White and Straley[46] have recently published the optical constants of AgCl at room temperature obtained by a Kramers-Krönig analysis of their measured reflectivity. The resulting values for α, κ, and ϵ_2 exhibit unphysical dips at 3.2 eV. This was not the first time that such anomalies have been observed in such calculations. Morrison also observed such dips for semiconductors and believed they were due to the arbitrariness of the extrapolation of the reflectance to higher energies.[117] We therefore studied the possible sources of such anomalies in the optical constants. The effects of the extrapolation of the reflectance, the expansion of the Kramers-Krönig integral, and features of the input reflectance values on the calculated optical constants will be discussed in this appendix. It will be shown that of these three possibilities, changes in the reflectance values in the region of the dip is only one which removes the anomalous structure.

A. Effects of the Extrapolation of the Reflectance

1. Kramers-Krönig Calculation Formalism

If the complex normal incidence reflectivity $r = |r| e^{i\Theta}$ is known, then all the optical properties can be determined from the Fresnel equation and the definitions of the constants. Further, if the reflectance $R = |r|^2$ is known at all photon energies $h\nu$ then the phase of the reflectivity at energy $h\nu_0$ is determined uniquely by the Kramers-Krönig transform,[118]

$$\Theta(h\nu_0) = \frac{1}{\pi} \int_0^\infty \frac{d\ln|r|}{d\nu} \ln\left|\frac{\nu + \nu_0}{\nu - \nu_0}\right| d\nu \qquad (A.1)$$

Since the reflectance cannot be measured over an infinite photon energy range, the data must be extrapolated in some manner in the unknown regions. The necessity of using an extrapolation of the data requires an examination of the uniqueness of the calculated optical constants in the region of measurement.

This question has been studied by calculations of Θ using the reflectance data of White and Straley for AgCl .[46] The Kramers-Krönig integral, Eq. (A.1), was performed using this laboratory's computer program which was written in Algol 60 by J. L. Shay based on[118] and translated into Fortran IV by D. H. Seib. For this work, it was modified to allow for the calculation to be performed using a high energy extrapolation which leads to the best agreement between the calculated low energy optical constants and known values in this region. In these calculations on AgCl , the phase shift, Θ , was fit to zero in the transparent region (0 through 3.0 eV). Though calculated for a specific set of data and fitting criterion, the results reported below should be characteristic of the calculation as performed using this laboratory's computer program.

The integral of Eq. (A.1) is performed by considering the reflectance as plotted on a log-log scale and straight lines drawn between the data points.[119] The solution for the contribution to Θ from each of these straight lines is known exactly.[119] Thus, a natural extrapolation to high energies which is continuous with the last measured value is

$$R = R_f \left(\frac{h\nu}{h\nu_f} \right)^{-A} , \quad h\nu_f \leq h\nu \leq h\nu_m , \quad \text{(A.2a)}$$

where R_f is the reflectance at the highest energy of measurement, $h\nu_f$. Being a straight line on a log-log scale, this extrapolation is uniquely specified by one point, R_m , calculated using Eq. (A.2a) at energy $h\nu_m$.

In performing the calculation of $\Theta(h\nu_0)$, $h\nu_m$ will be the largest energy in the numerical integration. Thus, in the calculation we are implicitly assuming that the contribution to Θ for energies greater than $h\nu_m$ is zero. From inspection of Eq. (A.1) it is seen that this

is equivalent to having assumed a constant reflectivity from $h\nu_m$ to infinity. Therefore, the numerical method inherently assumes

$$R = R_f \left(\frac{h\nu_m}{h\nu_f}\right)^{-A} = R_m = \text{constant} \, , \, h\nu \geq h\nu_m \qquad (A.2b)$$

There are thus two adjustable parameters in the choice of such an extrapolation: A and $h\nu_m$. It should be noted that since the optical constants depend on the energy that specifies the extrapolation of the data , E_m , the form of the extrapolation does not have any physical significance. One criterion that can be used in choosing the parameters is to obtain a fit of the calculated optical constants at low photon energies to known values. If A is chosen to satisfy this fitting criterion, then it is found that different choices of $h\nu_m$ will lead to different "optimum" values for A .

To obtain a more accurate knowledge of the optical constants in the high energy region of measurement, a second criterion must be used in choosing the extrapolation. If the measured R is decreasing at high energies, a reasonable choice is to require that the slope of the reflectance be continuous at $h\nu_f$. Using this criterion, the error in the optical constants can be estimated for a given R slope discontinuity (see Eqs. (A.3) and (A.4) below).

As can be seen from Eq. (A.2a), the slope of the extrapolation at $h\nu_f$ depends only on A . Thus, using our second criterion of R slope continuity, A can be chosen unambiguously. Then $h\nu_m$ can be varied to satisfy the fitting criterion at low photon energies.

2. Results

It is found that variation of either of these quantities (A or $h\nu_m$) while the other is held fixed affects the magnitude uniformly but not the position of optical constant structure in the region of measurement. Thus, the unphysical dips in the $AgCl$ optical constants were probably not due to the extrapolation of the reflectance as Morrison speculated.[117] In fact, if only A is adjusted to fit low energy optical data, then the absorption coefficient α is the same for all

pairs of $h\nu_m$ and corresponding "optimum" A at photon energies below 15 eV if $h\nu_m$ is reasonably (at least 50%) larger than the $h\nu_f$ of 21.1 eV for the AgCl data used.[46] Between 15 and 21.1 eV the variation in α was less than 5% even at $h\nu_f$. This is consistent with the analytical findings by Nilsson and Munkby.[120] In fact, it is found that the error in α at an energy $h\nu$ is given approximately by

$$\Delta\alpha \approx \Delta\alpha_f \left(\frac{h\nu}{h\nu_f}\right)^{8.6} , \quad h\nu \leq h\nu_f \tag{A.3}$$

where $\Delta\alpha_f$ is the maximum error of this optical constant which occurs at $h\nu_f$. The error can be related to the discontinuity in the slope of the reflectance at $h\nu_f$, ΔS, by using the second criterion described above. It is found that for all slope discontinuities

$$\Delta\alpha_f \cong \frac{1}{30} \Delta S \tag{A.4}$$

where the error $\Delta\alpha_f$ is now the deviation of α at $h\nu_f$ from the corresponding value calculated with reflectance having a continuous slope at $h\nu_f$.

We can conclude that except for energies near the end of the measurement range, the optical constants calculated by a Kramers-Krönig analysis of a set of reflectance data are insensitive to the extrapolation of the data to high photon energies when the extrapolation is chosen to make a few low energy calculated optical constants agree with known values. This very significant conclusion is further substantiated by calculations of the optical constants of amoorphous Ge by T. M. Donovan using this computer program.[121] By fitting Θ to zero over the very narrow transparent region, the resulting value for the index of refraction at zero frequency was well within one percent of the measured value for amorphous Ge . In addition, the calculated ϵ_2 at the absorption edge fit the measured values quite well.

B. Effects of the Expansion of the Kramers-Krönig Integral

The Kramers-Krönig relation is computed numerically by expanding the integral of Eq. (A.1) about ν_0 and calculating its value, point-by-point. Thus, the calculated optical constants may depend on how the expansion is made. In our computer program, the procedure of Kreiger, Olechna, and Story[118] was followed. White used a different expansion in his calculations[47] so it is important to determine if this caused the anomalies in the optical constants. Using the identical input data as White,[50] it was found that structure in the optical constants did not differ significantly in position or magnitude for the two computations including the unphysical dips in α, κ, and ϵ_2. It would thus seem that these anomalies are not peculiarities of the calculation.

C. Effects of the Input Reflectance Values

Because of the reliability of the optical constants calculated in the manner described above, the cause for the anomalous optical constant structure in AgCl (and other solids[117]) is probably not related to the use of the Kramers-Krönig transform. One is thus compelled to examine the reflectance data in the energy range corresponding to the unphysical calculated structure. This is done for White and Straley's data[46] in Fig. A.1. In this figure, their entire data (through $h\nu_f = 21.1$ eV) is presented by the curve except in the region from 3.2 through 4.3 eV where the points and not the curve are their data. Above 21.1 eV, the extrapolation [Eq. (A.2a)] is shown which was chosen to fit the calculated Θ to zero from 0 through 3.0 eV. A close inspection of White and Straley's data shown in the figure reveals that the reflectivity has a discontinuity in slope at 3.2 eV and through 4.3 eV has values greater than the underlying smooth "envelope" (i.e., solid curve) by up to 11%. Reports of earlier measurements of the reflectivity[53] and optical absorption[54,51,52] of AgCl show smooth optical constants in this energy region. "Smoothing" the reflectance in accordance with these earlier measurements in this region, as shown by the solid curve, resulted in the changes in calculated optical constants shown in Fig. A.2.
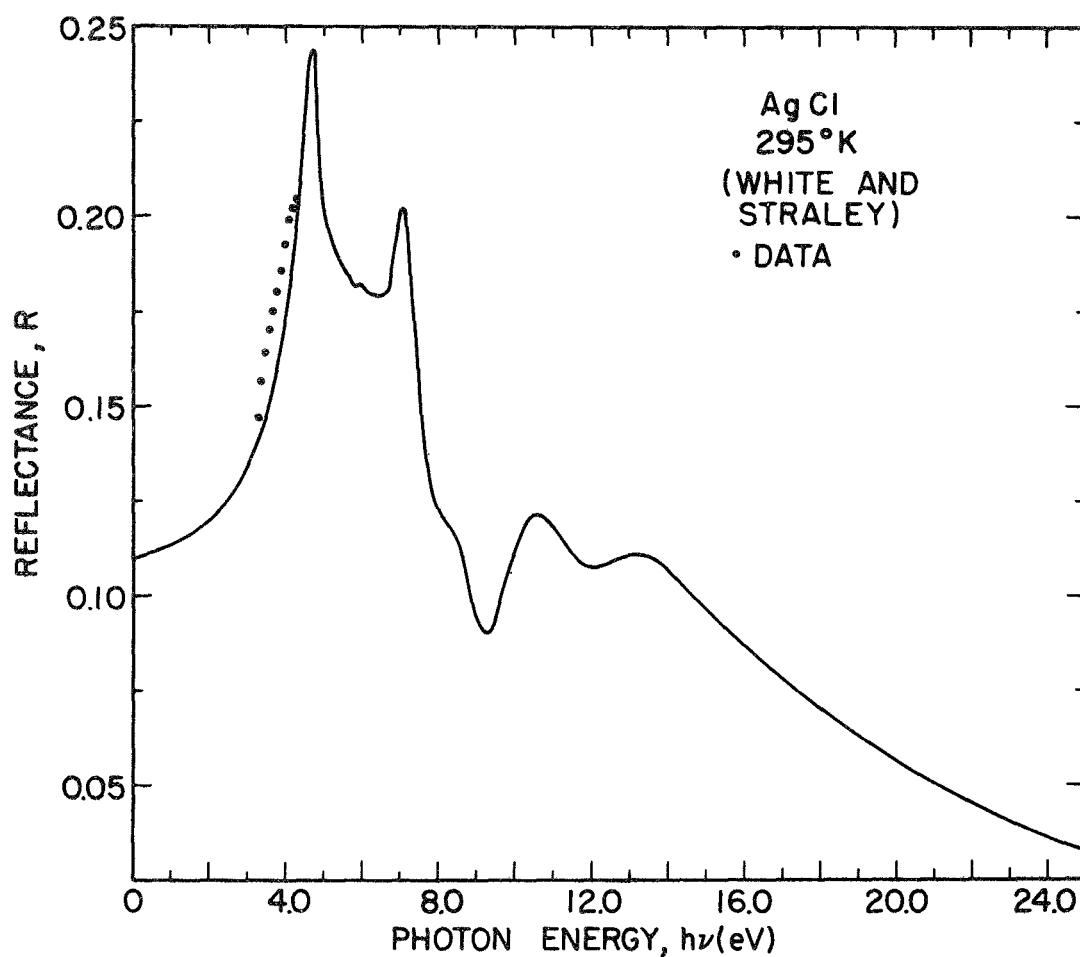
FIGURE A.1. The spectral distribution of the reflectance of AgCl at 295°K from the work of White and Straley (reference 46). In the region from 3.2 through 4.3 eV the points and not the curve are their data.
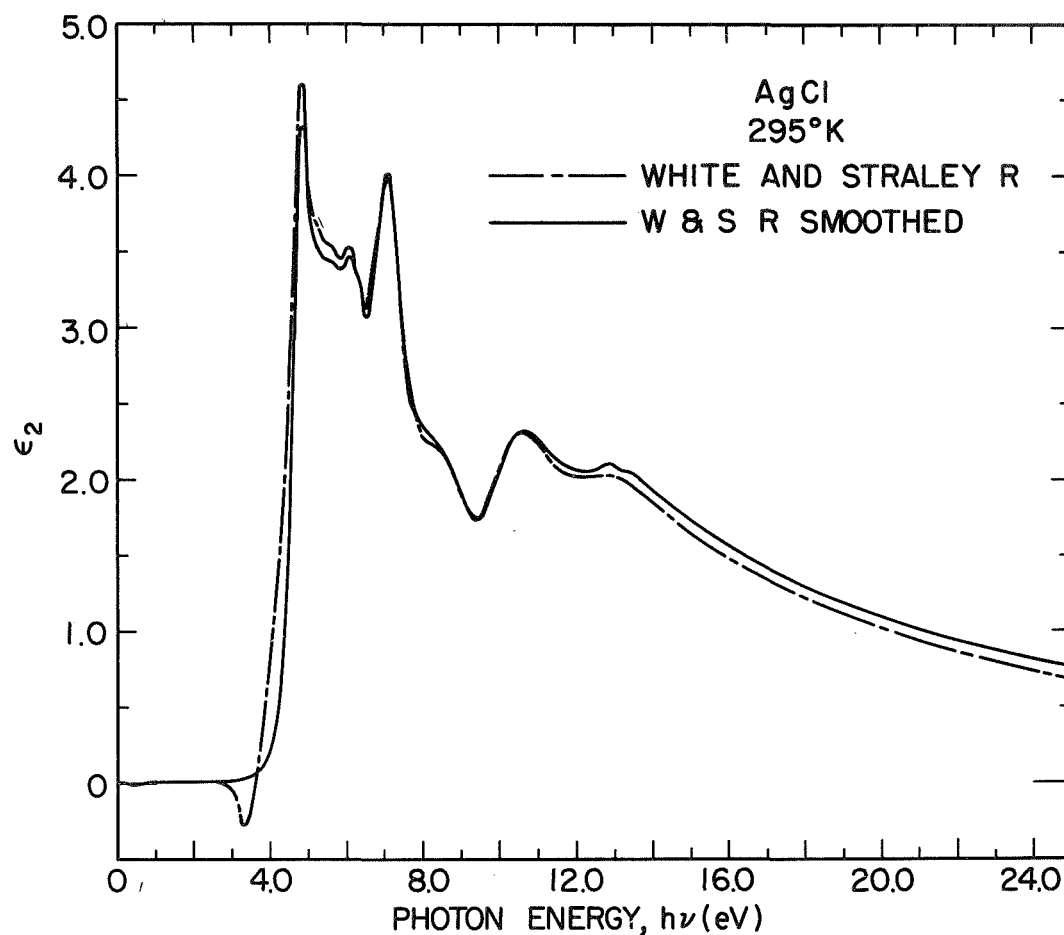
FIGURE A.2(a). Comparison of the spectral distributions of
the imaginary part of the dielectric constant
of AgCl at 295°K calculated from the re-
flectance of White and Straley (reference 46)
(— - —) and the same values but smoothed
from 3.2 through 4.3 eV (———).
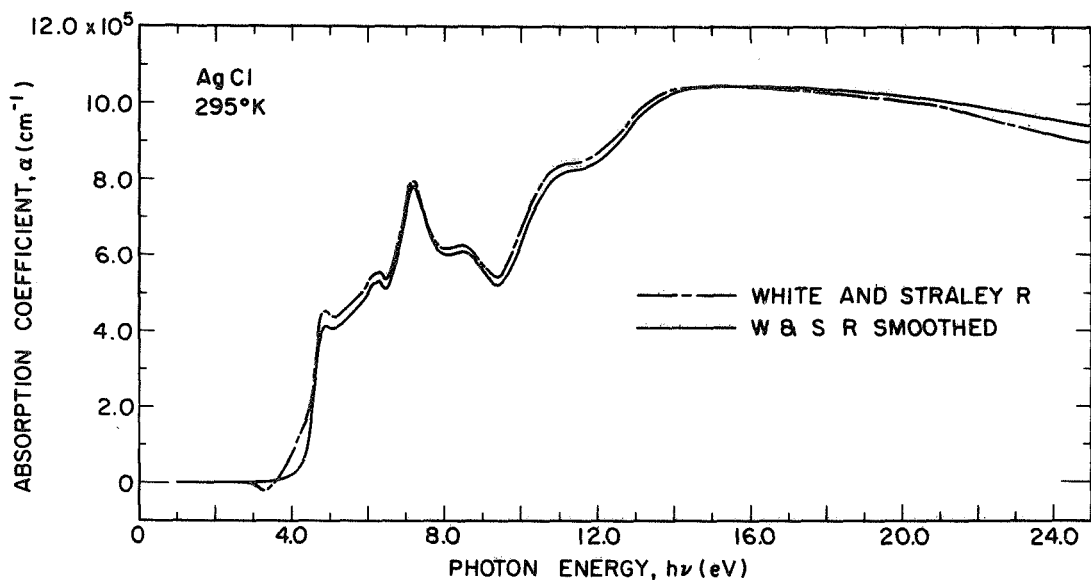
FIGURE A.2(b). Comparison of the spectral distributions of the absorption coefficient of AgCl at 295°K calculated from the reflectance of White and Straley (reference 46) (— - —) and the same values but smoothed from 3.2 through 4.3 eV (———).

The extrapolation of the reflectance was chosen to satisfy the same criterion for both sets of input values. As is readily evident, the optical constants with the White and Straley reflectance smoothed (i.e., "W&S R smoothed"), have the same structure as those calculated with the original data except for the complete absence of the unphysical dips at 3.2 eV. Except for the dips, the magnitude of these two sets of optical constants are in general quite similar, differing by less than 10% for energies above 3.2 eV.

This is a quite significant conclusion since it implies that the calculated optical constants which exhibit an unphysical dip near the edge[46,117] are quite reliable at energies other than these anomalies. Therefore, the dips can be neglected for all practical purposes. Further, because of the reliability of the optical constants calculated in this

252

manner, the Kramers-Krönig transform is a useful check of the measured reflectance data. In the case of AgCl discussed above, this analysis revealed an error in the experimental data (see Fig. A.1).

APPENDIX B. PHOTOEMISSION FROM VACUUM HEAT-CLEANED

Ag AND Pt

As was discussed in Chapter IV, 99.99% pure Ag and Pt were
used as substrate materials for the silver halide thin films. These
soft metals were pressed to work-harden them so they could be polished
to a mirror-like finish. They were then heat-cleaned at about $425^{\circ}C$
in the vacuum chamber until the pressure was around 1×10^{-10} Torr.
The photoemission from such specimens is believed to be some of the
best measured to date. The results as presented here, without theo-
retical analysis, are for future reference.

The EDCs for a typical Ag substrate is presented from $h\nu = 7.8$ eV
through 11.8 eV in Fig. B.1. The sample designation refers to the silver
halide film which was deposited onto its surface. This sample shows
some of the sharpest structure on the leading part of the curves measured
to date. They compare quite favorably to the work of Berglund and
Spicer,[122] Krolikowski,[1] and Walden.[123] A comparison to the photo-
emission from other samples is shown in Fig. B.2. Since these curves
are individually normalized, it can be seen that the major difference
between the AgBr-II-E sample of Fig. B.1 and AgCl-I-A substrate is
the much lower threshold in the later case; however, the higher energy
structure is completely lost for this sample. This is typical of the
Ag EDCs measured in previous studies. The information which is gained
concerning the stronger 4d EDC structure has been obtained in previous
cesiated studies (e.g., Walden's work[123]) and thus really offers nothing
particularly new. One other interesting thing that can be seen in this
data is that the Ag substrate can be heat-cleaned to almost its origi-
nal condition by evaporating the silver halide film off the substrate
once measurements of its properties have been completed. At $h\nu = 10.2$
eV, there is virtually no change in the EDC from the newly cleaned
Ag(AgBr-II-A) to its cleaned condition following the study of four
different AgBr samples (AgBr-II-E). It is important to note that

FIGURE B.1(a). Comparison of energy distributions normalized to absolute quantum yield (per absorbed photon) for electrons photo-emitted from Ag at 295°K for photon energies of 7.8 through 9.4 eV.

255
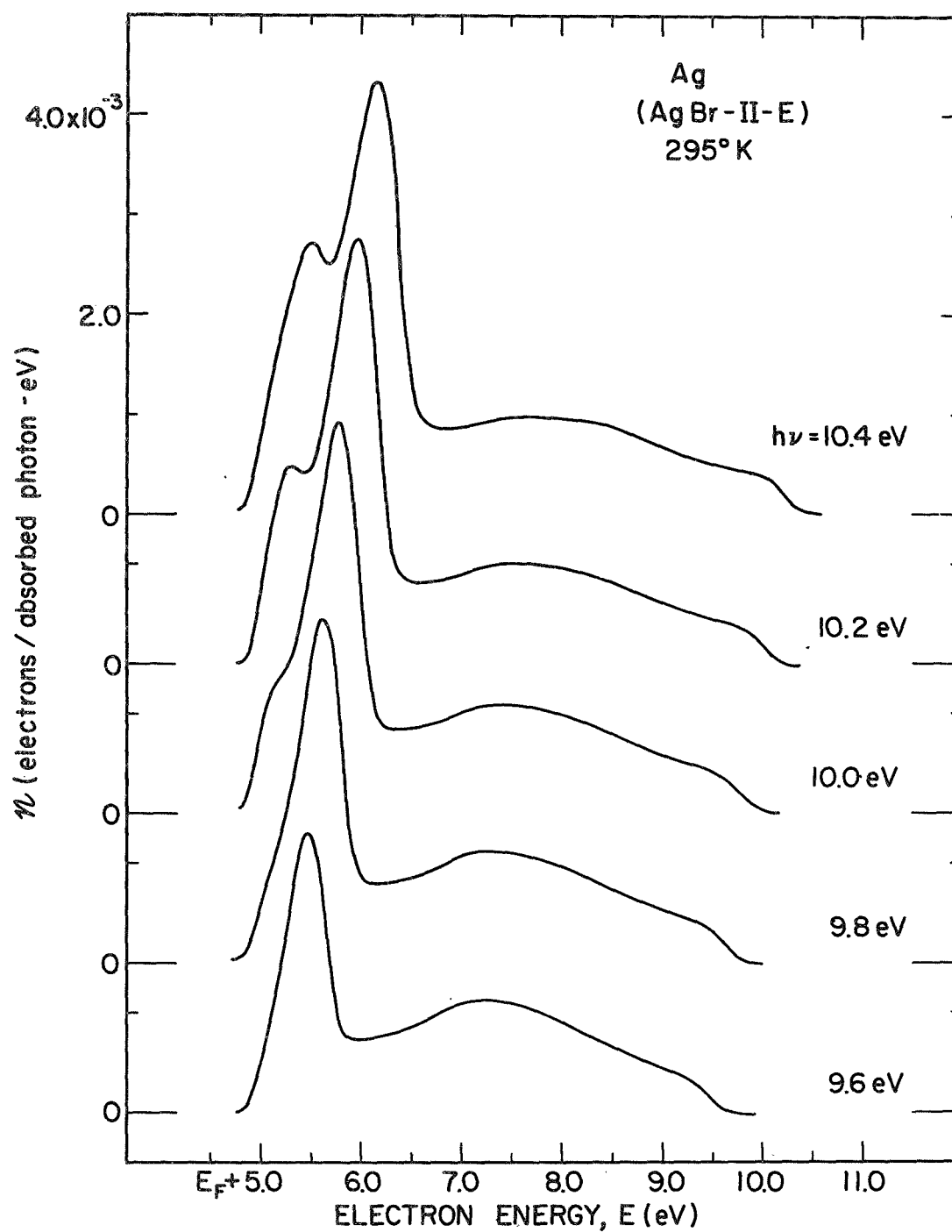
FIGURE B.1(b). Comparison of energy distributions normalized to
absolute quantum yield (per absorbed photon) for electrons photo-
emitted from Ag at 295°K for photon energies of 9.6 through 10.4 eV.

FIGURE B.1(c). Comparison of energy distributions normalized to
absolute quantum yield (per absorbed photon) for electrons photo-
emitted from Ag at 295°K for photon energies of 10.6 through
11.8 eV.
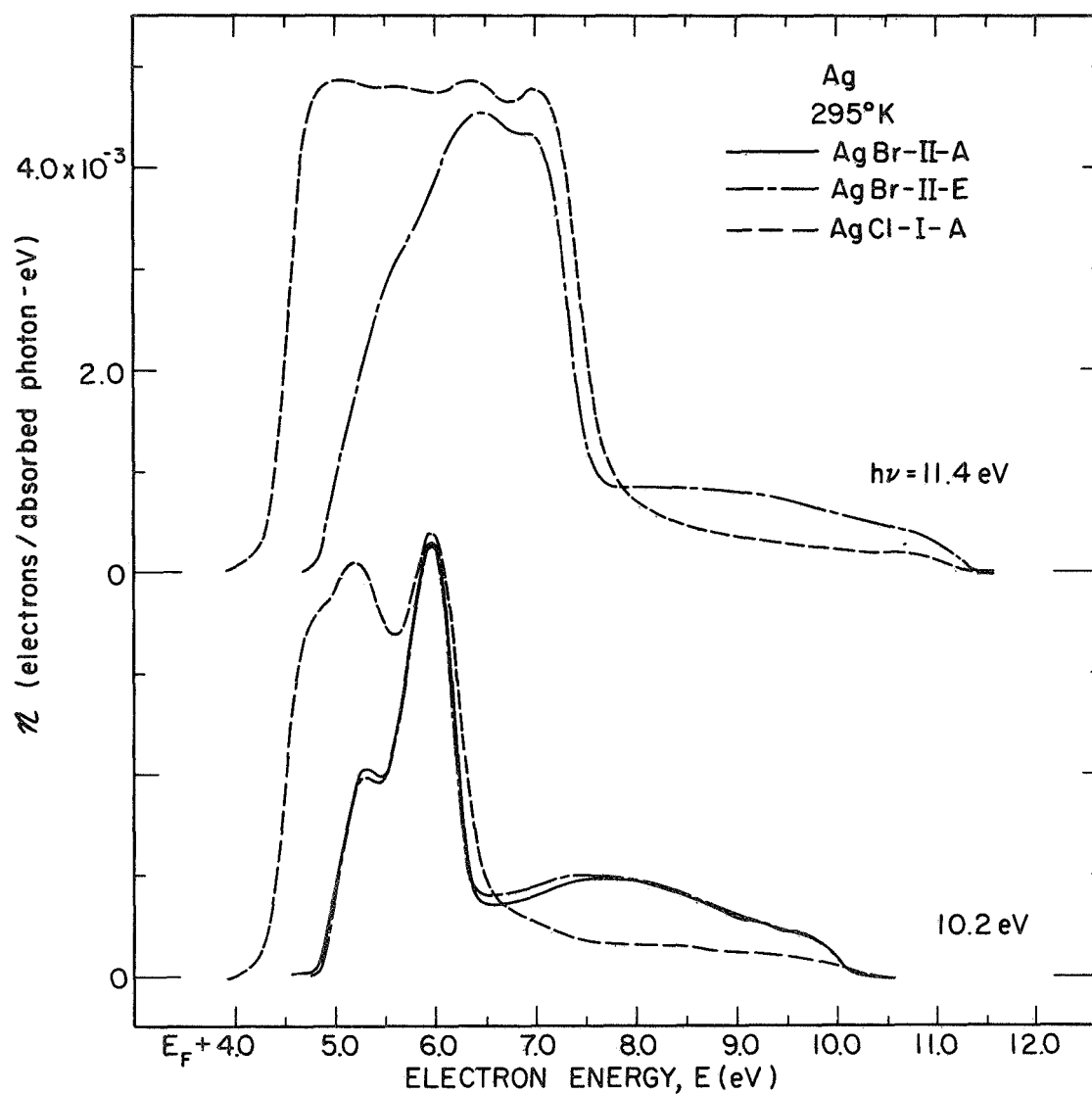
FIGURE B.2. Comparison of energy distributions normalized to
absolute quantum yield (per absorbed photon) for
electrons photoemitted from three Ag samples
at 295°K for photon energies of 10.2 and 11.4 eV.

the EDCs of Figs. B.1 and B.2 are normalized relative to the yield corrected for the Ag reflectance using the data of Ehrenreich and Philipp.[124] This yield is presented for three samples in Fig. B.3.
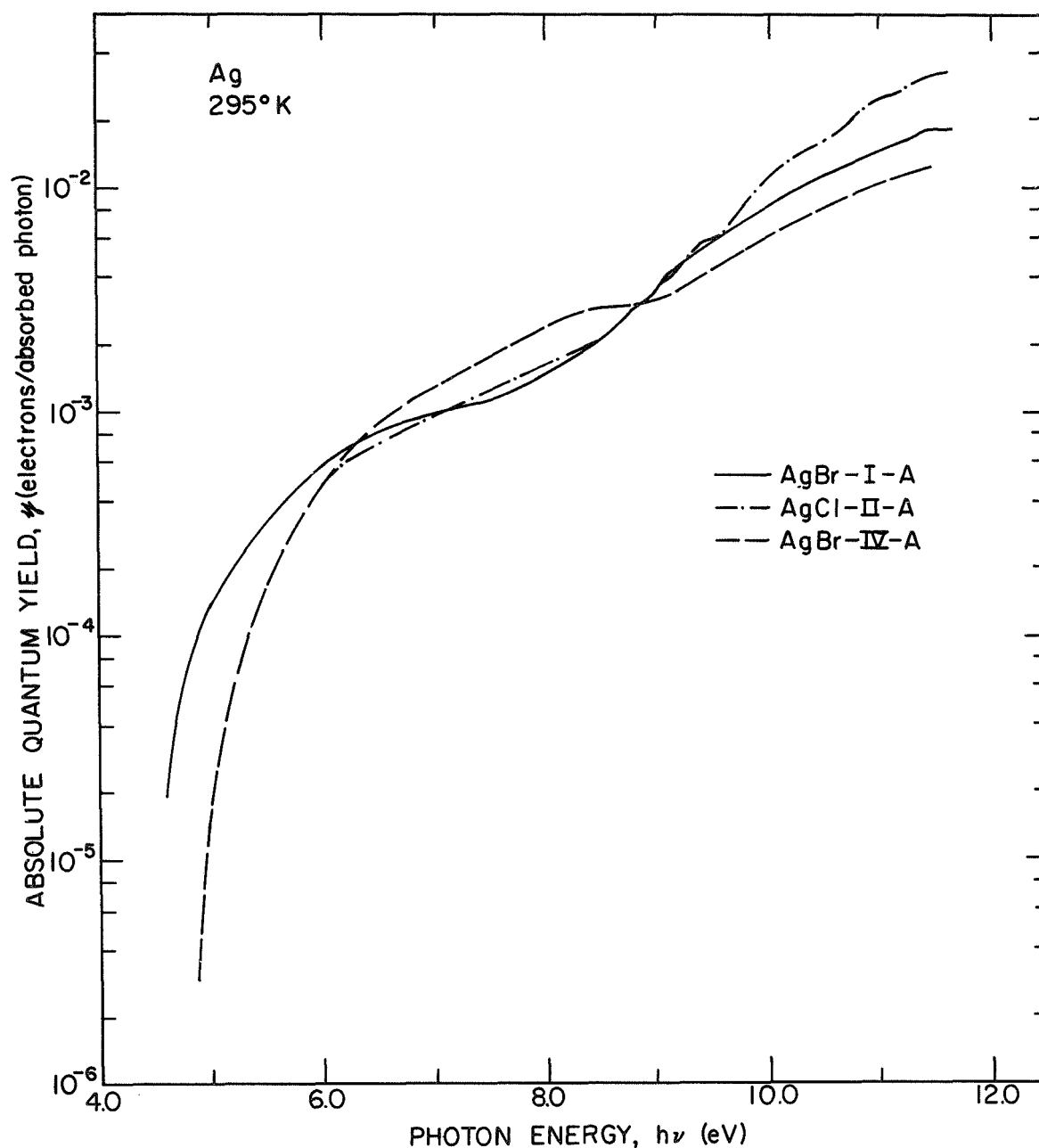
FIGURE B.3. Comparison of the spectral distributions of the yield of electrons photoemitted per absorbed photon from three Ag samples at 295°K.

No measurements of Ag photoemission below room temperature were taken.

The EDCs at three photon energies for the best sample of Pt are shown in Fig. B.4. Pt was much more difficult to reproducibly heat-
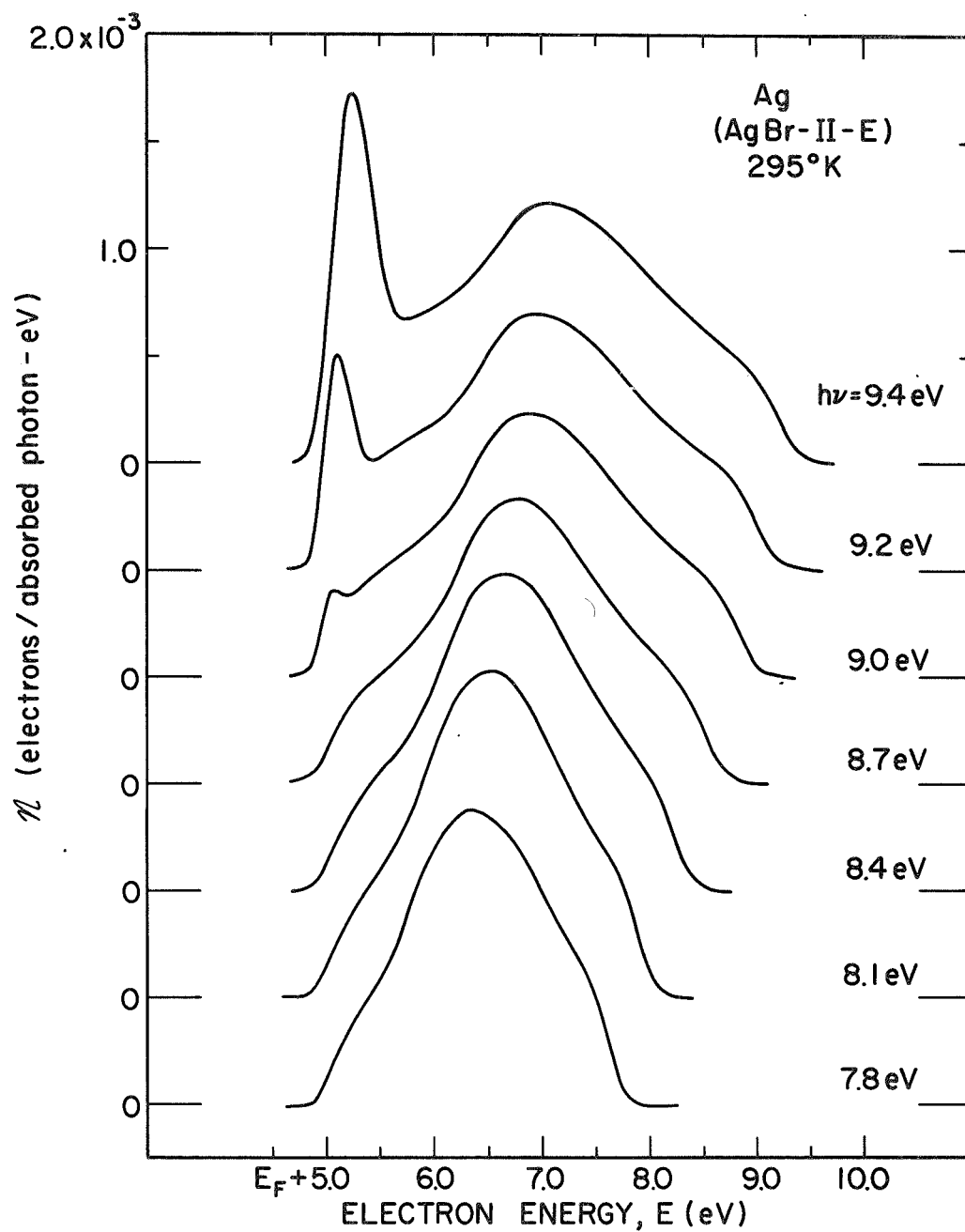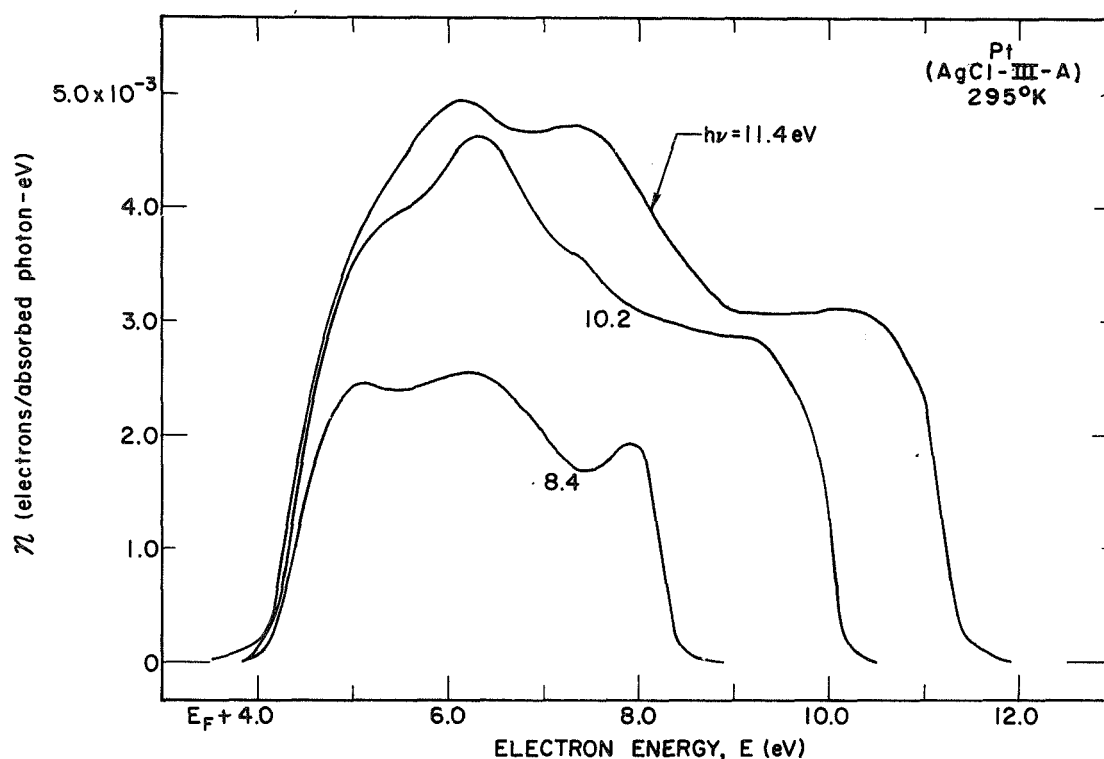

FIGURE B.4. Comparison of energy distributions normalized to absolute quantum yield (per absorbed photon) for electrons photoemitted from Pt at 295°K for photon energies of 8.4 through 11.4 eV.

clean than was Ag . Following a study of a AgCl or AgI sample, the photoemission of the cleaned Pt exhibited a higher threshold and less well-defined structure. Even following repolishing and reheat-cleaning the Pt , these excellent curves were not reproducible in all their details. These EDCs do exhibit much more structural detail than previous studies of heat-cleaned and E-gun evaporated Pt by Yu.[103]

The EDCs of Fig. B.4 are normalized relative to the absorbed photon flux.
The yield was corrected for reflectance using the data of G. Hass which
was presented in Yu's thesis.[103] This yield is presented in Fig. B.5.
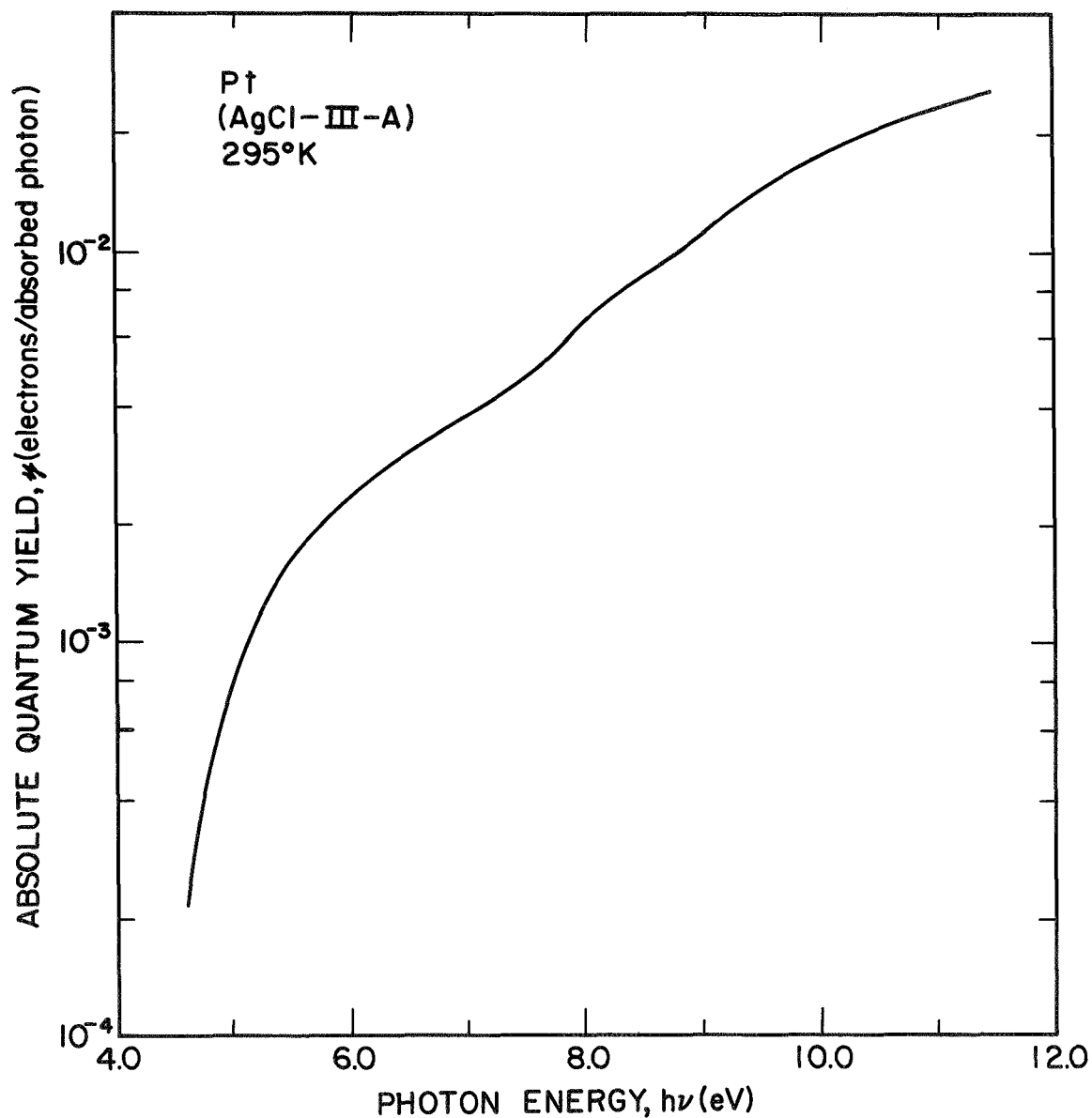
FIGURE B.5. The spectral distribution of the yield of electrons
photoemitted per absorbed photon from Pt at 295°K.

APPENDIX C. <u>CALIBRATION OF STANDARDS FOR THE MEASUREMENT</u>
<u>OF ABSOLUTE QUANTUM YIELD</u>

A reliable and accurate knowledge of the absolute yield of photo-
emitted electrons is important for interpreting the results of the
photoemission experiment. Since

$$Y = \mathcal{Y}(1 - R) = \frac{I}{q_e F} \quad , \quad (C.1)$$

the yield per incident photon, Y , is determined if the incident
photon flux, F , can be measured, since the photocurrent, I , is
readily measurable. If one has a calibrated photodiode, then the mea-
surement of its photocurrent gives the incident photon flux directly by
Eq. (C.1). Therefore, the absolute quantum yield of the solid under
study is determined by comparing the total photoemitted current from
the sample with the photoresponse to the same incident photon flux of
a calibrated photodiode standard. It is clear that this measurement
is only as accurate as the calibration of the quantum yield of the
reference cell. The reference tubes used in our laboratory are made
at Stanford of a Cs_3Sb photocathode with a LiF window using the
construction and design developed by A. J. Blodgett.[125] As part of our
study, new procedures were developed to calibrate the relative spectral
response and absolute response of these standards to a much greater
accuracy and reproducibility than had been possible before. One of the
reasons this was undertaken was because it became apparent early in
these studies that the responses of the tubes used for this purpose
had changed since they were originally calibrated by R. Y. Koyama over
two years before.[126]

A. Measurement Techniques

As a first step in the calibration procedure, the relative response is determined by measuring the photoresponse of the Cs_3Sb tube relative to a UV sensitive, narrow emission band phosphor, sodium salicylate (SS), which has a known photon energy conversion efficiency. Koyama investigated the SS quantum efficiency by comparing the response of the Cs_3Sb cell to that of an uncalibrated UV thermopile.[126] Since this device has a flat spectral response, it serves as a check of the spectral dependence of the SS quantum efficiency. Koyama found that the efficiency can be taken as constant from 3.7 through 10.5 eV but for photon energies greater than 10.5 eV, the quantum efficiency decreases. This general behavior of the quantum efficiency of SS agrees with many reported measurements.[127-129] The departure of the quantum efficiency from constancy is presented in Table C.1 from unpublished data of Koyama.[130]

TABLE C.1. Spectral distribution of the relative quantum efficiency of sodium salicylate from unpublished work of Koyama (reference 130).

$h\nu$ (eV)	SS RELATIVE QUANTUM EFFICIENCY (KOYAMA)
3.7 → 10.5	1.00
10.6	0.97
10.7	0.94
10.8	0.93
10.9	0.90
11.0	0.88
11.1	0.88
11.2	0.89
11.3	0.91
11.4	0.91
11.5	0.86
11.6	0.82
11.7	0.71
11.8	0.80

The Cs_3Sb tube response had been measured relative to that of SS in the manner depicted in part (a) of Fig. C.1 prior to this work (see reference 126). The cell being calibrated is mounted on a linear motion so it can be moved in and out of the light beam. After the photoresponse of the cell has been measured, it is removed from the beam and the same incident photon flux is incident on the phospher. It emits radiation at a fixed energy for all incident wavelengths (i.e., it is a photon energy converter). Thus, the yield of the photomultiplier is not important since this measuring device is always detecting the same energy radiation for all calibrating frequencies. In this way, the relative response is measured if the quantum efficiency of the SS is known. The use of a photomultiplier is a serious deficiency in this measurement procedure. Since the photomultiplier used to measure phosphor fluorescence intensity has a much higher sensitivity than the Cs_3Sb photodiode, it is necessary to place an aperture in front of the photomultiplier to avoid saturation. In a series of measurements using this technique, there was a general lack of reproducibility among the data sets. It is believed that this is due to the fact that using this method, only the fluorescence induced by a small portion of the photon flux incident on the Cs_3Sb tube is measured by the photomultiplier. Thus, any inhomogeneities in the light beam cause errors in the measurements.

To obtain more reliable data, a method has been developed wherein the Cs_3Sb tube being calibrated is also used to measure the phosphor fluorescence as shown schematically in part (b) of Fig. C.1. This is accomplished by having the SS mounted on the linear motion and moving it in and out of the light beam just in front of the Cs_3Sb photodiode. The need for a photomultiplier is thereby eliminated, and the same photon flux is incident on the photodiode being calibrated and the region of the calibrating phosphor being monitored. The actual ring which was used on the monochromator is pictured in Fig. C.2 with the Cs_3Sb tube and SS mounted on linear motions. In part (a) the entire ring is shown with the SS in front of the tube while in part (b), the closeup shows the SS withdrawn and the photoresponse of the tube being calibrated can be measured. Since the Cs_3Sb photodiode is such a broadband detector

264
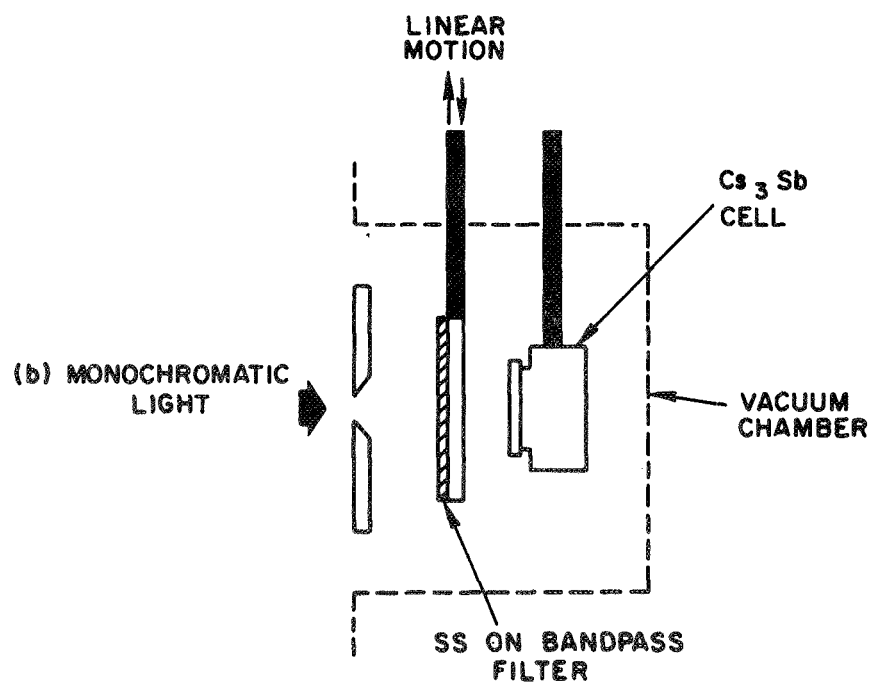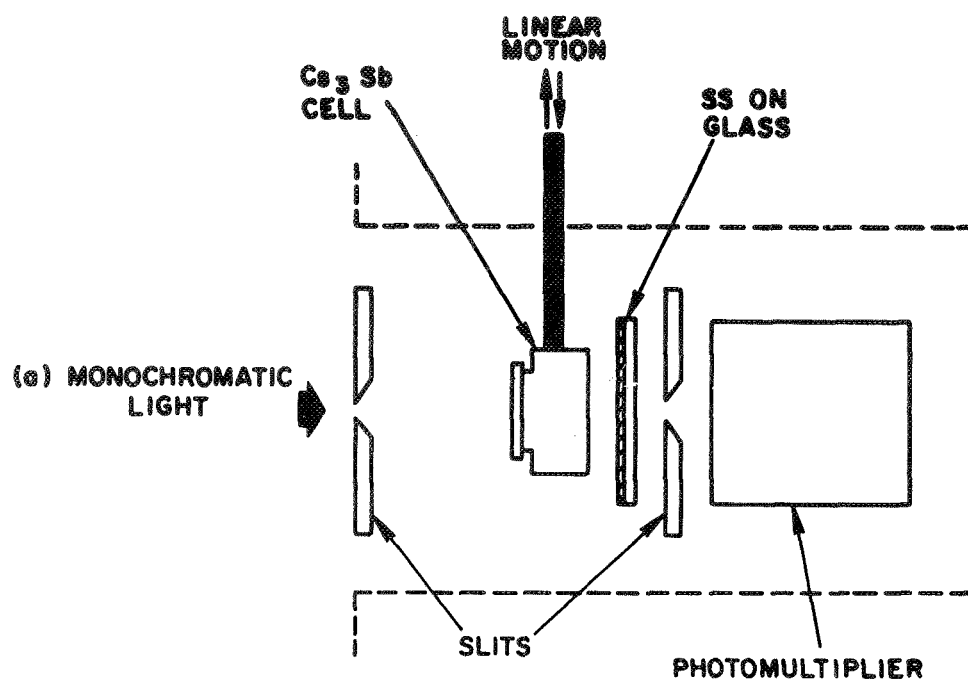
FIGURE C.1(a) and (b). Schematic diagram of the apparatus used to
calibrate the relative response of the Cs_3Sb cell by utilizing a
sodium salicylate phospher in (a) previous work and (b) the present
work.
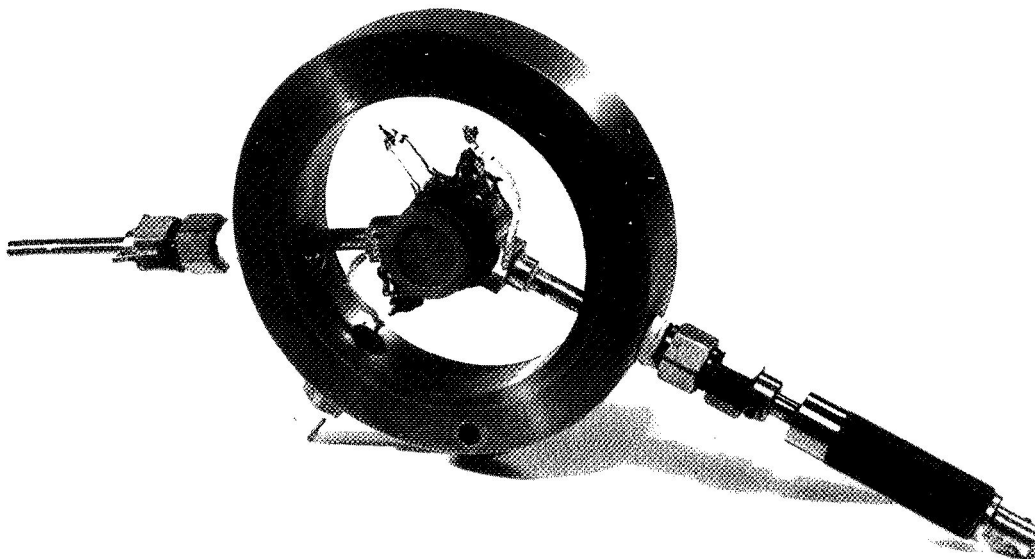
FIGURE C.2(a) and (b).

Photograph of the apparatus used to calibrate the relative
response of the Cs_3Sb standard showing the sodium salicy-
late phospher in the two positions used in making the
measurements.

SODIUM
SALICYLATE

Cs_3Sb
TUBE

FIGURE C.2(b)

267
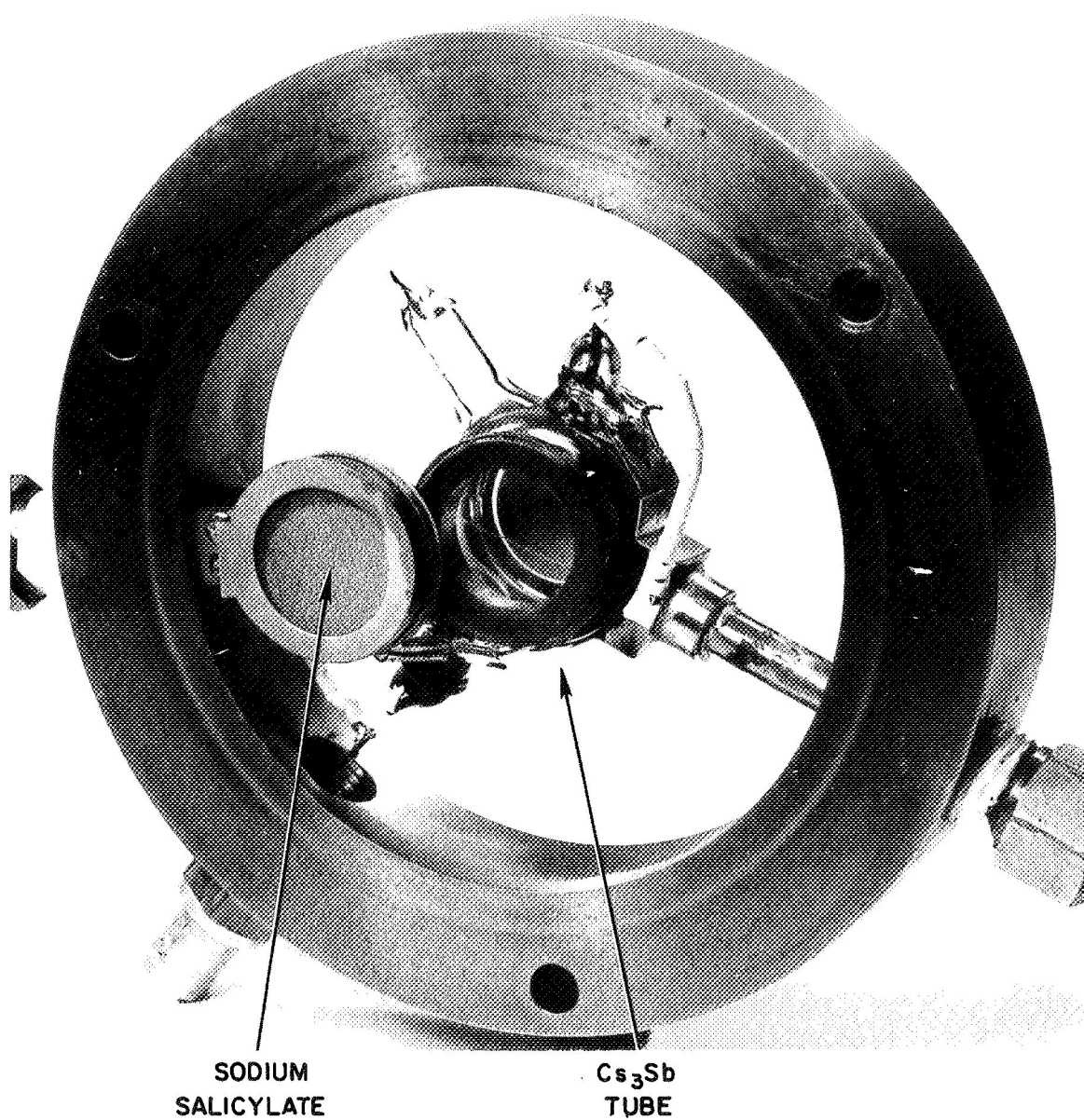
(see Fig. C.3 below), precautions must be taken to insure that only the
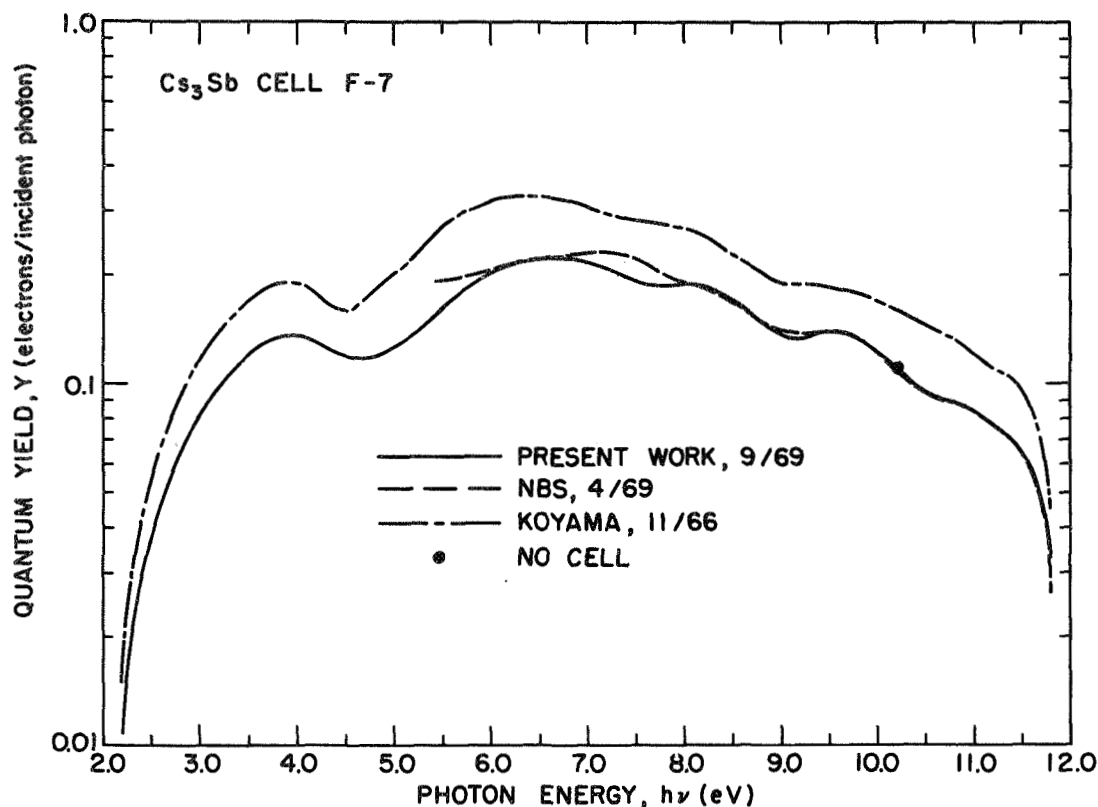
FIGURE C.3. Comparison of the spectral distributions of the yield
of electrons photoemitted per incident photon from
the Cs$_3$Sb cell F-7 from the present work and the
works of Canfield and Madden at the NBS (reference 132)
(— — —) and Koyama (reference 126) (— - —). The absolute
calibration point determined using a NO cell is also
shown.

phosphor fluorescent emission is being measured when it is placed in
front of the tube. Therefore, the SS is sprayed[126] directly onto a
narrow bandpass optical filter to eliminate any UV radiation which may
be transmitted through the phosphor from being detected by the Cs$_3$Sb
tube. This filter (Corning Glass Filter No. 5-60) was, of course,
chosen to have a maximum transmission near the approximately 2.9 eV

fluorescence maximum of SS. It should be noted that the phosphor
fluorescence occurs in the low photon energy cutoff region of the photo-
diode (see Fig. C.3). Though this emission spectrum has a sharp high
energy cutoff, it has a rather long tail at low photon energies.[131]
The optical filter thus also increases the reliability of the measure-
ment by confining the measured fluorescent radiation to a narrow energy
region over which the tube response does not change greatly. This tech-
nique has the additional advantage that only one ammeter is necessary.
Errors due to meter calibration differences in the two-meter technique
used previously are thereby eliminated. When the spectral dependence
of the SS quantum efficiency is taken into account (see Table C.1), the
relative spectral response of the standard cell will have been measured.

The absolute quantum yield of the UV standard had been determined
in the past by comparing the response of the Cs_3Sb to that of a cali-
brated visible thermopile from 4.0 to 5.0 eV.[126] This is somewhat
unsatisfactory since it is used to set the absolute response all the way
up to 11.8 eV. In order to determine the absolute quantum yield in the
UV directly, the Cs_3Sb photodiode was measured relative to a cali-
brated NO ion chamber at 10.2 eV. This calibrated gas cell was purchased
from Melpar, Inc. of Falls Church, Virginia. This then set the absolute
scale for the relative response determined by comparison with SS dis-
cussed above.

B. Results

A series of measurements were made using SS films ranging in
"thickness" from 2.4 to 6.6 mg/cm^2. The results were virtually identi-
cal in magnitude as well as relative structure for all the films. It
should be noted that the relative intensity of the fluorescence response
is independent of SS thickness for films 1.5 to at least 4.0 mg/cm^2.[131]
The average of these measurements were adjusted to the absolute value
determined by comparison to the NO cell. The resulting absolute cali-
bration of the Cs_3Sb cell number F-7 is presented in Fig. C.3. This
Cs_3Sb tube was also measured relative to another Cs_3Sb photodiode
whose photoresponse was subsequently compared to a calibrated UV thermopile

by Canfield and Madden of the National Bureau of Standards.[132] The resulting values for our tube are also plotted on Fig. C.3. The agreement between these two independent sets of measurements is remarkably good. The nearly identical values above 10.5 eV are evidence of how well the relative SS quantum efficiency had been determined by Koyama (i.e., the values of Table C.1). The deviation below 6.0 eV is probably due to inaccuracy in the NBS data caused by the low sensitivity of the thermopile to radiation at such low energies. The dip at 4.7 eV is probably characteristic of the Cs_3Sb cell and not the SS since it was reproduced by measurements using a visible thermopile.[126]

The absolute calibration of the cell is believed to be within ± 4% from 3.7 through 11.6 eV. The absolute yield of F-7 at 10.2 eV determined from the NO cell was 4% higher than the value measured at the NBS. As another check, the measurement program discussed above was performed on a second Cs_3Sb tube. When the F-7 cell was compared to it, the resulting yield was 4% higher than the value determined by comparison with the NO cell. Since the relative response using the newly developed procedures was reproducible to a higher accuracy than this, the values from $h\nu = 3.7$ eV through 11.6 eV are believed to be within ± 4%. Since the cell was rarely used below this energy, it was not extensively calibrated at the lower energies. The spectral dependence of the F-7 yield determined by Seib and Eden in 1966,[126] was fitted onto the newly determined yield from 3.7 through 5.0 eV. A rough check with the calibrated S-1 visible standard[133] showed these values to be reasonable but an estimate of the overall accuracy in this energy range could not be made. This resulting yield is tabulated in Table C.2 for future reference.

The original calibration of this cell by Koyama is also shown in Fig. C.3 for comparison. Our new calibration of 9/69 is reduced by about 29% from Koyama's values of 11/66. If the earlier absolute calibration was accurate, this would indicate a fairly uniform drop in sensitivity of the tube by this amount over a period of a little less than three years. This decrease is probably due to a loss in transmission of the LiF window on the Cs_3Sb tube.

TABLE C.2. Spectral distribution of the quantum yield (per incident photon) of the Cs_3Sb standard F-7 to ± 4% for $3.7 \leq h\nu \leq 11.6$ eV.

$h\nu$ (eV)	$Y \left(\dfrac{elec.}{inc.\ ph.}\right)$	$h\nu$ (eV)	$Y \left(\dfrac{elec.}{inc.\ ph.}\right)$	$h\nu$ (eV)	$Y \left(\dfrac{elec.}{inc.\ ph.}\right)$	$h\nu$ (eV)	$Y \left(\dfrac{elec.}{inc.\ ph.}\right)$
2.2	0.0108	4.6	0.119	7.0	0.218	9.4	0.140
2.3	0.0200	4.7	0.118	7.1	0.214	9.5	0.141
2.4	0.0310	4.8	0.120	7.2	0.210	9.6	0.139
2.5	0.0393	4.9	0.124	7.3	0.204	9.7	0.137
2.6	0.0480	5.0	0.127	7.4	0.198	9.8	0.135
2.7	0.0574	5.1	0.131	7.5	0.192	9.9	0.130
2.8	0.0668	5.2	0.139	7.6	0.188	10.0	0.123
2.9	0.0749	5.3	0.148	7.7	0.188	10.1	0.116
3.0	0.0840	5.4	0.158	7.8	0.186	10.2	0.111
3.1	0.0927	5.5	0.167	7.9	0.188	10.3·	0.105
3.2	0.101	5.6	0.173	8.0	0.189	10.4	0.100
3.3	0.108	5.7	0.181	8.1	0.191	10.5	0.0975
3.4	0.114	5.8	0.190	8.2	0.189	10.6	0.0938
3.5	0.122	5.9	0.198	8.3	0.182	10.7	0.0916
3.6	0.129	6.0	0.203	8.4	0.178	10.8	0.0903
3.7	0.133	6.1	0.211	8.5	0.172	10.9	0.0870
3.8	0.136	6.2	0.216	8.6	0.162	11.0	0.0854
3.9	0.139	6.3	0.219	8.7	0.154	11.1	0.0800
4.0	0.137	6.4	0.221	8.8	0.148	11.2	0.0771
4.1	0.135	6.5	0.222	8.9	0.141	11.3	0.0746
4.2	0.130	6.6	0.224	9.0	0.137	11.4	0.0711
4.3	0.126	6.7	0.225	9.1	0.134	11.5	0.0660
4.4	0.122	6.8	0.224	9.2	0.134	11.6	0.0603
4.5	0.120	6.9	0.221	9.3	0.137	11.7	0.0474
						11.8	0.0334

± 4% for $3.7 \leq h\nu \leq 11.6$ eV

This work allows us to measure the absolute quantum yield of the solids under study in our photoemission experiments with more accuracy and reliability than was previously possible. It also provides a direct measure of the absolute quantum efficiency of sodium salicylate. Once the relative response of the tube has been determined, this new method allows the photoresponse of the cell to be compared with and without the SS in front (see Fig. C.1b); the magnitude of the efficiency is then readily determined when the spectral distributions of the SS fluorescence and filter transmission are corrected for.

APPENDIX D. ADDITIONAL AgBr AND AgCl DATA

As noted in Chapter VIII, all of the photoemission data for AgI ,
and, except near threshold, all of the data for AgBr and AgCl has
been presented in the main text according to the characteristics of the
electronic states which could be determined from it. This omitted AgBr
and AgCl threshold data is presented in Figs. D.1 and D.2, respectively.
Since it does not contain any characteristics which are not seen at
higher energies, it was not included in the text. The positions of these
peaks were included in the structure plots, however. This data is pre-
sented here for completeness and future reference.

The room temperature results for the absorption coefficient and
imaginary part of the dielectric constant of AgCl , in the energy
range of our photoemission measurements of this solid, are presented
for easy reference in Fig. D.3. These are the computer plots of the
calculated optical constants using the reflectance data of White[50] which
we smoothed to correct for anomalous structure introduced by the original
data. The details of the calculation were described in Appendix A.

FIGURE D.1. Comparison of energy distributions normalized to quantum
yield (per incident photon) for electrons photoemitted from AgBr
at 80 and 295°K for photon energies of 7.8 through 8.6 eV.

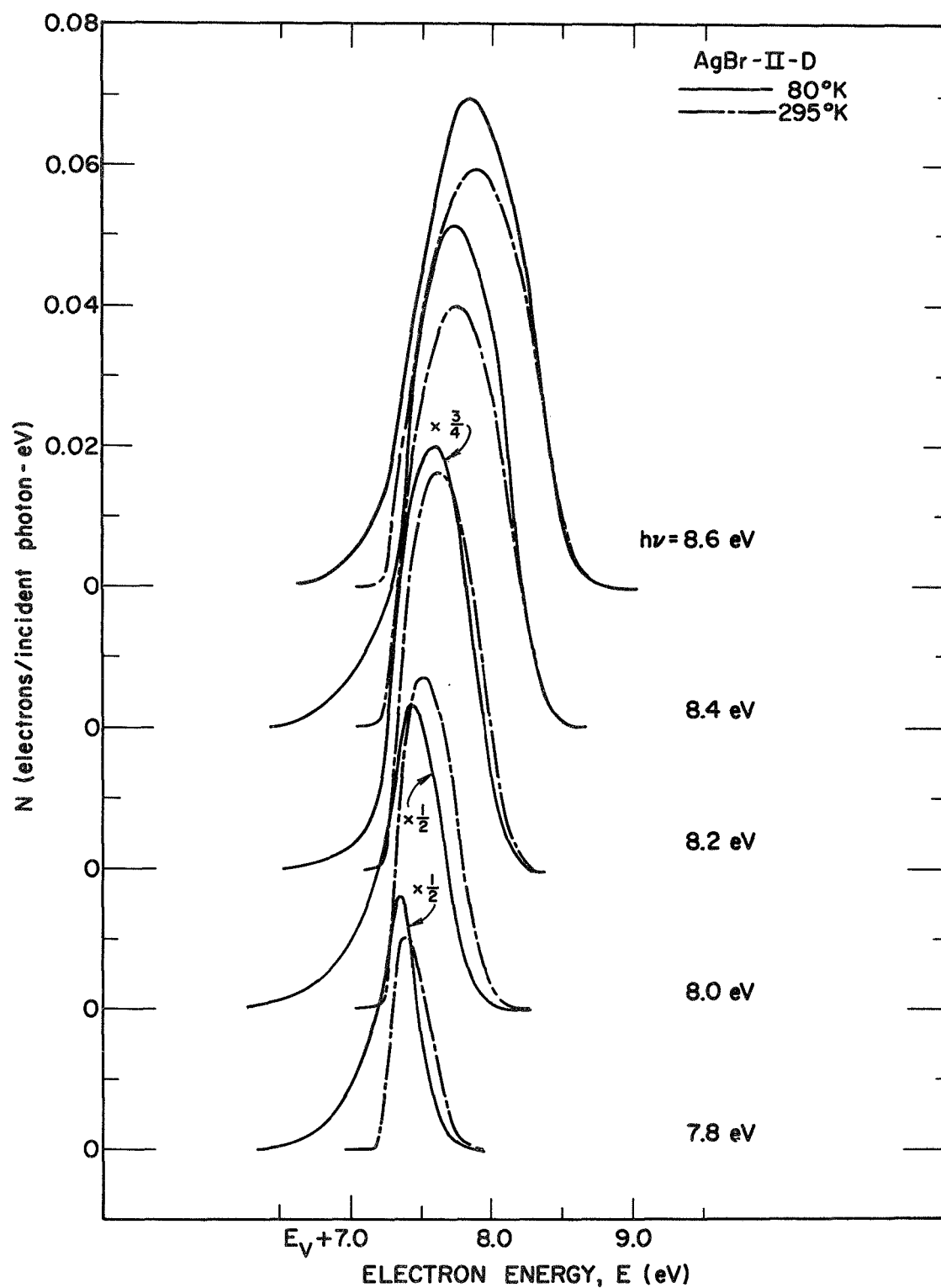FIGURE D.2. Comparison of energy distributions normalized to quantum yield (per incident photon) for electrons photoemitted from AgCl at 80 and 295°K for photon energies of 8.2 through 9.0 eV.
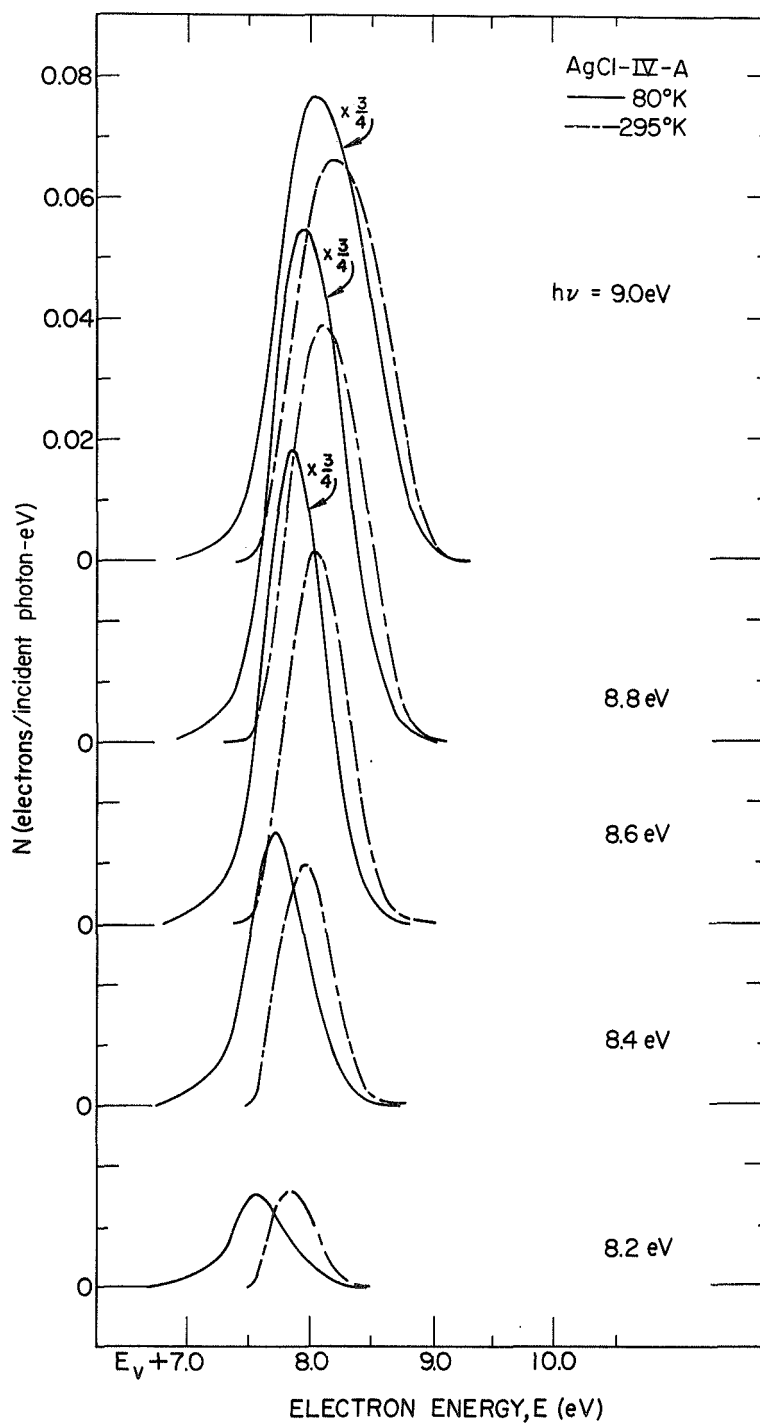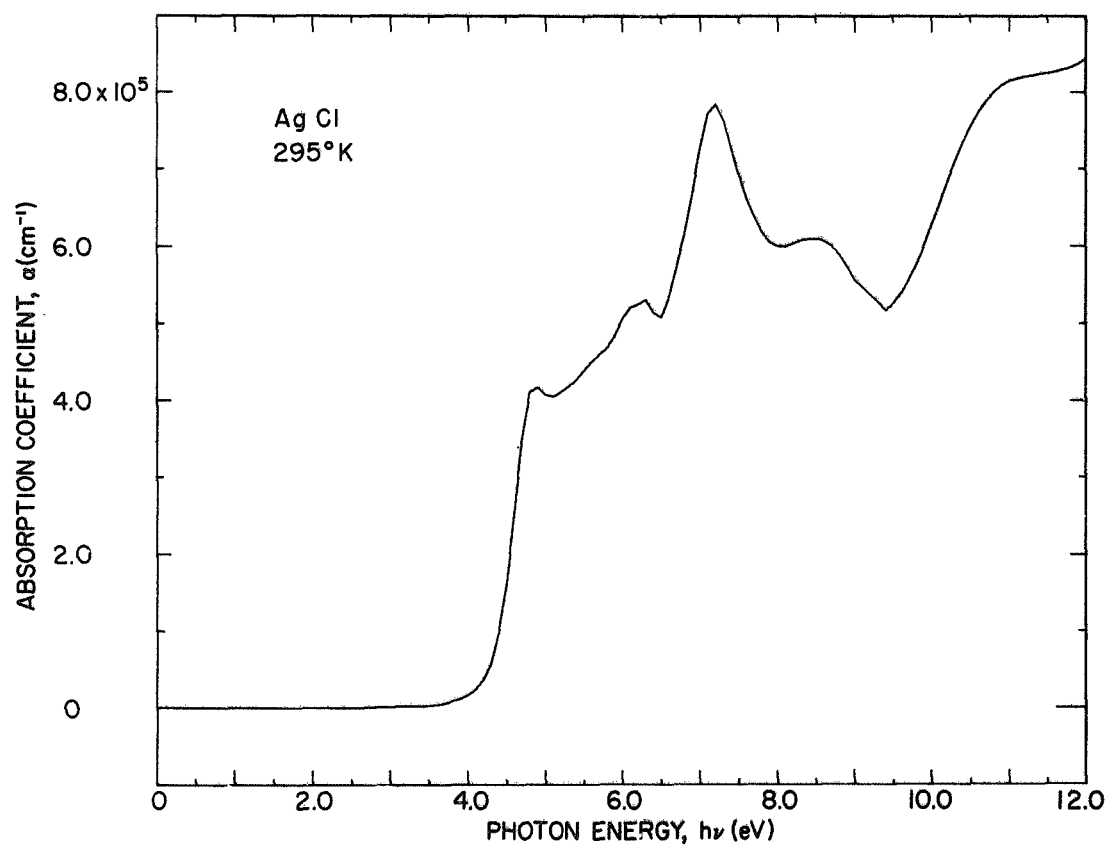
FIGURE D.3(a). The spectral distributions of the absorption
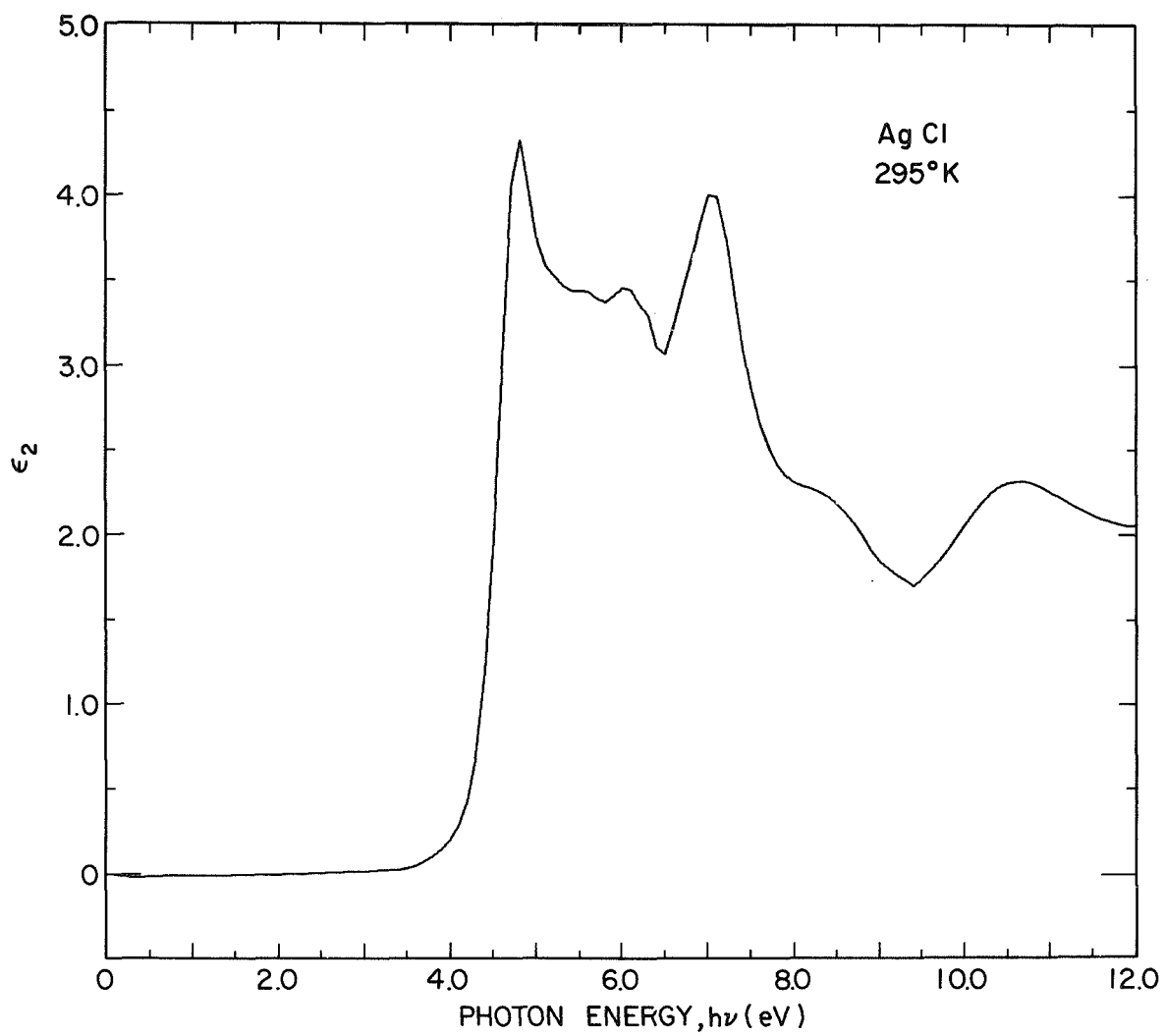coefficient of AgCl at 295°K.

FIGURE D.3(b). The spectral distributions of the imaginary
               part of the dielectric constant of AgCl
               at 295°K.

REFERENCES

1. W. F. Krolikowski, Ph.D. Dissertation, Stanford University, Stanford, California (1967).

2. T. H. DiStefano, Ph.D. Dissertation, Stanford University, Stanford, California (1970).

3. F. Bassani, R. S. Knox, and W. B. Fowler, Phys. Rev. 137, A1217 (1965).

4. R. B. Aust, Phys. Rev. 170, 784 (1968).

5. F. Herman and S. Skillman, Atomic Structure Calculations (Prentice-Hall, Inc., Englewood Cliffs, New Jersey, 1963).

6. P. M. Scop, Phys. Rev. 139, A934 (1965).

7. R. A. Smith, Wave Mechanics of Crystalline Solids (Chapman and Hall, Ltd., London, 1963).

8. J. M. Ziman, Principles of the Theory of Solids (Cambridge University Press, London, 1965), p.60.

9. W. Hidshaw, J.T. Lewis, and C.V. Briscoe, Phys. Rev. 163, 876 (1967).

10. A. J. Dekker, Solid State Physics (Prentice-Hall, Inc., Englewood Cliffs, New Jersey, 1957).

11. J. S. Blakemore, Solid State Physics (W. B. Saunders Company, Philadelphia, 1969), p. 113.

12. Karl A. Gschneidner, Jr., Solid State Physics, edited by F. Seitz and D. Turnbull (Academic Press, New York, 1964), Vol. 16, p.370.

13. G. Ascarelli, Phys. Rev. Letters 20, 44 (1968).

14. G. Ascarelli, Phys. Letters 26A, 269 (1968).

15. K. K. Thornber and R. P. Feynman, Phys. Rev. B, 1, 4099 (1970).

16. R. Stuart, F. Wooten, and W. E. Spicer, Phys. Rev. 135, A495 (1964).

17. H. Y. Fan, Phys. Rev. 82, 900 (1951).

18. D. L. Dexter, Nuovo Cim., Supl. VII, No. 2, 245 (1958).

19. F. Urbach, Phys. Rev. 92, 1324 (1953).

20. R. S. Knox, Theory of Excitons, Suppl. 5 to Solid State Physics, edited by F. Seitz and D. Turnbull (Academic Press, Inc., New York, 1963), p.155.

43. F. C. Brown, J. Phys. Chem. 66, 2368 (1962).

44. W. Martienssen, Proceedings of the International Conference on Semiconductor Physics (Czechoslovak Academy of Science, Prague, 1960), p.760.

45. N. J. Carrera, Ph.D. Dissertation, University of Illinois (1970).

46. J. J. White, III and J. W. Straley, J. Opt. Soc. Am. 58, 759 (1968).

47. J. J. White, III., Ph.D. Dissertation, University of North Carolina (1965).

48. C. W. Peterson, Phys. Rev. 148, 335 (1966).

49. C. J. Koester and M. P. Givens, Phys. Rev. 106, 241 (1957).

50. J. J. White, III, Private Communication (1968).

51. Y. Okamoto, Nachr. Akad. Wiss. Gottingen Math. Physik. KL. IIa, 14, 275 (1956).

52. P. D. Millman, Masters Dissertation, Cornell University (1953) and cited references.

53. P. L. Hartman and R. C. Merrill, J. Opt. Soc. Amer. 51, 168 (1961).

54. P. G. Aline, Phys. Rev. 105, 406 (1957).

55. J. J. White, III, Bull. Am. Phys. Soc. 13, 1720 (1968).

56. R. C. Brandt and F. C. Brown, Phys. Rev. 181, 1241 (1969).

57. B. L. Joesten and F. C. Brown, Phys. Rev. 148, 919 (1966).

58. B. L. Joesten and F. C. Brown, Phys. Letters 17, 202 (1965).

59. F. C. Brown, T. Masumi, and H. H. Tippins, J. Phys. Chem. Solids 22, 101 (1961).

60. K. L. Shaklee and J. E. Rowe (to be published).

61. F. C. Brown, Private Communication (1970).

62. G. Ascarelli and F. C. Brown, Phys. Rev. Letters 9, 209 (1962).

63. G. Baldini and B. Bosacchi, Phys. Rev. 166, 863 (1968).

64. K. Vacek, J. Ringeissen, and S. Nikitine, J. De Chim. Phys. 59, 850 (1962).

65. S. Tutihasi, Phys. Rev. 105, 882 (1957).

66. B. U. Barshchevskii, Soviet Phys. - Solid State 10, 2930 (1969).

67. K. V. Loskutov, Soviet Phys. - Solid State 8, 766 (1966).

68. V. K. Subashiev, Soviet Phys. - Solid State 6, 1545 (1965).

69. R. S. Van Heyningen and F. C. Brown, Phys. Rev. 111, 462 (1958).

21. D. L. Dexter, Phys. Rev. Letters $\underline{19}$, 1383 (1967).

22. A. Radkowsky, Phys. Rev. $\underline{73}$, 749 (1948).

23. C. Keffer, T. M. Hayes, and A. Bienenstock, Phys. Rev. Letters $\underline{21}$, 1676 (1968).

24. J. C. Slater, Quantum Theory of Molecules and Solids (McGraw-Hill Book Company, New York, 1965), Vol. 2.

25. W. A. Harrison, Solid State Theory (McGraw-Hill Book Company, New York, 1970).

26. R. S. Knox, F. Bassani, and W. B. Fowler, Photographic Sensitivity (Maruzen and Co., Ltd., Tokyo, 1963), Vol. 3, p.11.

27. W. B. Fowler, Phys. Rev. B. (to be published, 1971).

28. B. R. Lawn, Acta Cryst. $\underline{16}$, 1163 (1963).

29. R. S. Bauer and W. E. Spicer, Phys. Rev. Letters $\underline{25}$, 1283 (1970).

30. J. C. Slater, Quantum Theory of Molecules and Solids (McGraw-Hill Book Company, New York, 1963), Vol. 1, p.9.

31. T. M. Donovan, Ph.D. Dissertation, Stanford University, Stanford, California (1970).

32. A. D. Baer, Private Communication (1970).

33. N. V. Smith, Private Communication (1970).

34. F. M. Mueller, Phys. Rev. $\underline{153}$, 659 (1967).

35. G. F. Derbenwick, Ph.D. Dissertation, Stanford University, Stanford, California (1970).

36. B. H. Schechtman, Ph.D. Dissertation, Stanford University, Stanford, California (1969).

37. B. H. Schechtman and W. E. Spicer, Chem. Phys. Letters $\underline{2}$, 207 (1968).

38. J. C. Slater and G. F. Koster, Phys. Rev. $\underline{94}$, 1498 (1954).

39. M. Hamermesh, Group Theory and its Application to Physical Problems (Addison-Wesley: Palo Alto, 1962).

40. M. Tinkham, Group Theory and Quantum Mechanics (McGraw-Hill Book Company, New York, 1964).

41. F. Seitz, Rev. Mod. Phys. $\underline{23}$, 328 (1951).

42. J. A. Krumhansl, in Photoconductivity Conference, edited by R. G. Breckenridge et al., (John Wiley and Sons, Inc., New York, 1956), p.450.

70. E. A. Taft, H. R. Philipp, and L. Apker, Phys. Rev. 110, 876 (1958).

71. M. S. Egorova and P. V. Meikliar, Soviet Phys. JETP 3, 4 (1956).

72. W. Lekfeldt, Nachr. Ges. Wiss. Gottingen Fachgruppe [II] 1, 171 (1935).

73. K. Hecht, Zeit. f. Physik. 77, 235 (1932).

74. R. Fleischmann, Ann. Physik 5, 73 (1930).

75. M. A. Gilleo, Phys. Rev. 91, 534 (1953).

76. L. P. Smith, in Semiconducting Materials, edited by H. D. Henish (Academic Press, Inc., New York, 1951), p.114.

77. C. W. Peterson, Ph.D. Dissertation, Cornell University (1964).

78. W. E. Spicer, in Optical Properties of Solids, edited by F. Abelés (North-Holland Company, Amsterdam, 1970).

79. R. S. Bauer and W. E. Spicer, Bull. Am. Phys. Soc. 13, 1658 (1968).

80. W. H. Kohl, Materials and Techniques for Vacuum Devices (Reinhold Publishing Corp., New York, 1967), p.434.

81. L. E. Brady, J. W. Castle, and J. F. Hamilton, Appl. Phys. Letters 13, 76 (1968).

82. N. J. Carrera, Private Communication (1969).

83. N. Wainfan, Phys. Rev. 105, 100 (1957).

84. R. C. Weast, editor, Handbook of Chemistry and Physics, 48th Ed., (Chemical Rubber Company, Cleveland, 1967) p.D-117.

85. G. Martin, Rev. Sci. Instr. 34, 708 (1963).

86. W. Espe, Werkstoffkunde der Hochvakuumtechnik (Veb Deutscher Verlag der Wissenschaften, Berlin, 1961), Vol. 111, p.336.

87. L. E. Brady, Private Communication (1969).

88. G. L. Bottger and A. L. Geddes, J. Chem. Phys. 46, 3000 (1967).

89. P. C. McKernan, Private Communication (1968).

90. R. P. Riegert, Research/Development, June 1968, p.46.

91. O. S. Heavens, Optical Properties of Thin Solid Films (Dover Publications, Inc., New York, 1965), p.11.

92. H. Reiss, J. Appl. Phys. 39, 5045 (1968).

93. H. P. Klug and L. E. Alexander, X-ray Diffraction Procedures (John Wiley and Sons, New York, 1954) p.494.

94. N. F. Mott and R. W. Gurney, Electronic Processes in Ionic Crystals, 2nd Ed., (Dover Publications, Inc., New York, 1964) Chap. VII, p.227.

95. C. B. Childs and L. M. Slifkin, Brit. J. Appl. Phys. $\underline{16}$, 771 (1965).

96. F. Moser, N. R. Nail, and F. Urbach, J. Phys. Chem. Solids $\underline{9}$, 217 (1959).

97. F. Moser, J. Opt. Soc. Amer. $\underline{51}$, 603 (1961).

98. C. N. Berglund and W. E. Spicer, Rev. Sci. Instr. $\underline{35}$, 1665 (1964).

99. R. C. Eden, Ph.D. Dissertation, Stanford University, Stanford, California (1967).

100. R. C. Eden, Rev. Sci. Instr. $\underline{41}$, 252 (1970).

101. T. H. DiStefano and D. T. Pierce, Rev. Sci. Instr. $\underline{41}$, 180 (1970).

102. A. Ennos, Appl. Opt. $\underline{5}$, 51 (1966).

103. A. Y-C. Yu, Ph.D. Dissertation, Stanford University, Stanford, California (1967).

104. R. S. Bauer and W. E. Spicer, Bull. Am. Phys. Soc. $\underline{14}$, 1166 (1969).

105. R. W. James and E. M. Firth, Proc. Roy. Soc. (London) $\underline{A117}$, 62 (1927).

106. P. R. Vijayaraghavan, R. M. Nicklow, H. G. Smith, and M. K. Wilkinson, Phys. Rev. B., $\underline{1}$, 4819 (1970).

107. W. B. Fowler, Private Communication (1970). The author is grateful to W. B. Fowler for providing the estimates for the effect of lattice-constant variation on the tight-binding band parameters.

108. S. Doniach, Private Communication (1970).

109. P. M. Scop, M.I.T. Solid-State and Molecular Theory Group, Quarterly Progress Report No. 54, October 15, 1964 (unpublished), p.15.

110. D. E. Eastman, Phys. Rev. Letters $\underline{24}$, 310 (1970).

111. J. G. Endriz and W. E. Spicer, Phys. Rev. B., $\underline{2}$, 1466 (1970).

112. A. B. Kunz, Phys. Rev. B., to be published (December 15, 1970).

113. W. E. Spicer and R. C. Eden, IX International Conference on the Physics of Semiconductors, Moscow, July 23-29, 1968, Vol. 1, p.65 (Nauka: Leningrad, 1968).

114. J. L. Shay and W. E. Spicer, Phys. Rev. $\underline{161}$, 799 (1967).

115. R. Bloch and H. Möller, Z. Physik. Chem. $\underline{A152}$, 245 (1931).

116. M. Cardona, Phys. Rev. $\underline{129}$, 69 (1963).

117. R. E. Morrison, Phys. Rev. $\underline{124}$, 1314 (1961).

118. E. L. Kreiger, D. J. Olechna, and D. S. Story, G.E. Technical Information Series No. 63-RL-3458G. (1963).

119. J. L. Shay, "Kramers-Krönig Analysis using B5500 Computer," unpublished (1966).

120. P. O. Nilsson and L. Munkby, Phys. Kondens. Materie 10, 290 (1969).

121. T. M. Donovan, Private Communication (1969).

122. C. N. Berglund and W. E. Spicer, Phys. Rev. 136, A1044 (1964).

123. L. Wallden, Phil. Mag. 21, 571 (1970).

124. H. Ehrenreich and H. R. Philipp, Phys. Rev. 128, 1622 (1962).

125. A. J. Blodgett, Jr., Ph.D. Dissertation, Stanford University, Stanford, California (1965).

126. R. Y. Koyama, Ph.D. Dissertation, Stanford University, Stanford, California (1969).

127. E. C. Bruner, Jr., J. Opt. Soc. Amer. 59, 204 (1969).

128. J. A. R. Samson, J. Opt. Soc. Amer. 54, 6 (1964).

129. K. Watanabe and E.C.Y. Inn, J. Opt. Soc. Amer. 43, 32 (1953).

130. R. Y. Koyama, Private Communication (1969).

131. R. Allison, J. Burns, and A. J. Tuzzolino, J. Opt. Soc. Amer. 54, 747 (1964).

132. R. Canfield and R. Madden, Private Communication (1969).

133. L. W. James, Ph.D. Dissertation, Stanford University, Stanford, California (1969).